MESOSCALE FLOW FEATURES IN THE BEAUFORT SEA

SOME MESOSCALE FLOW FEATURES IN THE BEAUFORT SEA DURING AIDJEX 75-76

by

BHARAT DIXIT

Being a thesis submitted to the Faculty of Graduate Studies and Research at McGill University in partial fulfillment of the requirements for the degree of Doctor of Philosophy.

Department of Physics
McGill University
Montreal Quebec Canada
August 1978

ABSTRACT

Mesoscale (0.1 to 30 km) flow features of the Beaufort Sea are analysed from observations made during the AIDJEX main experiment in 1975-76. The principal portion of this thesis deals with the calculation of the geostrophic currents from the S T D (salinity, temperature and depth) measurements made. These currents and the associated mass transports are compared with the measured currents. The agreement seems to be good. Other oceanographic features studied are baroclinic eddies, step structure, internal wave activity and changes in the mixed layer thickness.

Baroclinic eddies are found to be in nearly geostrophic balance and contribute large amounts of kinetic energy at depths of 100 to 200 m. Their origin is postulated to be in the Chukchi Sea region. Step like structures are observed at depths of 300 to 400 m. These steps are roughly 3 m in height with a salinity change of 0.025 °/₀₀. Internal wave activity was detected in the pycnocline, lasting for about one and one half hours , with a period of about ten minutes and a height of 6 m. Seasonal changes in the thickness of the mixed layer is presented showing the spacial and temporal variability.

RESUMÉ

Les phénomènes d'écoulement à échelle intermediaire (0.1 à 30 km) de la mer Beaufort sont analysés à partir d'observations recueillies en 1975-76 dans le cadre du projet AIDJEX. Cette thèse porte principalement sur le calcul du courant géostrophique (basé sur les valeurs de température, salinité et profondeur obtenues par S T D). Ces courants et les transport de masse associés sont comparés aux mesures directes de courant. La correspondance semble bonne. Parmi les autres phénomènes océanographiques étudiés, mentionnons les turbulences baroclíniques, la structure " en palliers" , l'activité des ondes internes et les variations d'épaisseur de la couche de mélange.

Les turbulences Baroclíniques montrent une balance pratiquement géostrophique et fournissent une importante part de l'énergie cinétique dans la couche de 100 à 200 m. Leur provenance postulée serait la mer de Chukchi. Structures étagée sont observée à des profondeur variant de 300 a 400 mètres. D'une hauteur d'environ 3 mètres, ces "palliers " montrent un changement de salinité d'environ 0.025°/₀₀ . Des ondes internes sont décelées au niveau de la picnocline, se maintenant pendant 1½ heure, avec une période de 10 minutes environ, et une amplitude de 6 mètres. Les fluctuations saisonnières d'épaisseurs de la couche de mélange sont présentées suivant leur variabilité spaciale et temporelle.

PREFACE

The following elements of this thesis are considered to be contributions to original research.

1. The thesis represents the reduction of substantial portion of the oceanographic data collected at AIDJEX. AIDJEX was a unique experiment in which vasts amounts of data was collected over a span of a year at three sites and for six months at four sites. This is equivalent to having four ships at station for a year. The data represent the most extensive time series ever assembled. With the ice as a very stable platform, very high quality and resolution data was obtained. This would not have been possible for shipborne measurements because of the rolling of the ship. The data collected was over a 100 square km area with great coherence in spacial and temporal measurements. The position error was always smaller than 25 m and represents a very high accuracy in position measurement.

2. Time series (for a period of a year) of geostrophic currents and mass transports of the Beaufort Sea area, across one leg of the AIDJEX array.

3. Observation and calculation of the upper mixed layer history and changes for one year at one camp.

4. Step structures at depths of 300 to 400-m that are so far unexplained.

TABLE OF CONTENTS

LIST OF FIGURES

LIST OF PLATES

LIST OF TABLES

ACKNOWLEDGEMENTS

I sincerely thank my research director Dr. Elton R Pounder for suggesting this research project, for giving me needed encouragement and advice throughout the course of the work and for providing valuable insights to the Arctic environment. In addition, thanks are due to Dr. Kenneth L Hunkins (of the Lamont Doherty Geological Observatory) for directing my attention to some of the important aspects of the research.

Thanks are also due to Alain LeBlanc for hours of discussion, criticism, moral support and assistance in the planning of some computer programs.

To Tom Manley and Ed Bauer (of LDGO) many thanks for discussions on the ice, at Palisades N.Y. and at Seattle Wa. as well as for assistance in preparing and compiling the data used in this analysis. To all those who assisted in the data acquisition in the field experiment, especially Paul Peltola and Brian Hill, my sincerest thanks.

I thank each and every member of the Ice Research Project for a pleasant working atmosphere which they created, and a special thanks to Frank J Dias for help in preparing of this manuscript.

Very special acknowledgement of thanks to the personel at Snow Bird in the summer Of 75 - namely Betty Bell, Darrell Brown, Mel Clarke, Richard Heffernan and Phillip Resch - with whom I spent a very special time.

It is a pleasure to also acknowledge the efforts of Betty Pedersen in the typing of the manuscript.

Financial assistance of the National Research Council in the form of scholarships is gratefully acknowledged. Polar Continental Shelf Project provided financial assistance to the AIDJEX program as a whole and to the McGill contribution in particular. This financial assistance is also gratefully acknowledged.

Chapter One · INTRODUCTION

1.1. Introduction

Observation of the Arctic from drifting stations began long before the AIDJEX program, the program from which this work is derived. Systematic records exist from the voyage of the JEANETTE in 1879-81. JEANETTE's was the first long drift in the Arctic Basin. Although the voyage ended in tragedy, the problems encountered in that expedition led to Nansen's epic drift with the FRAM in 1893-96. The FRAM expedition is probably the most efficient and productive Arctic expedition ever conducted.

Sverdrup extricated the FRAM from the ice in 1896 and crossed trails at Spitsbergen with Andree and Froenkel's fatal attempt in 1897 to cross the Arctic in an unpowered balloon. This was the first attempt to explore the Arctic from the air. In the late 19'th and early 20'th century there were many shipborne expeditions to explore the Arctic. The voyages of the MAUD (1918-25) and SEDOV (1937-40) count amongst the more famous.

In 1920 Otto Shmidt, head of the Arctic Research Institute in the Soviet Union suggested the use of aircraft with the drifting laboratory technique shown by Nansen. In 1937, a drifting station, known as NORTH POLE 1, was set up near the pole. This was the forerunner of the type of stations used in the AIDJEX experiment. The drift of the station NP1 is shown in Fig. 1.1.

After the initial NP1 station the Soviet work in the Arctic was slowed down. In 1954 they established NP2. In addition to these drifting stations, the Soviets had flying laboratory stations where

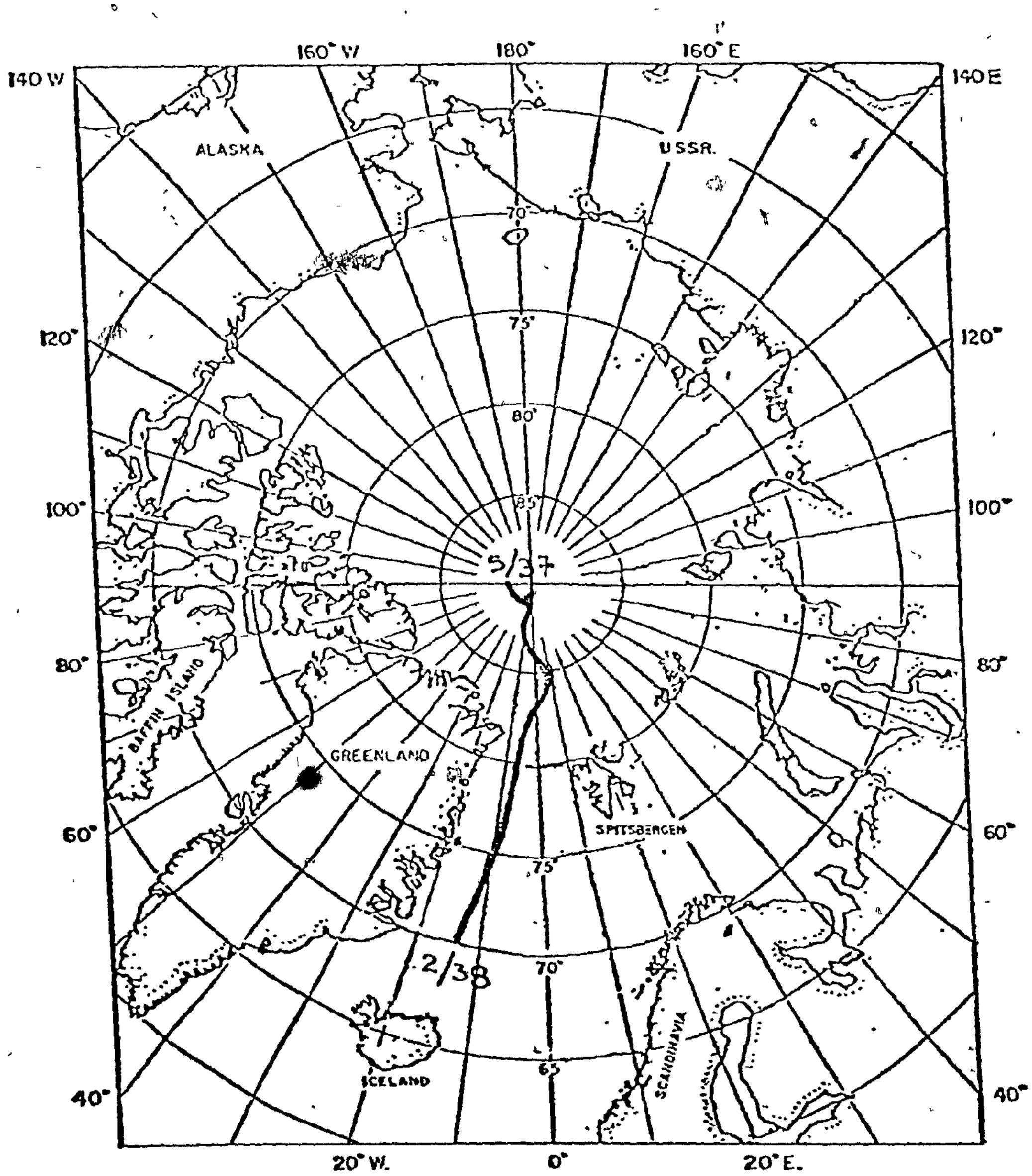

Fig 1.1 Drift track of ice station NORTH POLE - 1 (NP-1)
May 1937 to Feb 1938

they used aircraft to study the north. By 1956 the Soviets had, at one time or another, camps and data from all over the Arctic, as seen in Fig. 1.2. It is worthwhile to note however, that the Beaufort Sea had been sparsely covered. The Soviet program for Arctic understanding is continuing and at present they are manning NP27 in the Canadian Arctic.

The American initiative got underway in 1950 when an experimental camp was set up on the ice north of Barter Island but ice movement soon destroyed the camp.

In 1952, the Americans established a station on Fletcher's ice island - T-3, a tabular piece of shelf ice that had been under surveillance for more than a year. T-3 had been manned, more or less continuously, until it was abandoned in 1974. The drift of T-3 in the Beaufort Sea area is shown in Fig. 1.3.

BRAVO and ARLIS-II are other ice islands that have been manned to study the ice movement and the Arctic environment. Ice islands are an ideal platform to study the oceanography of the Arctic Ocean. Ice islands, like T-3, are huge pieces of shelf ice - presumably broken off from the Ward Hunt Ice Shelf. Although able to go anywhere, these ice islands have deep draughts - an atypical feature of the Arctic ice cover, and create peculiarities of their own when taking ocean measurements. T-3, for example, has a thickness of approximately 25 meters.

AIDJEX - an acronym for Arctic Ice Dynamics Joint Experiment was proposed in the late 1960's to study the ice motion and the ocean parameters. Ice stations, of AIDJEX, are manned camps on the pack ice and are more typical of sea ice encountered in the north (thickness typical 1-3 meters). Details of the AIDJEX experiment, as it pertains to this work, are in the following chapter.

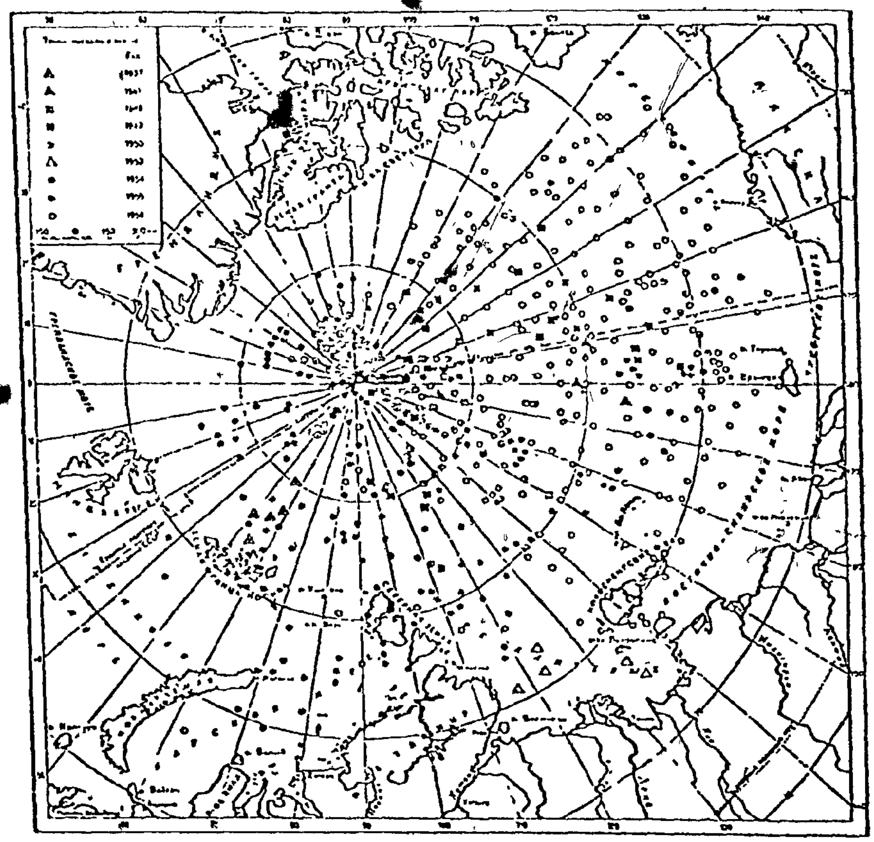

Fig 1.2 Geographical distribution of all Soviet stations during the period 1937 to 1956. (after Fletcher 1968)

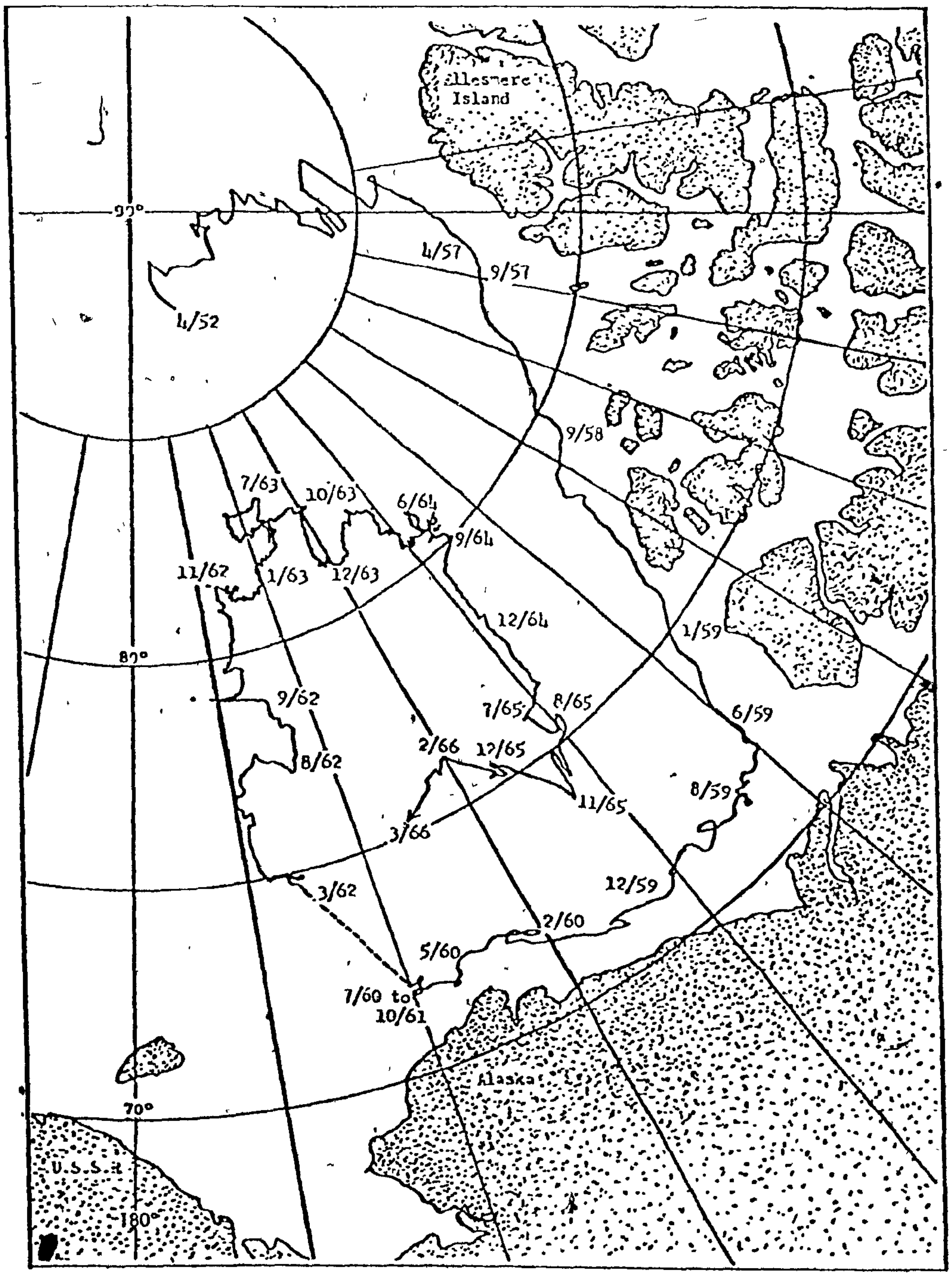

Fig 1.3 Drift track of Fletcher's Ice Island , T-3 , from April 1962 to March 1966. (Schindler 1968)

As part of the continuing understanding of the Arctic, McGill University annually sends people to study the oceanography of the Arctic. In 1979 or later the proposed Nansen Drift experiment is to begin. In this experiment, the U.S. icebreaker BURTON ISLAND will be allowed to drift with the ice in an attempt to duplicate the famous FRAM voyage.

Our ideas of the circulation of the Arctic Ocean, more particularly of the Beaufort Sea, is based on data collected over a 75-year span. The vertical subdivision of the water column into the various water masses, the dynamic height analysis and the distribution of temperature, salinity and densities are obtained from ice stations and the flying laboratory stations described above. (Timofevyev 1960; Coachman and Barnes 1961, 1962, 1963; Coachman 1963)

These historical data provide us with long-term mean fields for the parameters like temperature and salinity but little information can be extracted about time dependent phenomenon. Farmer (1960) and LeBlond (1964) report results on theoretical studies on long-term time dependent motion. AIDJEX modelers are also working on models to predict the motion of ice and explore dynamic and time dependent currents of the Arctic. (Pritchard et al, 1976; Colony and Pritchard, 1975; Brown, 1975; McPhee, 1975; Solomon, 1970; and many others). Measurements have been difficult to obtain in long time series because of logistic problems in maintaining and establishing stations to get oceanographic data.

1.2 Physical Oceanography

The Lomonosov ridge lies between the New Siberian Islands and Ellesmere Island, dividing the Arctic Ocean into two major basins, the Amerasia and Eurasia Basins. The Eurasia Basin is bounded by the Lomonosov ridge, Kara and Barents Seas, Spitsbergen and Greenland.

Its floor lies at depths greater than 4200m. This Basin is connected with the Atlantic Ocean via the Norwegian and Greenland Seas. Large amounts of water are exchanged between the Atlantic and Arctic Oceans through the opening between Spitsbergen and Greenland. In the Norwegian Sea the relatively warm and saline waters of the North Atlantic Current and the cold, fresher water of the Arctic Ocean meet and this is where most of the Arctic Ocean water gets its characteristics.

On the Pacific side of the Lomonosov ridge, there are two major basins, the smaller Makarov Basin and the larger Canada Basin. The Canada Basin is bounded by Alaska and Siberia and has a flat floor at about 3800m. The Beaufort Sea, which lies west of the Canadian Arctic islands and north of Alaska, is physiographically an integral part of the Canada Basin. The Canada Basin is linked to the Pacific Ocean via the Bering and Chukchi Seas. The Bering Strait is narrow and shallow limiting the water exchange with the Pacific to the near surface waters. The influx of the Pacific water influences the upper 150m of the Canada Basin water. The bathymetry of the Beaufort Sea, the Canada Basin is shown in Fig. 1.4. The major features are taken from the Canadian Hydrographic Service Chart # 897 (coverage 90°W to 180°W, north of 72°N - as discussed and interpreted by DeLeeuw (1967)). The central and major portion of the Canada Basin consists of the deep, flat,

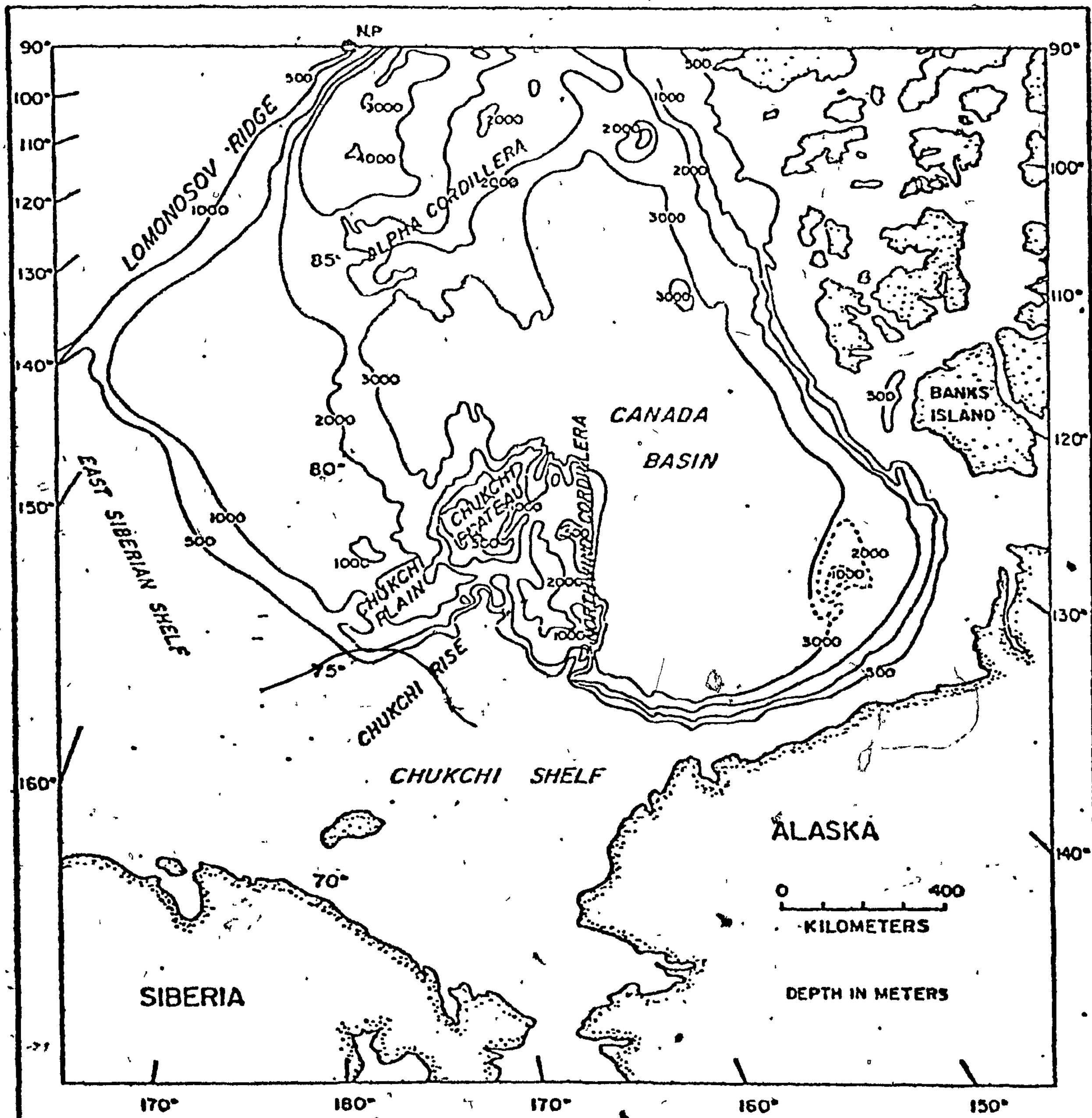

Fig 1.4 Bathymetry of the Canada Basin.

abyssal plain. On the eastern boundary is a rather wide continental slope rising steeply (1 : 50) to the shelf break at 500m. The southern boundary, added to DeLeeuw's chart from H.O. chart 15, 254-2, contains the narrow northern continental margin of Canada and U.S. and is steeper (1 : 25) with a shelf break at 250m. The major complex topographical feature, which forms the western boundary of the Canada Basin is called the Chukchi Province. It extends between 155°W and 175°W to a latitude of nearly 80°N. While there are shallow depths (less than 500m), in the northern part of the Chukchi Province, depths in excess of 1000m exist continuously across its southern portion (74-76°N).

1.3 Water characteristics

In Fig. 1.5, 1.6 and 1.7 we have a typical distribution, with depth, of temperature (T), salinity (S) and Sigma-t - a measure of density (σt) for the Canada Basin. Changes in the general shape of these profiles with time are relatively minor. The thickness of the mixed layer changes with time (described later) but the main features are consistent throughout the year. The T-S diagram for this water column is presented as Fig. 1.8. From T-S diagrams such as this we can identify the primary water masses and give some idea of their spreading throughout the basin (Coachman and Aagaard 1974). The four types of masses identified are

1) The Arctic surface water, from 0-50m, coinciding in the winter with the upper mixed layer. This is of great importance because of the frictional effects due to the ice motion occurring primarily in this layer. Water intrudes into the Arctic basins from both the Atlantic and the Pacific sides spreading

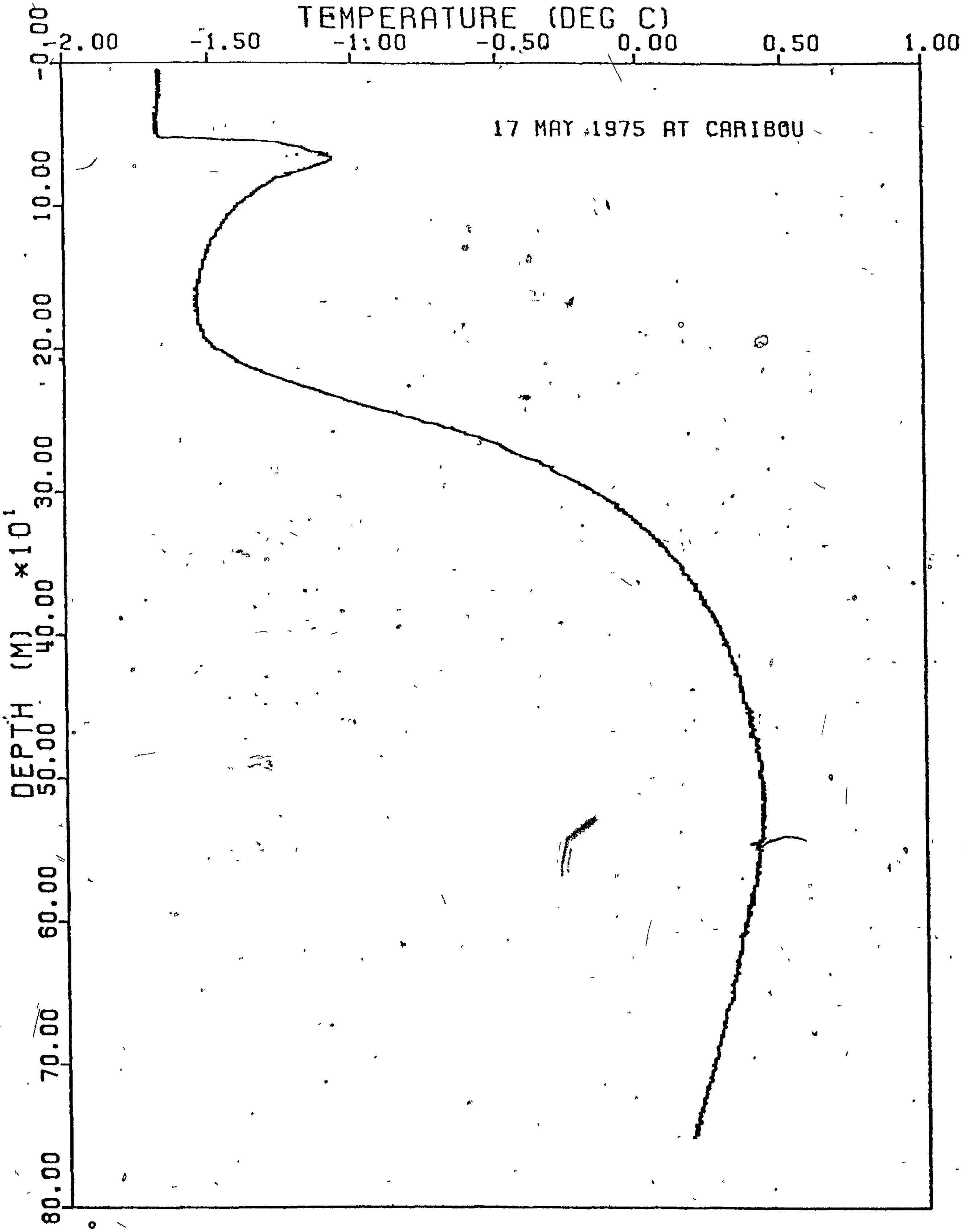

Fig 1.5 Typical temperature profile of the Beaufort Sea.

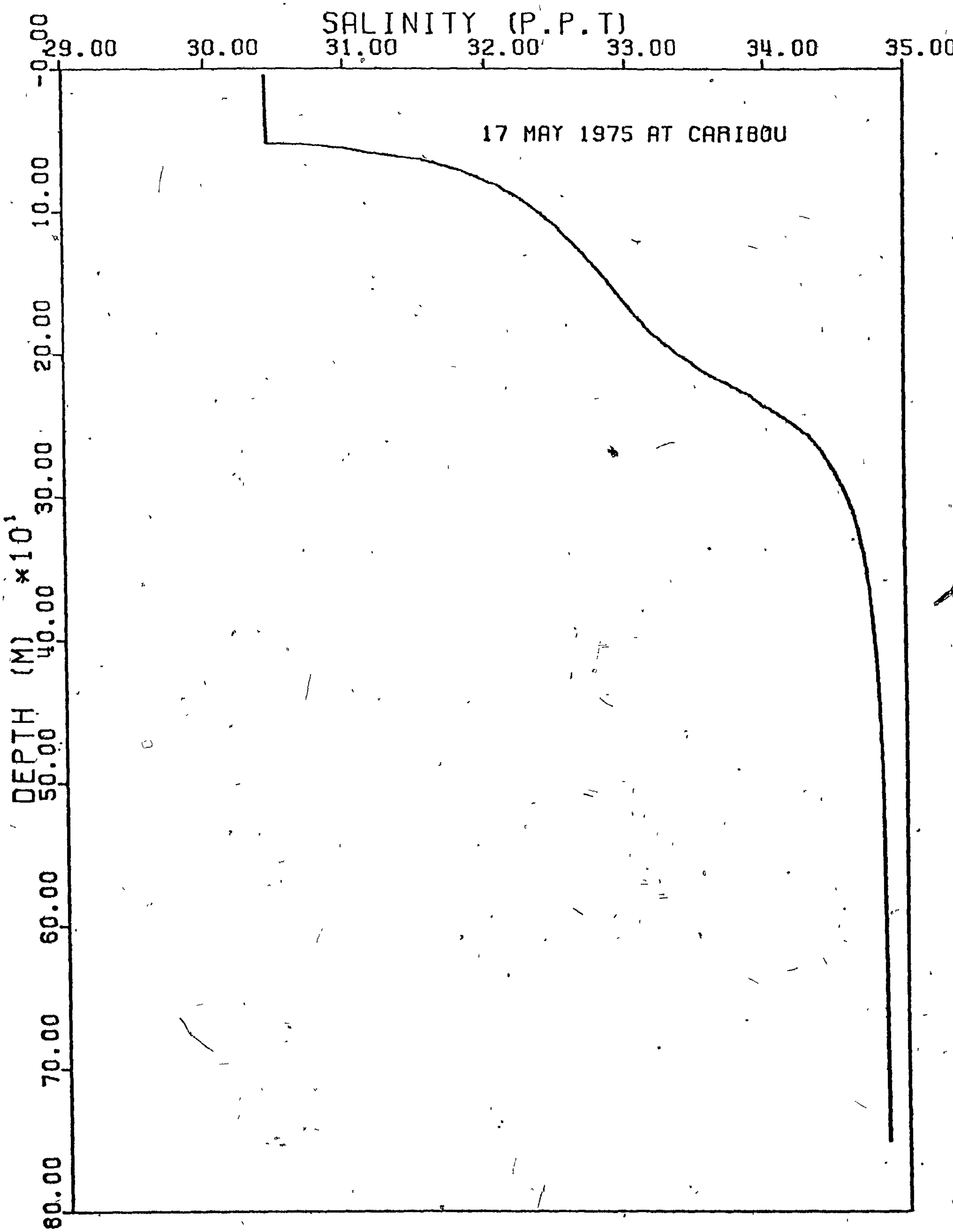

Fig 1.6 Typical salinity profile of the Beaufort Sea.

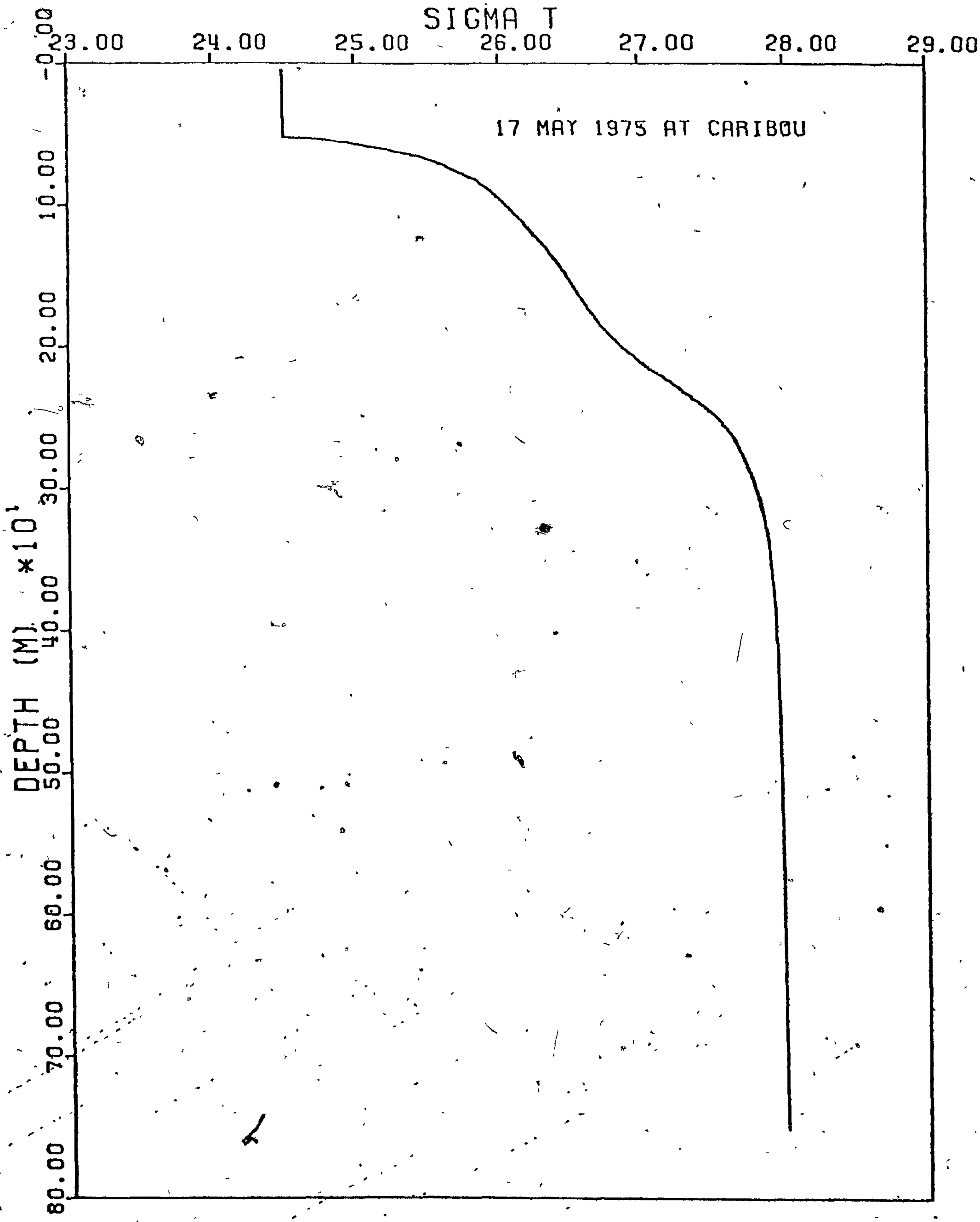

Fig 1.7 Typical density (σ_t) profile of the Beaufort Sea.

Fig 1.8 Typical T-S diagram for the Beaufort Sea.

T S DIAGRAM CARIBOU

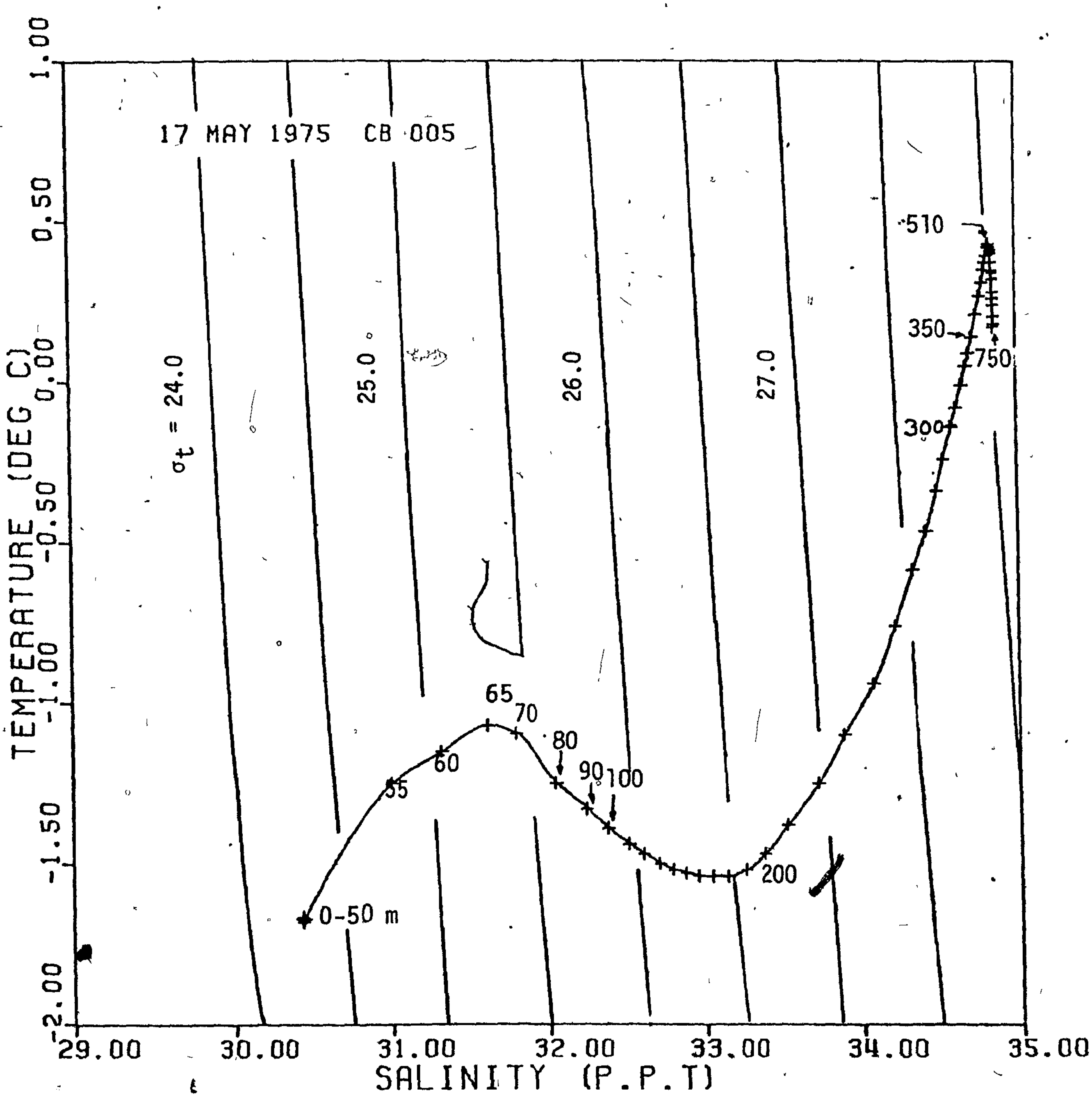

horizontally, essentially along isopycnal lines. The lower layers arrive here by this means.

2) The Pacific water occupies a level between 50-200m in the Beaufort Sea area (AIDJEX array - see chapter 2) and is the area of high kinetic energy with dynamic importance to exchange processes.

3) The Atlantic water, 200-900m depths, does not appear to be of such high kinetic energy but is a very large part of the water column.

4) The Arctic bottom water lies from 900 to the bottom of the ocean at 3800m.

The Arctic surface water is generally cold (less than -1°C - at or near the freezing point) and of relatively low salinity (28-30 $^{0}/oo$). This layer is characterised by its near homogeneity. The low salinity is maintained by the inflow of fresh water from the continental sources and the melting of about one and one half meter of snow and ice each summer. This fresh water is mixed to some extent with the underlying sea water through differential ice movements and through wind mixing of ice free areas. The surface salinity rarely falls below 28 $^{0}/oo$. Vertical convection occurs when dense water is formed at the base of the ice by salt exclusion during freezing (Pounder, 1963) and the mixing induced by the ice motion maintains the layer in a relative homogeneous state. This layer deepens with the approach of winter and is as deep as 60m (see later chapters for T-S diagrams and other profiles for mixed layer changes).

The Pacific water has a relative maximum of about -1°C at about 70m (i.e. just below the Arctic surface layer). This water is more saline but cooler till we get to the relative minimum of about -1.5°C at approximately 150m. This is maintained by the flow of cold water that comes from the Bering Strait.

Under this lies a core of warm water that is of Atlantic origin at depths of 200-900m. The Atlantic water enters the Norwegian Sea along Norway at the surface, where it is cooled and thus its density increases to such a degree that when it flows into the Arctic Basin near Spitsbergen, it slips below the Arctic water occupying depths from 150-200m and down as far as 900m. The temperature of the core when it enters the Arctic Basin may be +2 to +3°C but within the basin it continually cools so that the Atlantic water in the Beaufort Sea has a temperature of +0.5 to +0.6°C.

The Arctic bottom water has a temperature around 0°C and a uniform salinity of approximately 34.93 $^{o}/oo$. The bottom water is also formed in the Norwegian Sea but in this case only in the winter. At this time there is evidence that vertical convection reaches to great depths and also there is some mixing between the bottom water and the lower Atlantic water. The circulation of this water is generally unknown.

A comment on the profiles of water columns here is that since the temperature of the water is low, the density is almost exclusively a function of salinity. The σt profile closely resembles the salinity profile.

1.4 Circulation

Data on currents and wave motion in the Arctic Ocean are even scarcer than those on temperature and salinity. The surface circulation picture can be obtained (rather sketchily) by observing the drift tracks of the ice stations and ice islands. Current measurements show that on the average the drifting stations and the surface water tend to move in similar directions at similar speeds. There could be, however, considerable variations between them over shorter periods.

The circulation of the Arctic is in part created by density differences and in part is wind-induced. This is confirmed by theoretical studies. The net effect of the tides is unknown (and is looked into later).

The surface waters from the whole of the Eurasian side of the Arctic Ocean tend to move toward the North Pole. This flow is of the size 2-3 cm/s, but after passing the region of the pole, the flow becomes more concentrated and then exits from the basin and is called the East Greenland Current. In the Beaufort Sea, the surface waters have a clockwise (anticyclonic) movement. This is a result of the general wind pattern, such that they tend to flow to the southwest along the shelf off the Canadian Arctic islands and to the north in the area north of the Bering Strait. The anticyclonic gyre is also called the Beaufort gyre and was observed first by Worthington (1953) and has later been confirmed by many investigators (Coachman and Barnes, 1961; Gudkovich, 1959; Worthington, 1959). Fig. 1.9 shows the general surface circulation of the Arctic Ocean.

Newton (1973) has done calculations to obtain the circulation of the Atlantic water inferred from the percentage retention of its

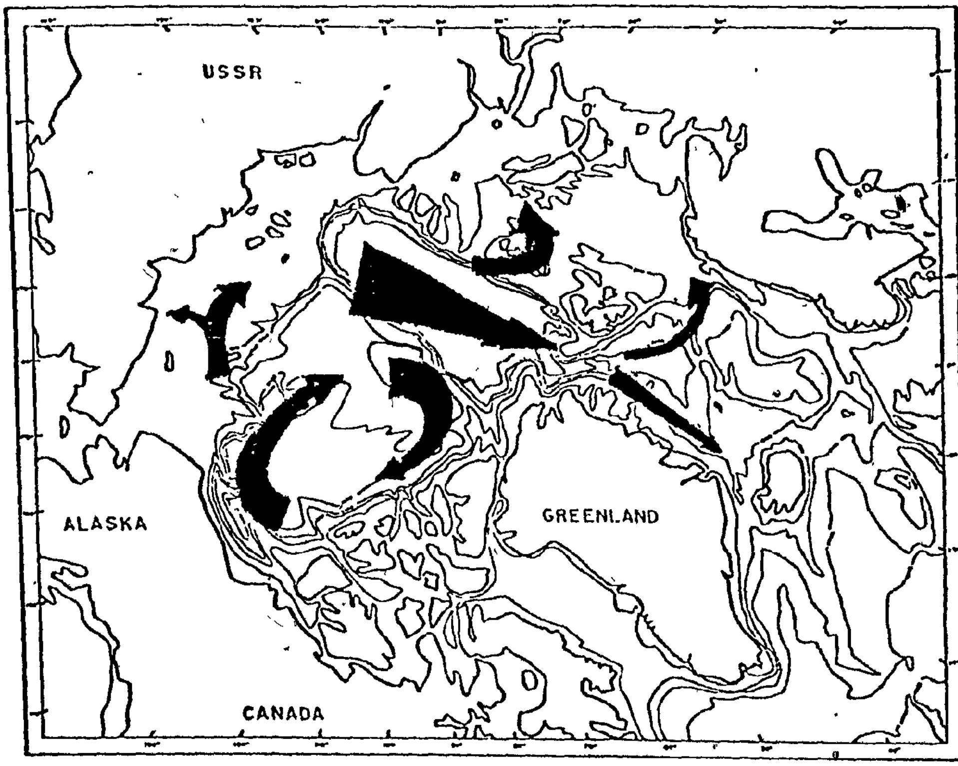

Fig 1.9 Principal features of the surface water movement in the Arctic Ocean.

characteristics (Fig. 1.10). The movement of the Atlantic water is anticyclonic and in agreement with that suggested by Worthington (1959) and Coachman and Barnes (1963). These have also been verified by deep current measurements.

1.5 Ice Cover

The waters of the deep Canada Basin are covered with ice throughout the year. The total ice cover is made up of smaller individual units of ice separated by leads, areas of thin ice and pressure ridge systems. The net effect is an ice cover of 8/10 to 10/10 concentration over the deep basin that varies in thickness from 1-3 m. (U. S.N. Hydrographic Office). In the winter the ice cover over the shallower continental shelf area is more concentrated (10/10) than over the deep basin. In the summer (August-September) open water may be present 100 km or more out from the coast (U.S.N. Hydrographic Office, 1958).

The pressure ridges provide relief of a few meters above and ten meters or so below the mean ice level. The leads provide an interface across which heat and water vapour are transferred to the atmosphere. (Badgley, 1967). The dense water thus formed, possibly localises a mechanism of convection for downward transfer of momentum. The net effect of the ice cover on the Arctic Ocean flow field has not been well determined. The surface and bottom topography of the ice cover affects the transfer of momentum from the wind fields to the ice and from the ice to water (Smith, 1971). Galt (1973) suggests that forcing on space scales smaller than the storm space scale may be an important result of the ice cover.

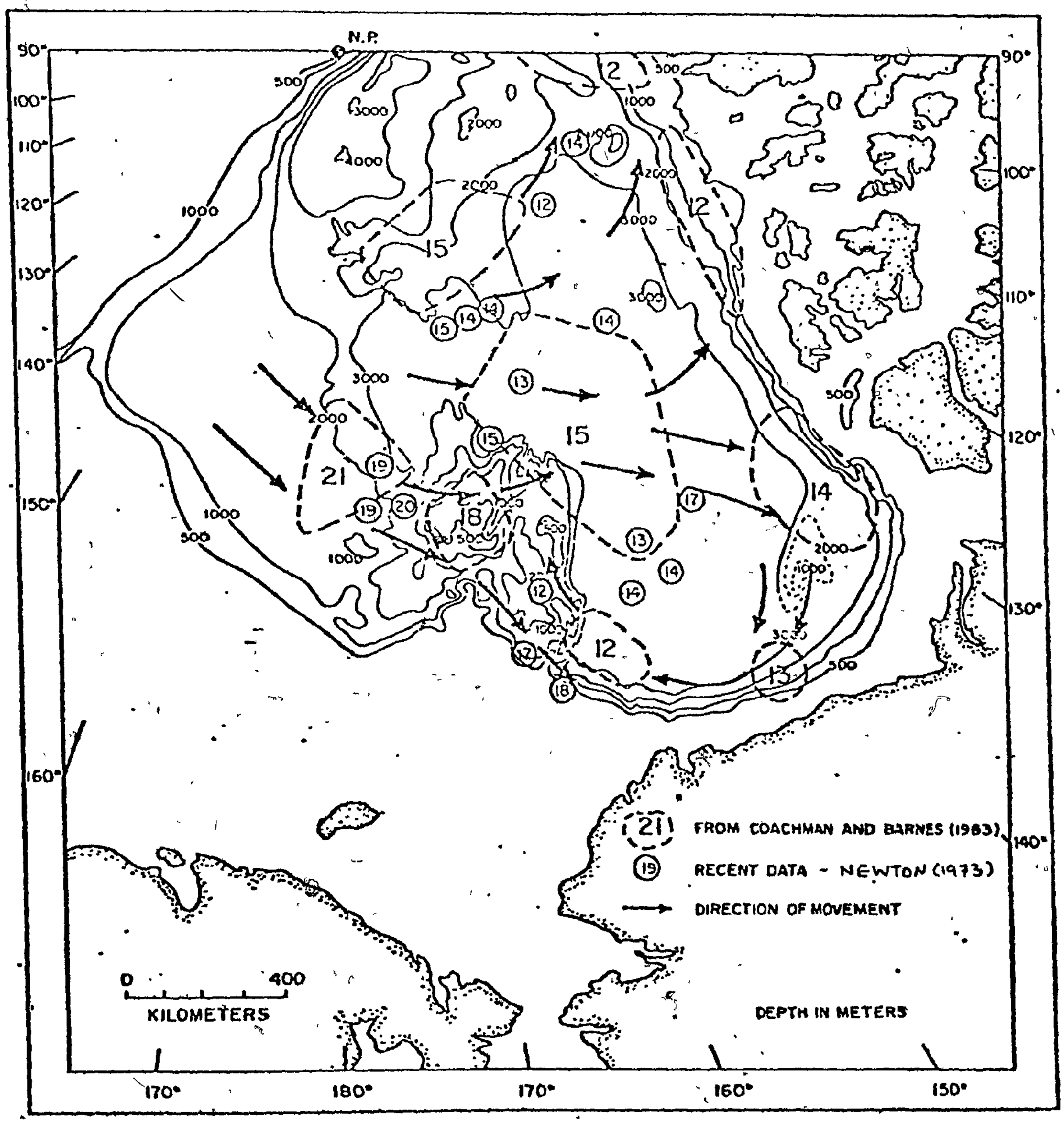

Fig 1.10 Circulation of the Atlantic water inferred from the percentage retention of characteristics. (Newton , 1973)

1.6 Atmospheric Conditions

The mean long-term average atmospheric pressure, the direction and magnitude of the wind stress computed by Campbell (1965) from Felzenbaum (1958) from pressure distribution is shown as Fig. 1.11.

The mean atmospheric circulation over the Canada Basin is dominated by a High centered approximately 78°N and 140°W. The wind stress is generally to the west along the southern part of the basin and to the northeast in the northern part. From the wind stress pattern the magnitude of the wind stress curl was calculated and is shown by dashed contours. The predominant feature of the wind curl distribution is the region of large negative curl over most of the Canadian Arctic islands.

1.7 Thesis Objective

The Arctic Ocean presents an environment for study that is ideal in many respects but is physically and economically more expensive to study than other areas of the world's oceans. The practical aspects dictate what oceanography can be attempted and this factor is so large that in the Arctic, scientific study must be an international effort. The ocean is complex and a great number of periods and scales are involved in the oceanic phenomenon. As Stommell pointed out "a single net does not catch fish of all sizes" (Stommell, 1963). Thus, some choice must be made about the problem to be studied in terms of time and space scales, and then the appropriate technique selected. AIDJEX was just such an experiment where an international effort was made to study the problems of ice dynamics. The AIDJEX experiment is described in detail in the next chapter.

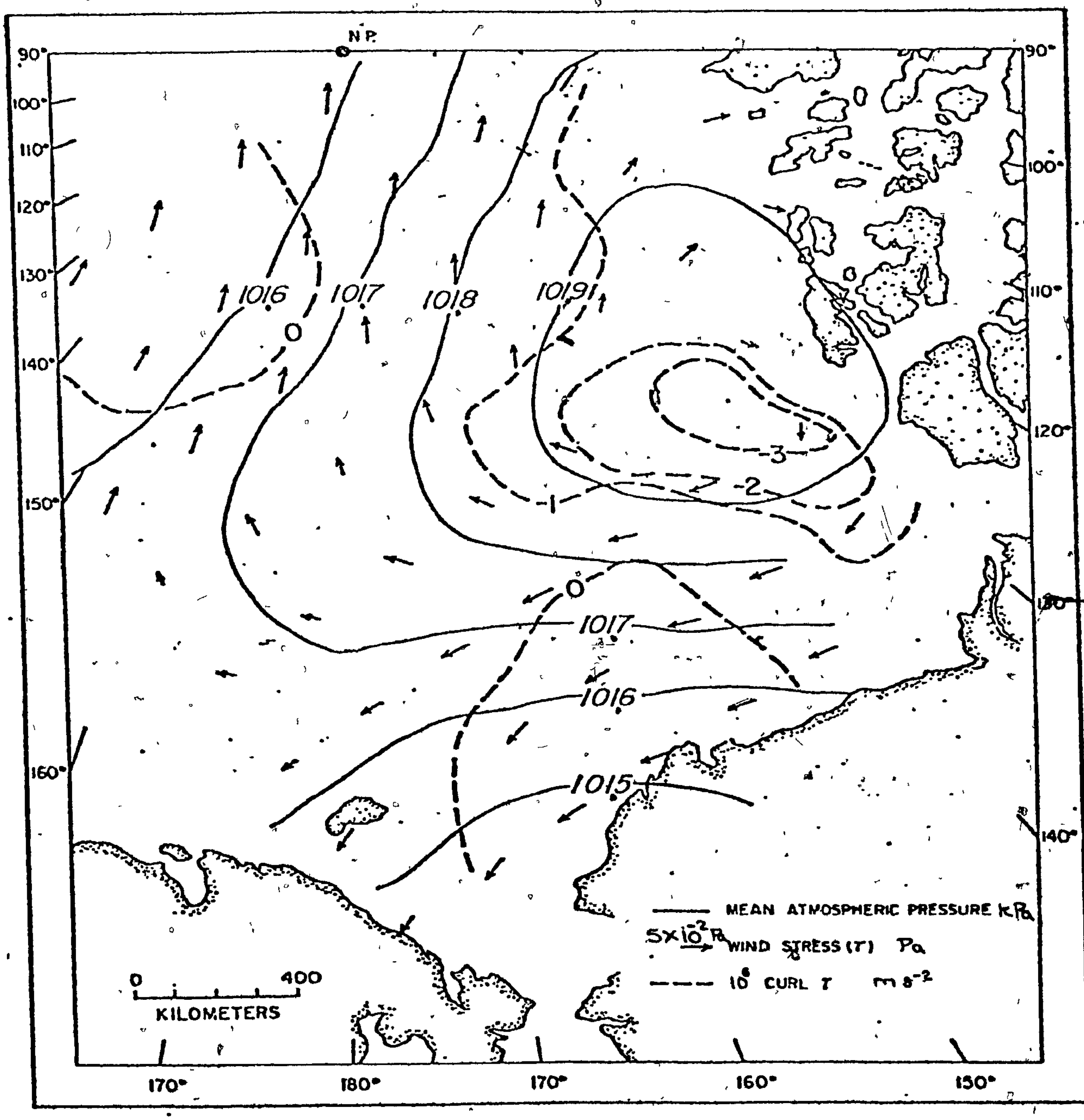

Fig 1.11 Long term mean atmospheric pressure (—) (Campbell , 1965 after Felzenbaum , 1958), wind stress (➞) (Campbell , 1965), and wind stress curl (---) . Length of wind stress legend vector indicates a stress of 5 x 10^{-2} Pascal.

This thesis is concerned with the analysis of the mesoscale flow features of the Beaufort Sea. The space scales are considered macroscale when contributions from individual features to the deformation of the ice pack are obscured and the ice can be considered as a continuum. Length scales are at least 30 km and are perhaps as much as 200-300 km. Motion which arises from the interaction of a small number of adjacent ice floes are defined as mesoscale motion. Motion occurring over distances of 0.1 to 30 km may, somewhat arbitrarily, be described as mesoscale. Phenomenon which occur in a single unbroken piece of ice or which involve fracture systems are defined as microscale. The oceanographic features studied include the geostrophic current, baroclinic eddies, step structure, internal wave activity and mixed layer changes.

Chapter Two FIELD EXPERIMENT

2.1 Overview

The Arctic ice cover has been studied scientifically since 1893 and is no longer thought of as a solid plate covering the ocean but as a continually moving, breaking and shifting layer under the stress and strains of the atmospheric and oceanic forces. The basic nature of the ice dynamics has been understood for decades: an ensemble of irregularly shaped, interlocking pieces of ice driven by air and water currents, influenced by internal stresses, deflected by the earth's rotation and subject to melting and freezing as dictated by regional climate. Very generally the ice dynamics can be written down as Newton's second law, i.e.

$$\rho_i h \frac{d\bar{V}_i}{dt} = \bar{\tau}_a + \bar{\tau}_w + \bar{D} + \bar{G} + \bar{R} \tag{2.1}$$

where the five major forces are

τ_a - wind stress at the air-ice interface.

τ_w - water stress at the water-ice interface.

D - the Coriolis force.

G - pressure gradient force, due to the tilting of the sea surface on which the ice floats.

R - internal stress, the stress transmitted thorugh the ice pack.

with

ρ_i and v_i as the ice densities and velocities and h as the ice thickness.

Without going into the exact nature and forms of these forces, it has become clear that significant progress is possible by acquiring a set of synoptic (rather than single station) data. AIDJEX, standing for

Arctic Ice Dynamics Joint Experiment, was conceived in November 1969, for just such a purpose.

After many workshops and consultations a final version of the AIDJEX scientific plan was set up in 1972. By this time two small pilot projects in the field had been performed (in 1970 and 1971). A larger pilot study with three manned camps and several automatic data buoys took place in March-April 1972. The main experiment was launched in March 1975. By early June 1975, four manned camps surrounded by a ring of eight data buoys were in operation. With the exception of the break-up of the main camp in October 1975, this array continued to function until its scheduled end in May 1976. AIDJEX has been the largest and most costly effort of its type to date and has produced a better understanding of the ice dynamics and the atmospheric and oceanic environment. The data analysis in this work is from data collected during the main experiment of AIDJEX in 1975-76.

In the final version of the scientific plan for AIDJEX in 1972, four basic questions were posed.

1) How is the large scale ice deformation related to the external stress field?
2) How can the external stresses be derived from a few fundamental and easily measured parameters?
3) What is the mechanism of ice deformation?
4) How do ice deformation and morphology affect the heat balance?

Untersteiner (1977)

The observation program, the methods used in data reduction, and the concepts employed in comstructing a theoretical sea ice model were designed to provide answers to the above basic questions. But these led to four more basic questions of their own -

1) Were the scales of observation chosen correctly?

2) Were the right observations taken?

3) Was it possible to deduce external stresses to sufficient accuracy?

4) Did the model development advance our understanding of sea ice mechanism and heat balance?

The answers seem to be a qualified "yes". A brief summary is attempted below, on these four major questions.

1) Scales of observation

It was noted that some observations cannot be made by automatic devices and that they need manned camps. A minimum of three is needed to resolve the horizontal strain tensor. This was increased to four, to build in redundancy and to provide an increased number of strain nets. In addition, the project had ten data buoys to get parameters from outside the manned array. The array had to be relatively close to shore for logistic manageability and yet far enough to be free of coastal effects.

Initially, the scales of motion were known for the atmosphere, but the scales of motion in the ocean were not. Early observation from T-3 and AIDJEX 72 showed inertial motion and eddies with a space scale of several tens of kilometers (Hunkins, 1974b). The large scale anticyclonic gyre (of space scale approximately 1000 km) of the Beaufort Sea has been known for a long time, but its synoptic monitoring by an array of manned camps of appropriate size was not feasible.

Scales of the ice motion were least well known. According to the drift data from earlier long term stations in the Arctic Basin, the power spectrum of velocity has a maximum at low frequency (seasonal) and decreases to negligible power at about 2 cycles per day. As a compromise between expected scales of motion in all media, the number of observation points, the array was chosen to be 100 km for the manned array and 1000 km for the data buoys. This choice is small for large scale motion and big for smaller eddy scale of motion in the ocean. For the study of subsurface eddies, we would have liked a higher density of points.

2) Choice of measurements

In the case of air stress, water stress and ice velocites there was little question about what parameters needed to be measured, and how the measurements should be made. This is described later in this chapter. A less clear cut case can be made for ice thickness measurements. Greater emphasis could have been placed on the ice thickness distribution since it has a great role in the ice dynamic equation.

3) External stresses

The 1972 pilot study showed that the surface pressure maps produced by the U.S. National Weather Service are based on data insufficient for the preparation of geostrophic wind charts of the Beaufort Sea. To avoid this problem additional pressure measurements were made at the data buoy sites. Geostrophic winds calculated from these data proved consistent with the measured surface winds. The water stress was determined with an accuracy comparable to that of the air stress (Pounder and LeBlanc, 1977; Langleben, 1977). In the determining of the drag coefficient at the underside of the ice it was particularly useful to study the ice drift during the summer months, when the internal stresses were small and the drift is essentially wind driven.

4) Sea ice mechanics and heat balance

One of the initial concepts of the AIDJEX modeling effort was derived from a study of a floe-to-floe interaction and the realization that pressure ridges can be formed by loading the edge of a thick ice with rubble from thin ice. In terms of its constitutive (stress as a function of strain) behaviour, the ice is modeled as an elastic-plastic continuum (Coon, 1977; Coon et al 1974) which under certain stresses may develop small scale as well as large scale discontinuities.

It was also found that during the summer the internal stress was absent and the ice drift was purely wind driven. During spring and winter the internal stress is important and in one case caused a shear discontinuity several hundred km long. The divergence of the internal ice stress may be derived as a residual of the equation of motion, 2.1. It may also be obtained by postulating a constitutive law and evaluate the strain rate and its derivatives at the position of the manned camps. The ice stress thus calculated is still a bit too low, and, as pointed out earlier, the ice thickness distribution is not well known. As a result it often had to be assumed as initial conditions for the model.

2.2 Description

The manned array, together with the data buoy configuration is shown in Fig. 2.1. The manned camps were deployed in a triangular array with one (main) camp located inside the triangle. The camps were assigned radio call names and are identified as such. The main camp was Big Bear with Caribou, Blue Fox and Snow Bird as the satellite

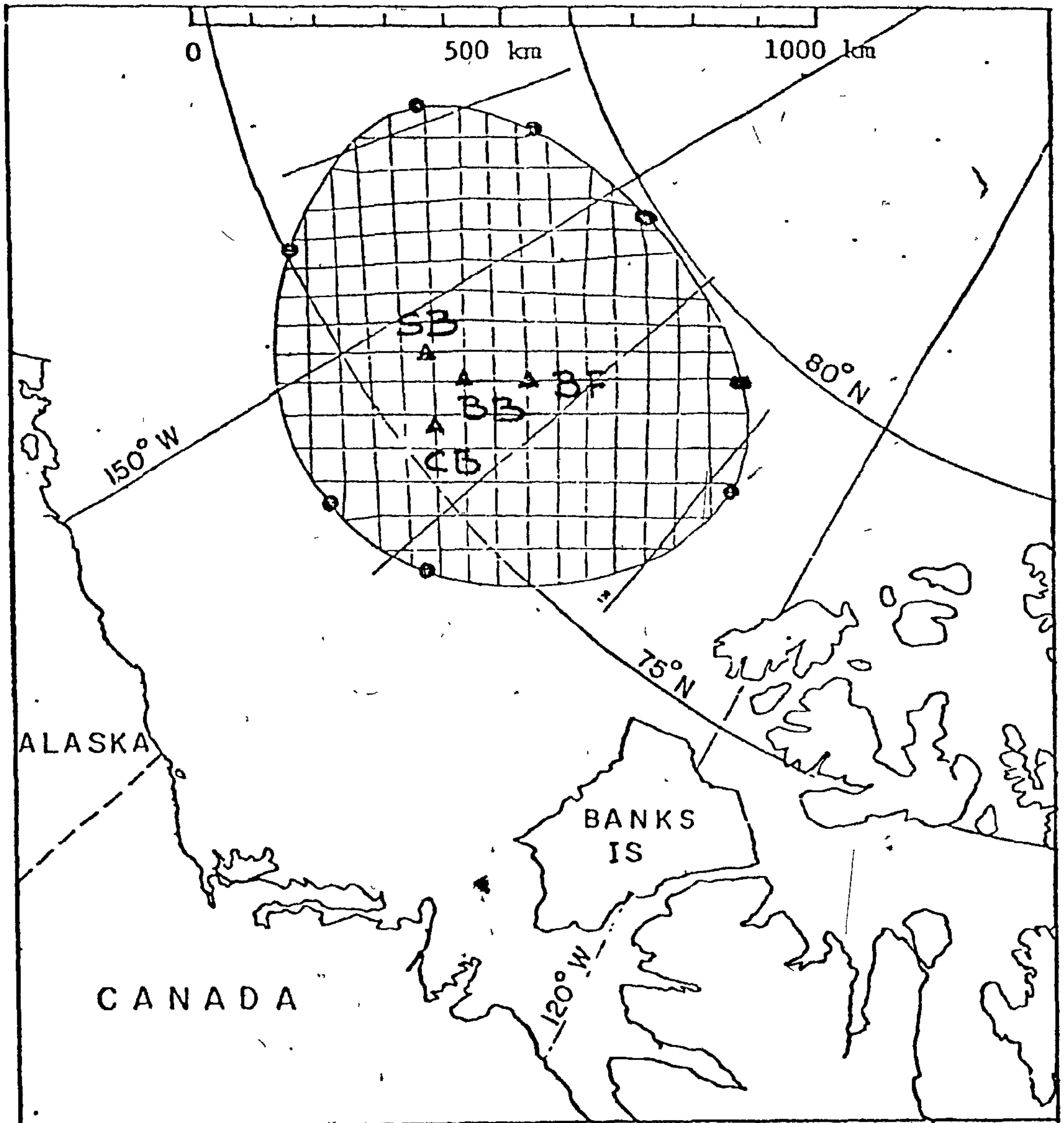

Fig 2.1 The manned AIDJEX array on 15 may 1975. The manned camps are denoted by triangles with the symbols BB , CB , BF and SB standing for Big Bear , Caribou , Blue Fox and Snow Bird respectively. Data buoys are located by dots. The gridded area shows where the data was collected.

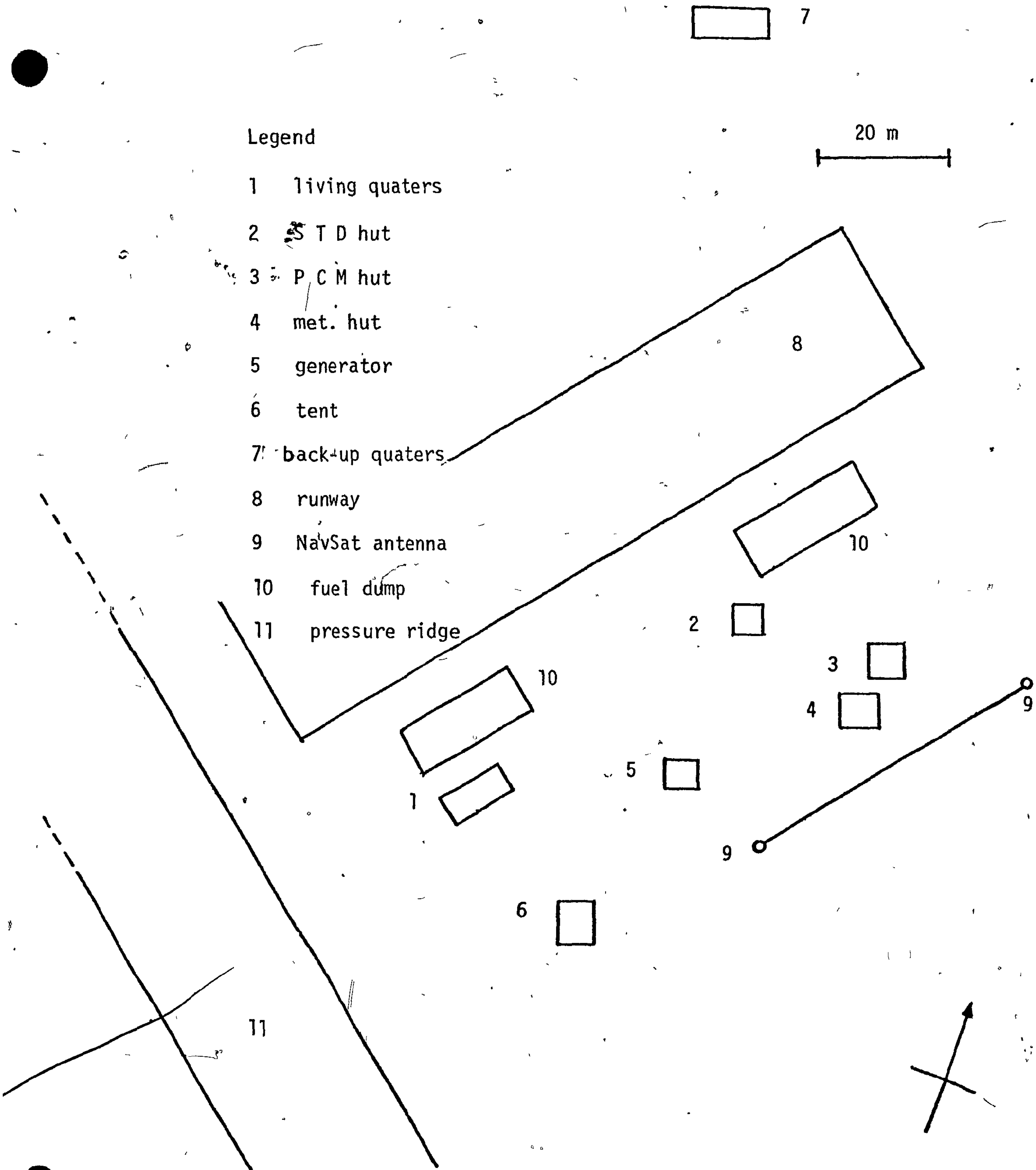

Fig 2.2 Layout of a typical satellite camp (Snow Bird)

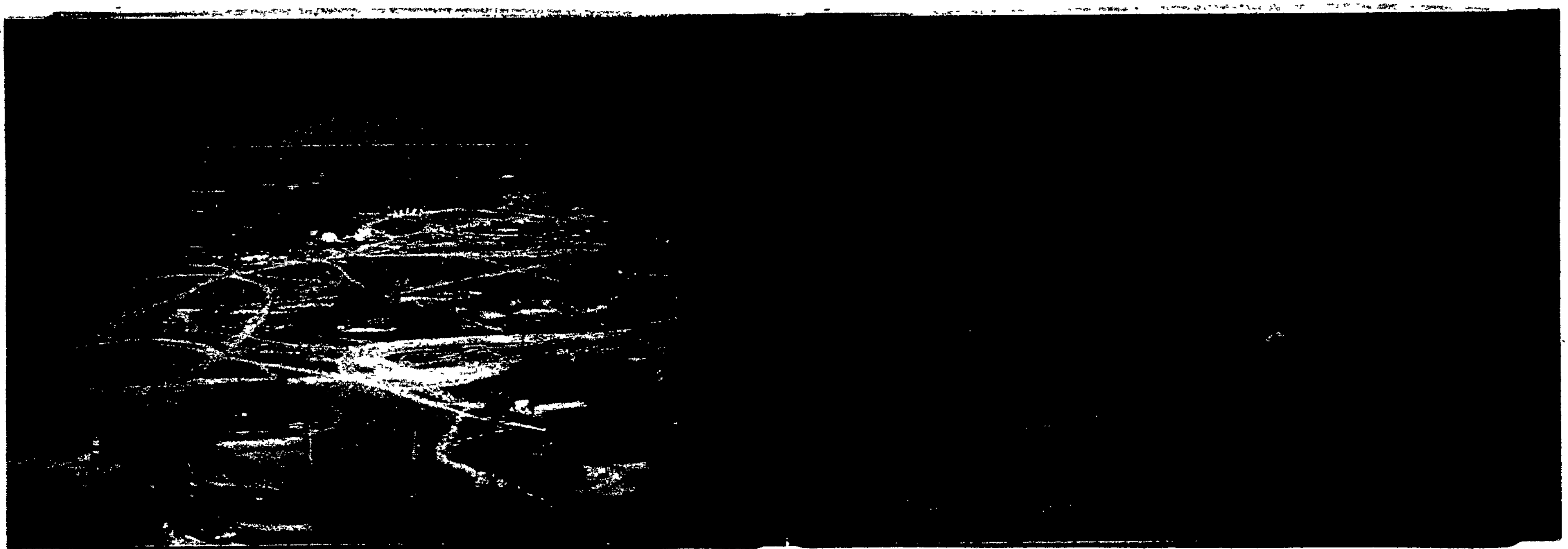

Plate 1   Main manned camp Big Bear of AIDJEX 75

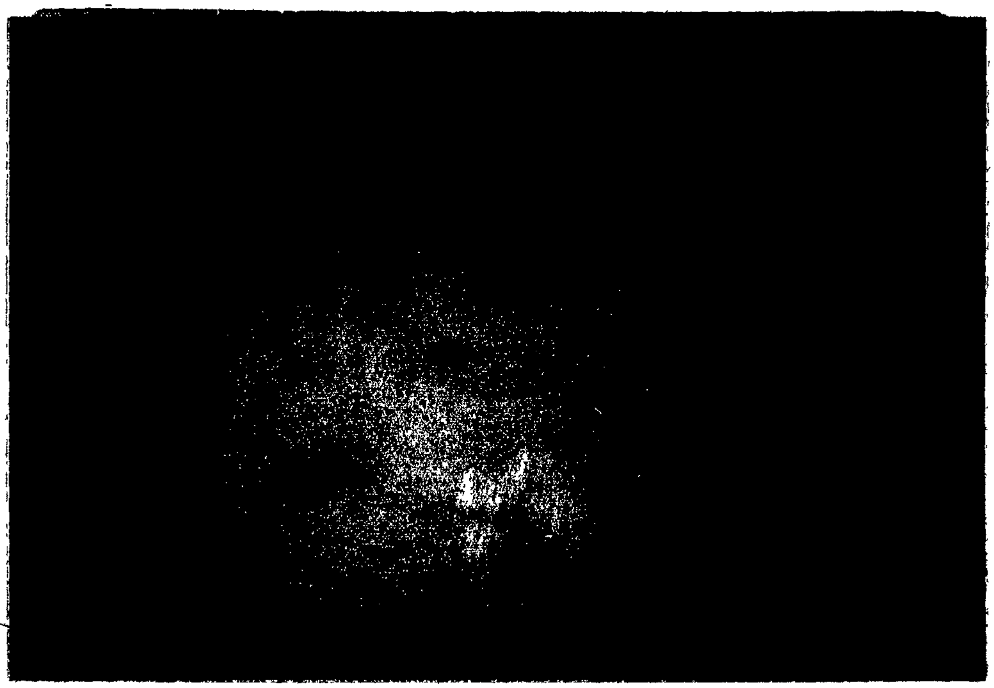

Plate 2 Satellite manned camp Snow Bird of AIDJEX 75

camps at the triangle apexes. At the time of deployment the lengths of the sides of the triangle were of the order 100 km. In the course of the experiment, the array was much distorted as it rotated, translated and deformed. The program of atmospheric and oceanographic measurements is described later in this chapter. Typical layout of a satellite camp is shown in Fig. 2.2.

The personnel at these camps varied from 25 to as high as 60 at the start of the experiment. At the satellite camps there were always 4 men throughout the year but at the main camp the population varied from time to time. The logistic support was provided by Polar Continental Shelf Project at Tuktoyaktuk, N.W.T. and by Naval Arctic Research Laboratory at Point Barrow, Alaska.

Two types of data buoys were deployed. The NIMBUS F satellite with Random Access Measurement System (RAMS) for data buoy positioning and data transmission was launched in June 1975. Ten automatic data buoys designed to use this system were deployed in a ring outside the main manned array. Since there was a possibility of failure or postponement of the NIMBUS F, ten additional buoys were obtained. These buoys when deployed, were to be interrogated using the operating Navy Navigation Satellite(NavSat) system. They were equipped with a high frequency radio link for data transmission to a central computer at the main camp, Big Bear.

After the deployment of the main camp, eight NavSat buoys were positioned in a ring approximately 400 km radius around the main camp. Some of the RAMS buoys were co-located with the NavSat buous but others were located separately. Four of the NavSat failed in the summer of 1975 but the remaining four and all eight RAMS continued to function until the end of the experiment.

2.3 Atmospheric program

The principal objective of the atmospheric program in AIDJEX was to provide estimates of the surface air stress suitable for deriving models of the ice dynamics. Becuase of the impossibility of routine direct measurements of the stress, it was necessary to devise methods of making estimates from more easily measured variables such as surface pressure fields. The approach followed during AIDJEX was to make direct measurements of surface stress at a few locations together with the measurement of wind and temperature profiles within the planetary boundary layer (PBL). The PBL in the atmosphere is of the order of 1000m. These observations were then combined with surface pressure measurements to construct models relating the surface stress to the geostrophic winds.

Observations of pressure were made at each of the manned camps and from buoys surrounding the manned array. These measurements were combined with routine observations from the perimeter of the Arctic Ocean to obtain the pressure field. Other routine observations at the manned camps included wind speed and direction, temperature~~, rad~~iation and the height of the PBL by use of an acoustic sounder. The meteorological observation taken are shown schematically in Fig. 2.3 after Paulson and Bell (1975). P, T, U are pressure, temperature and speed measurements.

Routine meteorological observations were supplemented by additional observations during two periods of a few weeks in the spring of 1975 and 1976. They include

1) direct measurement of surface stress by use of an acoustic anemometer
2) profile of temperature, wind speed and direction in the lower 30m from a tower

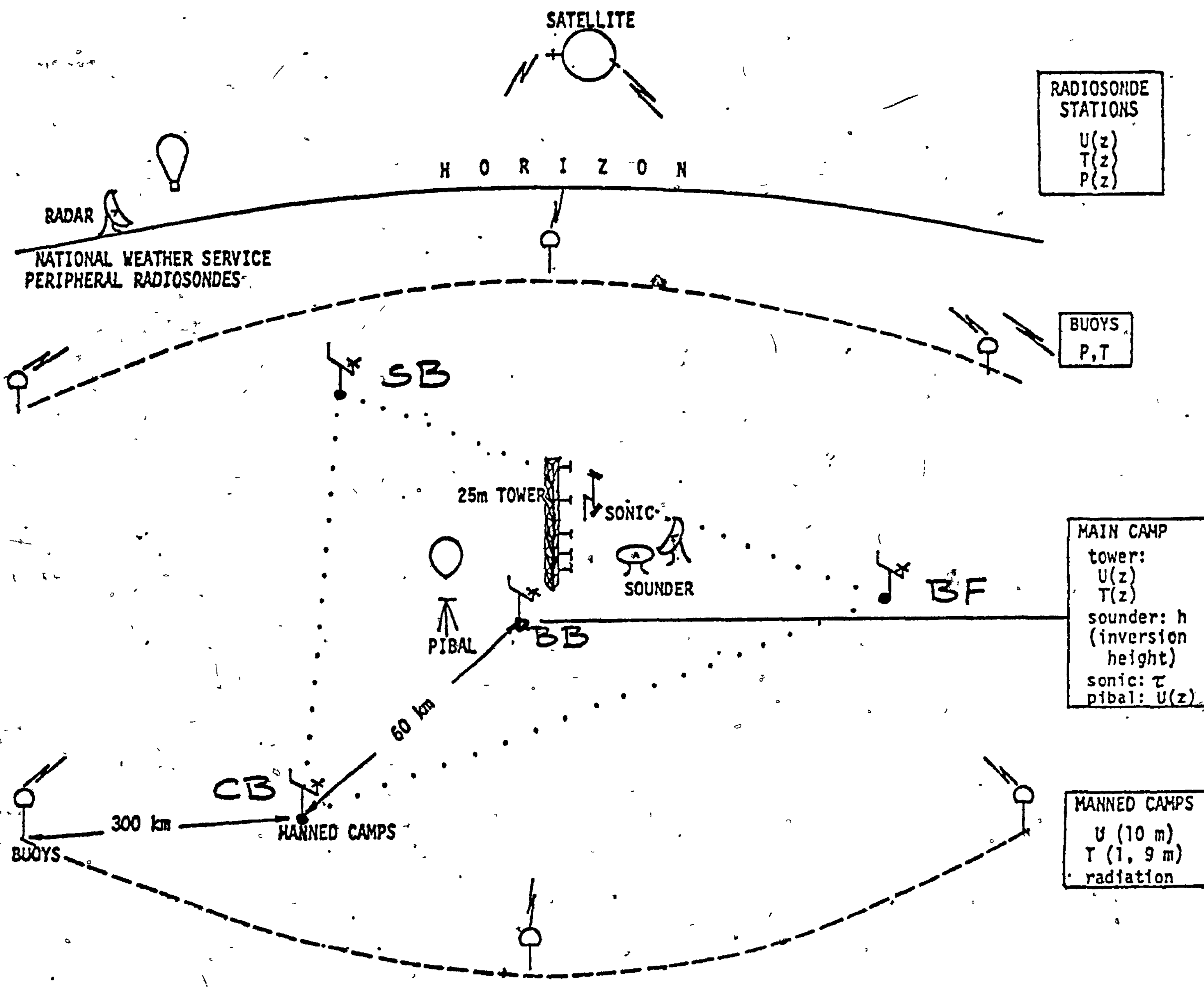

Fig 2.3 Meteorological observations. AIDJEX main experiment , 1975-76

3) profile of temperature, wind speed and direction to several hundred meter height using a kytoon with instruments suspended from it
4) measurement of mean and turbulent velocity and temperature from an aircraft (Electra overflights).

Among the conclusions the important one is that surface stress estimates can be made reliably from surface pressure fields, especially during high wind periods.

2.4 <u>Oceanographic program</u>

The AIDJEX oceanographic program was designed to investigate the Arctic Ocean on a space scale of 100 km in the horizontal and hundreds of meters in the vertical. It was directed to revealing oceanographic behaviour which directly influences the drift of the pack ice. This includes the drag of a quiescent ocean and its variation with changes in stratification and advection of the ice by currents both transient and steady. Data on salinity, temperature and currents were collected at three manned stations for a year and about half a year at a fourth station, which broke up.

The scales of time and space for oceanic parameters in the Arctic Ocean have been determined by previous AIDJEX programs. Fig. 2.4 shows the typical scales in the vertical extent. Briefly, the ice is of the order 1-3m thick with occasional keels of pressure ridges going down to depths of tens of meters. The boundary layer, the layer of frictional (skin) effect is generally said to be about 2m (Langleben, 1977; Pounder and LeBlanc, 1977). The Ekman layer is of the order 30-40m. This compares with a height of approximately 1000m in the atmosphere.

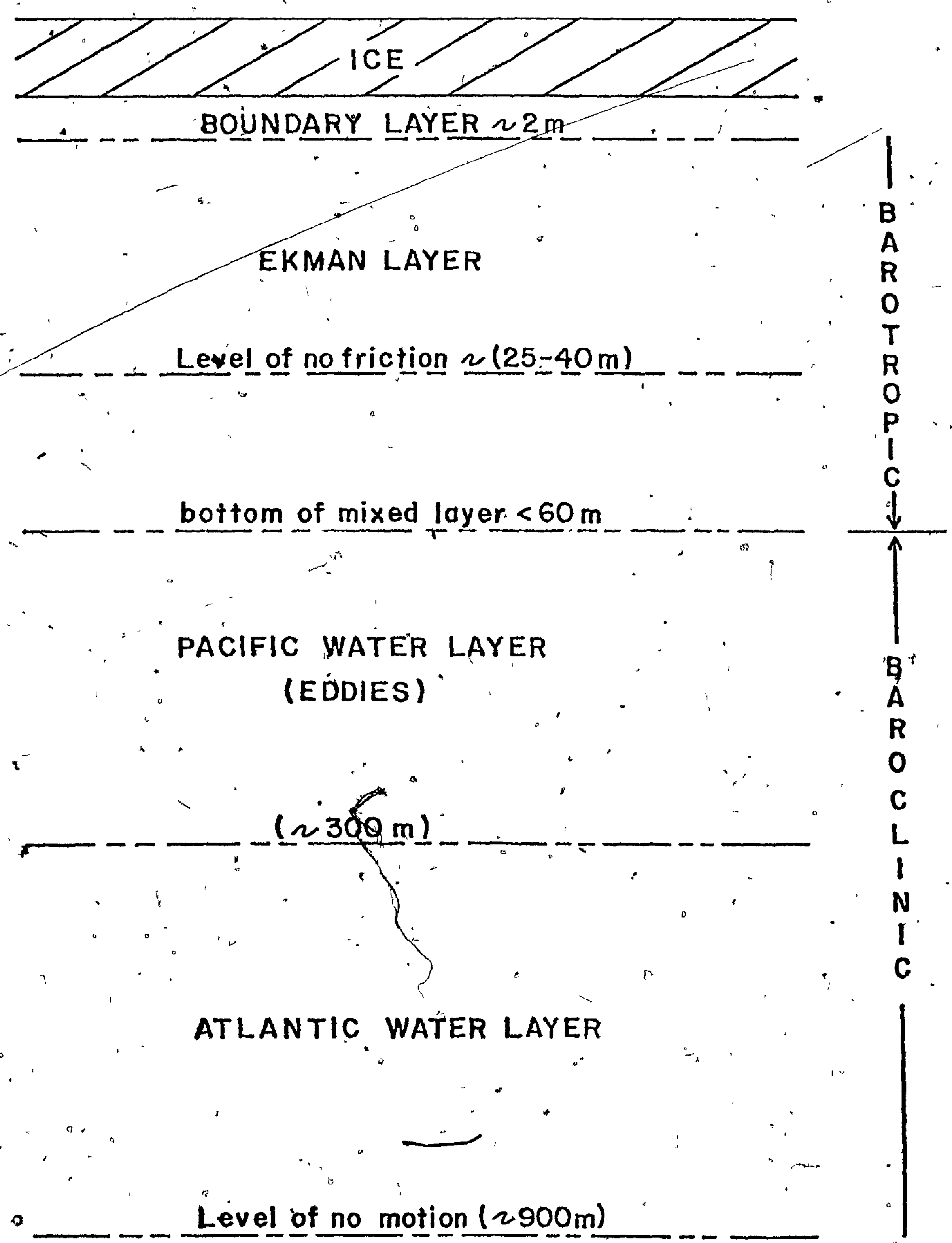

Fig 2.4 Typical space (vertical) scales in the Arctic Ocean.

The distance between the surface and the effective end of the Ekman spiral is sometimes referred to as the Planetary Boundary Layer (PBL). In the Arctic, the mixed layer is at depths less than 60m. This is the deepest that the frictional effects go. The barotropic effects are also limited to this depth.

In the depths of 100-300m, we observe the baroclinic eddies (Hunkins, 1974b) with a core at about 150m or so. They have diameters of about 10-20 km and have speeds up to 0.5 m/s (1 knot). There is no estimate of the life time of these phenomena. They travel at relatively low speeds (10 cm/s or less) and are observed at AIDJEX for periods of about a week to 10 days.

The layer of no motion can be thought of as the bottom of the Atlantic water at about 900m. These deeper regions are where baroclinic effects are predominant. The horizontal extent of these eddies is about 10-20 km as already indicated (Hunkins, 1974b; Newton, 1973).

In addition to these, there are observed step structures in the Arctic Ocean (Hunkins et al, 1977). These occur at depths about 300-400m. The horizontal extent is limited to about a few kilometers because of hydrodynamical arguments. These will be discussed in later chapters. The Beaufort Sea Gyre has currents in the clockwise rotation at about 2 cm/s. The time scale for a period is approximately 4-5 years.

The oceanographic program for the main experiment of AIDJEX 1975-76 was designed to ensure uniform observations at all four manned stations with supplemental observations at the main camp. Salinity and temperature were monitored with a Plessey Model 9040 STD system. The satellite camp's STD (for Salinity, Temperature and Depth) probes were limited to a depth of 750m because of the depth sensor and winch limitations. Data from camps Snow Bird and Caribou are used for analysis here. At the main camp there were weekly casts to depths of 3000m. Data were recorded digitally on magnetic tape with Plessey model 8400 data logger and on analog traces. Casts were taken once or twice daily at all four camps on a synchronized schedule. Between the casts the sensor was suspended in the pycnocline, the steep density gradient, at about 60m (Fig. 1.7). This was done to observe the time variation at this depth and to look for internal waves. The ocean measurements are summarized in Fig. 2.5.

Water velocity was recorded with both fixed and profiling current meter systems. Current meters, from Hydro Products, were attached to inverted masts to record current at each camp at 2 and 30m depths, the top and bottom of the planetary boundary layer (PBL) of the ocean. See Fig. 2.5. Rigid attachments to the ice were used to eliminate the need of a compass in these instruments. Magnetic direction is always a source of error in the high latitude. The fixed mast meters were referenced to ice floe azimuth, which was monitored regularly. A duplicate system of 2 and 30m meters was installed at the main camp to determine the effect of local change in the ice topography. The profiling current meter, PCM, was operated once or twice daily at each camp to depths of 200m. The PCM, like the fixed mast meters, measures current speed with a Savonius rotor. The PCM also has a direction vane and pressure sensor. The direction of the current was referenced to the magnetic north but was converted to true direction by calibrating the vane direction with the fixed mast velocities and with the magnetic declinations. More on the STD and current systems in the next chapter.

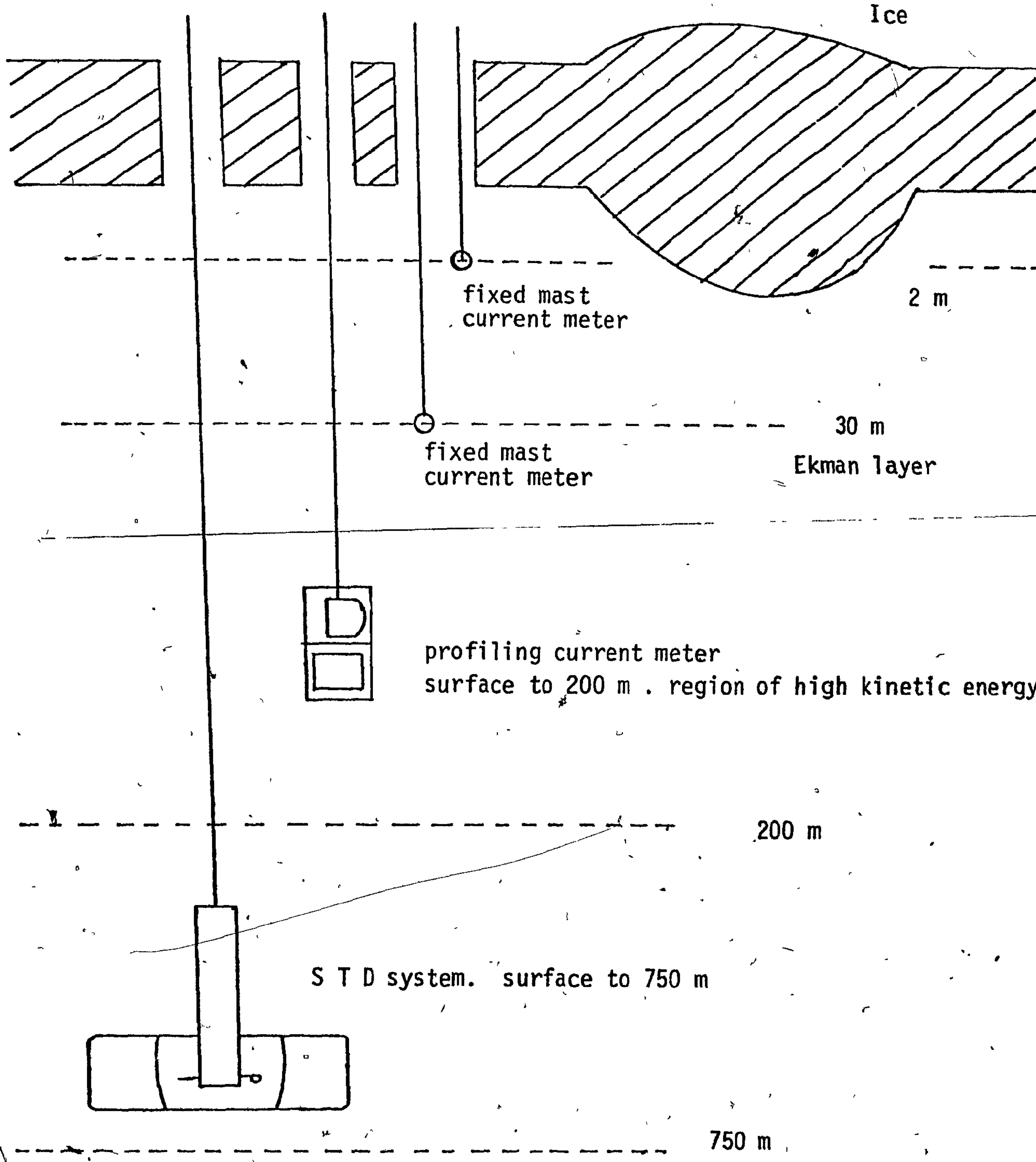

Fig 2.5 Oceanographic observations at satellite camps.

In addition to these measurements, standard water samples were taken at various depths. This was done to provide a reference source in order to correct for instrumental drift and to calibrate the probe. The temperature and depths were obtained independently by using reversing thermometers and the salinity by using a Guildline or Hytech laboratory salinometer.

2.5 Drift track

The array formed by the manned camps and the data buoys at the start of the experiment is shown in Fig. 2.1. Since the ice is under the influence of the forces of nature, and almost always in motion, the camps drifted with the pack ice. In Fig. 2.6, we see the drift of the manned array for AIDJEX days 100 to 270 (11 April 75 to 27 September 75). The outline of the camp at the start and end of these dates is delineated by heavy lines. The dashed lines represent the motion of the automatic data buoys in this time period.

The ice was expected to follow the Beaufort Sea gyre and move in the [illegible] clockwise direction. As it turned out, the motion was in the opposite direction for the time period shown. The drift changed direction at this time and the manned array was at roughly the same place at the end of the experiment in May 1976 as at the start in April 1975. The triangle was greatly distorted by this time and the main camp (Big Bear) had been destroyed by ice movements. The drift traces of the manned camps Snow Bird and Caribou, for the whole time period, are shown in Fig. 2.7 and 2.8 respectively (after Thorndike and Cheung, 1977). The day numbers referred to are AIDJEX days. The conversion from AIDJEX days to calendar days is in Appendix 1. The

Fig 2.6 Drift of the AIDJEX array; 11 april 1975 to 27 september 1975. Numbers at the start and end of drift tracks are AIDJEX days. Large numbers are buoy numbers.

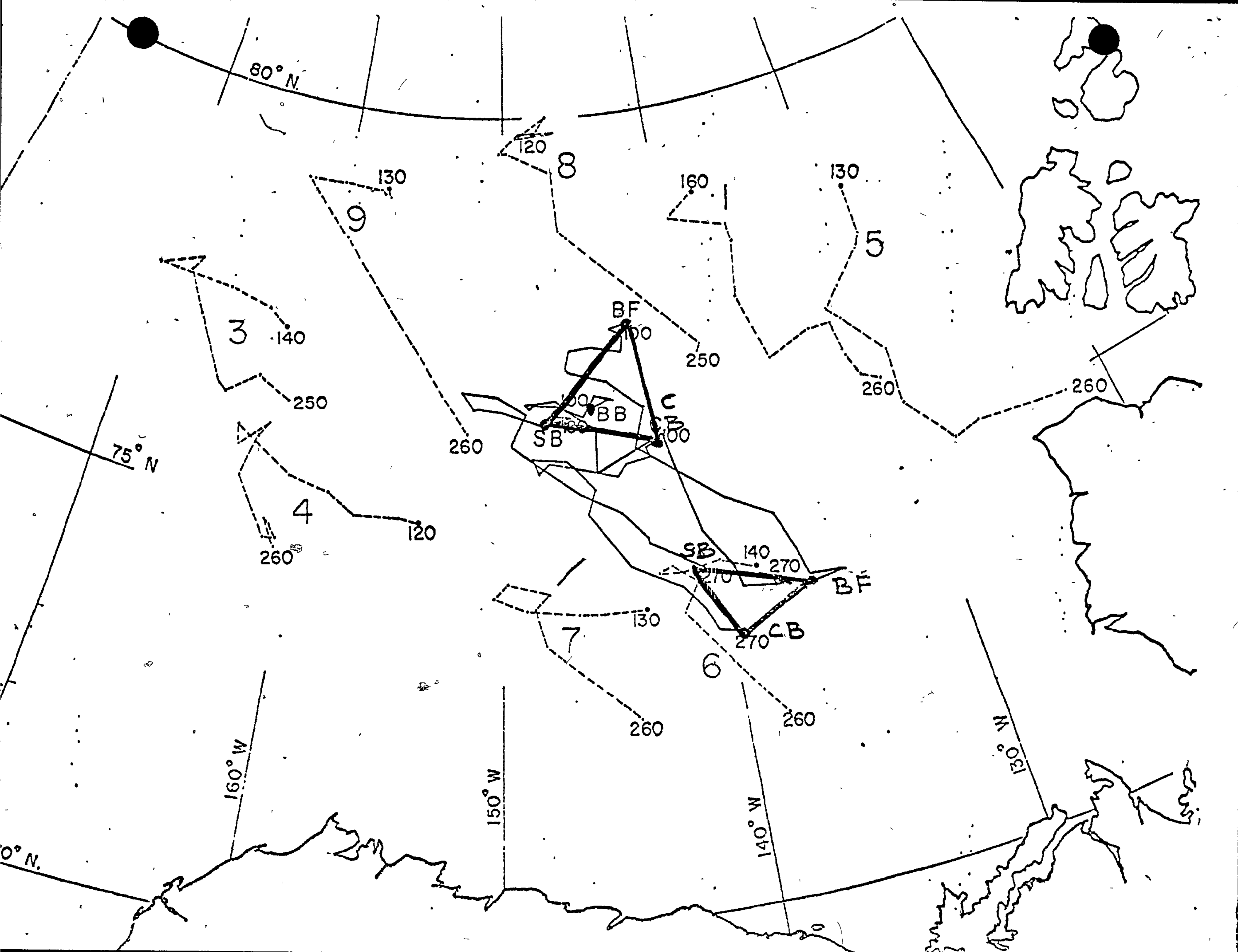
80° N.
75° N
160° W
150° W
140° W
130° W
120
8
130
9
160
130
5
3
140
250
BF
100
250
260
260
100
BB
C
SB
CB
100
260
4
120
260
SB
140
270
BF
130
7
CB
270
6
260
260

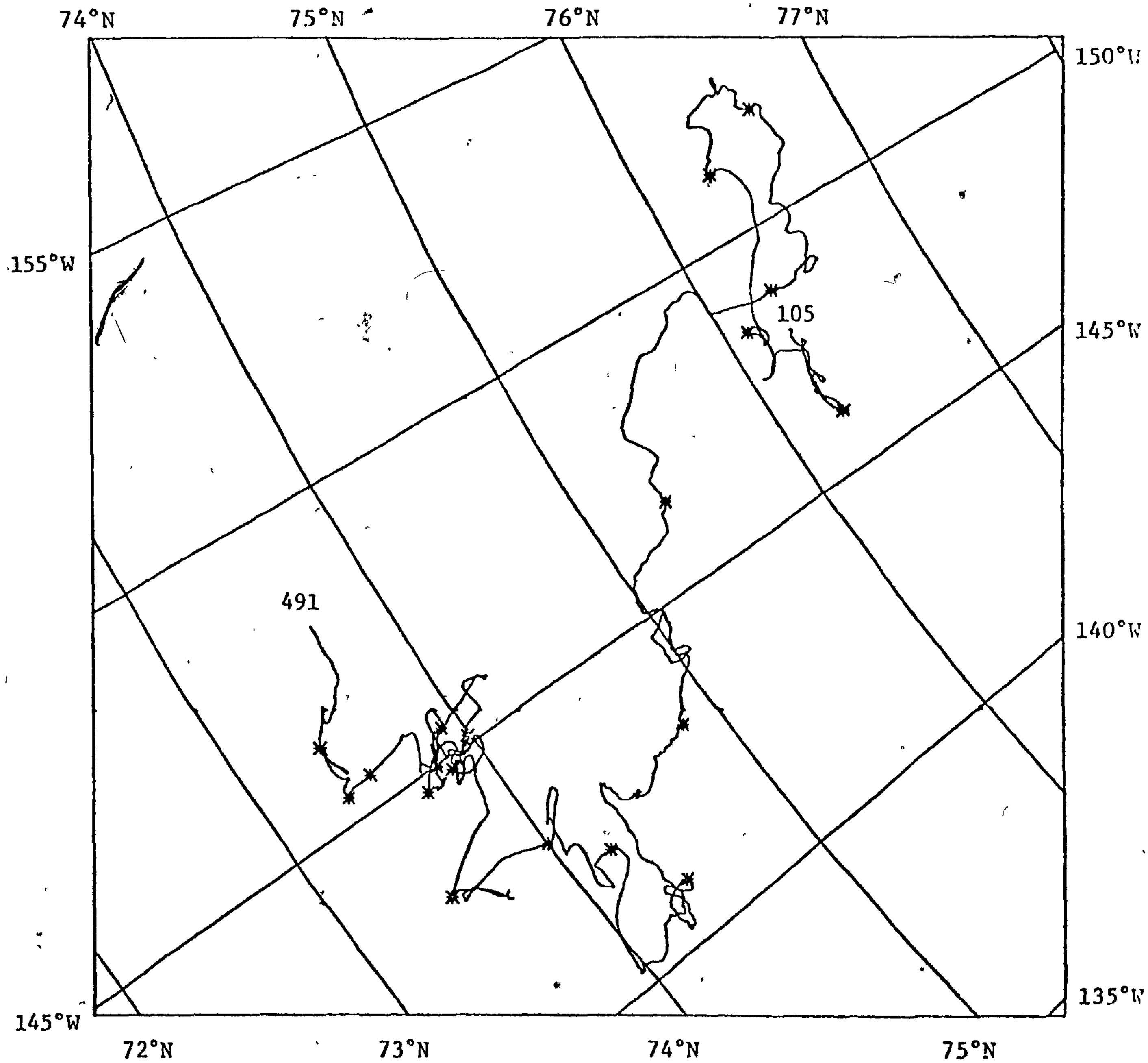

Fig 2.7 Drift track of station Snow Bird. Measurement by NavSat from day 105 to 491. This station was split by cracks during the winter and the NavSat antennas were moved short distances several times. * show location at integral multiples of 20 days.

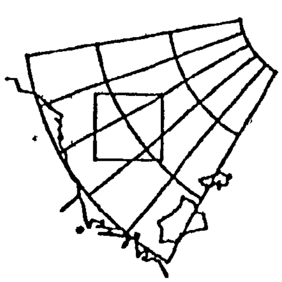

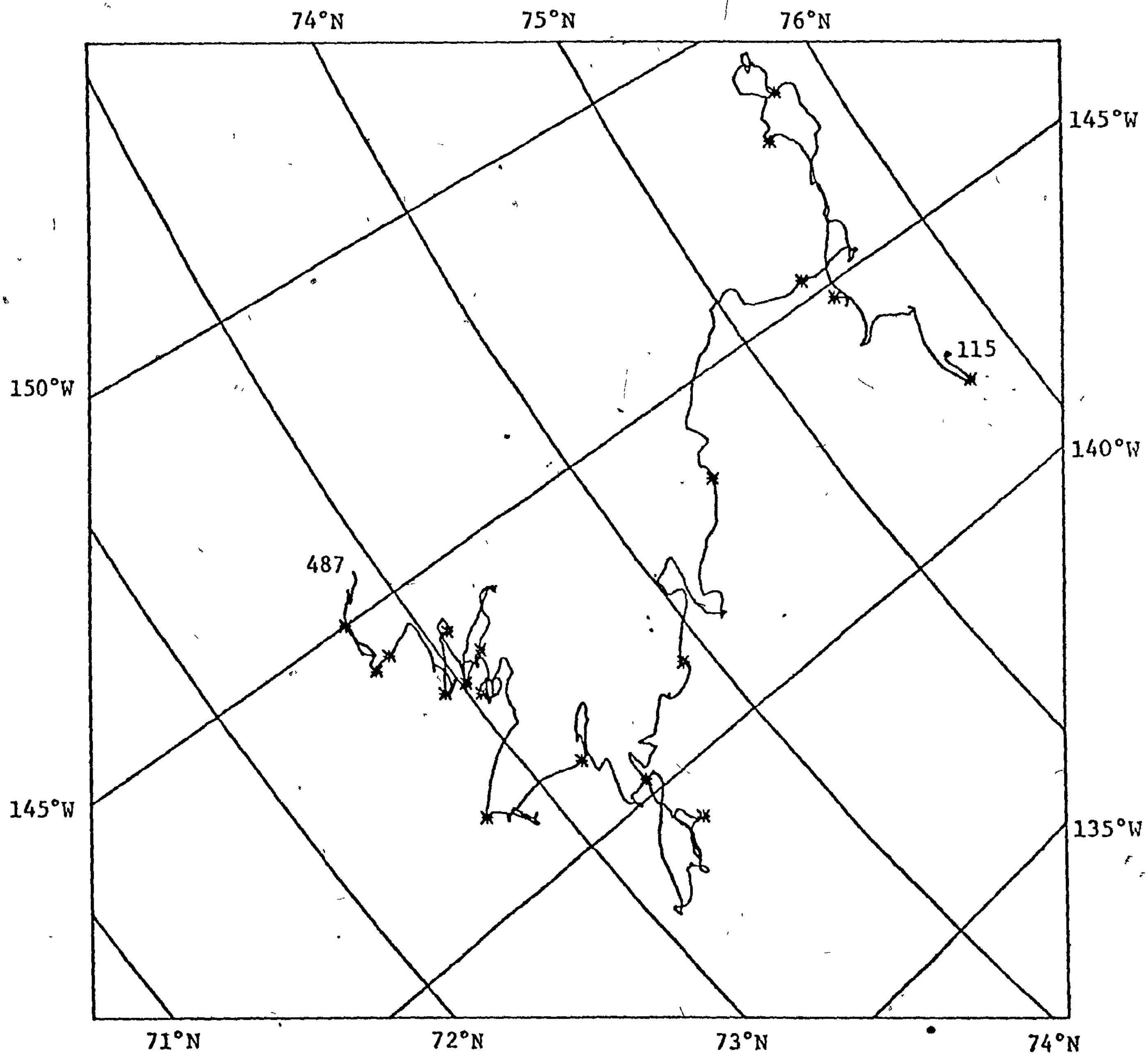

Fig 2.8 Drift track of station Caribou, became the main camp after Big Bear broke up. Measurements by NavSat from day 115 to 487.

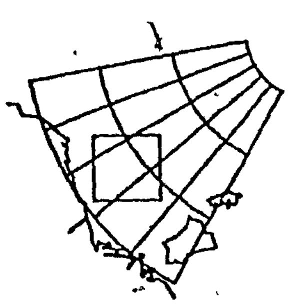

tracks of these two stations show the geographical distributions of the sites where measurements were made.

2.6 Data Bank

Vast quantities of data, of all sorts, were collected during the main AIDJEX experiment. In Appendix 2, we have a listing of all the data that are available at the main data bank, at AIDJEX offices in the University of Washington, to date. In addition to these, there are now oceanographic data from all manned camps at Lamont-Doherty Geological Observatory in Palisades, N.Y. At the McGill University Ice Research Project data bank the following oceanographic and other data are available.

1) Smoothed position, velocities and acceleration for Snow Bird
2) Hourly averages of observed wind speed and direction at 10m at Snow Bird
3) Ocean currents relative to the ice motion at 2 and 30m depth at three-hour intervals at Snow Bird (fixed mast currents).
4) Ocean current profiles, from the once or twice daily casts of PCM, at Snow Bird.
5) Standard STD measurements made twice a day at the camps Snow Bird and Caribou.

In the STD data there are about 600 stations for Snow Bird and about 800 stations for Caribou. Approximately 30% of SB and 13% of CB data had to be digitized manually because of the malfunction of the digital data logger.

6) Tide height at Tuktoyaktuk for 1975.

There were numerous people involved with the collection and interpretation of the oceanographic data at the main and satellite camps. The following people operated the oceanographic program at the camp Snow Bird:- Barry Allen, Brian Hill, Paul Peltola, and the author. At the camp Caribou - the ocean program was operated by Alan Gill.

Chapter Three DATA MANAGEMENT

3.1 STD system

Salinity, temperature, depth casts from the surface to 750m were made twice daily at 0600 and 1800 GMT with a Plessey model 9040 STD. Data were recorded with an XXY chart recorder and also on magnetic tape with a Plessey model 8400 digital data logger (DDL). The STD profiles taken were calibrated by Nansen bottles and by reversing thermometers. Samples were taken at just below the ice sheet and at 250, 500 and 750 meters. The STD accuracies are ± 0.01°C in the temperature, ± 0.001 $^{o}/oo$ in salinity and 1m in depth (Amos 1973). In this chapter we shall describe the system used and some of the problems (and solutions) in the acquisition and management of data.

3.1.1 Instrumentation

The model 9040 STD system (Plessey, 1969) consists of a compact rugged underwater unit, a cabinet containing surface deck terminal equipment and a hydraulic winch with slip rings. The underwater unit is equipped with precision transducers which sense salinity (from conductivity), temperature and depth data. The system is shown in plate 3. Further details about the terminal equipment, etc. are in Appendix 3.

Solid-state electronics in the underwater unit convert the sensed parameters into a composite FM data signal that is multiplexed and transmitted through a sea cable (single conductor, double armoured) to the surface deck equipment for processing and recording. The data terminal equipment separates individual data signals from the FM

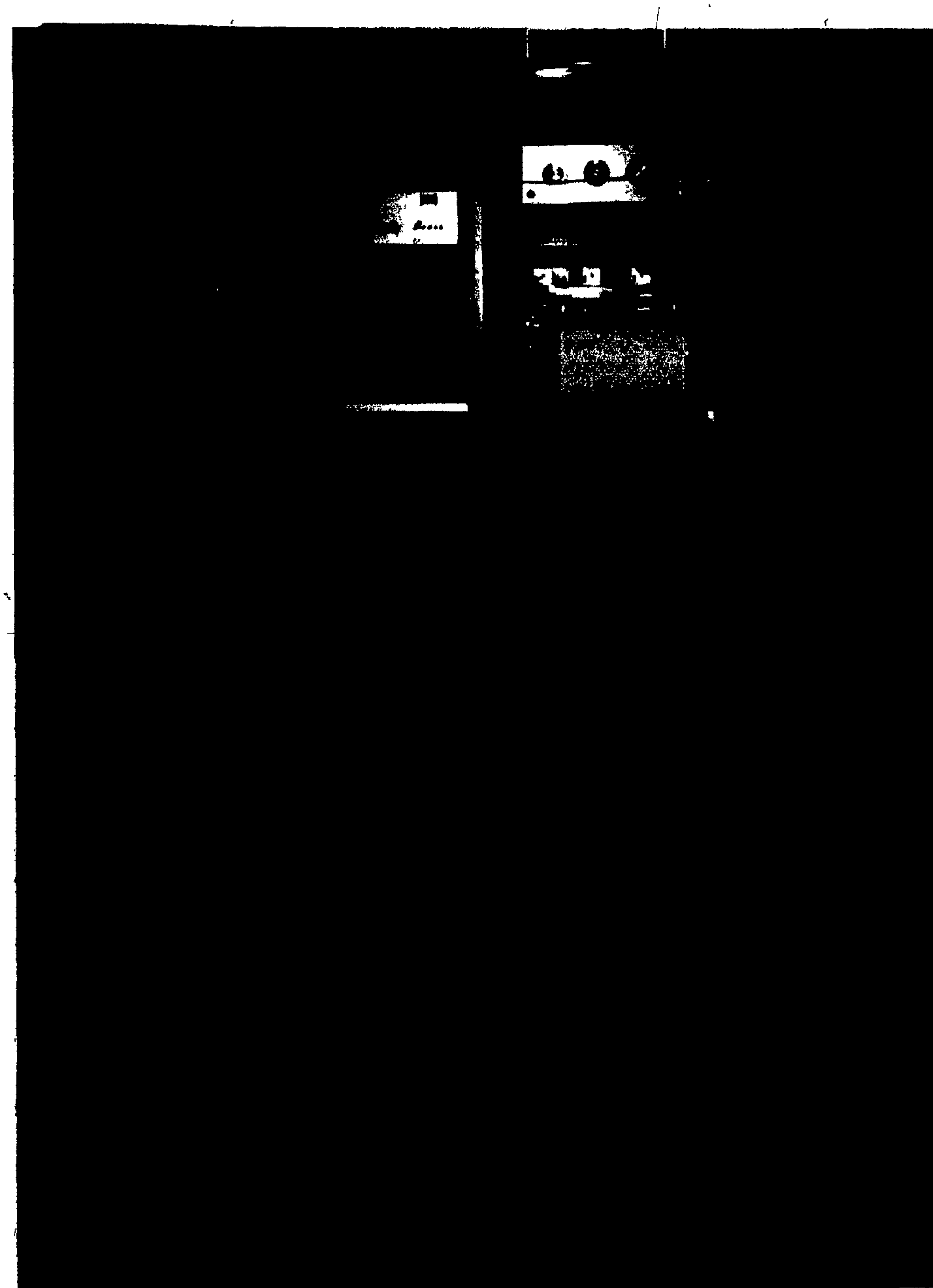

Plate 3 Surface deck equipment and underwater unit of the Plessey model 9040 S T D system.

composite and records salinity and temperature data as a function of depth on a chart recorder. A sample of the conversion table from FM periods to oceanographic parameters is also shown in Appendix 3.

The underwater unit, shown in Fig. 3.1, consists of the salinity, temperature and depth sensors (transducers), a Bisset-Berman Paraloc oscillator and a mixer circuit. The salinity, temperature and depth transducers together with their associated solid-state electronics are located in the sensor package section of the underwater unit.

Sea water salinity is determined in situ by sensing conductivity, temperature and pressure. Conductivity is measured by sensing the conductivity of dissolved salts in the sea water, which provides an inductive loop that couples two transformers in the conductivity head. Sea water conductivity is a complex function of temperature, pressure and salinity and in the 9040 system automatic compensation is continuously applied for the effect of temperature, and pressure change as well as for a temperature effect on depth. This provides an output that is a direct function of salinity alone and which is directed to the Paraloc that generates an FM signal which is an analog of the measured salinity.

The Paraloc is an A-C voltage to frequency convertor which operates within a fixed FM bandwidth that is established for each measured parameter. Output signal changes from the Paraloc are directly proportional to input voltage variations. The result then, of a change in sea water salinity is an FM signal, whose frequency increases with increasing salinity and conversely. This signal is applied to the mixer.

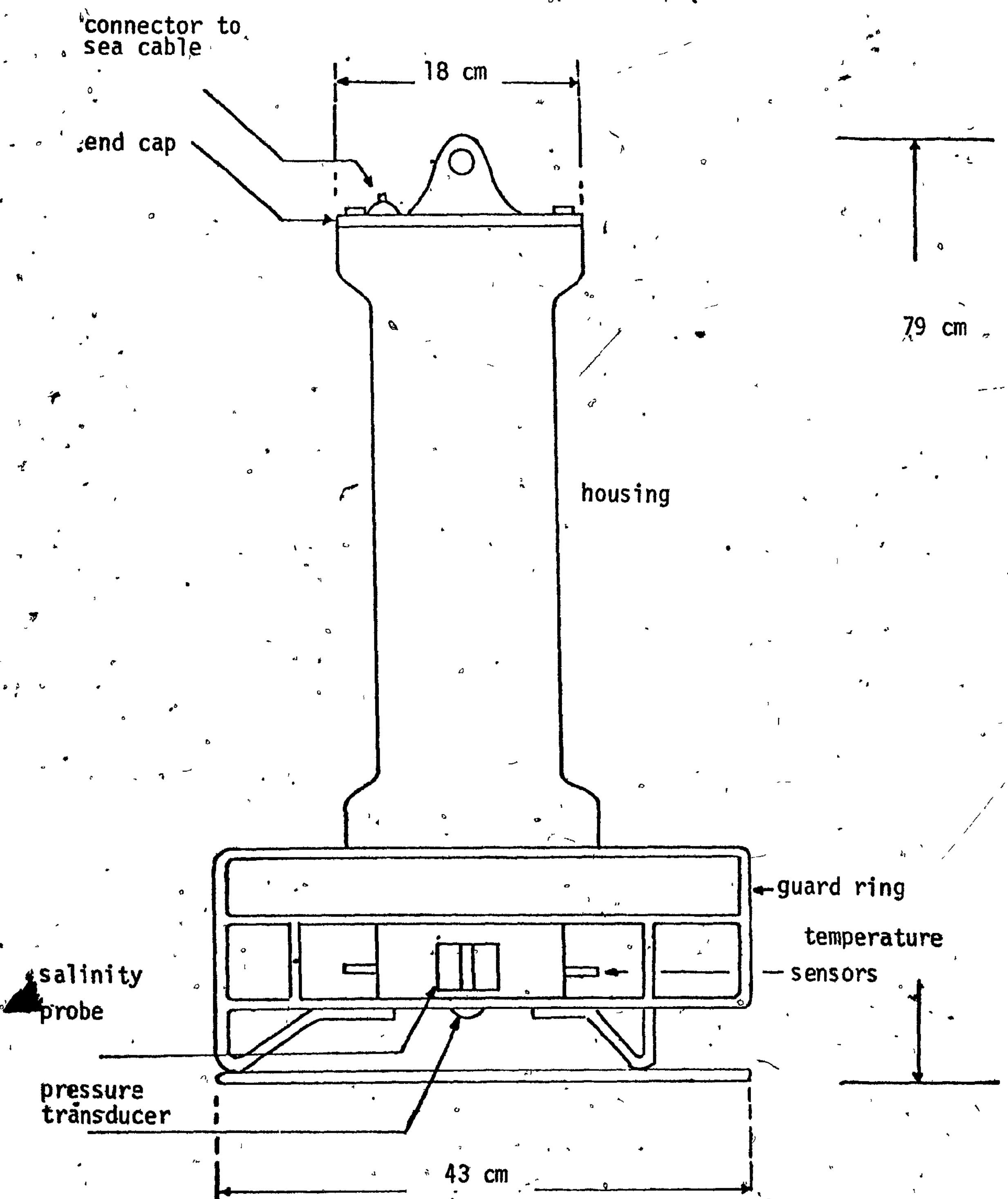

Fig 3.1 Underwater unit of the S T D system.

The temperature transducer is a platinum resistance thermometer which forms one leg of a bridge. The thermometer is protected from strain and has a short response time (0.35 s). The response times of the salinity and temperature sensors will be discussed later. Variations in the temperature change the resistance of the platinum conductor, and consequently change the voltage drop across it. This voltage drop is applied to the Paraloc circuit which generates an FM signal analog to the voltage differential created by change in temperature. The signal is transmitted to the mixer.

The depth system incorporates a pressure transducer containing a pressure transducer containing a strain-gage which is balanced at the surface (zero Pascals or zero psi) and becomes increasingly unbalanced as the pressure increases. Resulting changes in the bridge circuit are converted to a frequency analog in the Paraloc and are transmitted to the mixer.

The underwater signal mixer receives and regulates power from the deck terminal equipment and transmits it to the sensors. It also multiplexes and amplifies the FM signal from the Paralocs and transmits them up the sea cable to the deck terminal equipment. Multiplexing all data into an FM composite signal permits continuous and simultaneous transmission of all sensor data to the deck unit in a single conductor sea cable.

The terminal deck equipment is the signal converter unit and the hydraulic winch. The signal converter consists of a power supply, distribution amplifier and a discriminator. The band pass filter at the input of each discriminator accepts a specific sensor signal and rejects others in the FM composite signal. These signals are plotted on the XXY recorder and are passed to the DDL for digitizing and recording.

The data acquired by the STD measuring system is stored in the model 8400 DDL (Appendix 3). The DDL has the capability of recording data, digitally, and at various scan rates. Each sensor is digitized individually and then the signal is fed to the tape recorder for storing. The scan period can be changed from 0.1 to 10 seconds. For example, in the course of a typical STD profile, the probe was lowered at the rate of 10 m/min (1/6 m/s) in the steep gradient near the surface. The scan rate of 0.5 s meant that all sensors were sensed and recorded at a rate of 6 times for each meter of depth. This provided high resolution for the temperature and salinity gradients.

The data (digitized) was recorded on a 7-track tape in BCD (Binary Coded Decimal) on a Kennedy incremental tape recorder, model 1600. Limitations of the McGill University Computing Centre necessitated the translation from 7-track BCD to 9-track EBCDIC (Extended Binary Coded Decimal Interchange Code). This and other tape handling programs developed at McGill and Lamont-Doherty Geological Observatory are shown in Appendix 4. Fig. 3.2 shows the flow chart for acquisition and analysis.

3.1.2 Static Calibration

The STD system suffers from many irritating problems. Problems like 'spiking', noise, drift and calibration are the major ones that are encountered. 'Spiking' is caused when the sea cable is pinched and a short occurs. The result is irregularly spaced spurs in the

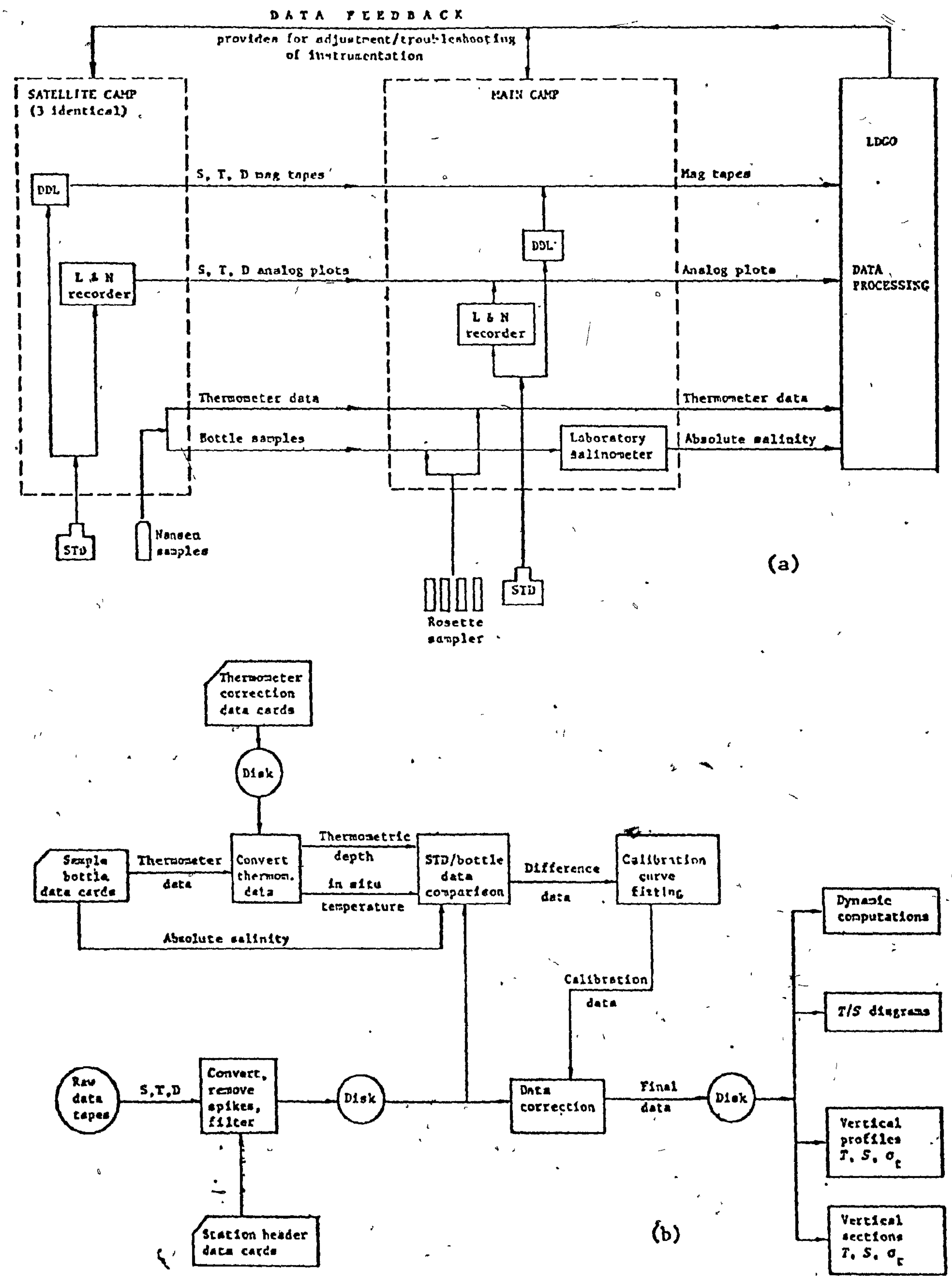

Fig 3.2 S T D data flow from (a) acquisition to (b) analysis.

salinity and temperature traces. Spiking usually occurs during bad level winding and if not corrected promptly can cause the loss of the cable. Noise becomes a problem of significant proportion when long lengths of cables are used. This deteriorates the signal and the resolution drops significantly. Also magnetisation of the conductivity cell and dirty slip rings in the winch can contribute to this problem. Careful and periodic checking and degaussing can reduce the problem.

In the STD, proper flushing of the conductivity cell is essential to the accurate reading of the salinity. When the STD was stopped to get water samples, the salinity valve drifted and it was thus important to log the periods (of salinity, temperature and depth) for later calibration. The drift was largest in the salinity. The parameters returned to their proper valves once the cast was resumed and proper flushing occurred. The logging of the STD periods is doubly important for calibration and comparison with the water samples that are taken by the Nansen bottles. Depth and temperature were compared with reversing protected and unprotected thermometers. Nansen bottles were tripped only in the downtraces to ensure that there was proper flushing and sampling by the sensor. In the uptrace, the sensor follows in the wake of the instrument package and this might possibly disturb the 'purity' of the reading.

The DDL was the weakest link of the STD program in the AIDJEX experiment. Out of the 1280 stations of AIDJEX, approximately 30% had to be digitized manually because of the DDL failure. Digitizing, calibrating and other programs for the handling of STD data are shown in Appendix 4.

3.1.3 Dynamic Calibration

The salinity, as stated above, is arrived at by making compensation for the temperature and pressure values and of the gradients of these parameters. The need for dynamic calibration arises primarily because of a mismatch between the time constants of the temperature probe (0.35 seconds according to the manufacturer) and the salinity probe (negligible in comparison). Several investigators (Scarlet, 1975; Gould and Culverhouse, 1972) who have used the 9040 system have found that estimates of the time constant vary from 0.2 to 3.0 seconds.

The correction because of the time lag is based on the assumption suggested by Scarlet (1975), and performed by Ed Bauer of the Lamont-Doherty Geological Observatory (LDGO), that the response is exponential with a time constant τ such that

$$T' = T + \tau \frac{\partial T}{\partial t} \qquad (3.1)$$

$$S' = S + \frac{\partial S}{\partial T} \times \tau \frac{\partial T}{\partial t} \qquad (3.2)$$

where the unprimed are the sensed parameters and the primed are the corrected parameters, τ the time constant, $\frac{\partial T}{\partial t}$ the temperature gradient and $\frac{\partial S}{\partial T}$ the slope of the TS curve, assumed to be unity. (Dantzler, 1974).

The assumption that $\frac{\partial S}{\partial T} = 1$ appears to be reasonable and produces less error than the other terms. The major source of error is in the computation of $\frac{\partial T}{\partial t}$. The DDL resolution in temperature is $\pm$ 0.003°C but this can be degraded by noise.

The temperature interface at the base of the mixed layer in the Arctic Ocean is usually stable, well defined and sufficiently large scale in temperature to afford a regular appraisal of the sensors' dynamic response. Comparison of the TS diagrams always shows a divergence along the mixed layer interface with the downtrace offset towards the higher salinity and the uptrace towards the lower salinity. From Eqn. 3.1 we expect this change in temperature $\frac{\partial T}{\partial t}$, and consequently the effect of lag in temperature response, are of opposite signs in the down and up traces. Dantzler (1974), in particular, has pointed out the importance of this type of systematic error in features of sustained temperature gradients.

In the series of figures 3.3 to 3.7, the T-S diagram is plotted for one Snow Bird station. The region shown is that part which is near the pycnocline. In the figures the dark line represents the up trace and the light line the down trace. By changing the τ in the two traces we can make both the up and down traces to be nearly congruent. The τ for this series appears to be about 0.75. τ seems to change with the sensor (unit) used and in table 3.1 we have a listing of the τ valves for the Snow Bird and Caribou stations. The changes usually occur when sensors were replaced or substituted.

3.2 Current measuring systems

The currents were measured in two manners. One was the profiling mode and the other was the time series at fixed depth.

3.2.1 Profiling Current Meter

The profiling current meter (PCM) was a TSK current meter. Instrumentation in the underwater unit consists of a Savonious rotor, a direction vane and a pressure sensor to measure the current speed, direction and depth. The unit was raised and lowered at a rate of

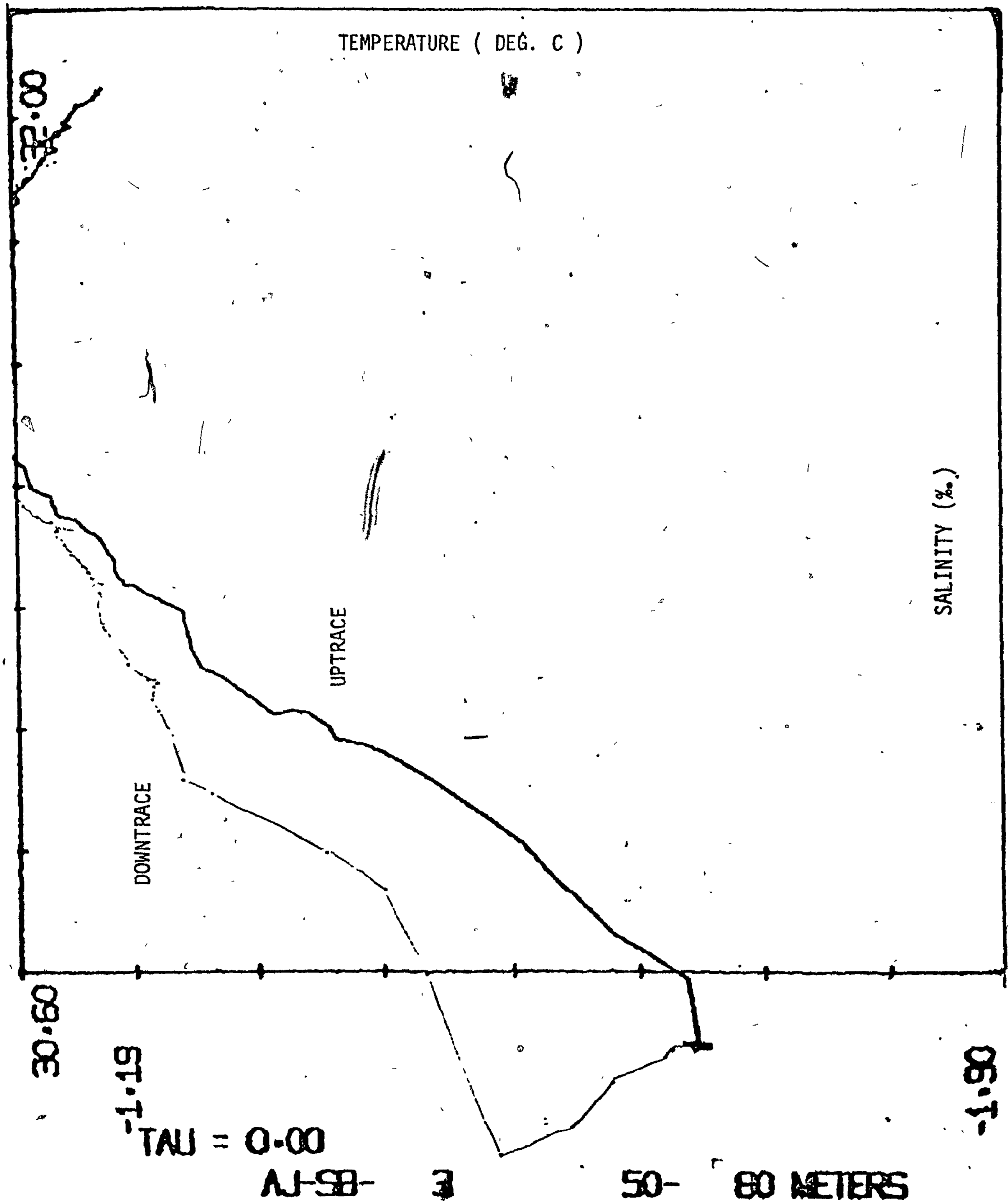

Fig 3.3 T-S diagram for dynamic calibration.

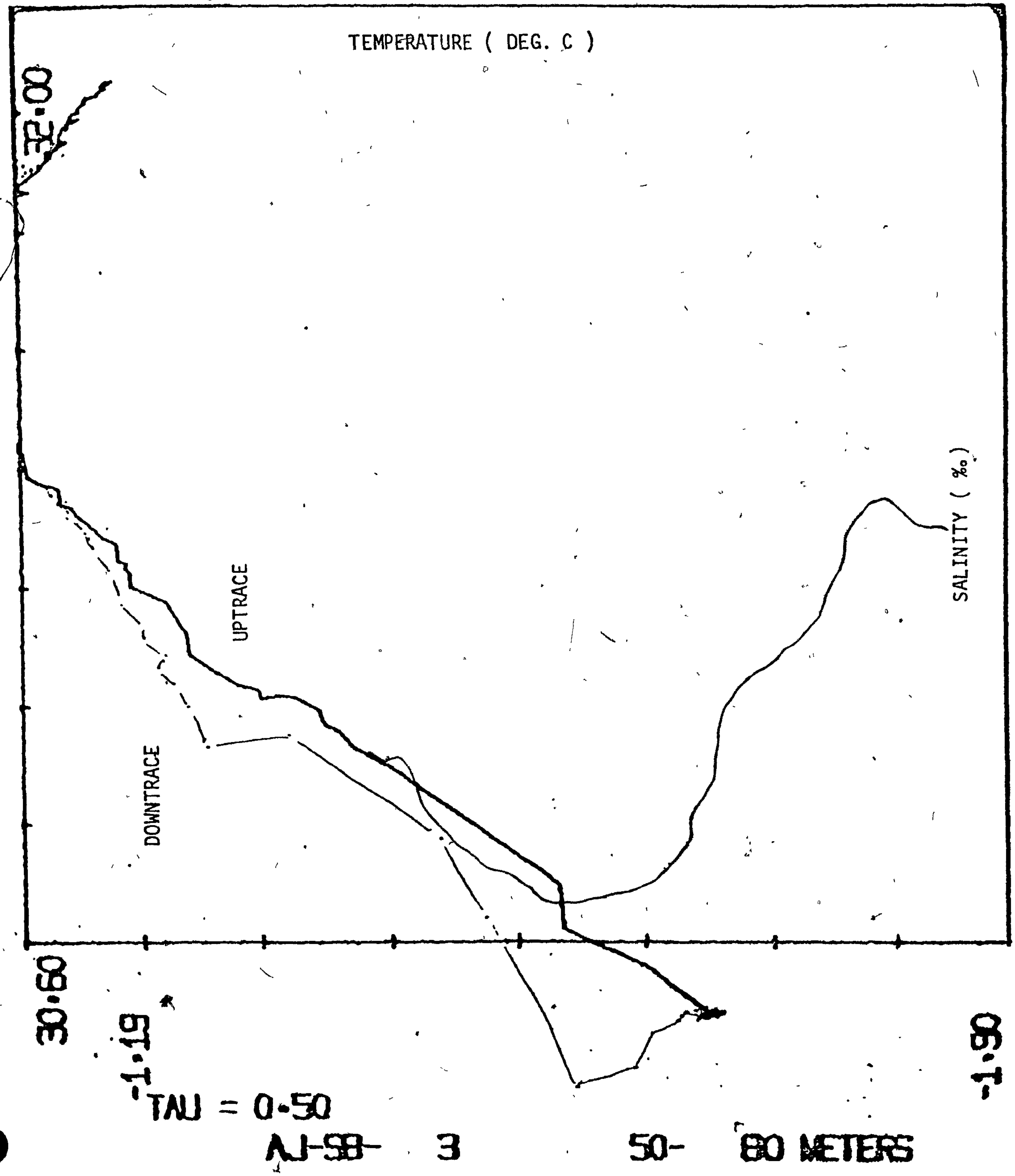

Fig 3.4 T-S diagram for dynamic calibration.

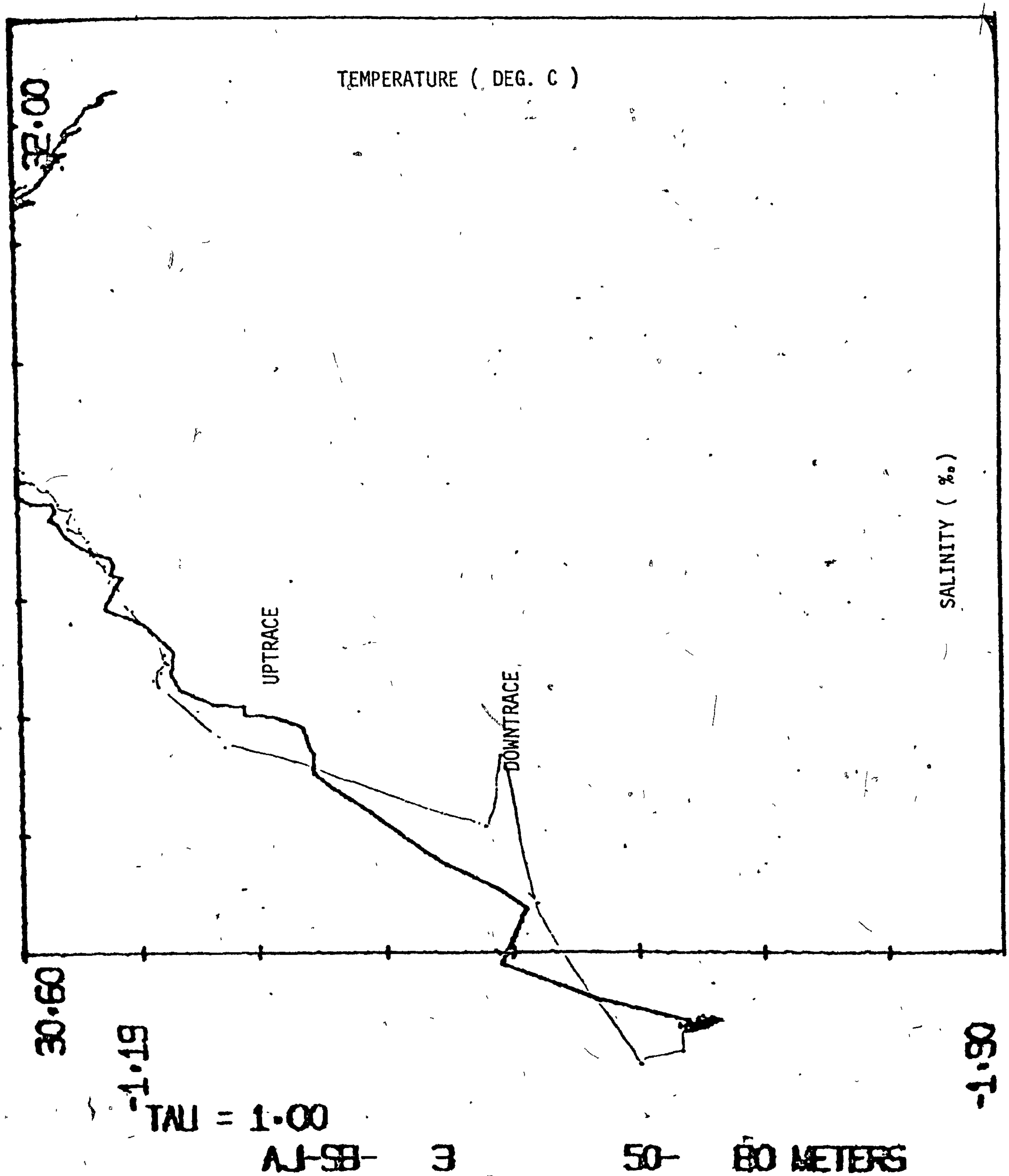

Fig 3.5 T-S diagram for dynamic calibration.

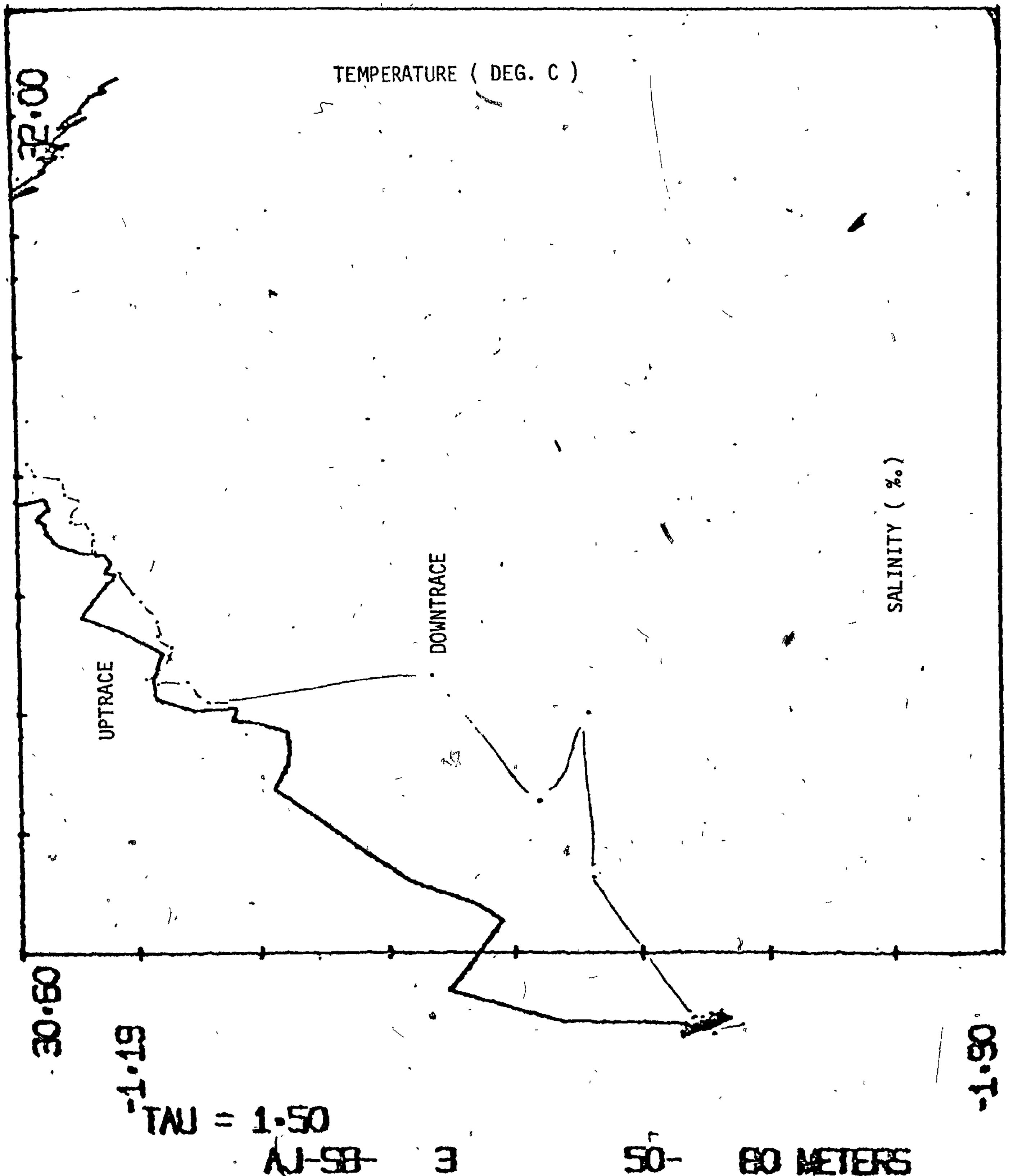

Fig 3.6 T-S diagram for dynamic calibration.

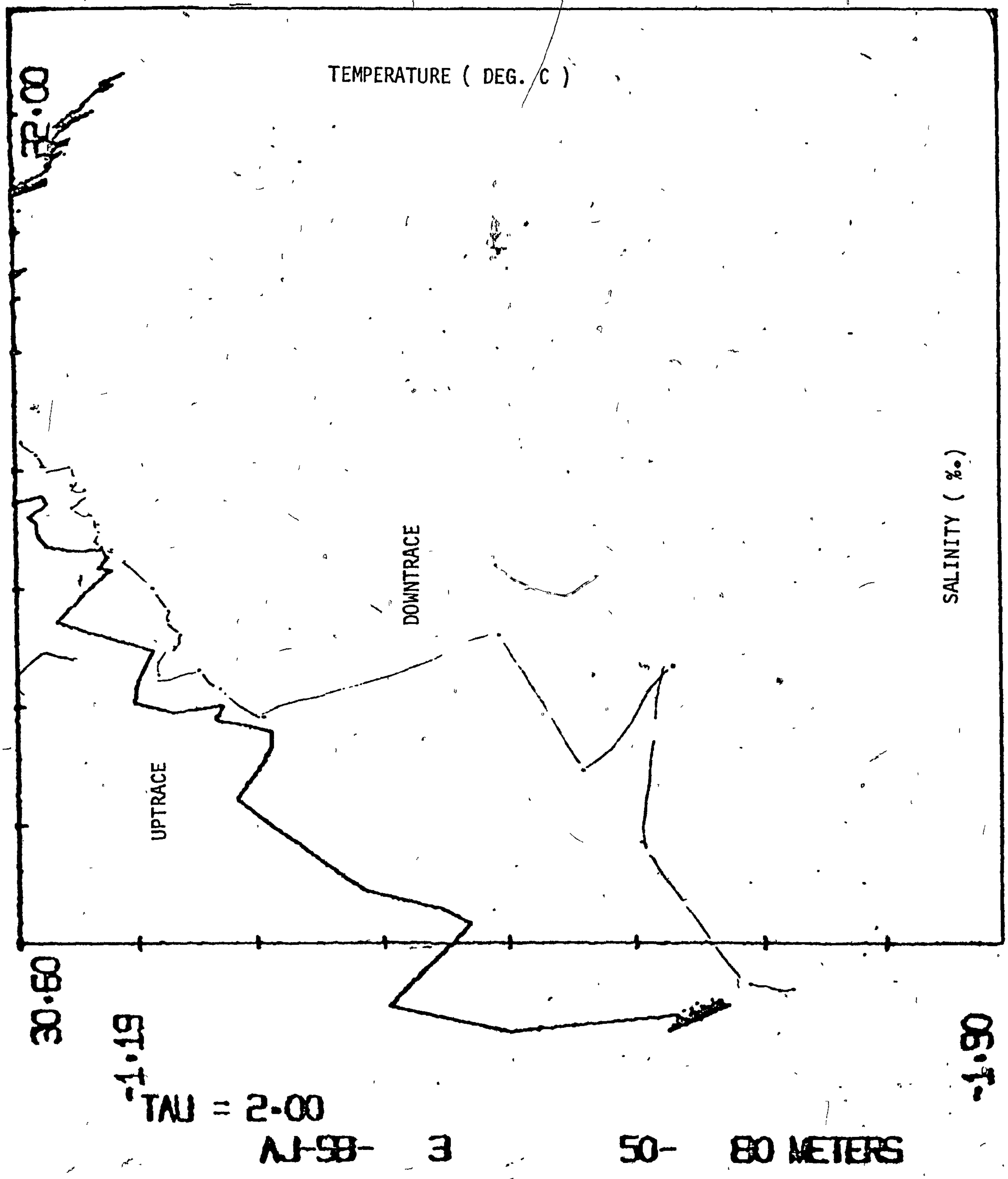

Fig 3.7 T-S diagram for dynamic calibration.

TIME CONSTANTS FOR AIDJEX STD SENSORS

Table 3.1

Camp	Calibration Period (Station Nos.)	Time Constant Range (Sec.)
Snow Bird	3 - 247	1.0 - 0.7
	249 - 299	0.7 - 0.5
	302 - 362	0.7 - 0.8
	530 - 592	0.8 - 1.0
Caribou	1 - 81	0.5 - 0.7
	83 - 221	0.7 - 0.5
	223 - 309	0.5 - 0.4
	310 - 558	0.5

The division into periods in table . is based on change of sensor, change of sensor components, or unexplained shift in observed response. Change of time constant is approximately linear between limits of each range.

5m/min (1/12 m/s) by an electric winch with 5 conductor slip rings. The speed was chosen after experiments on the station to determine rotor response to different axial velocities. Current directions were referenced to an internal magnetic campass. The direction vane follower and the compass were both sensed with photocells so that only the bearing friction limited the compass. This is an important factor in the weak horizontal magnetic fields in the high latitude. Magnetic declinations were measured at the surface before and after each cast. The depth was determined by the pressure transducer similar to that in the STD system. The speed was obtained from the calibrated Savonious rotor. The signals (voltages) from the underwater unit were carried up by a five-conductor cable and plotted on an XXXT plotter. the data were also digitized and recorded on the AIDJEX digital data logging system. The scan rate of the AIDJEX logging system was slow (once per minute) for the accuracy needed. Thus the data had to be all digitized manually from the analog traces. About 1242 of the 2133 casts were useful. The others had to be disregarded because of radio noise on the trace or because the currents were lower than the stall (threshold) speed of the rotor (about 5 cm/s).

The coherence of the vane in the up and down traces is good at speeds greater than 5 cm/s but the vane appears to be free swinging at speeds slower than this. The current structure can be followed in scales of 10m or more, in the up and down traces and from one station to another. One major problem with the PCM was the slugishness of the rotor when compared to the rotor of the fixed mast meters.

3.2.2 Calibration

Calibration of the PCM was done by forming linear regressions between PCM and the 30m fixed mast sectioned into fairly large data blocks. The digitizing was done by W. Tiemann. Calibration and reduction was done by T. Manley and B. Allen, all from LDGO (Hunkins and Manley, 1977). The direction of the currents was compared by noting the magnetic declination. This was done by aligning a surveyor;s compass along the camp azimuth. The reduction of the magnetic declination information was done so as to create blocks of data that were separated by naturally occurring breaks caused by rapid ice movements and rotations.

An averaged magnetic declination was then calculated for each data block. This usually falls into a 3 degree range. The magnetic declination thus obtained was accurate enough to be below the ± 6° accuracy of the PCM direction system. The depth resolution is 2m because of the digitizing. Speed resolution is ± 1.5 cm/s at speeds greater than the stall speed.

A hysteresis effect in the up and down traces was observed. This occurs as the current meter is pulled through the current in the up trace and this results in a higher velocity. The opposite would be true for down trace. In the analysis the hysteresis was reduced by averaging up and down traces.

The absolute speeds were obtained by adding the ice velocities (at the times of the station cast) to the velocities (relative) of the PCM profile. The cases when the relative speed was below the stall speed, no absolute speed calculations were performed. The problem of twisting of the sea cable and producing abrupt 180° changes in the direction was solved by attaching a big vane to the cable. This is a severe problem when studying the Ekman spiral. A total of 373 PCM stations of Snow Bird were used.

3.2.3 Fixed Mast Current Meters

The fixed mast meters were also of the Savonius rotor and vane type from Hydro Products. The stall speed and linearity of the rotors are superior to those of the TSK PCMs. These meters get their direction by measuring the voltage drop across a potentiometer as the vane swings. The absolute direction is obtained when magnetic declination and meter orientation (with respect to the camp azimuth) are added to the direction from meter. The meters were fixed in depth and orientation. The orientation was checked frequently and the meters were maintained at depths of 2 and 30m below the bottom of the ice surface. The accuracy of the direction is also $\pm$ 6 degrees and that of the speed is $\pm$ 1 cm/s. The stall speeds of these rotors are approximately 3 cm/s. These meters worked reliably and no major problems were encountered. The data were recorded on chart paper and digitized on the AIDJEX data logger. Readings were taken every minute but 3 hourly averages were used in calculation, calibration and comparison purposes. Fig. 3.8 shows the data flow from acquisition to analysis.

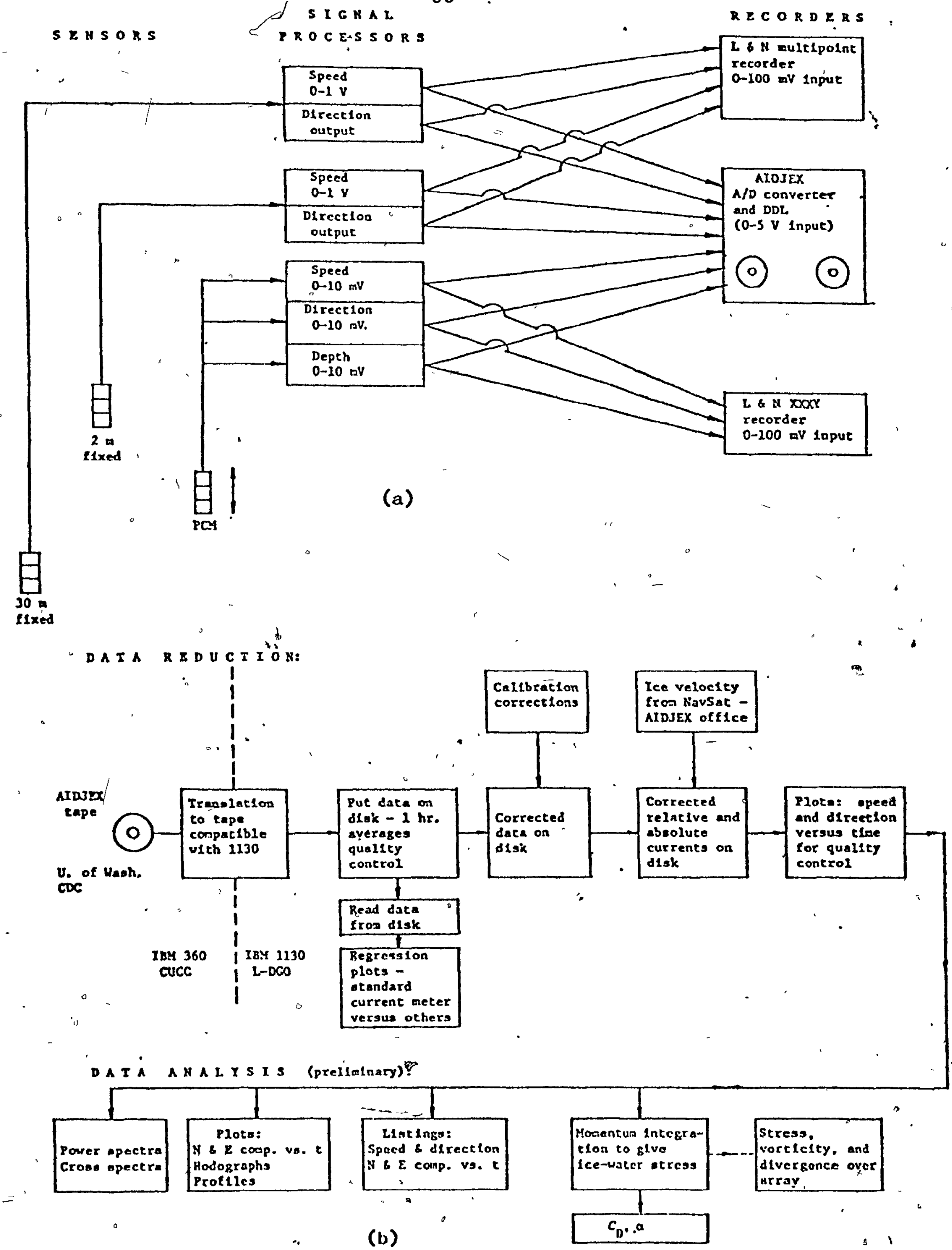

Fig 3.8 Current meter data flow from (a) acquisition to (b) analysis.

Chapter Four: DYNAMIC CALCULATIONS

A common practice in oceanography is to attempt to assess ocean current velocities by use of what is known as the geostrophic approximation, or the geostropic equation. This involves the assumption that the Coriolis force acting on a fluid particle in motion is balanced completely by the horizontal component of the pressure gradient force. If the density field in a body of water is known, it is possible to determine the vertical profile of the horizontal pressure gradient by the use of the hydrostatic equation and hence deduce a value for the vertical profile of the current velocity based on the geostrophic approximation. An absolute value for the pressure gradient and the deduced velocity fields can be obtained only if the actual pressure gradient is known in some reference surface. Currents, calculated on the basis of the geostrophic approximation are referred to as geostrophic currents and they resemble the actual currents only in so far as the basic assumptions are valid.

Measurement of the temperature and salinity of seawater at oceanographic stations provide the necessary data for determining the water density in the oceanic column. From the field of density, the field of pressure is obtained by means of the hydrostatic equation (4.1). The hydrostatic equation expresses the fact, that in an ocean at rest, the pressure p, at a given depth h is related to the weight of the water column above that depth.

$$p = g\bar{\rho}h \qquad (4.1)$$

Here $\bar{\rho}$ is the average seawater density in the vertical column between the sea surface and depth h; g is the acceleration due to gravity. Since the ocean is not at rest, the applicability of the hydrostatic equation in computing the pressure field from the density, may be questioned. However, it will be shown that for use in the classical dynamic method of current computation, the pressure field can be determined with sufficient accuracy by means of the hydrostatic equation.

4.1 Definitions

Before beginning the analysis of the current by the dynamic method, a few definitions are presented.

Since the numerical value of the density of seawater always starts with 1.00 (in cgs units), it has become customary to abbreviate these figures by introducing a quantity σ_{stp} as in (4.2)

$$\sigma_{stp} = (\rho_{stp} - 1)*10^3 \qquad (4.2)$$

where ρ_{stp} is the density as a function of salinity, temperature and pressure. Sigma-t, the more commonly used quantity, disregards the effect of pressure (i.e. ignoring the compressibility of water) on the density in situ. Sigma-t, thus is the density of seawater with effects of temperature and salinity at the depth of observation.

Dynamic depth is a term used to describe the work that must be done to lift a unit mass a given distance perpendicular to the geopotential surface. Thus, level surfaces in the ocean can be defined as surfaces of equal dynamic depth, D, below the ideal sea surface, and instead of using geometric depth to fix the position of a point below the sea surface, dynamic depth is used. As a practical unit of dynamic depth, the dynamic meter (dyn-m) is defined.

$$D\ (\text{dyn-m}) = \frac{gh}{10} \qquad [m^2 s^{-2}] \tag{4.3}$$

where h is expressed in meters and g in ms^{-2}. Thus the unit of geopotential (1 dyn-m) corresponds numerically approximately to a geometric distance of 1.02 m, if g = 9.801 ms^{-2}.

In oceanography, cgs units have been used historically. Thus the density is expressed in $gmcm^{-3}$, velocity in cms^{-1} (sometimes as knots with 1 knot = 50 cm/s) and pressure in decibars. (The SI unit for pressure being Pascal . 1 decibar = 10 kPa). In this presentation these units are used with SI equivalent given wherever possible.

From the hydrostatic equation (4.1) the infinitisimal form becomes (4.4)

$$\delta p = g\rho\ \delta z \tag{4.4}$$

where z , the usual notation for depth is used. Then, from the definition of dynamic depth D, we can write

$$dD = \frac{1}{\rho} dp = \alpha . dp \tag{4.5}$$

with α , the specific volume, the reciprocal of the density. If p is measured in dbar, D is in dyn-m.

The dynamic depth between two isobaric surfaces with pressure p_o and p respectively, is then obtained as

$$D = \int_{p_0}^{p} \alpha \, dp \qquad (4.6)$$

If p_o refers to the sea surface as the uppermost isobaric surface in the sea, and taking $p_o = 0$, then D is the dynamic depth of an isobaric surface with sea pressure p. Of course D can only be measured relative to a sea surface where $p_o = 0$. If the sea surface is inclined, the dynamic depth, as calculated from (4.6) is only the relative dynamic depth. One of the most important problems in dynamic oceanography is the determination of absolute dynamic topographics. If the absolute dynamic topographics are known, the oceanographer can apply theoretical relationships between the pressure forces and other forces that cause and affect ocean current in order to arrive at current speeds and directions at various depths.

From (4.5) we see that for static equilibrium, the fields of pressure and geopotential must be parallel to each other. That is to say surfaces of equal specific volume (isosteric surfaces) and isobaric surfaces coincide with level surfaces. A field in which isosteric and isobaric surfaces coincide is called a barotropic field. A field of mass for which these surfaces intersect is called a baroclinic field. A baroclinic field cannot remain without motion, but barotropic fields can be at rest, but do not have to be motionless. Only when isobaric, isosteric and geopotential surfaces coincide is a barotropic field at rest.

4.2 Geostrophic Currents

When a frictionless current flows horizontally without change of velocity and the only external force is gravity, the component equations of motion on a rotating earth (4.7) become (4.8)

$$\frac{du}{dt} = -\frac{1}{\rho}\frac{\partial p}{\partial x} - 2\omega\sin\phi v + F_x$$

$$\frac{dv}{dt} = -\frac{1}{\rho}\frac{\partial p}{\partial y} - 2\omega\sin\phi u + F_y \tag{4.7}$$

$$\frac{dw}{dt} = -\frac{1}{\rho}\frac{\partial p}{\partial z} - 2\omega\cos\phi u + F_z + g$$

$$2\omega\sin\phi\rho v = \partial p/\partial x$$

$$2\omega\sin\phi\rho u = -\partial p/\partial y \tag{4.8}$$

$$2\omega\cos\phi\rho u = -\partial p/\partial z + g\rho$$

where the velocity $\underline{U}$ is

$$\underline{U} = u\underline{i} + v\underline{j} + w\underline{k}$$

with $\underline{i}$, $\underline{j}$ and $\underline{k}$ as unit vectors in the x, y, z direction. (X is positive to the east, Y is positive to the north and Z positive vertically down to the center of the earth.) ϕ is the latitude and ω the angular velocity of rotation of the earth. Fx, Fy and Fz are the force per unit mass of the external force field. The axes are shown in Fig. 4.1.

From (4.8) we see that in each of the horizontal coordinate directions, the component of the Coriolis force (e.g. $2\omega\sin\phi\rho v$) is balanced by the pressure gradient force ($\partial p/\partial x$). In the vertical direction the pressure gradient force is balanced by the vertical component of the Coriolis force.

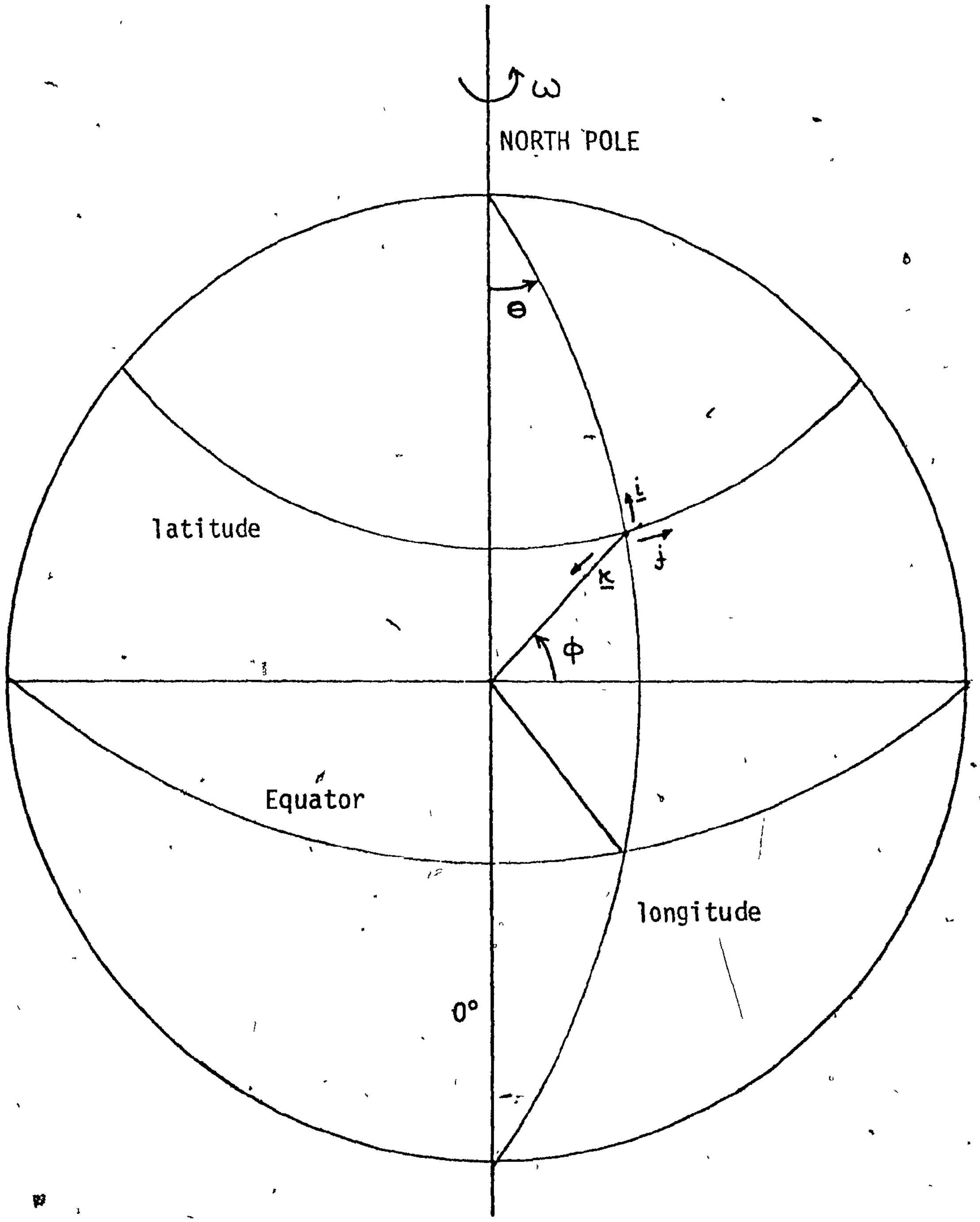

Fig. 4.1 The coordinate system showing the positive X, Y and Z axis.
($\underline{i}$, $\underline{j}$ and $\underline{k}$ vectors)

and the gravitation force.

In the third equation of (4.8) we see that g, the acceleration due to gravity, is much bigger than the contribution of the Coriolis force. Thus for most of the world's oceans, the term $2\omega\cos\phi\rho u$ is vanishingly small compared to g. In the Beaufort Sea, the mean latitude is 76°N and thus the contribution is smaller still. Then the third equation reduces to the hydrostatic equation (4.4).

Squaring and adding the first two equations in (4.8) we get

$$\partial p/\partial n = 2\omega\sin\phi\rho c = f\rho c \qquad (4.9)$$

where

$$c = (u^2 + v^2)^{\frac{1}{2}} \qquad \text{, the speed}$$

$$f = 2\omega\sin\phi \qquad \text{, the Coriolis parameter}$$

and

$$\partial p/\partial n = \left\{ (\partial p/\partial x)^2 + (\partial p/\partial y)^2 \right\}^{1/2} \qquad (4.10)$$

The equilibrium of forces in (4.9) shows that the Coriolis force must be equal and opposite to the horizontal pressure gradient force. Equation (4.9) is a scalar equation, and in the geostrophic balance, the speed c is perpendicular to the pressure gradient. This means that the horizontal current vector c, must be parallel to the isobars. See Fig. 4.2. The direction is such that, for the northern hemisphere, the higher pressure is to the right when one faces in the direction of the current. This type of

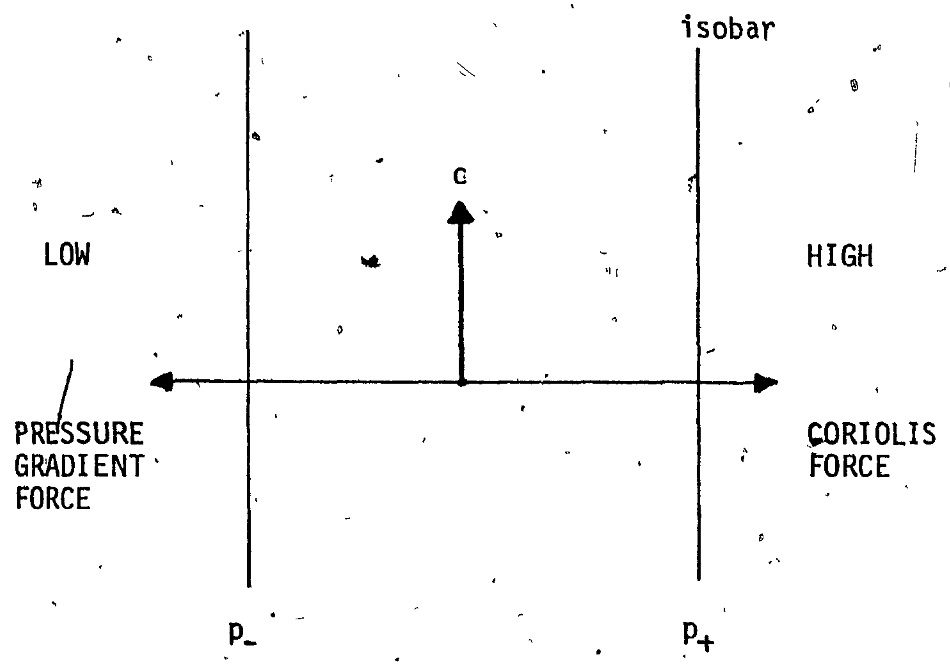

Fig. 4.2 Direction of the current in the northern hemisphere, under the geostrophic balance.

current is called a geostrophic current and the balance of forces thus expressed in (4.9) is called the geostrophic equilibrium.

Instead of using the horizontal pressure gradient along level surface, the slope of the isobaric surface can be introduced in (4.9). Fig. 4.3 shows two isobaric surfaces, in the vertical plane, p and Δp which are inclined against a level surface n. The vertical nz plane is perpendicular to the current velocity c. The pressure at point 1 on the level surface is p and at point 2 is $p + \Delta p = p + g\rho\Delta z$ where ρ is the density of the water column between points 2 and 3. Then

$$(\Delta p / \Delta n) = - g \rho (\Delta z / \Delta n) \qquad (4.11)$$

or

$$(\partial p / \partial n) = g \rho \tan\beta$$

A negative sign on the right of (4.11) is used when the positive Z axis points down. Here β is positive in the clockwise direction.

The classical dynamical method of computing ocean currents is done by directly applying (4.9) and (4.4). If p is the pressure at depth z in the ocean with p_a the constant atmospheric pressure at the surface ζ and $\rho(z)$ is the density of seawater as a function of depth, then

$$p = p_a + g \int_{\zeta}^{z} \rho(z) \, dz \qquad (4.12)$$

We get the horizontal pressure gradient by differentiating, i.e.

$$(\partial p / \partial n) = g \int_{\zeta}^{z} (\partial \rho / \partial n) \, dz - g \rho(\zeta) (\partial \zeta / \partial n) \qquad (4.13)$$

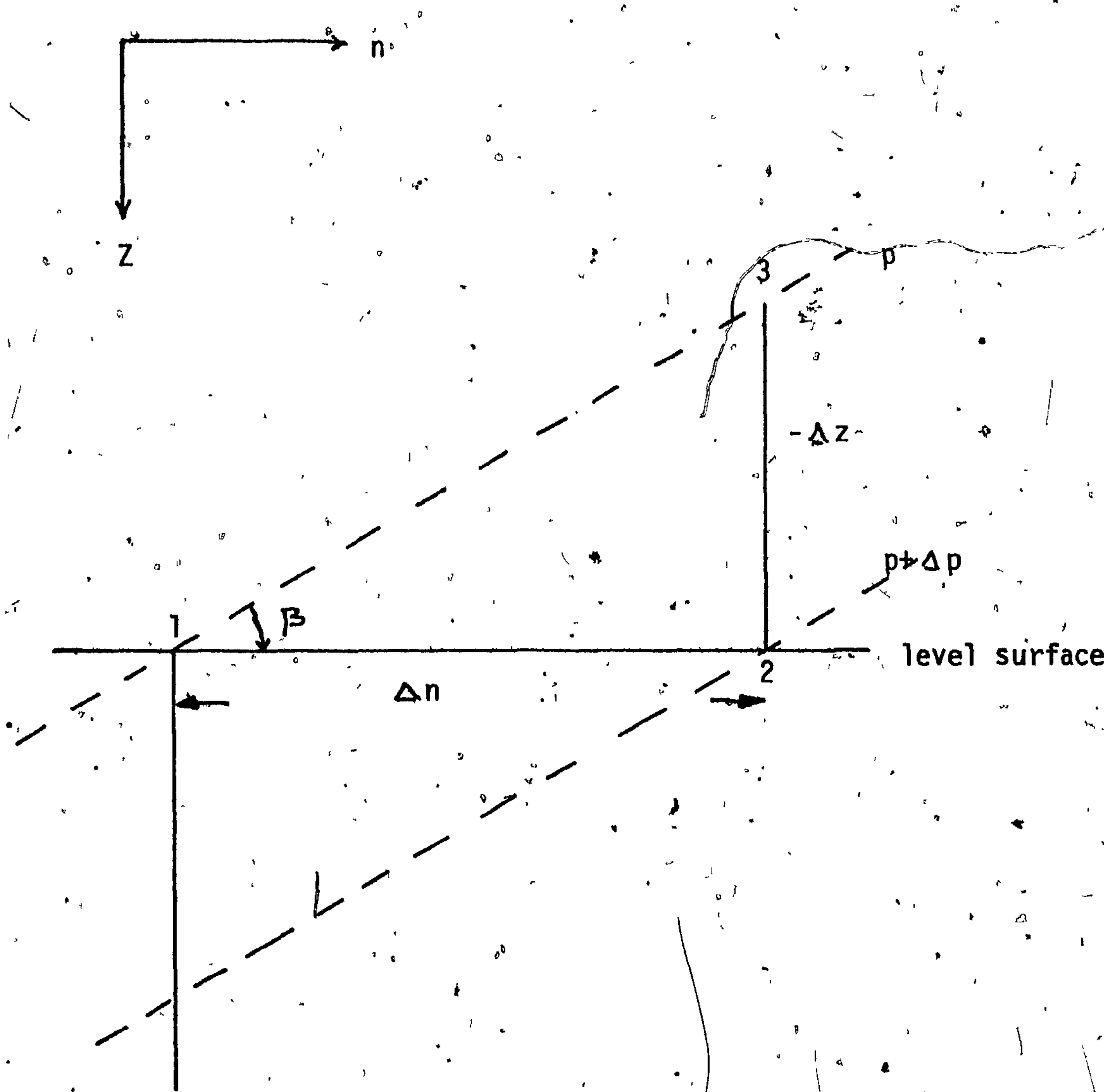

Fig. 4.3 Two isobars in the vertical n-z plane.

In a homogeneous ocean where the density is constant, the first term in (4.13) is zero and the horizontal pressure gradient at depth z is the same as the gradient resulting from the slope of the sea surface $(\partial \zeta/\partial n)$. $\rho(\zeta)$ is the seawater density at the surface. In a stratified ocean then the horizontal pressure gradient has two components. The first is the contribution of a sloping free sea surface (as in the case of the homogeneous ocean) and the second is a component due to horizontal density difference in the water. The term depends on the vertical coordinates and usually increases its value with depth. This means that with increasing depth, the contribution of the sea surface to the total horizontal pressure gradient $(\partial p/\partial n)$, can be gradually compensated by the first term in (4.13). If this is the case at depth $z = H$, then $\partial p/\partial n\big|_{z=H} = 0$

$$\text{i.e.,} \quad \int_{\zeta}^{H} (\partial \rho/\partial n)\, dz - \rho(\zeta)(\partial \zeta/\partial n) = 0 \qquad (4.14)$$

According to (4.14) the absolute geostrophic current should also be zero at this depth $z = H$. This depth is often called 'layer of no motion'. There may be none or more than one layer of no motion in a stratified ocean.

Equation (4.14) demands that $(\partial p/\partial n)$ be a negative quantity, and the isopycnals must slope in a direction that is opposite to the sea surface slope, as in Fig. 4.4. If this were not the case, and the isopycnals sloped in the same direction to the sea surface, then the first term in (4.14) would have the same sign as $\rho(\zeta)(\partial \zeta/\partial n)$, the free surface slope, and the pressure gradient as well as the current speed must increase continuously to the bottom. In the ocean usually this is not the case. Normally currents

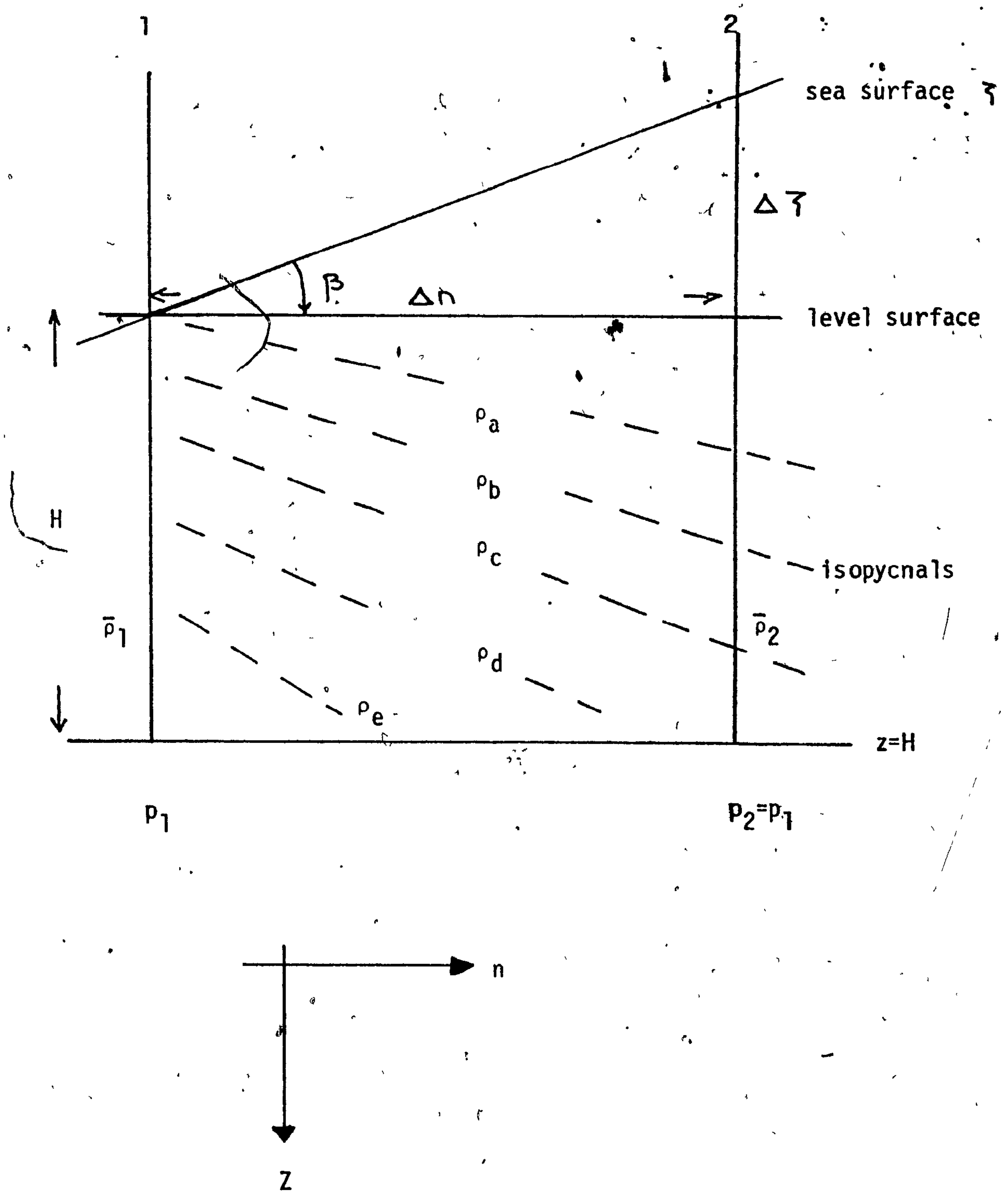

Fig. 4.4 Vertical section showing density distribution and slope of sea surface against a level surface.

decrease with depth, although important exceptions exist in the world. But these exceptions are usually non-geostrophic.

In Fig. 4.4 we have a vertical section between two oceanographic stations 1 and 2. The sea surface rises from station 1 to 2 over a distance Δn along a level surface by an amount $\Delta \zeta$. The isopycnals, ρ_a to ρ_e, are given by the temperature and salinity observations obtained at the stations 1 and 2 respectively. As shown they slope in the opposite direction to the sea surface. The average density of a vertical water column between ζ and the depth, $z = H$ is $\bar{\rho}_1$, at station 1 and $\bar{\rho}_2$ at station 2. The pressure p_1 , at depth H is

$$p_1 = g\,\bar{\rho}_1 H + p_a \qquad (4.15)$$

and the pressure p_2, at station 2, at depth H is

$$p_2 = g\,\bar{\rho}_2 H + p_a + g\,\rho\,(\zeta)\,\Delta\zeta \qquad (4.16)$$

If p_1, p_2 and $\Delta\zeta$ are such that $p_1 = p_2$ at $z = H$, then

$$(\Delta p\ / \Delta n)_{z=H} = 0 \qquad \text{if}$$

$$\bar{\rho}_1 H = \bar{\rho}_2 H + \rho\,(\zeta)\,\Delta\zeta \qquad (4.17)$$

or putting it another way, H, the depth at which the two terms compensate is

$$H = \rho(\zeta)\Delta\zeta \,/\, (\bar{\rho}_1 - \bar{\rho}_2) \qquad (4.18)$$

From (4.18) we can get the depth of the layer of no motion, provided $\Delta\zeta$ is known in addition to the vertical density distribution at two adjacent oceanographic stations. From (4.18) we also see that for a given the depth H increases as $(\bar{\rho}_1 - \bar{\rho}_2)$ decreases. In strongly stratified water the layer of no motion is found at shallower depths than in weaker stratification. In a very weakly stratified part of the ocean, H becomes very deep and approaches infinity as $(\bar{\rho}_1 - \bar{\rho}_2)$ approaches zero. This can happen in the nearly homogeneous water masses that are found in the deeper Beaufort Sea.

Again, if 1 and 2 are our two oceanographic stations for which the distribution of density with depth is known from observation of temperature and salinity with depth, the dynamic depth difference D, in dynamic meter [m^2s^{-2}] between two isobaric surfaces p_a and p_b is obtained by numerically intergrating (4.6).

Defining α_{STP}, the specific volume in situ, as the sum of the contribution from a 'standard ocean' (of 0°C and 35 /oo - α_{350p}) and the anamoly of specific volume δ (the dependence of the specific volume on salinity, temperature and pressure) i.e.

$$\alpha_{STP} = \alpha_{350p} + \delta \qquad (4.19)$$

then

$$D = \int_{p_0}^{p} \alpha_{350p}\, dp + \int_{p_0}^{p} \delta\, dp = D_{350p} + \Delta D \qquad (4.20)$$

In oceanography, we are interested in the differences of D between stations, at a given isobaric surface (p say). From (4.20) we note that the contribution to this difference by the 'standard ocean' ($D_{35,0,p}$) cancels out leaving the dynamic depth anomaly as the only significant term. Thus with the introduction of the specific volume anomaly, the dynamic depth differences at isobaric surfaces p_a and p_b between two adjacent stations (1 and 2) depends only on the term that contains the anomaly of specific volume, i.e.

$$D_1 - D_2 = \Delta D_1 - \Delta D_2 = \int_{p_a}^{p_b} \delta_1 \, dp - \int_{p_a}^{p_b} \delta_2 \, dp \qquad (4.21)$$

(p_a and p_b are the two isobaric surfaces).

Expressing the horizontal pressure gradient ($\partial p/\partial n$) in terms of the slope of the isobaric surface (4.11) and combining with (4.3) we get

$$(\partial p/\partial n) = -10\rho(\partial D/\partial n) \qquad (4.22)$$

then (4.9) becomes

$$2\omega \sin\phi \, c = -10 \frac{\partial D}{\partial n} = -10 \frac{(\Delta D_2 - \Delta D_1)}{\Delta n}$$

or

$$c = \frac{10}{fL} (\Delta D_2 - \Delta D_1) \qquad (4.23)$$

with $f = 2\omega \sin\phi$ the Coriolis parameter and $L = \Delta n$ is the horizontal distance when proceeding from station 1 to 2 in the positive n direction. ΔD_2 and ΔD_1 represent the relative dynamic height anomaly between the isobaric surface at station 2 and 1 respectively, c is the relative current between the two isobaric surfaces p_a and p_b. The relative velocity (or the velocity difference) is in ms^{-1} if the dynamic depth differences are in dynamic-meters (m^2s^{-2}) and L is in m. The expression (4.23) was first derived by Helland-Hansen (1905) from Bjerknes' circulation theorem (1900).

4.3 Sample Calculations

In the application of (4.23) to the data from the AIDJEX main experiment 75-76, station 1 and 2 are taken to be CARIBOU (CB) and SNOWBIRD (SB) respectively. Throughout the experiment, SB was the more northerly of the pair of stations (Fig. 2.6, 2.7 and 2.8). Table 4.1 and 4.2 show the values for density and dynamic height values for a pair of stations. The pair chosen for demonstration purposes is SB 302 and CB 318 of 09 Nov. 75. At this time the camp SB was located at 73.699°N, 142.658°W and CB at 72.877°N, 140.852°W, the distance between the camps being 108 km. The camp positions and relevant directions are depicted in Fig. 4.5.

As stated earlier in the chapter on data collection, measurements of salinity and temperature were made in a very fine scale. Sampling depths were never greater than a meter apart. Because of the continuous nature of the observed data, standard level intervals were much closer than those normally used. In addition, the interpolation error for these standard levels is minimal since observed levels were seldom greater than 0.5 m apart. It would take pages to present the dynamic computations for every station. In

Table 4.1

DYNAMIC DEPTH CALCULATIONS

CB318 09 Nov. 75 1800Z

LAT 72.877°N Long 140.85°W

depth (m)	temp (°C)	salinity (‰)	density (σ_T)	dyn depth (dyn-m)
0.0	-1.89	30.250	24.351	0.0
5.0	-1.89	30.247	24.348	0.018
10.0	-1.89	30.247	24.348	0.036
15.0	-1.89	30.252	24.352	0.054
20.0	-1.89	30.255	24.355	0.072
25.0	-1.89	30.256	24.356	0.090
30.0	-1.89	30.257	24.356	0.107
35.0	-1.88	30.409	24.480	0.125
40.0	-1.78	31.409	25.289	0.140
45.0	-1.76	31.528	25.385	0.153
50.0	-1.74	31.585	25.431	0.167
55.0	-1.75	31.652	25.485	0.179
60.0	-1.78	31.755	25.569	0.192
65.0	-1.84	31.883	25.674	0.203
70.0	-1.76	31.993	25.762	0.215
80.0	-1.62	32.238	25.958	0.236
90.0	-1.63	32.430	26.113	0.256
100.0	-1.67	32.556	26.216	0.275
110.0	-1.72	32.667	26.307	0.292
120.0	-1.75	32.760	26.383	0.309
130.0	-1.74	32.861	26.465	0.325
140.0	-1.73	32.957	26.543	0.341
150.0	-1.74	33.080	26.643	0.355
160.0	-1.73	33.202	26.741	0.369
170.0	-1.63	33.372	26.877	0.381
180.0	-1.51	33.558	27.024	0.393
190.0	-1.39	33.748	27.175	0.402
200.0	-1.23	33.931	27.318	0.411
210.0	-1.06	33.080	27.433	0.418
220.0	-0.85	34.234	27.550	0.424
230.0	-0.68	34.356	27.642	0.429
240.0	-0.52	34.467	27.725	0.433
250.0	-0.41	34.546	27.784	0.436
260.0	-0.31	34.606	27.827	0.439
270.0	-0.23	34.649	27.859	0.442
280.0	-0.17	34.685	27.884	0.445
290.0	-0.12	34.714	27.905	0.447
300.0	-0.08	34.733	27.918	0.449

Table 4.1 (Cont.)

depth (m)	temp (°C)	salinity (‰)	density (σ_T)	dyn depth (dyn-m)
310.0	-0.05	34.752	27.932	0.451
320.0	0.00	34.767	27.942	0.453
330.0	0.03	34.783	27.953	0.454
340.0	0.06	34.796	27.962	0.456
350.0	0.09	34.808	27.970	0.457
370.0	0.14	34.821	27.978	0.460
390.0	0.17	34.830	27.983	0.463
410.0	0.19	34.843	27.993	0.465
430.0	0.21	34.851	27.998	0.468
450.0	0.21	34.858	28.004	0.470
470.0	0.22	34.863	28.007	0.473
490.0	0.21	34.868	28.012	0.475
510.0	0.20	34.871	28.015	0.477
530.0	0.18	34.875	28.019	0.479
550.0	0.17	34.877	28.021	0.481
570.0	0.15	34.880	28.025	0.483
590.0	0.12	34.883	28.029	0.485
610.0	0.10	34.885	28.031	0.487
630.0	0.08	34.886	28.034	0.489
650.0	0.05	34.887	28.036	0.490
670.0	0.03	34.888	28.037	0.492
690.0	0.01	34.890	28.041	0.494
710.0	-0.02	34.893	28.044	0.495
730.0	-0.05	34.892	28.045	0.497
750.0	-0.06	34.893	28.047	0.498
755.0	-0.08	34.895	28.049	0.499

Table 4.2

DYNAMIC DEPTH CALCULATIONS

SB302 09 Nov. 75 1800Z

LAT 73.699°N LONG 142.658°W

depth (m)	temp (°C)	salinity (‰)	density (σ_t)	dyn depth (dyn-m)
0.0	-1.49	30.098	24.223	0.0
5.0	-1.66	30.051	24.187	0.019
10.0	-1.66	30.049	24.185	0.037
15.0	-1.66	30.049	24.185	0.056
20.0	-1.66	30.051	24.187	0.075
25.0	-1.67	30.052	24.188	0.093
30.0	-1.66	30.053	24.188	0.112
35.0	-1.51	30.877	24.853	0.129
40.0	-1.51	31.080	25.018	0.144
45.0	-1.52	31.223	25.134	0.159
50.0	-1.53	31.335	25.225	0.173
55.0	-1.47	31.483	25.343	0.186
60.0	-1.41	31.625	25.457	0.199
65.0	-1.34	31.775	25.577	0.212
70.0	-1.34	31.871	25.654	0.223
80.0	-1.32	32.172	25.897	0.245
90.0	-1.37	32.366	26.056	0.266
100.0	-1.43	32.491	26.158	0.285
110.0	-1.47	32.597	26.245	0.304
120.0	-1.50	32.702	26.331	0.321
130.0	-1.51	32.801	26.411	0.338
140.0	-1.53	32.898	26.490	0.353
150.0	-1.53	32.999	26.572	0.369
160.0	-1.53	33.082	26.640	0.383
170.0	-1.50	33.195	26.730	0.397
180.0	-1.46	33.321	26.831	0.409
190.0	-1.38	33.494	26.969	0.421
200.0	-1.30	33.638	27.083	0.431
210.0	-1.09	33.863	27.259	0.441
220.0	-0.95	34.015	27.377	0.448
230.0	-0.77	34.166	27.492	0.455
240.0	-0.60	34.296	27.590	0.460
250.0	-0.42	34.412	27.676	0.465
260.0	-0.30	34.480	27.725	0.469
270.0	-0.19	34.549	27.776	0.472
280.0	-0.12	34.592	27.806	0.476

Table 4.2 (Cont.)

depth (m)	temp (C)	salinity (‰)	density (σ_t)	dyn depth (dyn-m)
290.0	-0.07	34.625	27.831	0.479
300.0	0.00	34.661	27.856	0.481
310.0	0.06	34.690	27.877	0.484
320.0	0.11	34.705	27.886	0.486
330.0	0.14	34.729	27.904	0.488
340.0	0.18	34.742	27.912	0.490
350.0	0.21	34.759	27.924	0.492
370.0	0.27	34.780	27.937	0.496
390.0	0.31	34.792	27.945	0.500
410.0	0.34	34.805	27.953	0.503
430.0	0.36	34.817	27.963	0.506
450.0	0.38	34.826	27.968	0.509
470.0	0.40	34.832	27.972	0.512
490.0	0.41	34.838	27.976	0.515
510.0	0.43	34.841	27.977	0.518
530.0	0.43	34.846	27.982	0.520
550.0	0.42	34.849	27.985	0.523
570.0	0.42	34.855	27.989	0.526
590.0	0.40	34.856	27.992	0.528
610.0	0.39	34.859	27.995	0.531
630.0	0.37	34.863	27.999	0.533
650.0	0.37	34.863	27.999	0.536
670.0	0.35	34.866	28.002	0.538
690.0	0.33	34.864	28.002	0.541
710.0	0.32	34.865	28.003	0.543
730.0	0.29	34.868	28.008	0.545
750.0	0.25	34.869	28.010	0.547
757.0	0.24	34.870	28.012	0.548

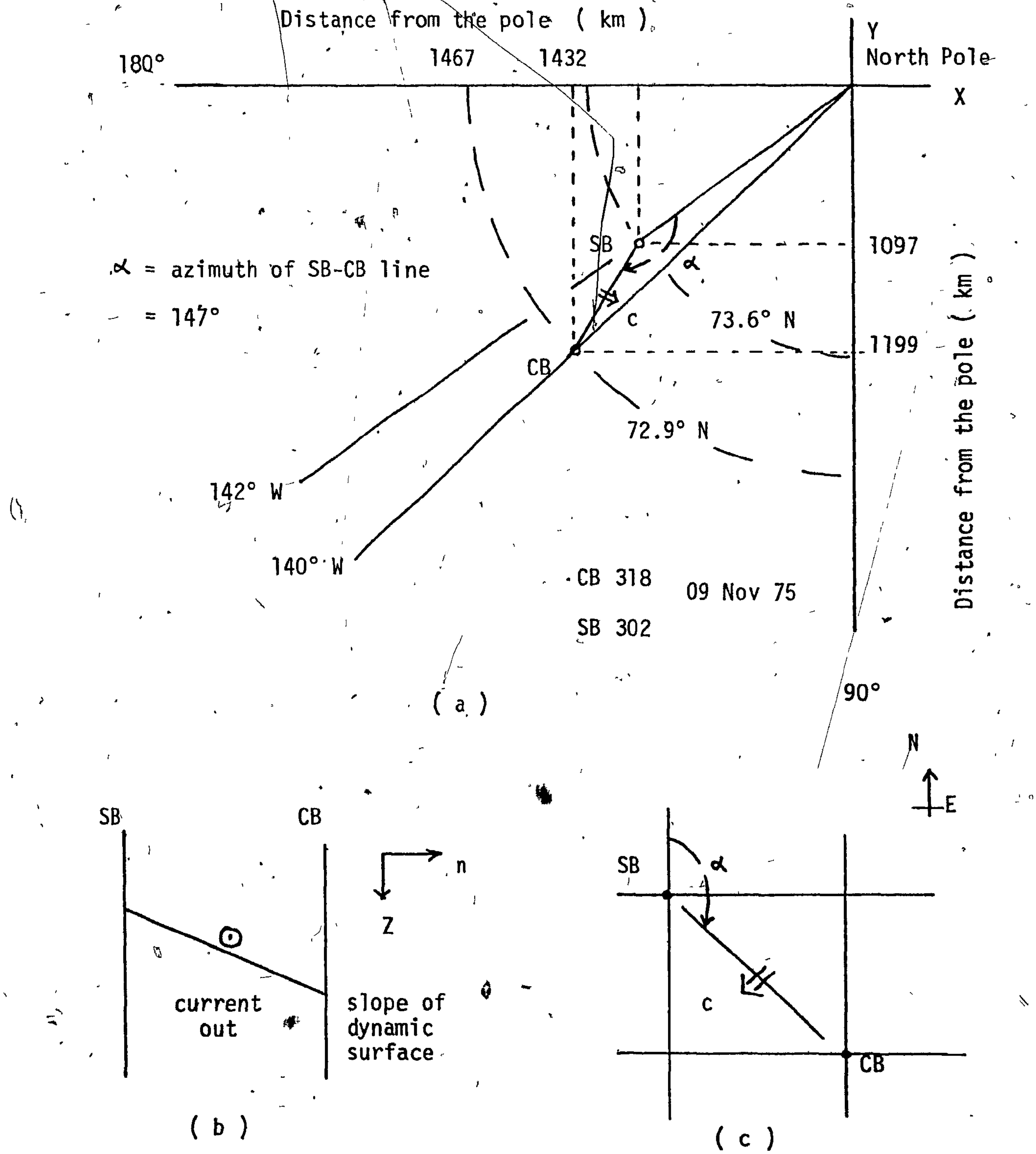

Fig. 4.5 a Camp position and current direction

b Slope of dynamic depth surface (vertical n-z plane)

c Direction of current (horizontal N-E plane)

Table 4.1 and 4.2 we present, the temperature, salinity, density (σ_T), and dynamic height at standard levels for the representative pair of stations SB 302 and CB 318 (09 Nov. 75). Also at this point we present the σ_T, S and T profiles together with the TS diagram of these stations, to show the nature of the water column for each of the stations. (Fig. 4.6, 4.7, 4.8 and 4.9 are salinity, temperature and sigma-t profiles and TS diagram for CB 318 and 4.10, 4.11, 4.12 and 4.13 for SB 302.)

Next, we show in Table 4.3, the relative currents calculated from this pair of stations. In the example shown here and all the others for which calculations are done SB is taken as station 2 and CB as station 1. SB is the more northerly of the pair of stations. The geometry of the stations was shown in Fig. 4.5a. Fig. 4.5b shows the relative slope of the Dynamic depth surfaces. If Δ Dynamic depth = $\Delta D_{SB} - \Delta D_{CB} > 0$ at all depths, the relative currents have a negative sign which means that they are directed such that SB is on the left hand side when one faces in the direction of the relative current. Fig. 4.5b shows the camps in the vertical nz plane and Fig. 4.5c in the horizontal xy plane. The direction of the relative current calculated then is determined by the above relation.

Neither the total relative current nor the actual direction of the current can be calculated as above because we have used only one pair of stations. With the use of another pair (say SB and Blue Fox) it is possible to span the whole two dimensional (horizontal) space and get the total speed and direction. In the meanwhile we have to be satisfied with only that component of the current that is perpendicular to the line joining the camps or the component parallel to the isobars calculated from these pair. It is emphasized that these are relative currents and not the absolute

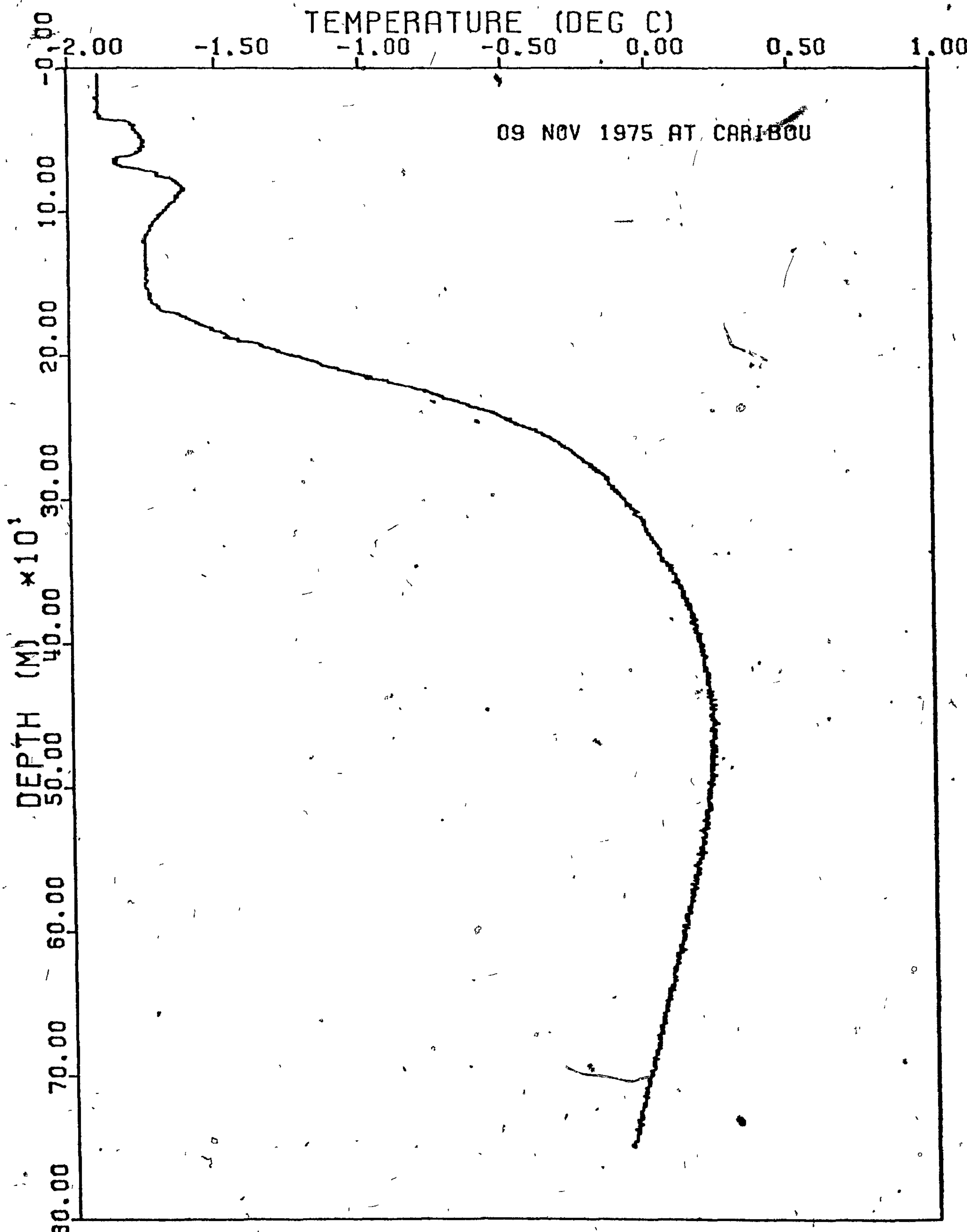

Fig. 4.6 Temperature profile for CB 318 09 NOV 75.

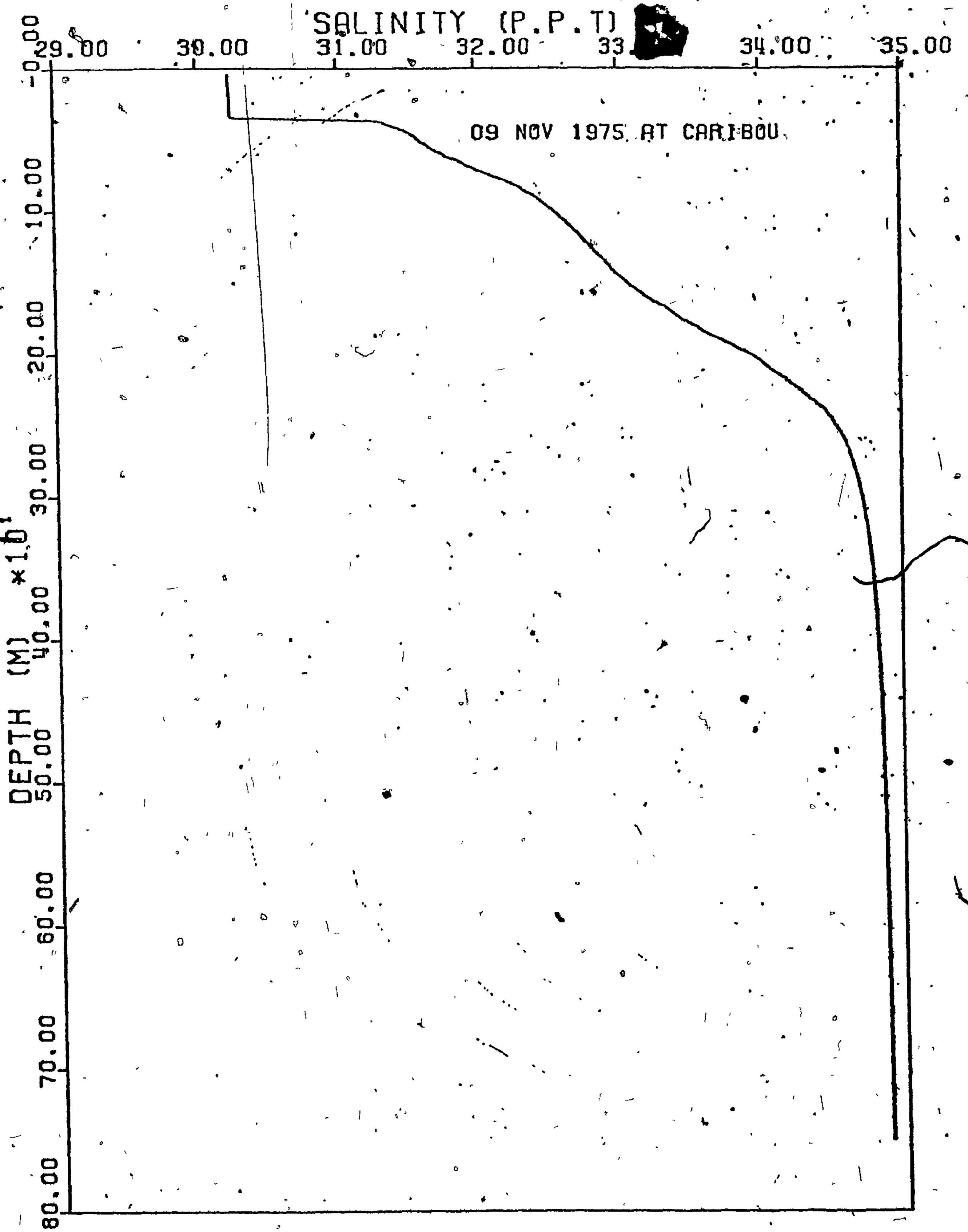

Fig. 4.7. Salinity profile for CB 318 09 NOV 75.

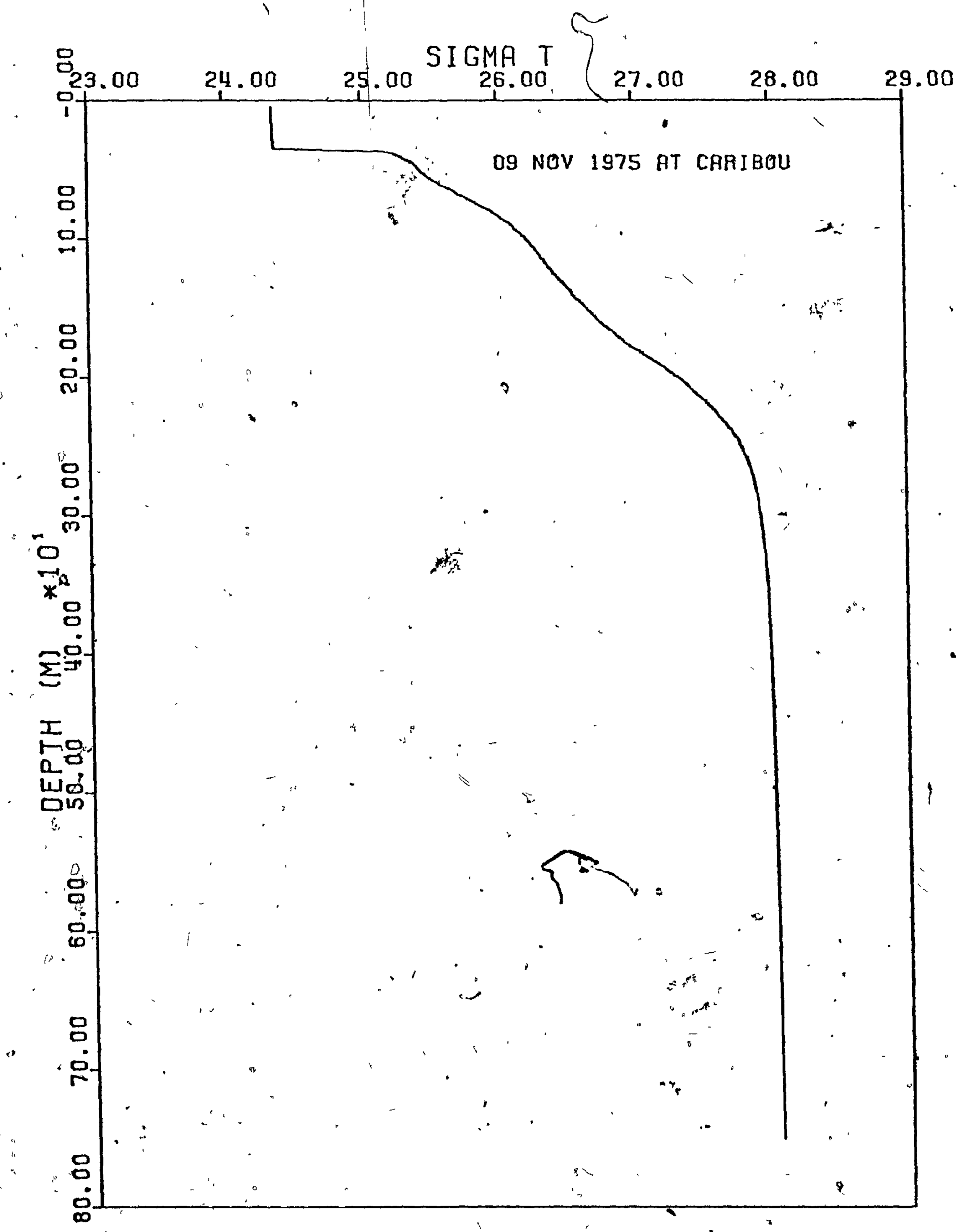

Fig. 4.8 Density (σ_t) profile for CB 318 09 NOV 75.

Fig. 4.9 T-S diagram for CB 318 09 NOV 75.

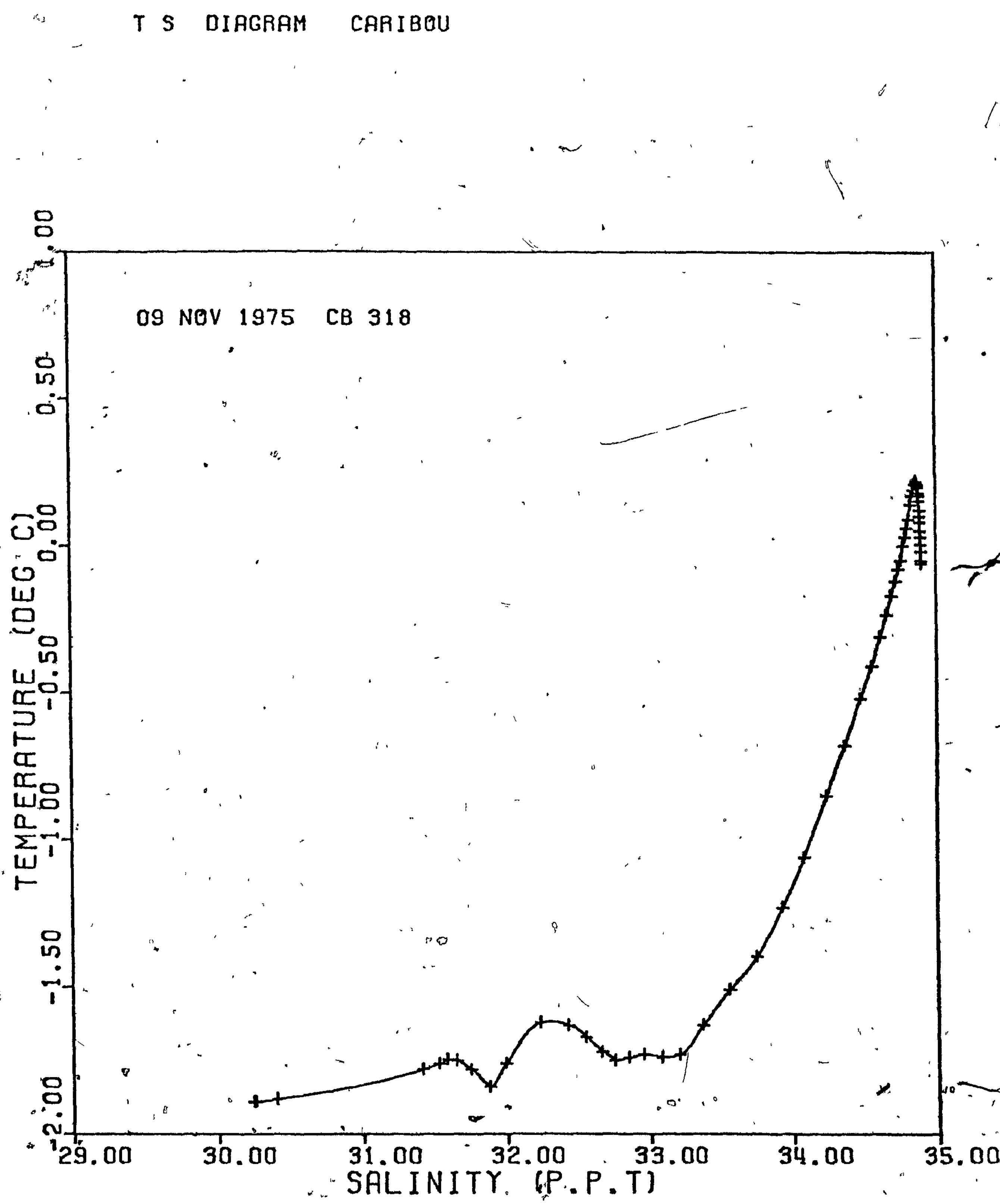

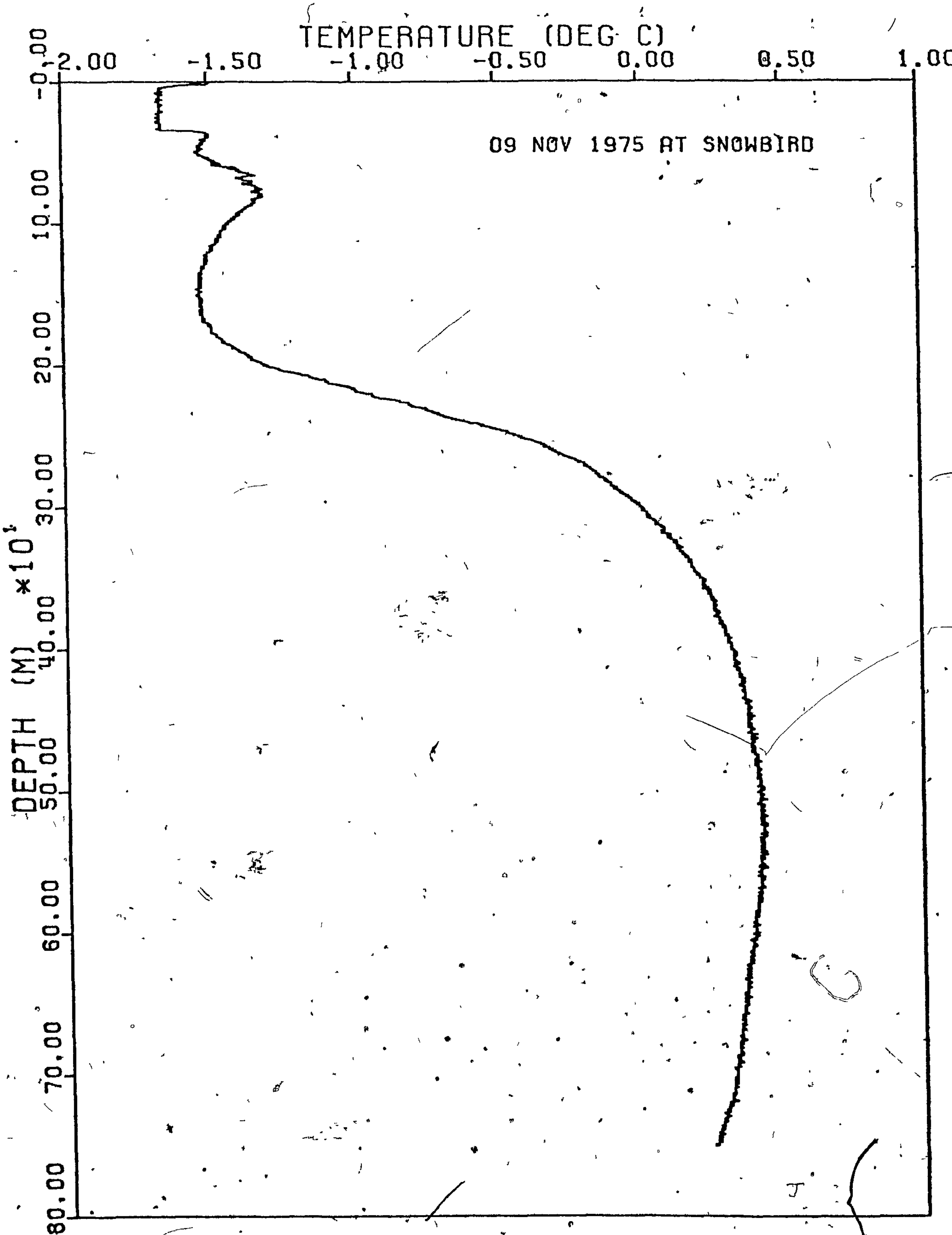

Fig. 4.10 Temperature profile for SB 302 09 NOV 75.

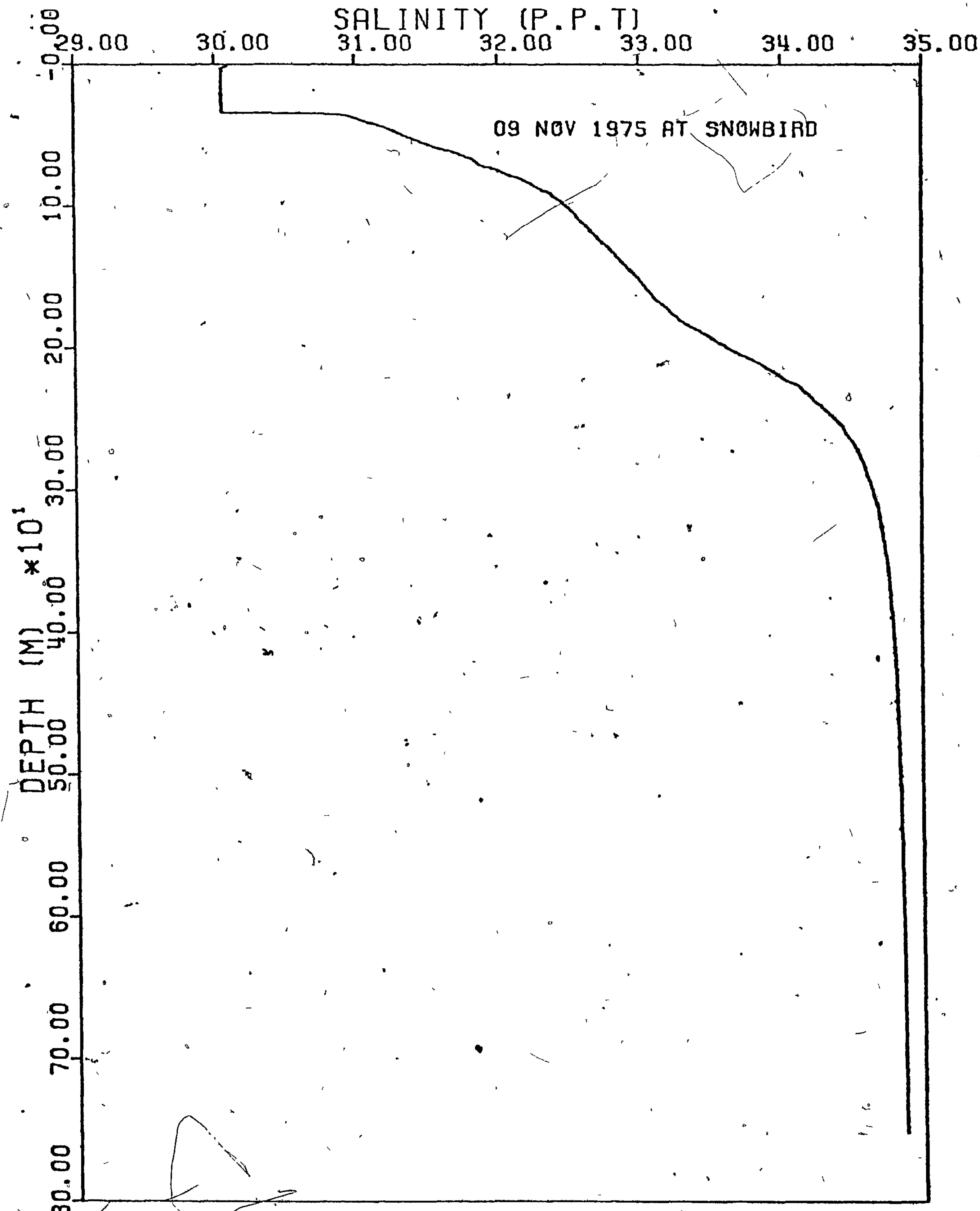

Fig. 4.11 Salinity profile for SB 302 09 NOV 75.

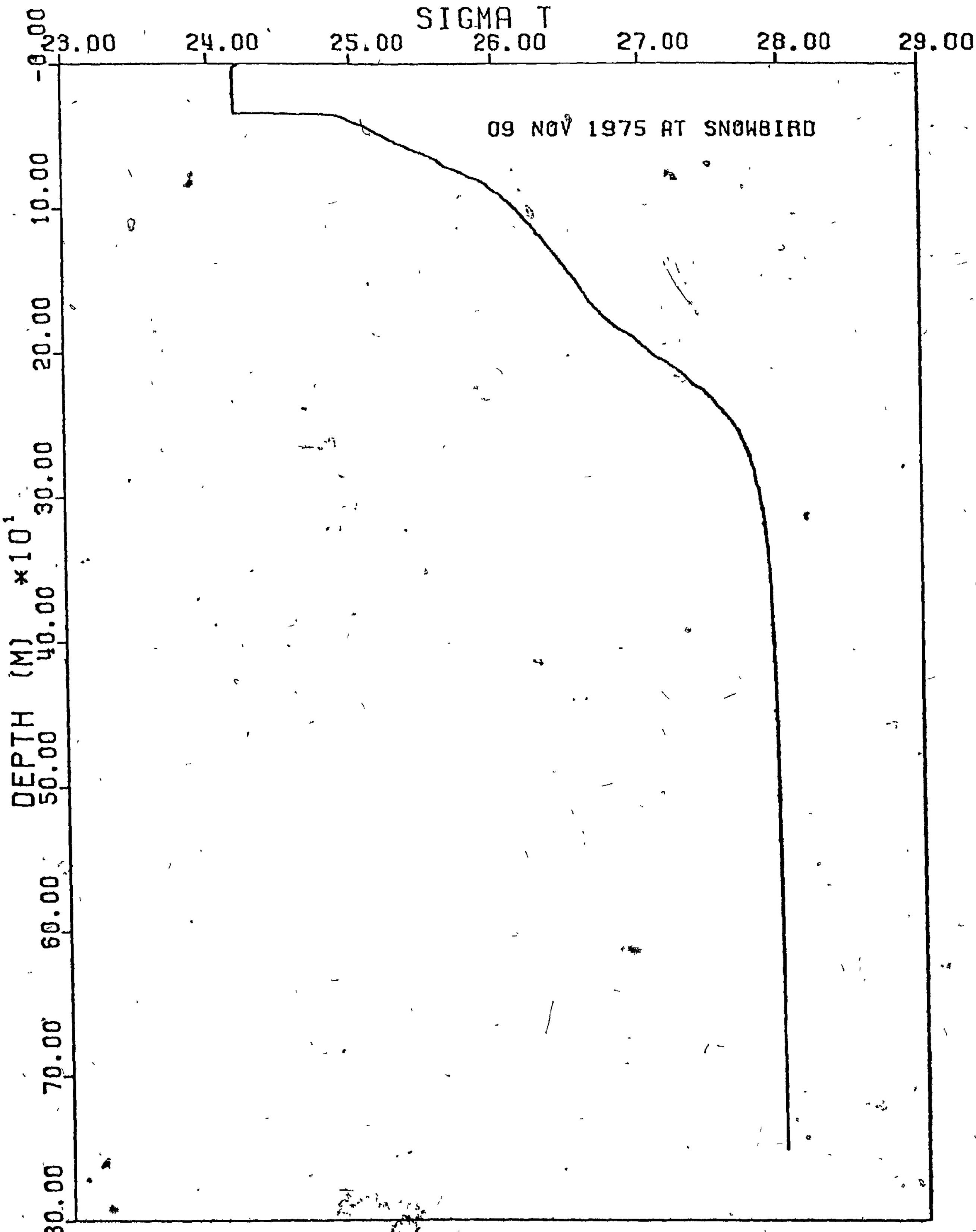

Fig. 4.12 Density (σ_t) profile for SB 302 09 NOV 75.

Fig. 4.13 T-S diagram for SB 302 09 NOV 75.

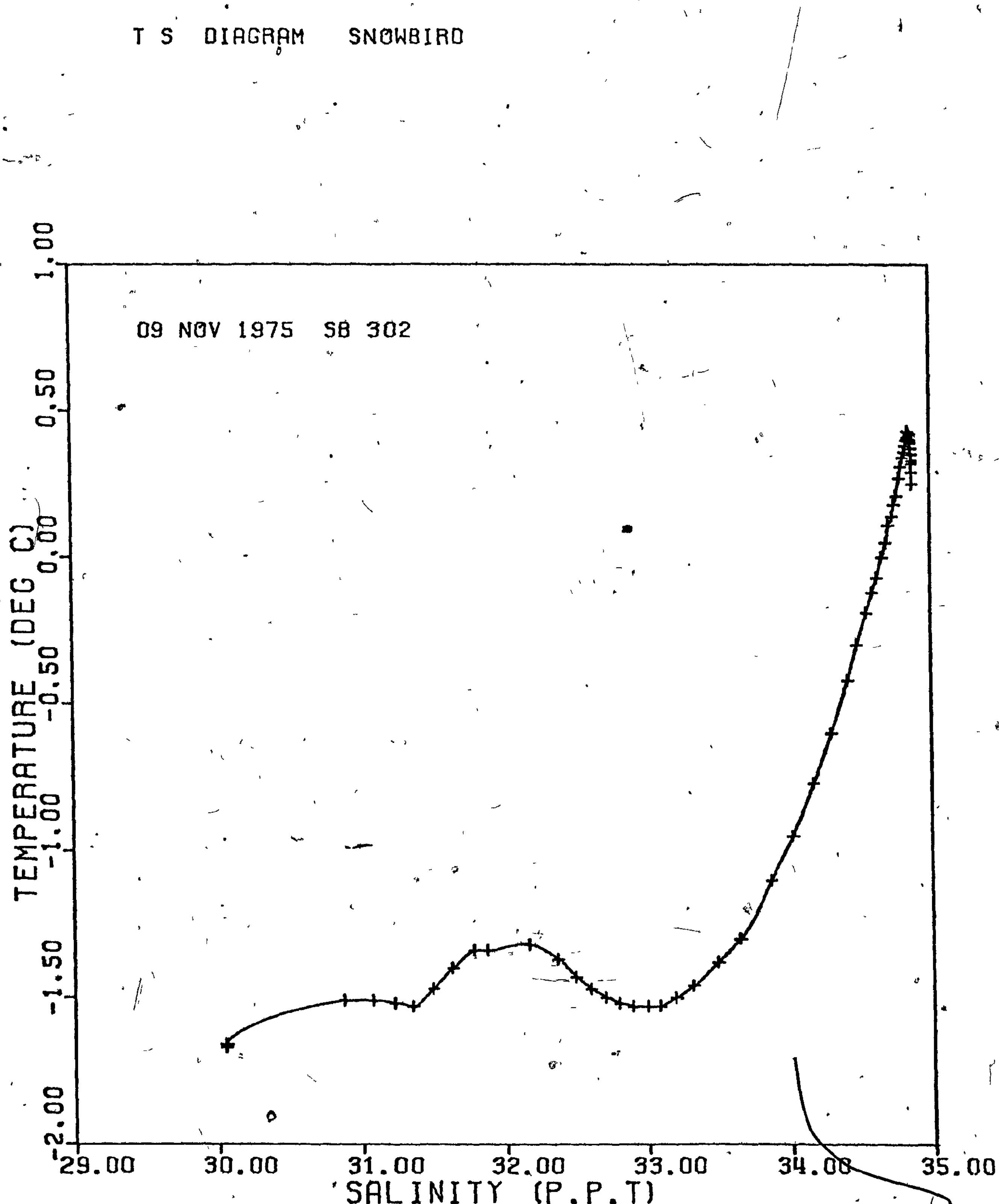

Table 4.3

RELATIVE CURRENT CALCULATIONS

depth (m)	ΔD_{SB} (dyn-m)	ΔD_{CB} (dyn-m)	ΔD_{SB-CB} (dyn-m)	rel. current (cm/ s)
0.0	0.0	0.0	0.000	0.0
5.0	0.019	0.018	0.001	0.04
10.0	0.037	0.036	0.001	0.10
15.0	0.056	0.054	0.002	0.15
20.0	0.075	0.072	0.003	0.20
25.0	0.093	0.090	0.004	0.25
30.0	0.112	0.107	0.005	0.31
35.0	0.129	0.125	0.004	0.28
40.0	0.144	0.140	0.004	0.26
45.0	0.159	0.153	0.005	0.34
50.0	0.173	0.167	0.006	0.41
55.0	0.186	0.179	0.007	0.47
60.0	0.199	0.192	0.008	0.51
65.0	0.212	0.203	0.008	0.54
70.0	0.223	0.215	0.009	0.57
80.0	0.245	0.236	0.009	0.63
90.0	0.266	0.256	0.010	0.66
100.0	0.285	0.275	0.011	0.70
110.0	0.304	0.292	0.011	0.74
120.0	0.321	0.309	0.012	0.77
130.0	0.338	0.325	0.012	0.81
140.0	0.353	0.341	0.013	0.84
150.0	0.369	0.355	0.013	0.88
160.0	0.383	0.369	0.014	0.93
170.0	0.397	0.381	0.015	1.01
180.0	0.409	0.393	0.017	1.12
190.0	0.421	0.402	0.019	1.24
200.0	0.431	0.411	0.021	1.38
210.0	0.441	0.418	0.023	1.51
220.0	0.448	0.424	0.024	1.62
230.0	0.455	0.429	0.026	1.72
240.0	0.460	0.433	0.027	1.81
250.0	0.465	0.436	0.029	1.89
260.0	0.469	0.439	0.030	1.95
270.0	0.472	0.442	0.030	2.01
280.0	0.476	0.445	0.031	2.06
290.0	0.479	0.447	0.032	2.11
300.0	0.481	0.449	0.033	2.15
310.0	0.484	0.451	0.033	2.19

Table 4.3 cont.

depth (m)	ΔD_{SB} (dyn-m)	ΔD_{CB} (dyn-m)	ΔD_{SB-CB} (dyn-m)	rel. current (cm/s)
320.0	0.486	0.453	0.034	2.22
330.0	0.488	0.454	0.034	2.26
340.0	0.490	0.456	0.035	2.29
350.0	0.492	0.457	0.035	2.32
370.0	0.496	0.460	0.036	2.37
390.0	0.500	0.463	0.037	2.42
410.0	0.503	0.465	0.037	2.47
430.0	0.506	0.468	0.038	2.51
450.0	0.509	0.470	0.039	2.61
490.0	0.515	0.475	0.040	2.65
510.0	0.518	0.477	0.041	2.70
530.0	0.520	0.479	0.041	2.74
550.0	0.523	0.481	0.042	2.79
570.0	0.526	0.483	0.043	2.84
590.0	0.528	0.485	0.043	2.88
610.0	0.531	0.487	0.044	2.93
630.0	0.533	0.489	0.045	2.97
650.0	0.536	0.490	0.045	3.02
670.0	0.538	0.492	0.046	3.06
690.0	0.541	0.494	0.047	3.11
710.0	0.543	0.495	0.048	3.16
730.0	0.545	0.497	0.048	3.21
750.0	0.547	0.498	0.049	3.25
755.0	0.548	0.499	0.050	3.28

currents. The program that calculates the speed and direction of these relative currents is shown in block form in Appendix 4.

In order to get the absolute currents, either the absolute pressure field or the absolute current velocity must be known. The inclination of the isobaric surfaces against level surfaces is very small and no method exists in oceanography at present to measure these inclinations directly. In using measured currents care must be taken to note if the currents are close enough to geostrophic equilibrium in order to relate the measured absolute currents to the horizontal pressure gradients. The layer of no motion referred to here is the layer of no horizontal motion. A layer of no absolute motion would involve the vertical component too, and the three-dimensional current field is even more difficult to obtain.

Defant's (1941) method to get the layer of no motion starts with the assumption that the strongest currents occur in the uppermost stratified structure of the sea. Upon comparing the differences of the relative dynamic depth of a given isobaric surface between adjacent oceanographic stations (e.g. Table 4.3) it is found that in the deep sea layers, this difference was practically constant over large depth intervals. It would be unreasonable to assume that these deep layers are moving with uniform speed and that the surface layers are motionless. Thus, Defant, suggested that these deep layers, with constant or nearly constant horizontal pressure gradients, are motionless in the horizontal direction, rather than at a uniform high speed as compared to the sea surface. The absolute currents at any depth, are then obtained, by taking the relative current at this depth and subtracting the calculated current at the supposed layer of no motion. This would yield zero speed at the layer of no motion and a non zero speed at the surface.

In applying these assumptions to the data on the stations SB and CB we have to choose the maximum depth of the oceanographic casts as the depth of the layer of no motion. A qualifying remark is needed to justify this choice. We assume that large changes occur in the upper layer and that the deeper Atlantic water (at depths up to 900 m) is relatively stationary (or slow moving). It is not correct to say that the Atlantic water is motionless as the deep circulation in the Beaufort Sea is of this water (Fig. 1.10). Due to the lack of any other data (current meter and/or deeper oceanographic casts at these two stations) the layer of no motion is placed at 750 m -- the maximum depth of these casts. Table 4.4 has the absolute and relative currents for 09 Nov 75. The absolute currents are referenced to a depth of 750 m. Fig. 4.14 and 4.15 show the currents as calculated and as measured from the PCM casts at that time.

The PCM casts are only to a depth of 200 m or less. The PCM currents measured are relative to the ice. By adding the ice velocity to the water speeds we get the absolute currents (plotted in Fig. 4.15). In comparing the absolute speed (geostrophic) and the PCM measured speeds (to 200 m) we see that the geostrophic current is smaller. One possibility is that the layer of no motion is significantly deeper than that assumed here. As was pointed out earlier the layer of no motion is deeper in nearly homogeneous water in the deeper part of the basin. Typically, Defant found that the layer of no motion in the Atlantic to be 1500 m or more. Another possibility is a barotropic current arising from the sloping sea surface possible because of atmospheric pressure differences. This pressure difference would result in a current even in an ocean of uniform σ_t. The information on this is not available for the SnowBird and Caribou stations.

Table 4.4

Absolute and Relative Currents

depth (m)	relative current (cm / s)	absolute current (cm / s)
0.0	0.00	-3.28
5.0	0.04	-3.23
10.0	0.10	-3.18
15.0	0.15	-3.13
20.0	0.20	-3.08
25.0	0.25	-3.03
30.0	0.31	-2.97
35.0	0.28	-3.01
40.0	0.26	-3.02
45.0	0.34	-2.94
50.0	0.41	-2.87
55.0	0.47	-2.81
60.0	0.51	-2.77
65.0	0.54	-2.74
70.0	0.57	-2.71
80.0	0.63	-2.65
90.0	0.66	-2.62
100.0	0.70	-2.58
110.0	0.74	-2.54
120.0	0.77	-2.51
130.0	0.81	-2.47
140.0	0.84	-2.44
150.0	0.88	-2.40
160.0	0.93	-2.35
170.0	1.01	-2.27
180.0	1.12	-2.16
19-.0	1.24	-2.03
200.0	1.38	-1.90
210.0	1.51	-1.77
220.0	1.62	-1.66
230.0	1.72	-1.56
240.0	1.81	-1.47
230.0	1.89	-1.39
260.0	1.95	-1.33
270.0	2.01	-1.27
280.0	2.06	-1.22
290.0	2.11	-1.17
300.0	2.15	-1.13

Table 4.4 Cont.

depth (m)	relative current (cm / s)	absolute current (cm / s)
310.0	2.19	-1.09
32-.0	2.22	-1.05
330.0	2.26	-1.02
340.0	2.29	-0.99
350.0	2.32	-0.96
370.0	2.37	-0.91
390.0	2.42	-0.86
410.0	2.47	-0.81
430.0	2.51	-0.76
450.0	2.56	-0.72
470.0	2.61	-0.67
490.0	2.65	-0.63
510.0	2.70	-0.58
530.0	2.74	-0.54
550.0	2.79	-0.49
570.0	2.84	-0.45
590.0	2.88	-0.40
610.0	2.93	-0.35
630.0	2.97	-0.31
650.0	3.02	-0.26
670.0	3.06	-0.22
690.0	3.11	-0.17
710.0	3.16	-0.12
730.0	3.21	-0.07
750.0	3.25	-0.03
735.0	3.28	0.00

Fig. 4.14 Geostrophic current profile for 09 NOV 75.

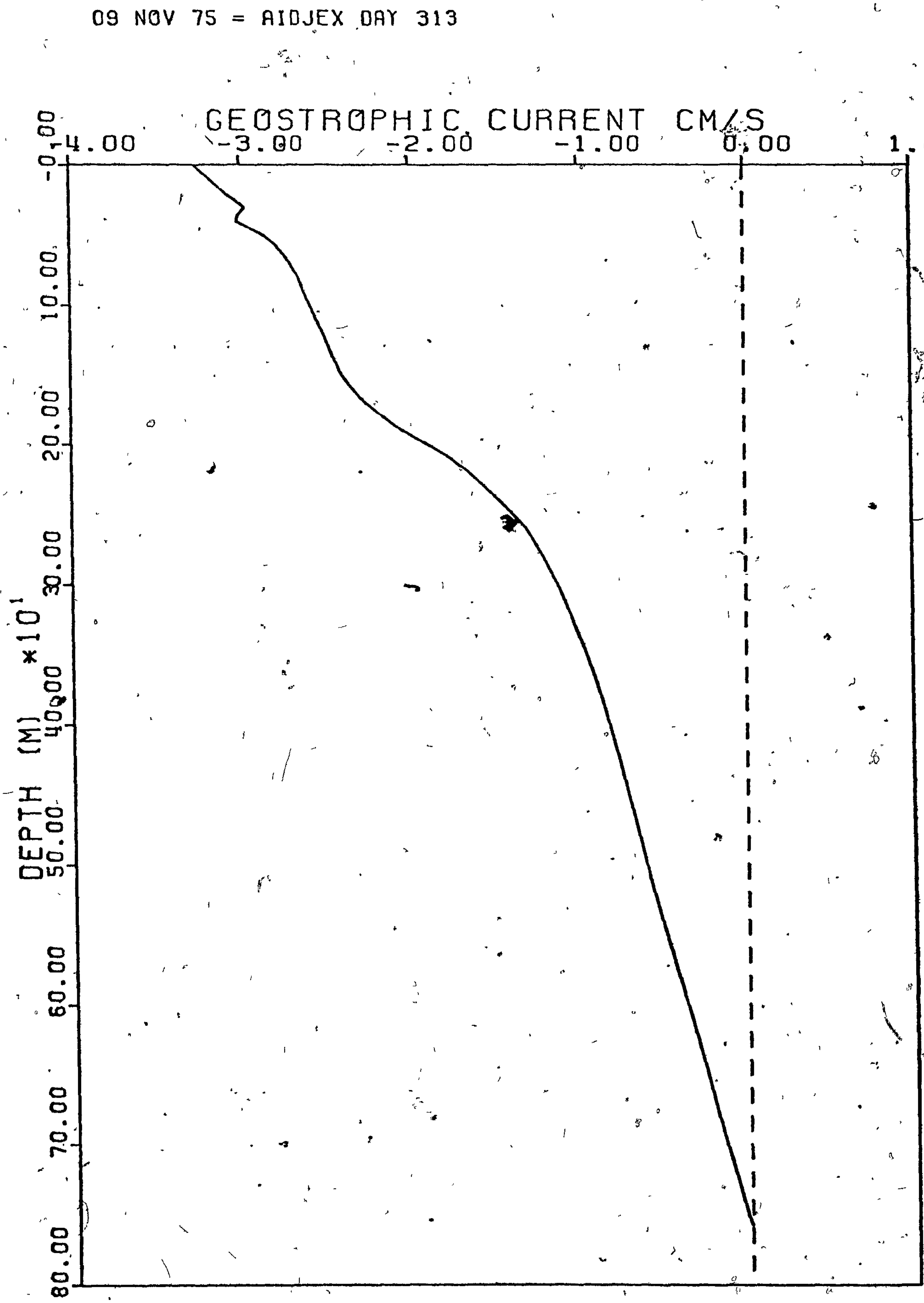

Fig. 4.15 Measured currents at Snow Bird for 09 NOV 75.

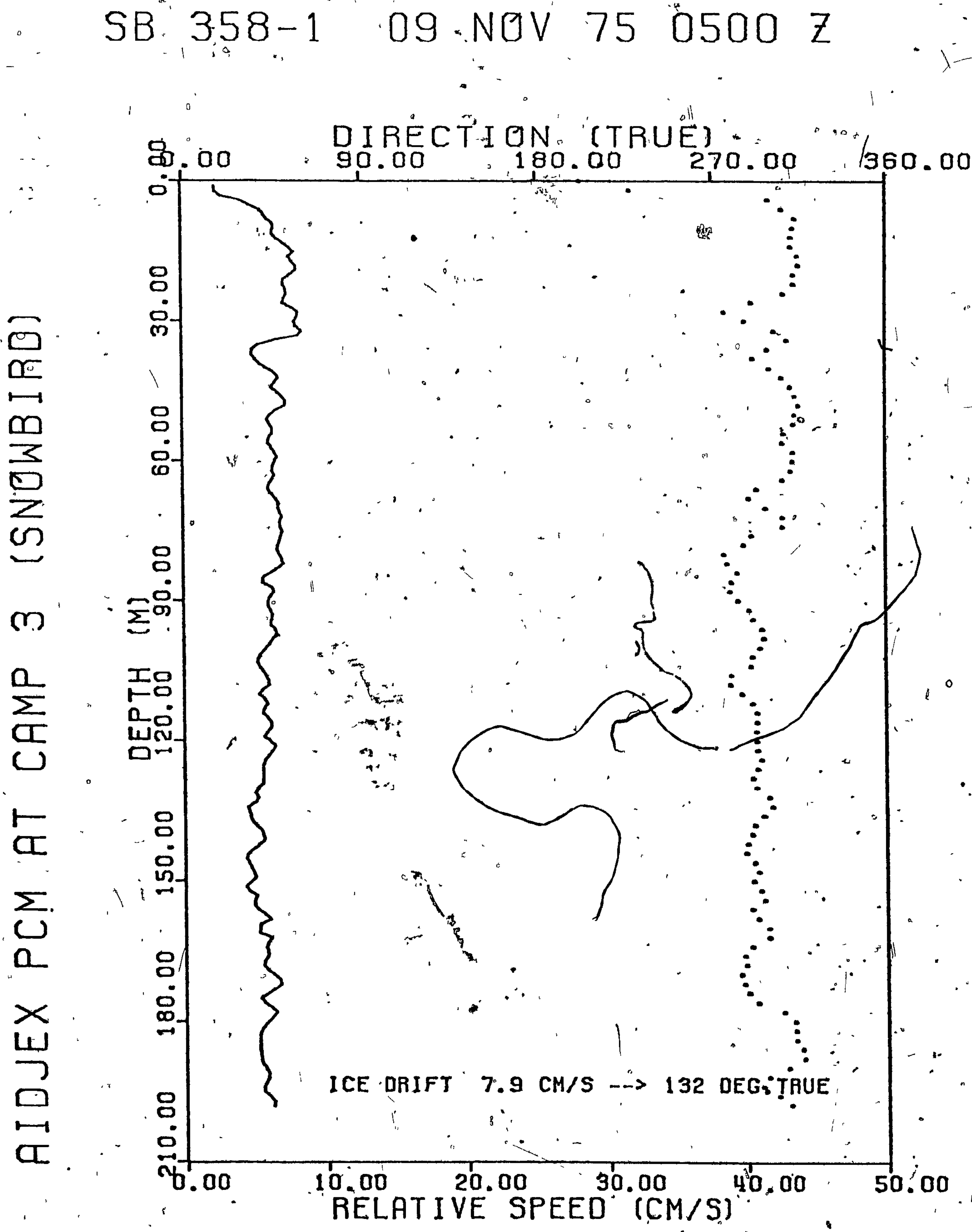

4:4 Mass Transport

Defining the mass transport components as

$$Mx = \int_0^d \rho \, u dz$$

$$Mx = \int_0^d \rho' \, v dz \qquad (4.24)$$

, till the depth = d, we can calculate the mass transport from the current meter data and the calculated absolute geostrophic currents. The mass transport (total) for the PCM currents is given by M, i.e.

$$M = (Mx^2 + My^2)^{\frac{1}{2}}$$

and the mean direction as

$$\Theta = \arctan \left(\frac{My}{Mx}\right)$$

In Table 4.5 comparison of the mass transport (total - to 200 m) from the PCM currents and the mass transport (perpendicular to the line joining camps CB and SB - also to 200 m) is given. Taking the projection of the total mass transport (M) (to 200 m) along the direction of the absolute calculated current, we see that the mass transport from calculated currents is low by about 50%. A possible explanation is the probable deeper layer of no motion as explained earlier. This may well be compounded by the possible

Table 4.5

Mass Transport

Date	measured currents (M)		calculated currents (m)	Projection of M along m	Possible barotrop current (cm/s)
	magnitude (gm/cm-s)	direction (true)	magnitude (gm/cm-s)		
20 Jun	66831.62	73	23913.18	56302.46	1.6
23 Jun	52241.54	89	26591.95	35561.91	0.4
30 Jun	119805.12	334	19999.69	33625.31	0.6
04 Aug	75416.56	277	11909.11	43364.34	1.5
06 Aug	56751.11	357	13080.31	37678.55	1.2
08 Aug	97842.37	239	11012.08	94977.20	4.2
09 Aug	99352.75	324	12512.50	14513.64	0.1
10 Aug	153638.06	347	23336.15	85913.31	3.1
12 Aug	102523.81	289	16187.38	41863.59	1.3
13 Aug	105726.44	302	17474.54	25040.05	0.4
14 Aug	134522.87	294	23489.75	51696.51	1.4
15 Aug	132573.75	134	20048.63	11093.49	0.4
17 Aug	77650.31	354	20513.51	39293.68	0.9
19 Aug	103678.81	87	16344.05	86256.01	3.5

Table 4.5 Cont.

Date					
12 Oct	159299.19	212	57323.39	138095.95	4.0
13 Oct	170292.06	272	57049.73	142980.59	4.2
15 Oct	180622,75	104	44590.75	140766.17	4.8
18 Oct	197949.56	127	58939.54	88633.71	1.4
21 Oct	108669.50	246	69616.44	107764.41	1.9
24 Oct	93520.69	247	25996.00	92291.43	3.3
25 Oct	124947.50	260	29897.93	124947.50	4.7
29 Oct	183281.37	344	28234.51	61180.58	1.6
06 Nov	109445.94	224	41840.77	106726.14	3.2
07 Nov	136418.36	216	46228.38	106316.16	3.0
09 Nov	115208.12	296	53457.53	58125.68	0.2
13 Nov	118332.56	40	50013.84	111545.18	3.1

barotropic current (as before). A barotropic flow of about 3.0 cm/s will make the two mass transports comparable for most cases.

In this presentation only one station pair has been used. There exist hundreds of more pairs for which current calculations have been done (and are to be done). It would be too voluminous to present these here. The calculated geostrophic currents are always smaller than the measured currents. The mass transports (in Table 4.5) are presented for some representative times. Again the mass transports are less (by 50% or more). Another problem in comparing the mass transports is the presence of baroclinic eddies. Baroclinic eddies are described in the following chapter.

In Table 4.5, we have divided the data into four groups. The first is for the period in June. This is to be representative of the spring conditions and early summer. The mass transports are small and there is relatively good agreement in comparing the component of the total mass transport along the calculated current direction line. The mass transports from the geostrophic calculations are smaller by about 50% or so. In this time a barotropic current of about 0.5 cm/s would make the transports comparable.

In the next section i.e. 04 to 19 Aug we see the effect on the mass transports when there is a sustained period of high winds. The time from 09 to 14 Aug was marked with fairly large ice movements (more than 25 cm/s) and large winds (more than 10 m/s). In this sequence we see an increase in the mass transport as calculated from the actual currents till the period of high winds and continued large values for 4 days beyond the subsidence of the high winds. The same general trend is observed in the mass transport from the geostrophic currents as well but the relationship is not as smooth as that for the measured currents. Again there is a need for a barotropic current of 1.0 cm/s or so to bring the transport from calculated currents in accordance with the measured currents.

The third period is from Oct 12 to 29. In this time there is little rapid ice movement and the period is indicative of autumn. In this time the mass transports (both) from the calculated and measured currents are much bigger than for the previous instances and for the period in November. The mass transport from the geostrophic currents underestimates the mass transport from the measured currents by a bigger amount and a current of about 3.0 cm/s is now needed to make the two transports comparable.

The period from 06 to 13 Nov is similar to that in October but with winter more entrenched. The mass transport agreement is fairly poor but the trends seem to be consistent.

The only seasonal trend observed was that there is a larger mass transport in winter than in the spring time but this statement is based on only a few data points. Analysis has not been done for current in Dec 75 to April 76.

4.5 Error Analysis

Before leaving the discussion on the dynamic calculation, a bit of error analysis is presented.

The values used in the computation of the relative current in expression (4.23) are D, L, and ϕ. The position (including the latitude) is known very accurately as the NavSat navigation system gives the position of the camps to a square 10 m on the side. This gives high resolution for the calculation of the value of Δn (or L) the horizontal distance between the camps.

Typically L was of the order 100 km and the accuracy of positioning will put the distance error to ± 100 m (at the outside) Thorndike and Cheung (1977) (i.e. 0.1%). The dynamic depth computation of Δ D involves the calculation of the specific volume anomaly which in turn is calculated from the knowledge of the salinity and temperature measurements. As stated earlier, salinity was measured to an accuracy of ±0.001‰ and the temperature to ±0.01°C and ±1 m in depth. The temperature of the sea water was measured by the deep-water reversing thermometer with an accuracy of ±0.02°C. In the laboratory the salinity of the sea water using titration was measured to ±0.005‰. The 9040 STD has better accuracy than this.

The sigma-t (σ_t) depends on the water temperature and salinity. The empirical formula is cumbersome and is given in Bjerkner and Sandstörm (1912) or Soule (1932). For brevity we write down the expression obtained from the formula needed for estimation of the error in the computation of for given errors in the determination of sea water temperature and salinity.

$$d\sigma_t = C_1 dS + C_2 dT \tag{4.25}$$

where C_1 and C_2 are easily computed quantities. Fomin (1964) presents them in tabular form and the results are quoted here. It is seen that σ_t depends on salinity and considerably on temperature. Generally the temperature in the Arctic water is near the freezing point at the surface (-1.86°C) and usually approaching 0°C in the deeper part. Salinity variations are from 30 - 35‰. With these variations in mind, the ultimate error in σ_t is constant and equal to 0.02 σ_t units (or less) in the large part of the ocean we study.

The specific volume, α, is used in the dynamic depth anomaly (4.6). The computation error in α is

$$d\alpha = \frac{d\sigma_t \times 10^6}{(\sigma_t + 1000)^2} \tag{4.26}$$

and is approximately 95% of the error in the computation of σ_t. For our purposes we take it to be 0.02 σ_t units too.

The correction to allow for the compressibility of sea water in the calculation are two orders of magnitude smaller and they do not alter the computation error in α or σ_t.

The most serious error that might occur in the determination of ΔD would probably be a constant error in the pressure assigned to the calculation of the dynamic depth. The error in using depth instead of pressure incurs an error of 1 %. Denoting the pressure error as Δp, the corresponding error in ΔD is $\Delta(\Delta D)$ from (4.6) is

$$\Delta(\Delta D) = \int_{p_0}^{p} \frac{\partial\alpha}{\partial p} \Delta p dp = \Delta p \int_{\alpha_0}^{\alpha} d\alpha$$

$$= \Delta p\,(\alpha - \alpha_0) \tag{4.27}$$

A reasonable estimate for the error in determining the difference of ΔD (i.e. $\Delta D_{SB} - \Delta D_{CB}$) between two stations is $\sqrt{2}$ times the expression (4.27). Thus the estimate of error in getting the relative current is

$$\Delta C = \frac{\sqrt{2}\,\Delta p}{fL}(\alpha - \alpha_0) \tag{4.28}$$

Using representative values of α , f and L we get typically the biggest error in the current to be 3% or less.

The biggest uncertainty in all these calculations is the estimation of the layer of no motion and this involves inaccuracies that far outweigh and mask the errors of the measuring and computational nature. The difference in the value of the mass transport from PCM and geostrophic values attest to that. The errors in computation of the mass transport of the PCM current is about 15% and that for the geostrophic current is 3%. the latter error excludes a systematic error introduced by the choice of the layer of no motion. The large error in the PCM mass calculation arises because of the measurement of the PCM speed. The speed, as stated earlier, has an accuracy of ±1.5 cm/s (and thus for a 15-20 cm/s current an uncertainty of about 10%). The directional accuracy is ±6° (2%). The errors typically found are summarized in Table 4.6.

4.6 Tides

No measurements were made of the tide in the AIDJEX experiment. Information on the tidal regime is inferred from the tides measured at Tuktoyaktuk Canada and Pt. Barrow, U.S.A. Fig. 4.16 shows a typical tidal curve for one phase of the moon at Tuktoyaktuk. The tide is mixed, mainly semi-diurnal with a mean value of 0.3 m. At Tuktoyaktuk, the highest high water is 2.3 m and the lowest low water is -0.8 m.

During the AIDJEX experiment a recording gravimeter was operated at the main camp by Bower and Weber (1978) of the Earth Physics Branch of the Department of Energy, Mines and Resources. They examined the gravity data at Caribou during periods of little drift motion. The study concluded that

Table 4.6

ERROR SIZES

	parameter	typical value	error
measured	position	100 - 135 km	± 100 m
	salinity	30 - 35 ‰	± 0.001‰
	temperature	0.5 - -1.5°C	± 0.01°C
	depth	0 - 750 m	± 1 m
	current	0 - 50 cm/s	± 1.5 cm/s
	direction	0 - 360°	± 6°
calculated	sigma-t	24 - 26 units	± 0.02 units
	specific volume	18 - 350	± 0.02 units
	dynamic depth	0 - 0.5 dyn-m	± 20 dyn-mm
	current	0 - 4 cm/s	± 0.12 cm/s

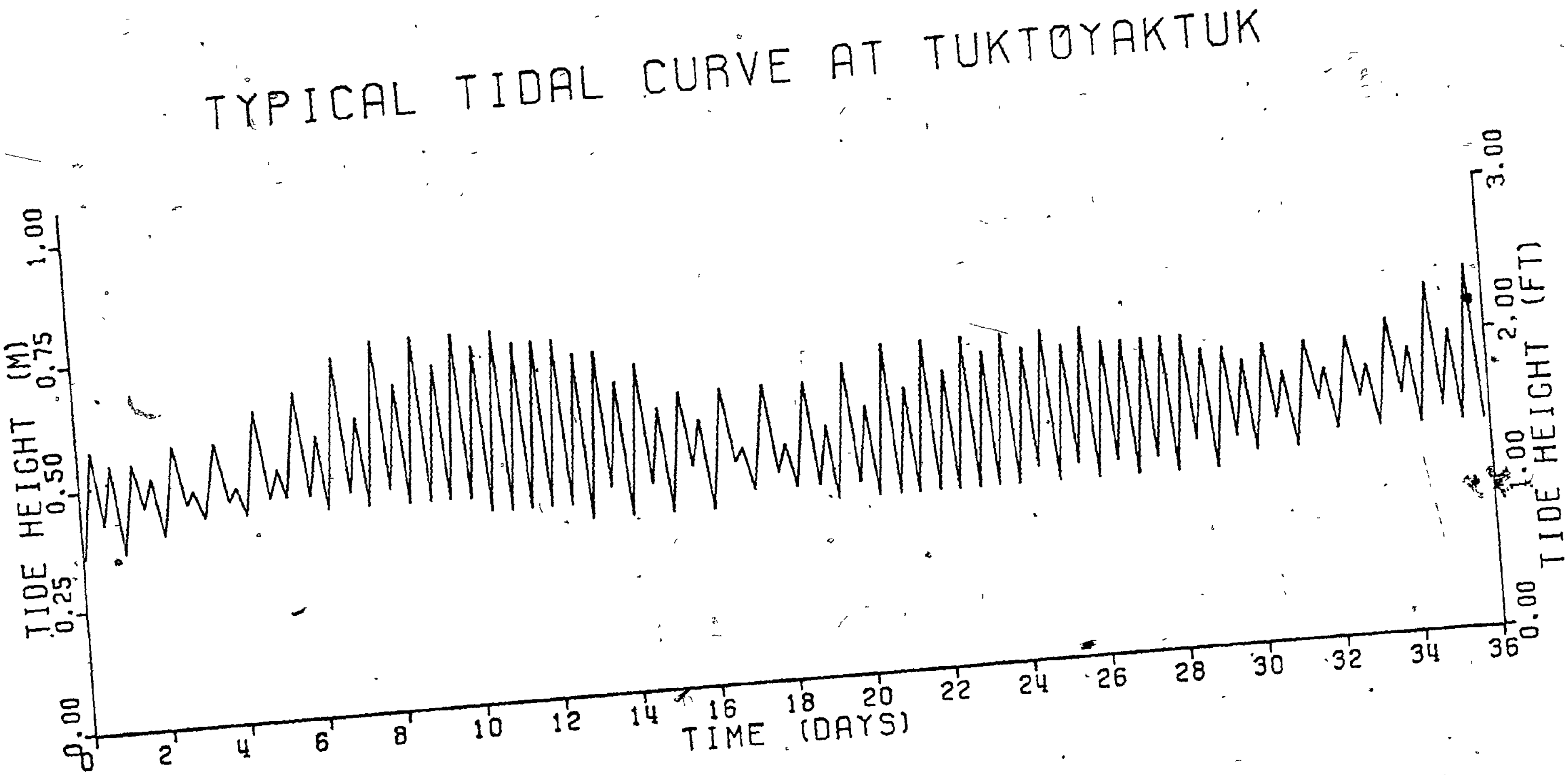

Fig. 4.16 Typical tidal curve at Tuktoyaktuk N.W.T. Canada

the gravity changes were mainly due to tidal effects. Using a standard tidal analysis technique the following amplitude and Greenwich phase lags of the local ocean tide for the two main semi-diurnal (M_2 and S_2) and for the two main diurnal (O_1 and K_1) constituents were obtained.

M_2:	5.6 cm ± 0.5	280° ± 7
S_2:	2.0 cm ± 1.4	303° ± 25
O_1:	1.6 cm ± 2.5	329° ± 58
K_1:	6.0 cm ± 2.8	100° ± 28

Fig. 4.17 (from Bower and Weber, 1978) shows the tidal data for the Beaufort Sea area.

From these low tidal heights we conclude that tidal factors do not significantly affect the anomaly of the specific volume and hence the geostrophic currents thus calculated. Also the tidal effect on internal waves (discussed later) at the bottom of the mixed layer is minimal.

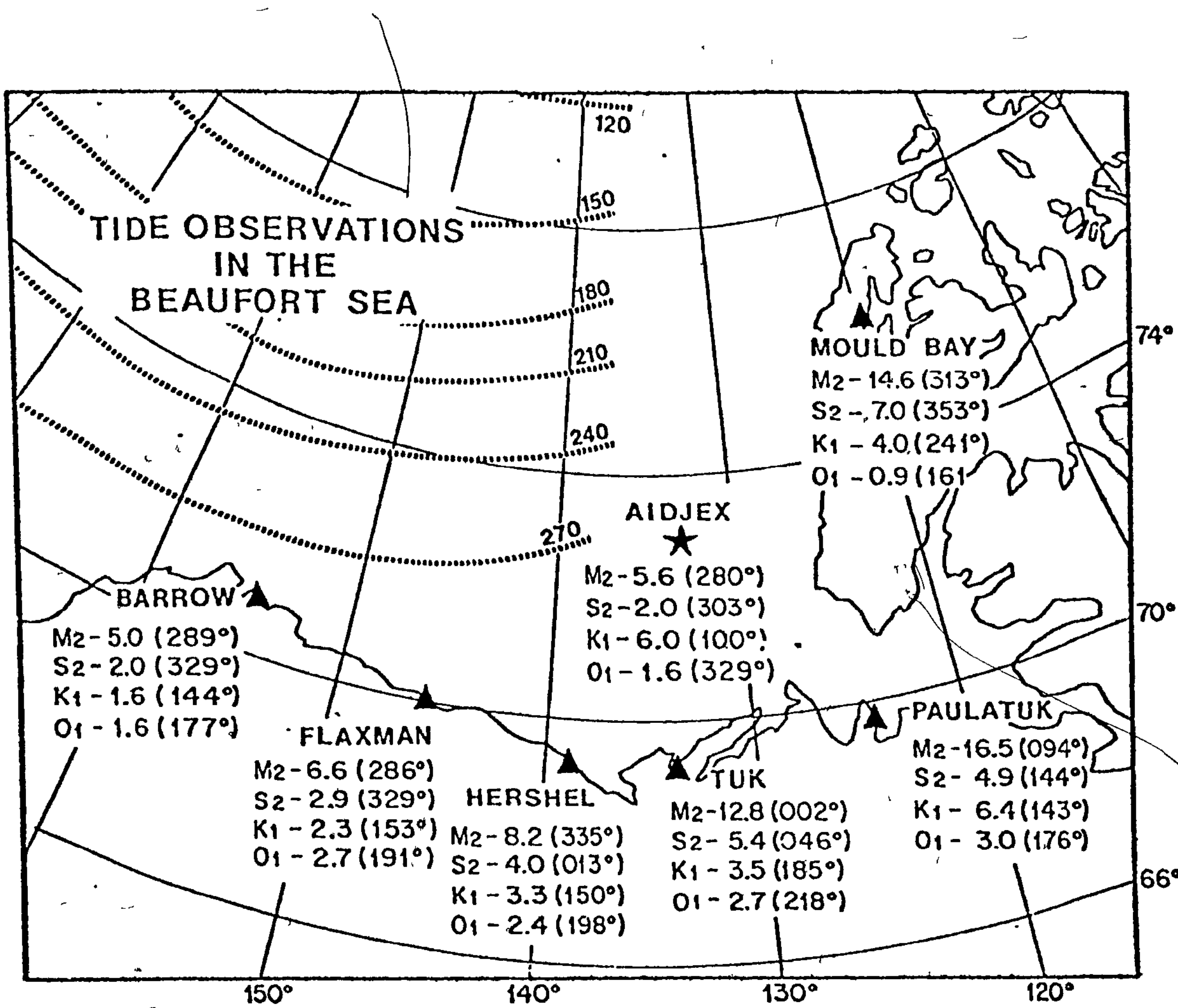

Fig. 4.17 Map of the Beaufort Sea showing the relation between tidal data reported by Bower and Weber (1978) for AIDJEX and that of Fjeldstad's cotidal contours for the M_2 constituent (dashed curves) and of six shore stations. Amplitude are in centimeters. (Bower and Weber , 1978)

Chapter Five BAROCLINIC EDDIES AND STEP STRUCTURE

5.1 Baroclinic Eddies

One of the unexpected oceanographic results of the AIDJEX '72 program was the detection of swift subsurface currents localized in the pycnocline. These currents coincide with the region of steepest density gradient between 50 and 300m. The maximum speeds found in the '72 experiment were 40 cm/s (0.80 knots) at a depth of 150m. This speed far exceeded the mean current of 1.8 cm/s (Hunkins, 1974b; Newton, 1973; Newton et al, 1974).

Although there had been indications of transient undercurrents by P.P. Shirshov as early as 1937 (Belyakov, 1972), the details and horizontal extent were not known. From the 1972 study, these transient currents were shown to occur as nearly circular eddies with a diameter of 10-20 km (Fig. 5.1). Hunkins' studies indicate that individual eddies were separated by a spacing of 20-50 km (Hunkins, 1974b) but the present data do not indicate as close a spacing as this. Both cyclonic and anticyclonic eddies were observed. The eddies were strongly baroclinic with signatures in both the velocity and the density fields. The force balance was nearly geostrophic (Hunkins, 1974b) although centrifugal force was also of some significance since the eddies had such small radii.

In the main experiment of 1975-76, eddies were detected at all four camps. The eddies (baroclinic) differed from the barotropic wind driven motion by often occurring when there was little or no ice motion. They had a nearly parabolic velocity profile and a strong vertical shear. Although the '72 eddies had a depth of maximum current at 150m, the '75-'76 eddies were shallower, at 100-125m, and swifter, with maximum currents over 60 cm/s (1.2 knots).

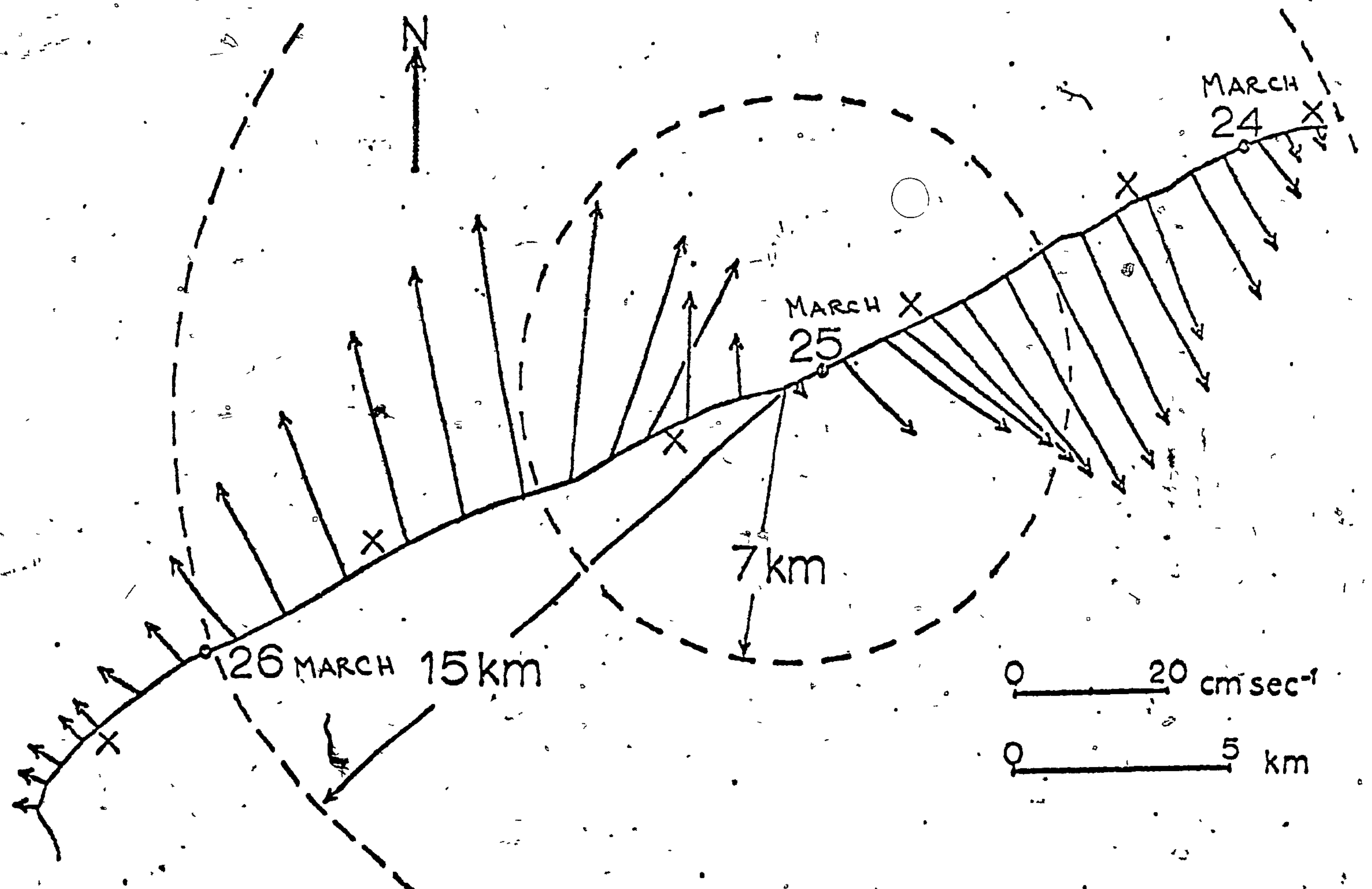

Fig 5.1 Currents at the core of an eddy and it's drift track during AIDJEX 72. (From Newton 1973)
Circles indicate extent of current and location of maximum. X locates hydrographic stations.

Measurements with increasing time and space scale observations have resulted in the detection of baroclinic eddies in the Atlantic Ocean. They were the object of detailed study during the U.S. MODE I (Mid Ocean Dynamic Experiment - 1971-72) (Gould et al, 1974) and the Soviet POLYGON (a large scale multi buoy experiment in the tropical Atlantic) experiment (Brekhovskikh et al, 1971). Many other investigators have reported eddies in the Atlantic (Gill et al, 1974) and the Arctic (Galt, 1967; Bernstein, 1972). The Arctic eddies differ from the Atlantic ones in two ways. The horizontal and vertical space scales of the Arctic eddies are much smaller (20 km and 200m respectively) than those of the Atlantic eddies (at 100 km and 4000m). This may be related to the steeper and shallow pycnocline in the Arctic Ocean. The depth of maximum velocity also differs in the two oceans. In the Atlantic it is near the surface, but data on this are not conclusive. In the Arctic, it is definitely below the surface from 80-150m. This appears related to the presence of the ice cover against which the eddy is frictionally dissipated. By these deeper eddy observations, we enlarge the type of conditions under which the eddies are known to exist.

5.1.1 Eddy at Snow Bird

Several eddies were observed at Snow Bird during the AIDJEX year (April 75 - May 76). Not all the eddies have been completely examined but one is presented here as typical of those encountered in the Arctic. Fig. 5.2 (a-i) show the velocity profile for an eddy. This event occurred between 29 May and 02 June 75. As seen from these figures

Fig 5.2 (a to i) Velocity profiles during an eddy in AIDJEX 75.

SB 047 29 MAY 75 2000 Z Fig 5.2 a

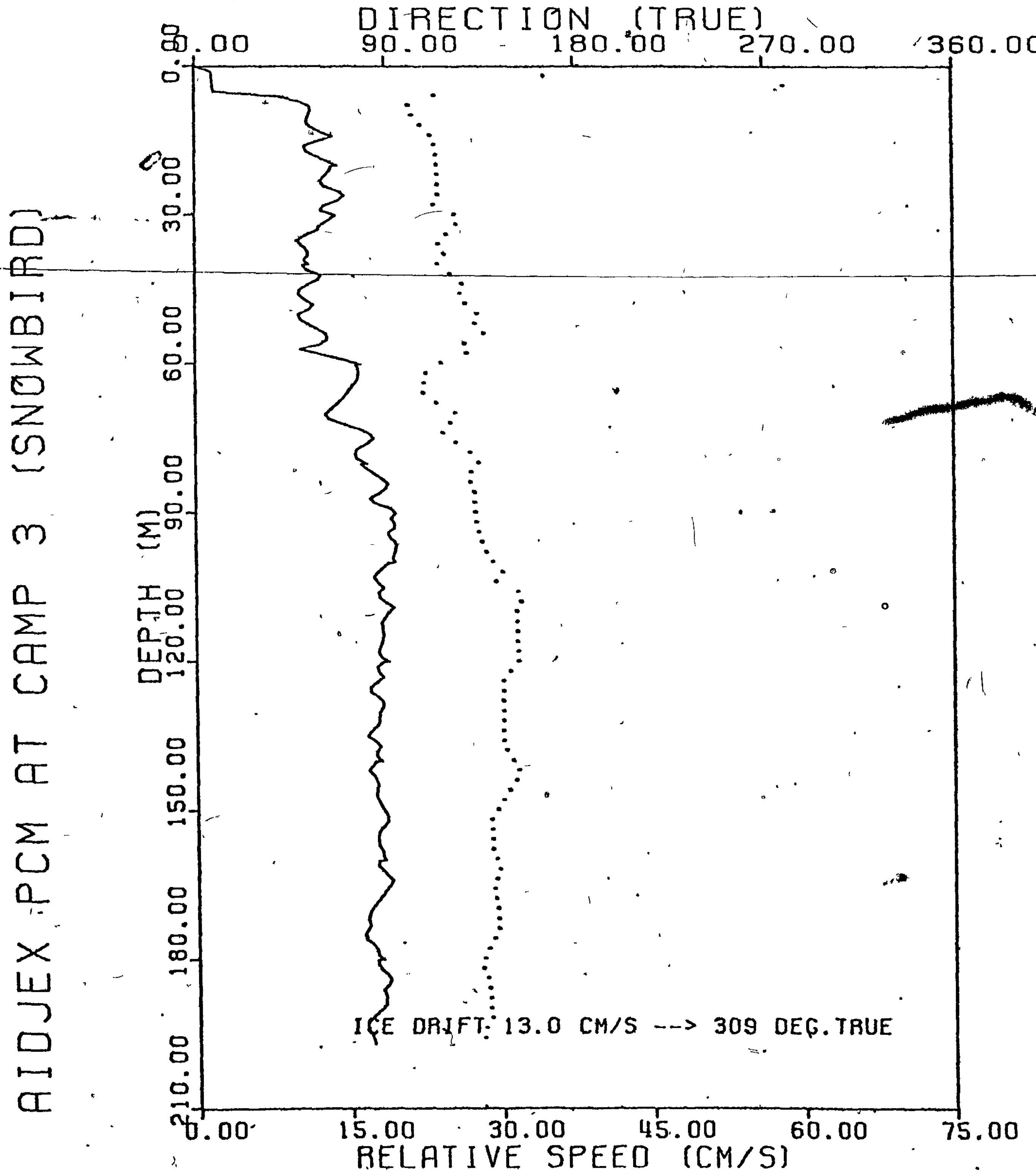

SB 048 30 MAY 75 0500 Z Fig 5.2 b

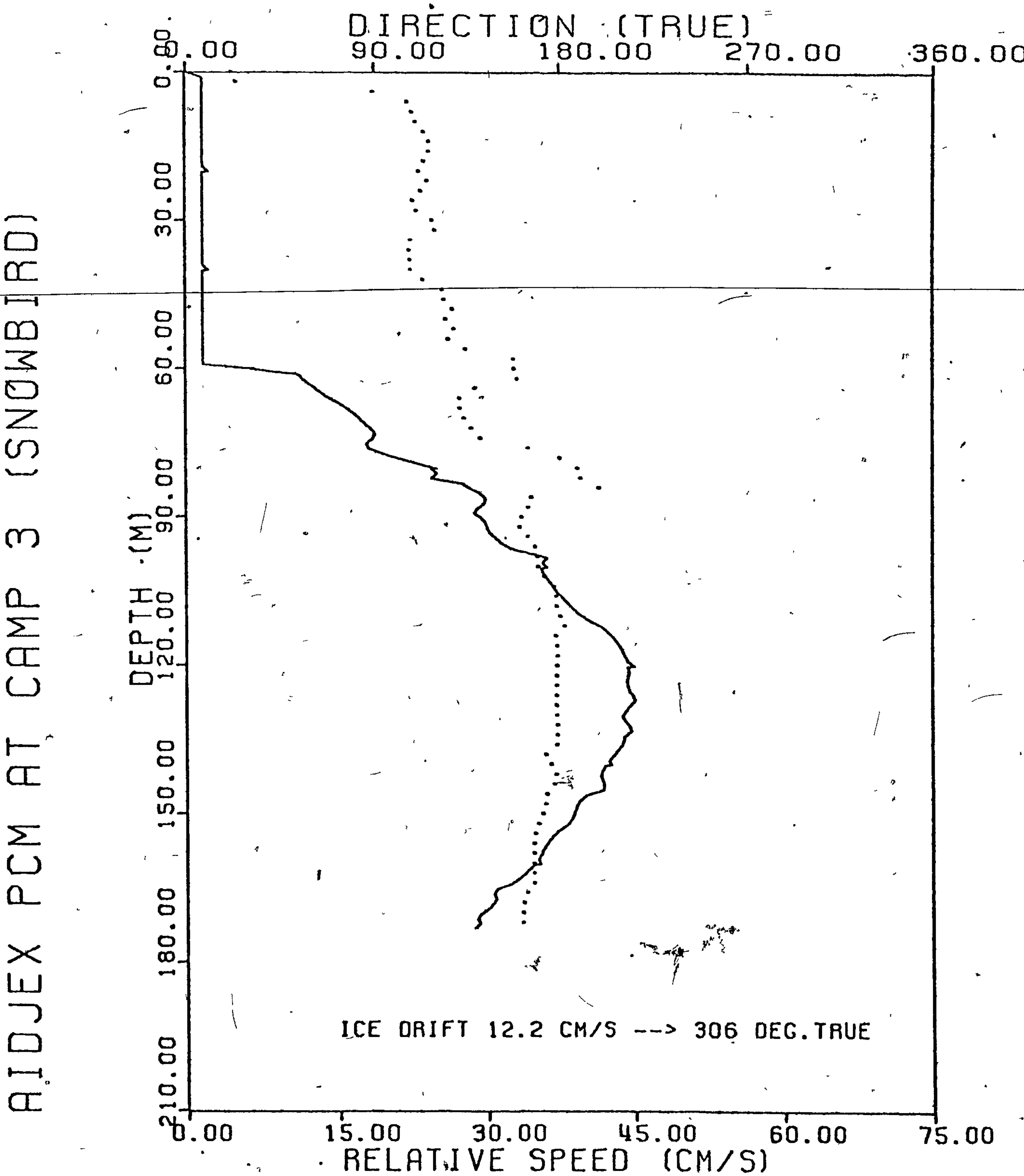

SB 049 30 MAY 75 2000 Z Fig 5.2 c

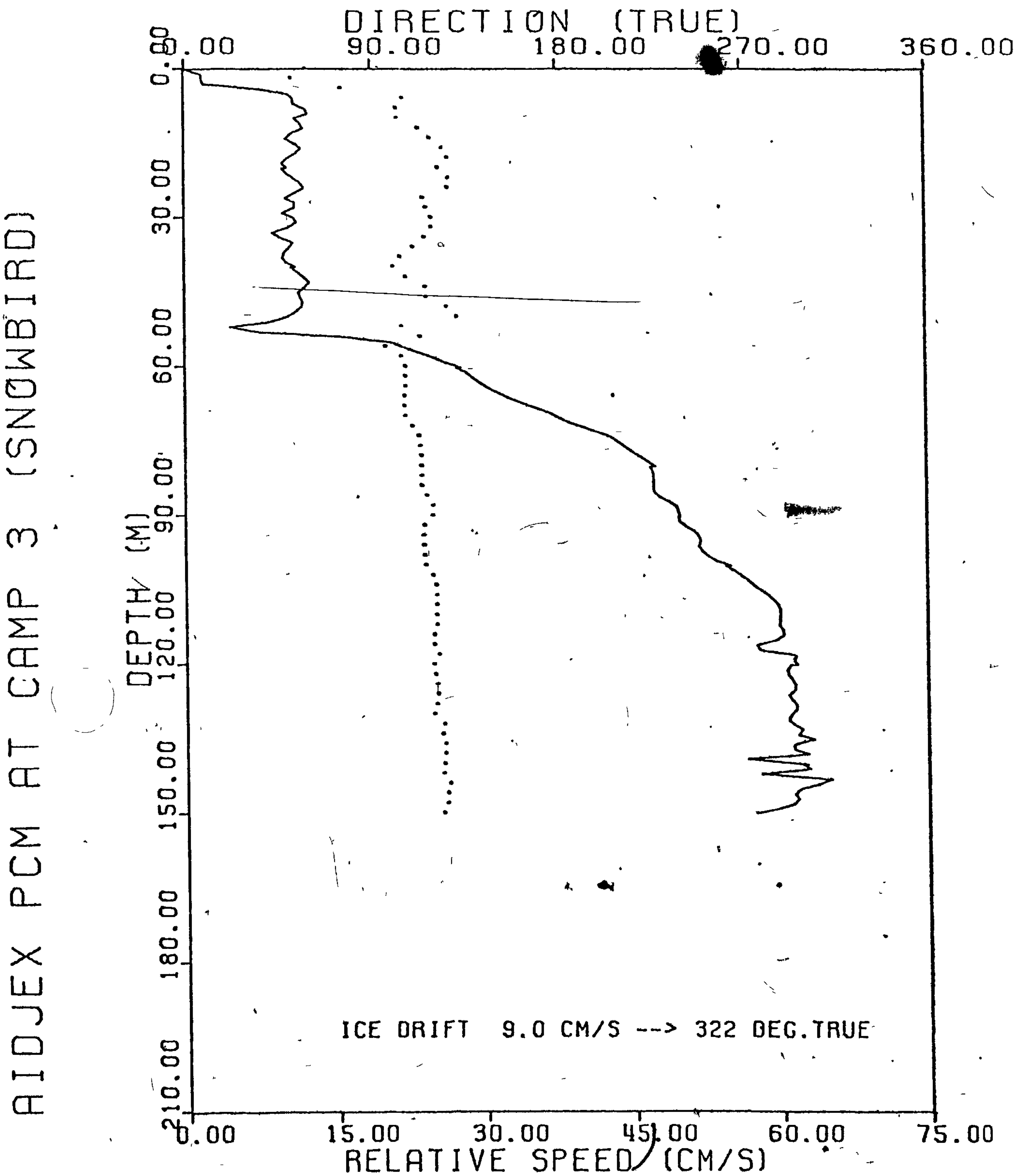

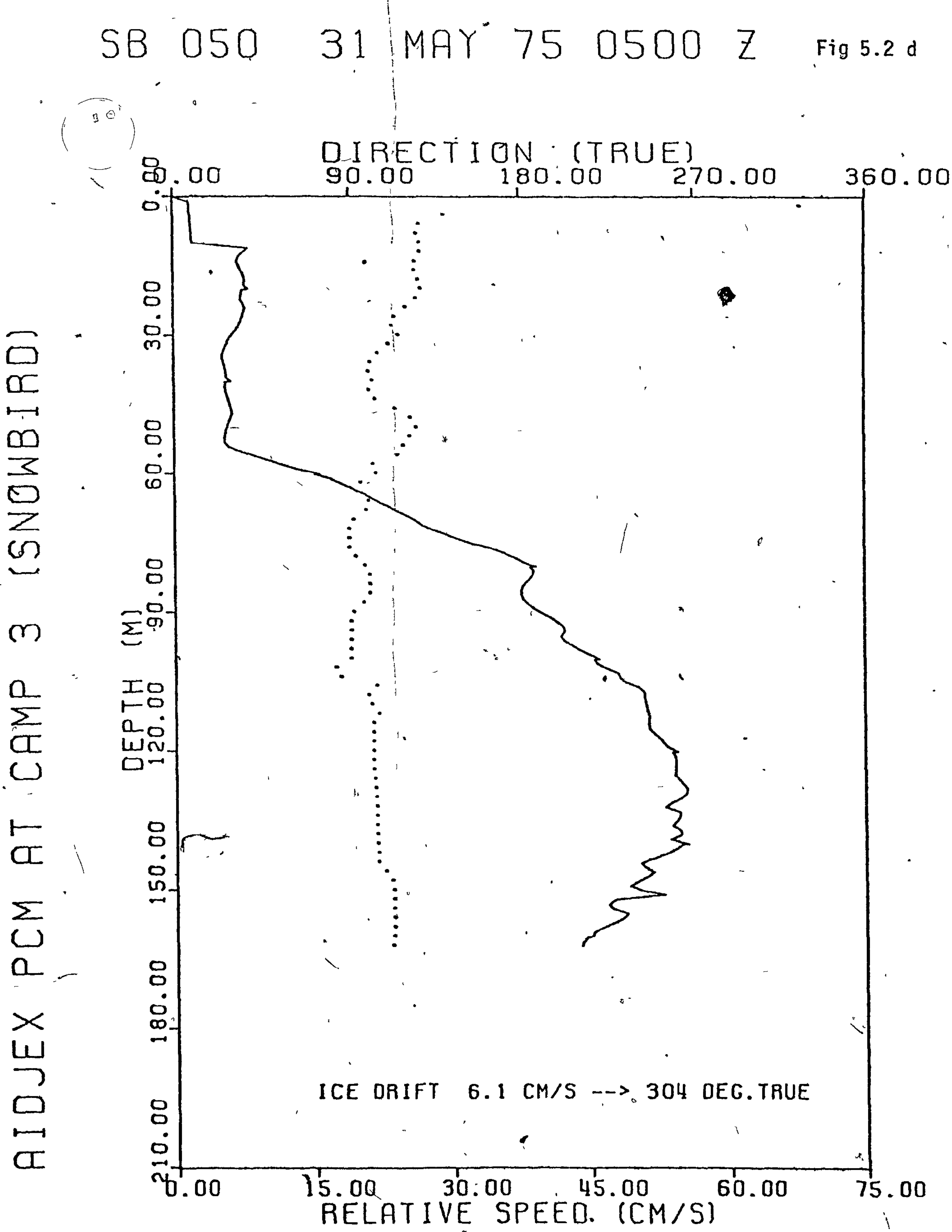
SB 050 31 MAY 75 0500 Z
Fig 5.2 d
AIDJEX PCM AT CAMP 3 (SNOWBIRD)
DIRECTION (TRUE)
0.00
90.00
180.00
270.00
360.00
DEPTH (M)
0.00
30.00
60.00
90.00
120.00
150.00
180.00
210.00
ICE DRIFT 6.1 CM/S --> 304 DEG.TRUE
0.00
15.00
30.00
45.00
60.00
75.00
RELATIVE SPEED. (CM/S)

SB 051 31 MAY 75 2000 Z Fig 5.2 e

AIDJEX PCM AT CAMP 3 (SNOWBIRD)

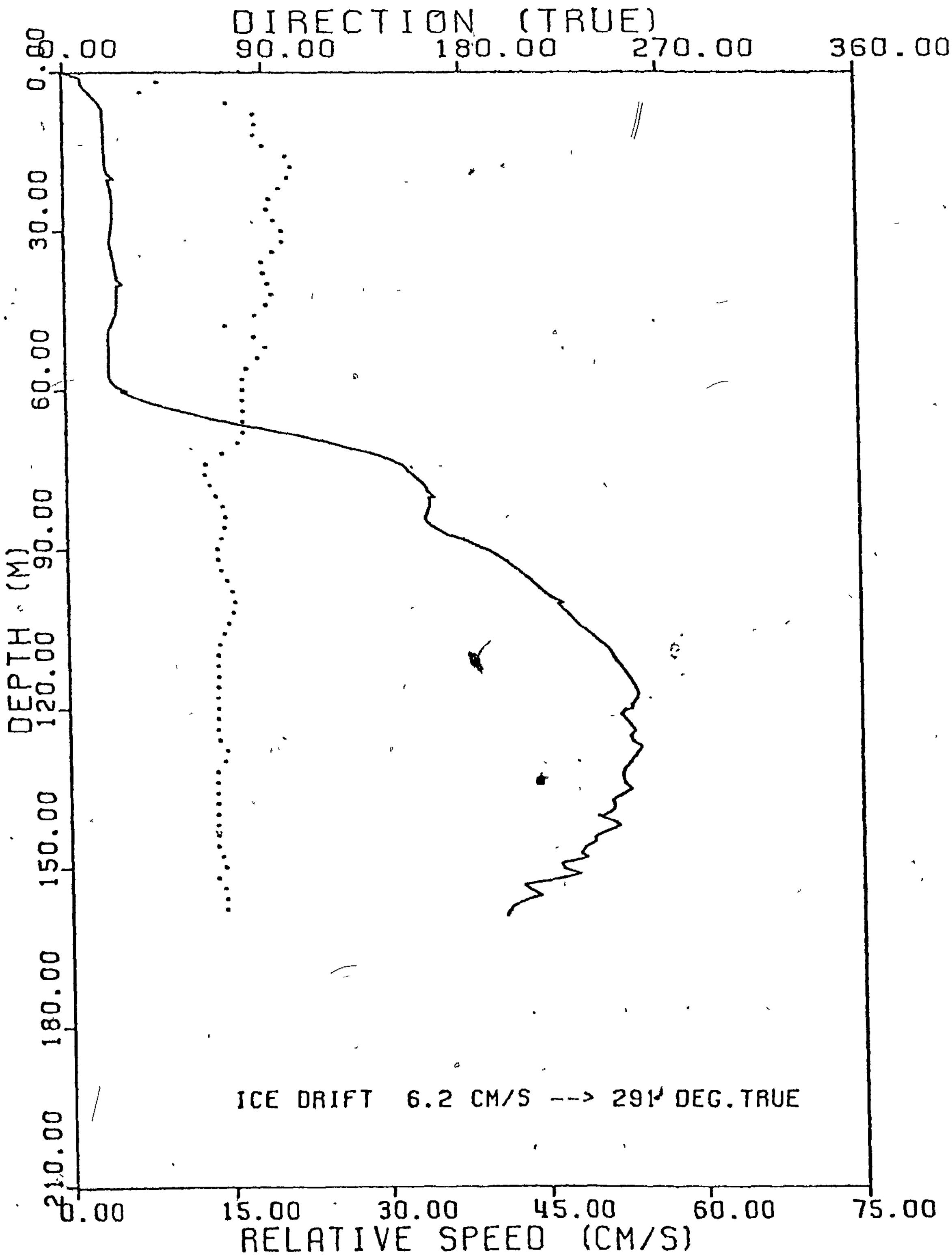

SB 052 01 JUN 75 0500 Z Fig 5.2 f

AIDJEX PCM AT CAMP 3 (SNOWBIRD)

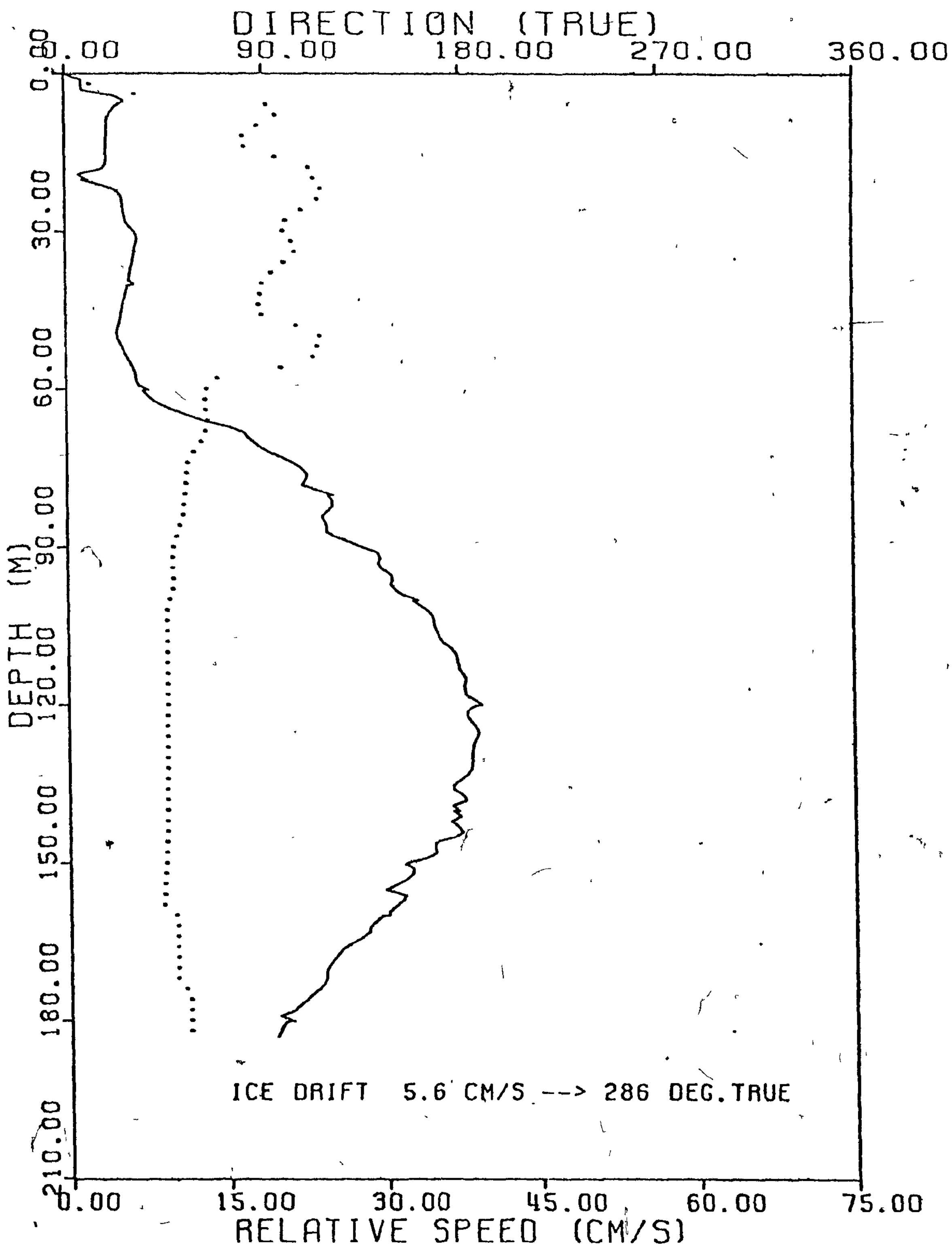

SB 053 01 JUN 75 2000 Z Fig 5.2 g

AIDJEX PCM AT CAMP 3 (SNOWBIRD)

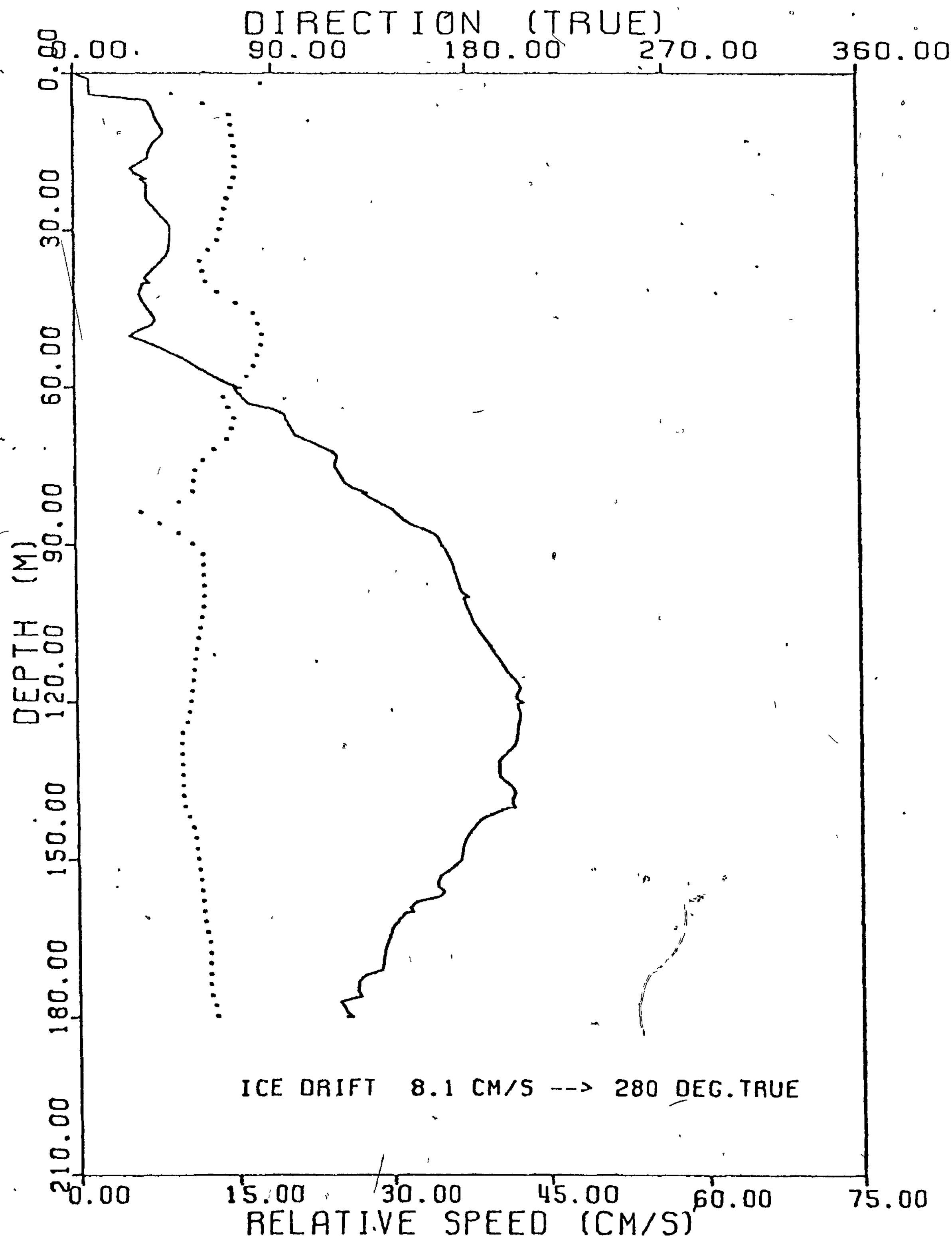

SB 054 02 JUN 75 0500 Z Fig 5.2 h

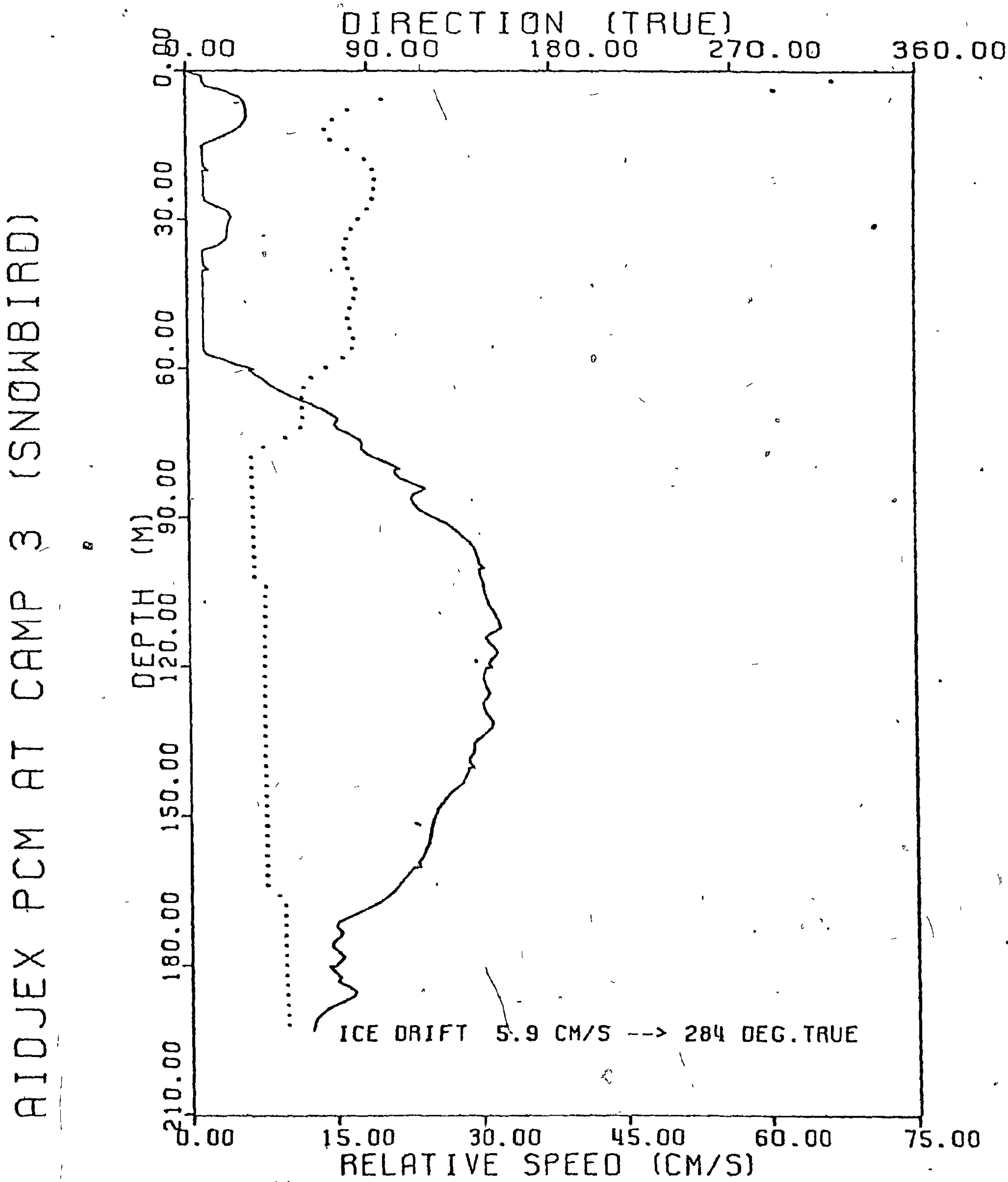

SB 055 02 JUN 75 2000 Z Fig 5.2 i

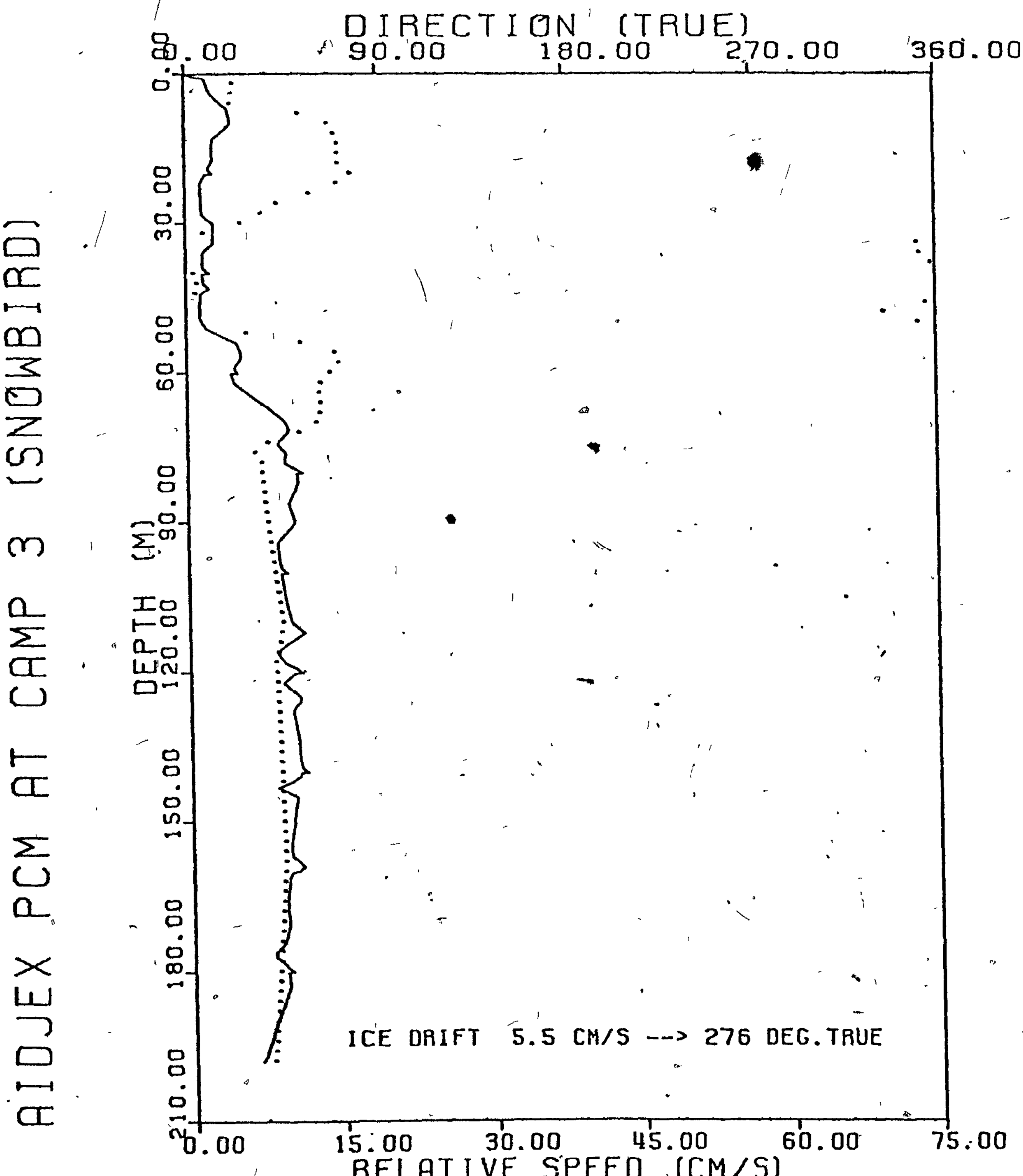

the speed increases dramatically from 13 cm/s or so at the start of the event to over 60 cm/s at the height of the disturbance. Table 5.1 lists the maximum velocity as the eddy is traversed. The shape of the profile is roughly parabolic and the depth of maximum current is about 125m. Although casts (PCM) do not show the bottom part, the trend is towards slowing down and the eddy seems to be limited to a depth of 200m. After the passage of this transient, the conditions return quickly to their predisturbance state. Usually, as in this example, there is little or no directional shear through an eddy, although in some cases there may be directional as well as speed shear through the eddy depth. Again as is typical, the upper water motion is about 5 cm/s and the eddy was observed at a time of low ice movement. The duration of this eddy is 4 days. Fig. 5.3 shows speed vectors on the eddy as a function of time. The velocity is plotted at three depths (75, 100 and 125m). This shows the temporal and the vertical extent of the eddy. Typically the time scale of observation is four days, as the ice camp moves over the eddy (or in times of no movement, the eddy passing under the camp). The vertical extent of this eddy is about 150m and is representative of the eddies encountered.

As stated earlier the AIDJEX manned array space scales were chosen to give information on the wind induced effects. It was too large for detailed study of these baroclinic eddies. Eddies were observed at only one ice station at a time and no evidence is yet found of an eddy passing under two camps. At one occasion two of the eddies at different camps overlap in time. Since the camps were 170 km apart thus they were undoubtedly two distinct eddies.

Fig 5.3 Water velocity at 75, 100 and 125 m during an eddy.

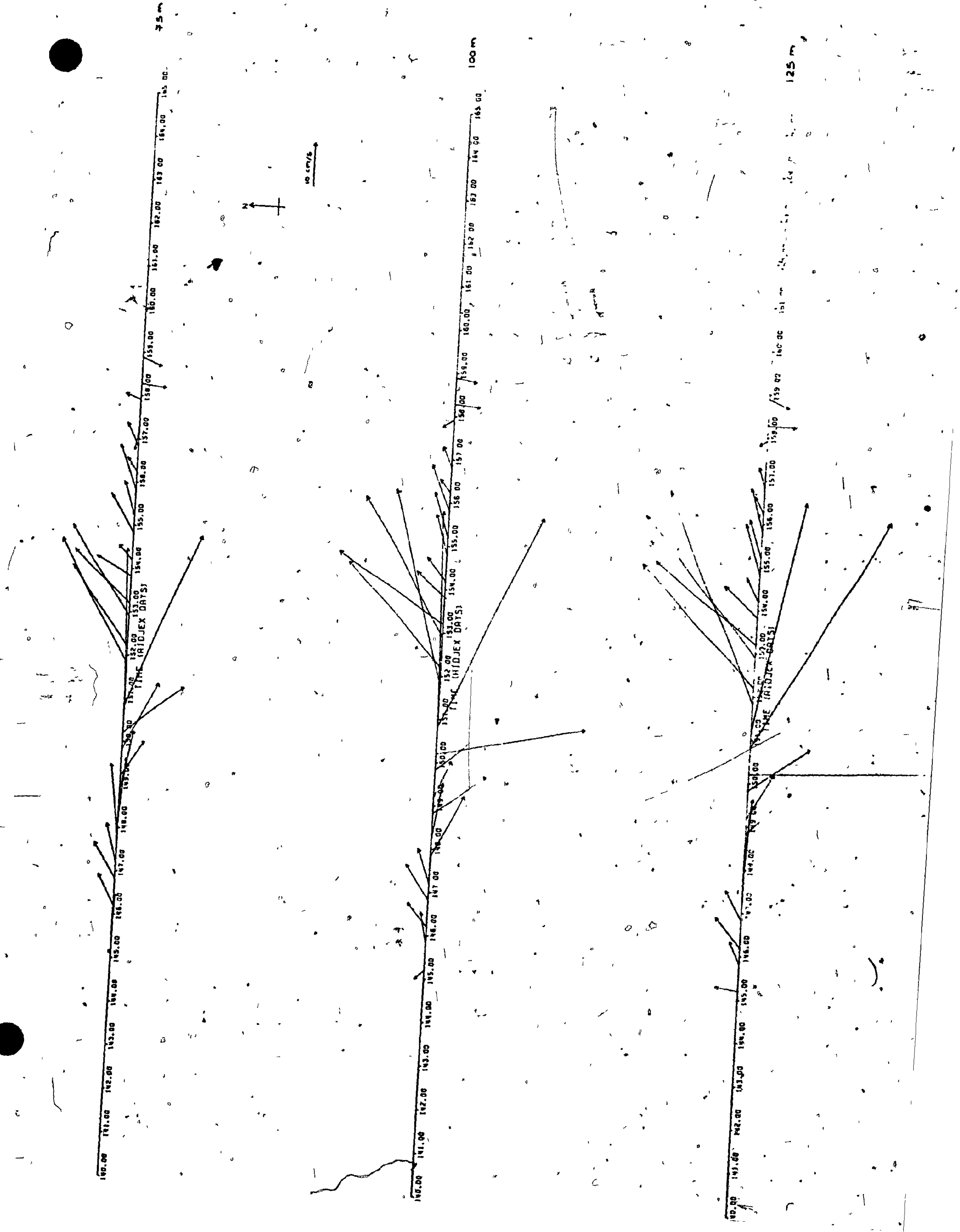
75 m
100 m
125 m
10 cm/s
N
TIME (RIDJEX DAYS)

TABLE 5.1

BAROCLINIC EDDY

SNOW BIRD

29 May 75 - 02 Jun 75

Date	PCM time	STN stn # mode 1	max speed cm/s	STD time	stn #
May 28	2000	45	< 10	1800	26
29	0300	46	< 10		
29	2000	47	20	1800	28
30	0545	48	60		
30	2000	49	50	1800	30
31	0545	50	45		
31	2000	51	50	1800	32
Jun 01	0545	52	40		
01	2000	53	42	1800	34
02	0545	54	37		
02	2000	55	10	1800	36
03	0545	56	< 10		
03	2000	57	< 10	1800	38

The data does give some idea of their number by looking at the frequency of encountering them. For the camp Snow Bird there were eight occasions of observing an eddy (either whole or in part).

The lateral extent is hard to delineate because it is a matter of chance when and how an eddy is traversed. The life time of these eddies is even harder to calculate. In an analog to Fig. 5.1, the track of the eddy is shown in Fig. 5.4. The eddy was not observed along the diameter (as in Fig. 5.1) but rather along the chord. From this figure the horizontal extent is about 3 km. This agrees with the horizontal space scale of 10-20 km calculated by Hunkins (1974b) and Newton (1973).

5.1.2 Water characteristics

One of the first steps in the examination of an eddy is to study the correlation between temperature and salinity within the eddy to see if it agrees with that of the surrounding water.

The eddies were first detected by current observations but they are accompanied by a distortion of the temperature and salinity field. This is evident from the STD profiles. Fig. 5.5 (a-n) show the changes in the water column with the passage of the eddy. The distortions are evident at a first glance and are even more enhanced in the corresponding TS diagram for this time (Fig. 5.6 a-f). Of especial interest in the temperature plot is the presence of anomalously "warm" water of close to -1.2°C at 150m level, near the eddy center. From Figs. 5.5 and 5.6 we see that things are quite changed during the duration of the eddy but return to their quiescent state after its passage.

Fig 5.4   100 m current velocity plotted on the ice drift track.

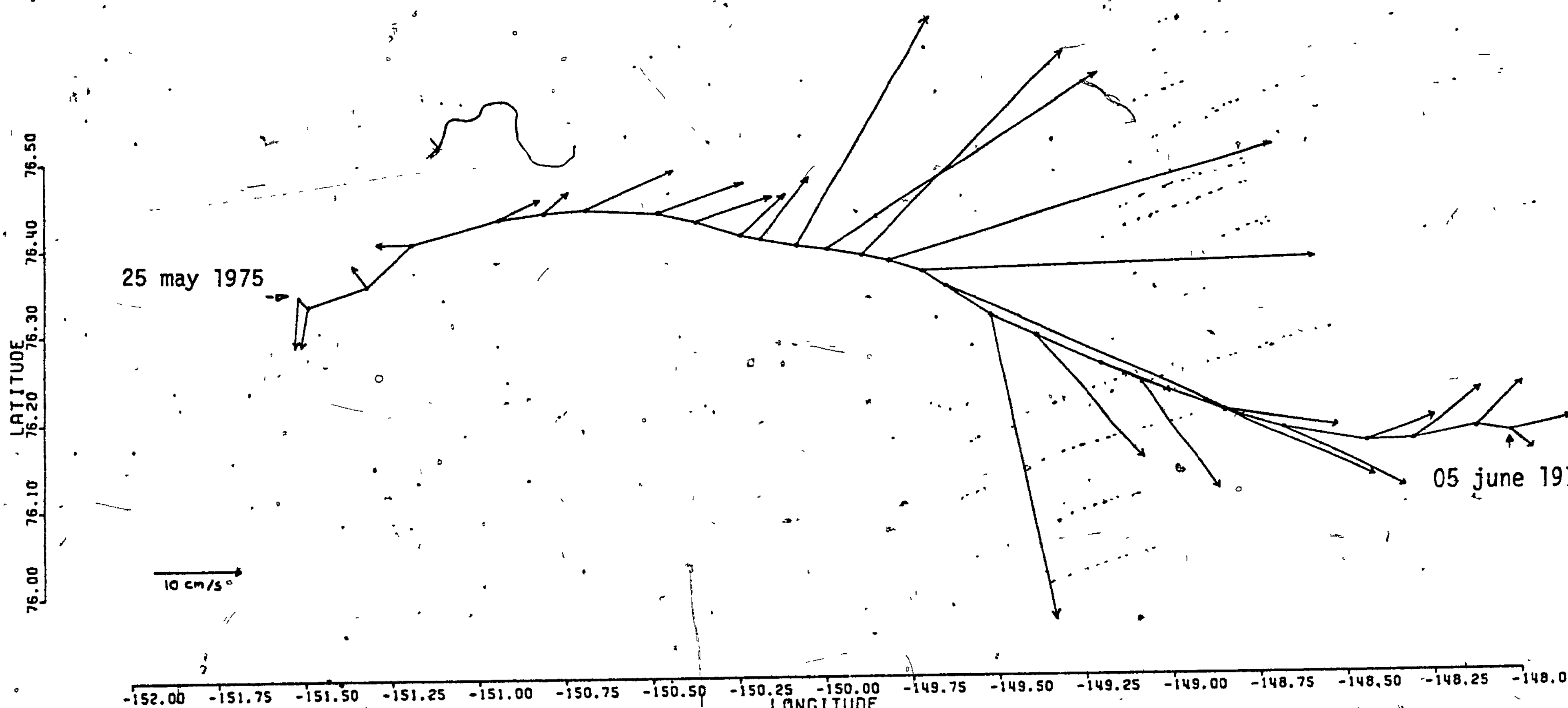

Fig 5.5 (a to g) Temperature profile during an eddy.

(h to n) Salinity profile during an eddy.

Fig 5.5 a

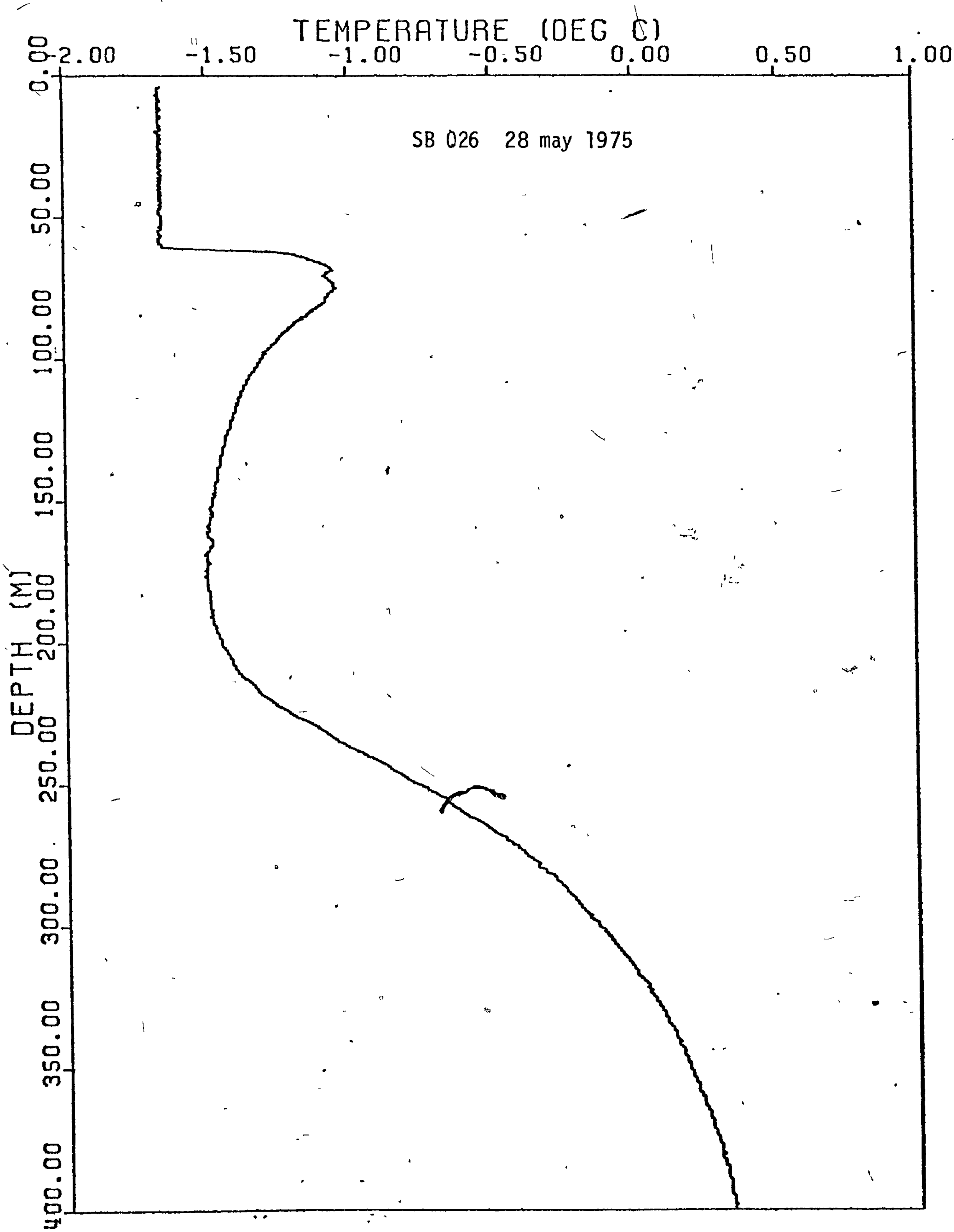
TEMPERATURE (DEG C)
-2.00
-1.50
-1.00
-0.50
0.00
0.50
1.00
SB 026 28 may 1975
DEPTH (M)
0.00
50.00
100.00
150.00
200.00
250.00
300.00
350.00
400.00

Fig 5.5 b

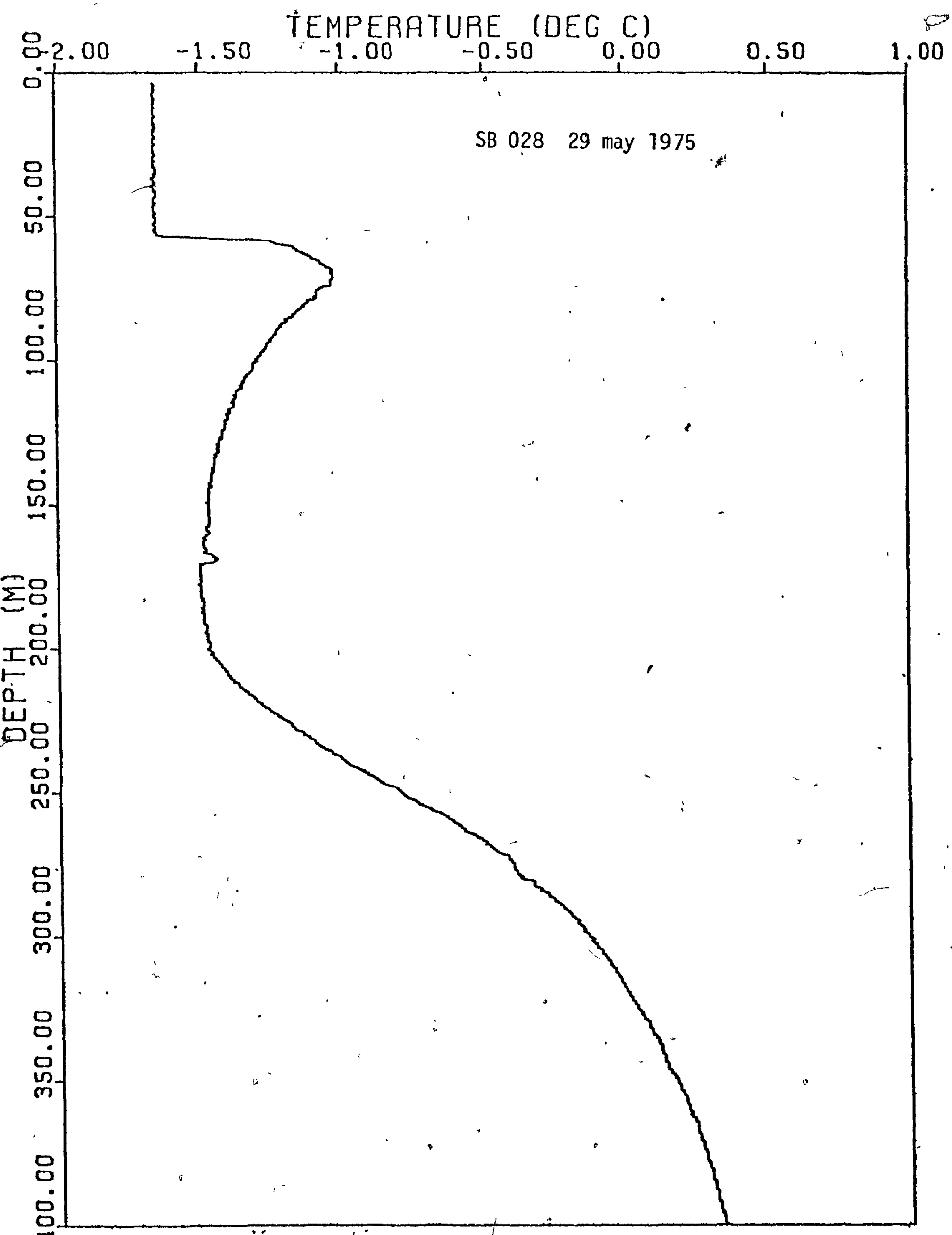
TEMPERATURE (DEG C)
-2.00
-1.50
-1.00
-0.50
0.00
0.50
1.00
SB 028 29 may 1975
DEPTH (M)
0.00
50.00
100.00
150.00
200.00
250.00
300.00
350.00
400.00

Fig 5.5 c

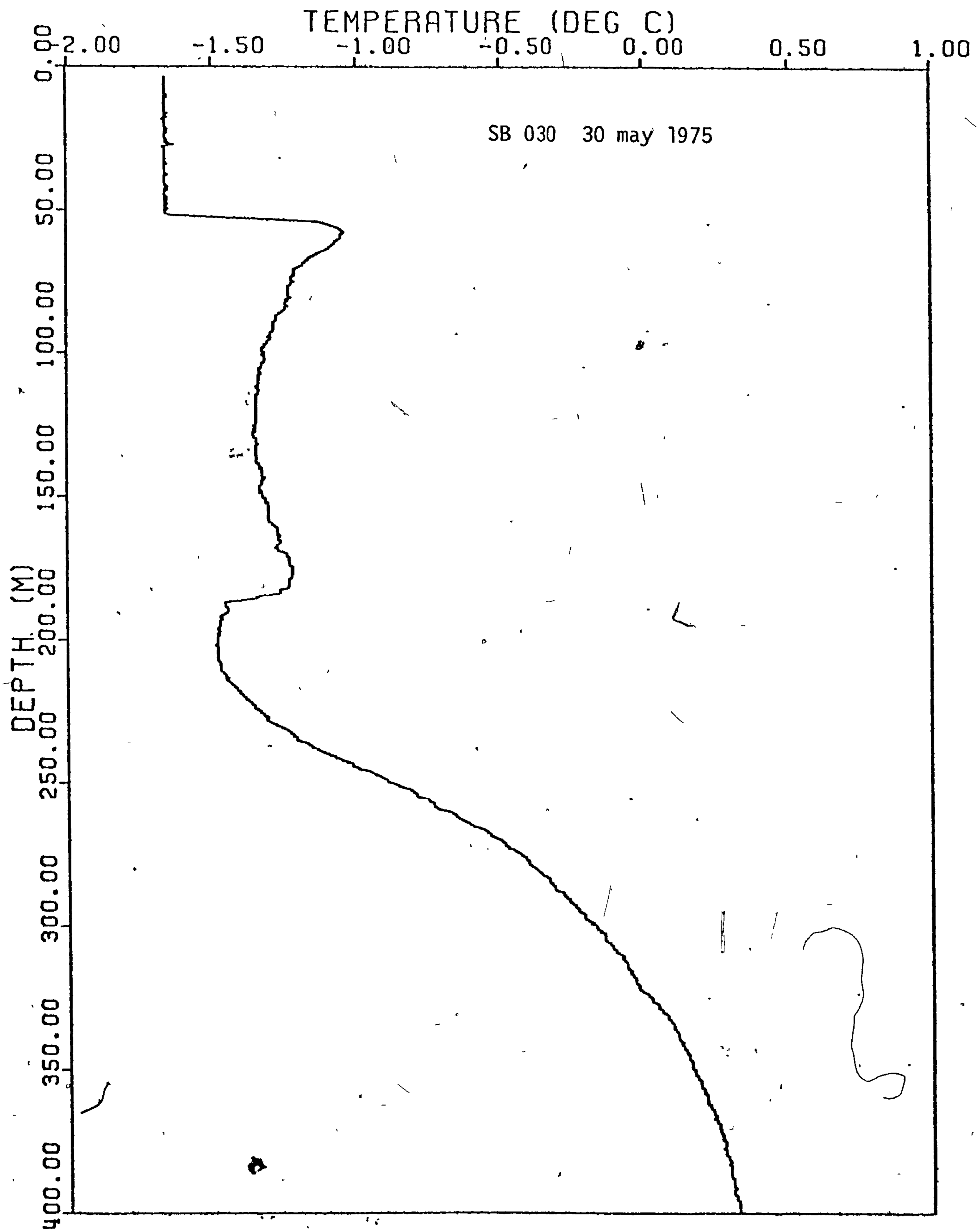
TEMPERATURE (DEG C)
-2.00
-1.50
-1.00
-0.50
0.00
0.50
1.00
SB 030 30 may 1975
DEPTH (M)
0.00
50.00
100.00
150.00
200.00
250.00
300.00
350.00
400.00

Fig 5.5 d

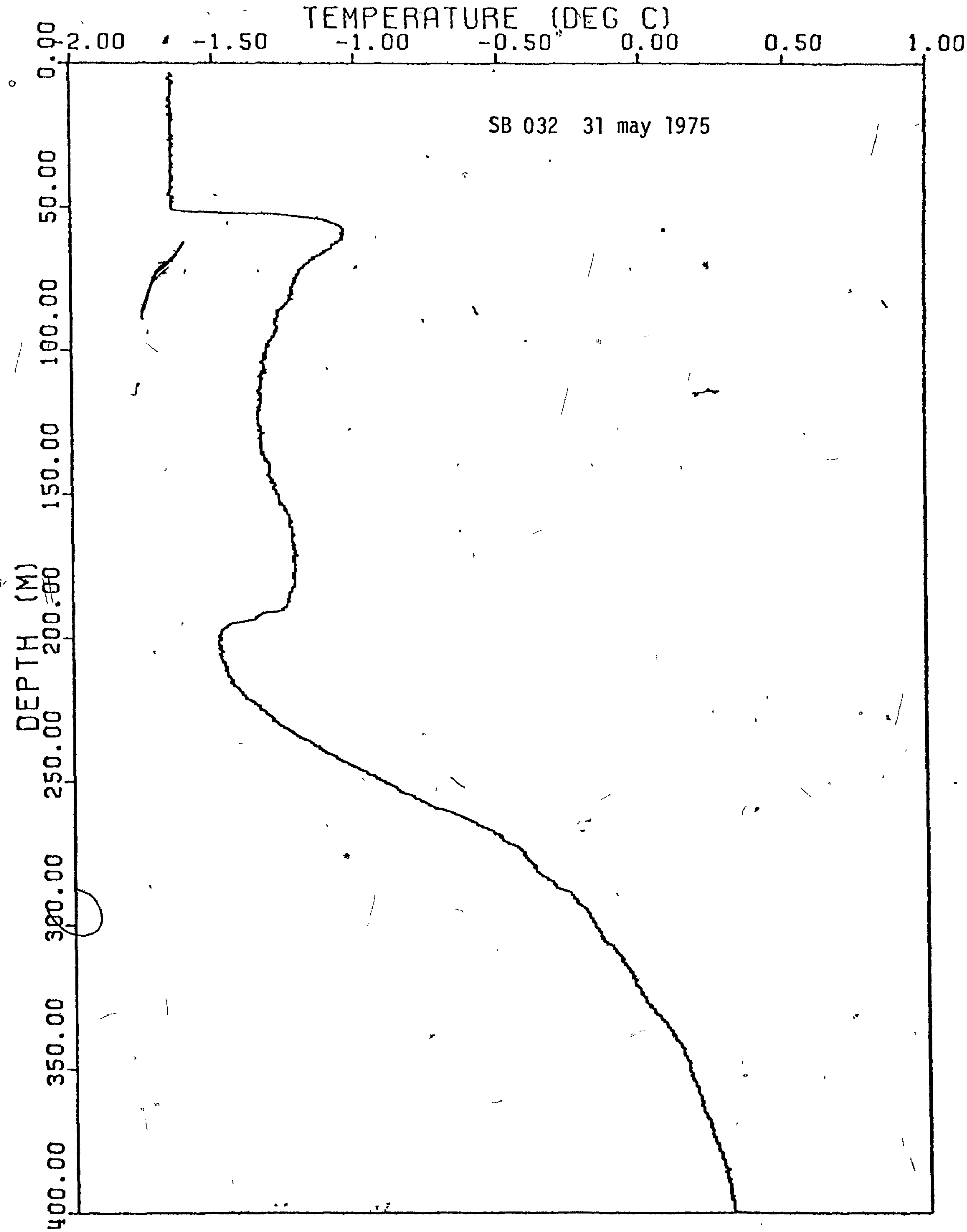
TEMPERATURE (DEG C)
-2.00
-1.50
-1.00
-0.50
0.00
0.50
1.00
SB 032 31 may 1975
DEPTH (M)
0.00
50.00
100.00
150.00
200.00
250.00
300.00
350.00
400.00

Fig 5.5 e

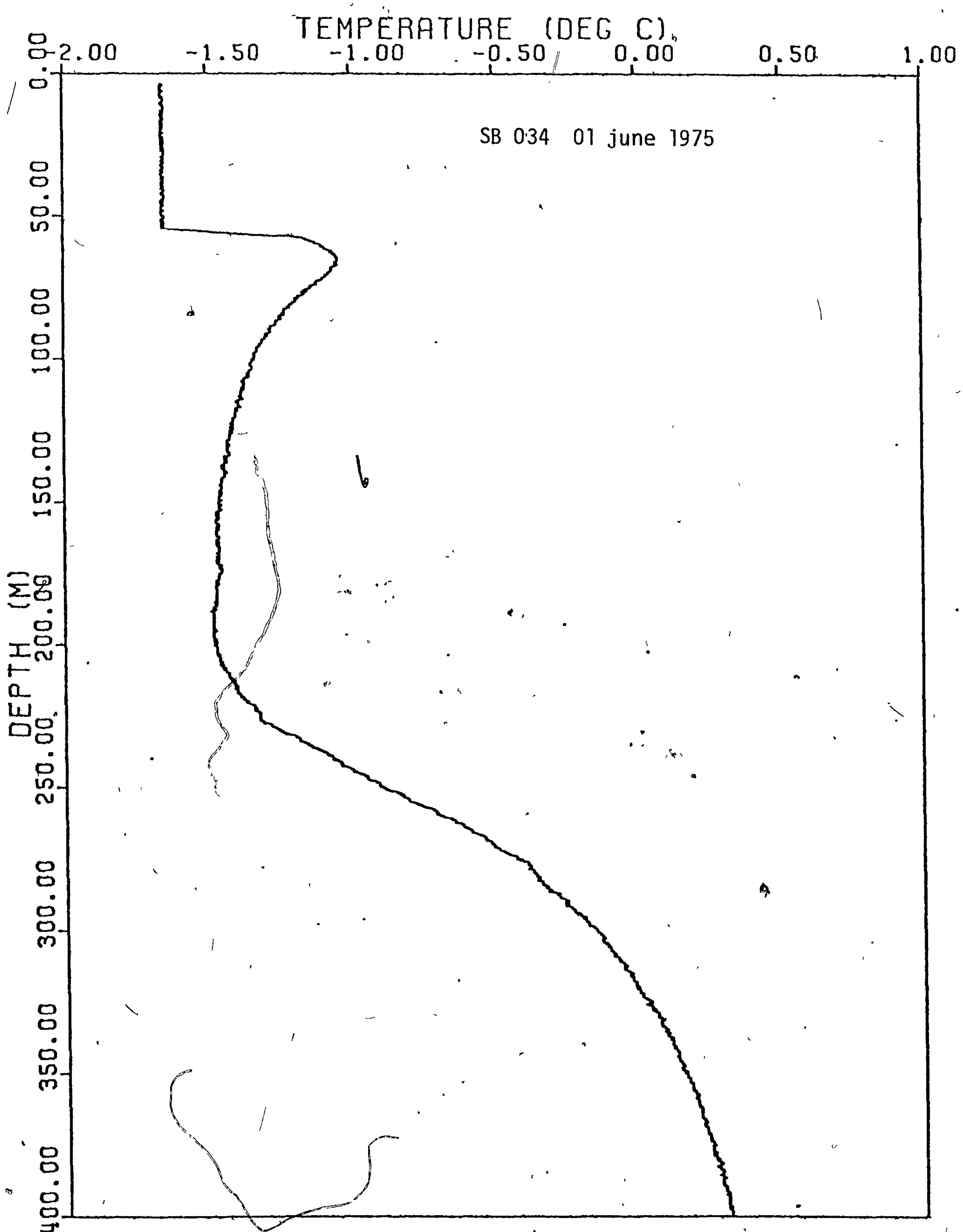
TEMPERATURE (DEG C)
-2.00
-1.50
-1.00
-0.50
0.00
0.50
1.00
SB 034 01 june 1975
DEPTH (M)
0.00
50.00
100.00
150.00
200.00
250.00
300.00
350.00
400.00

Fig 5.5 f

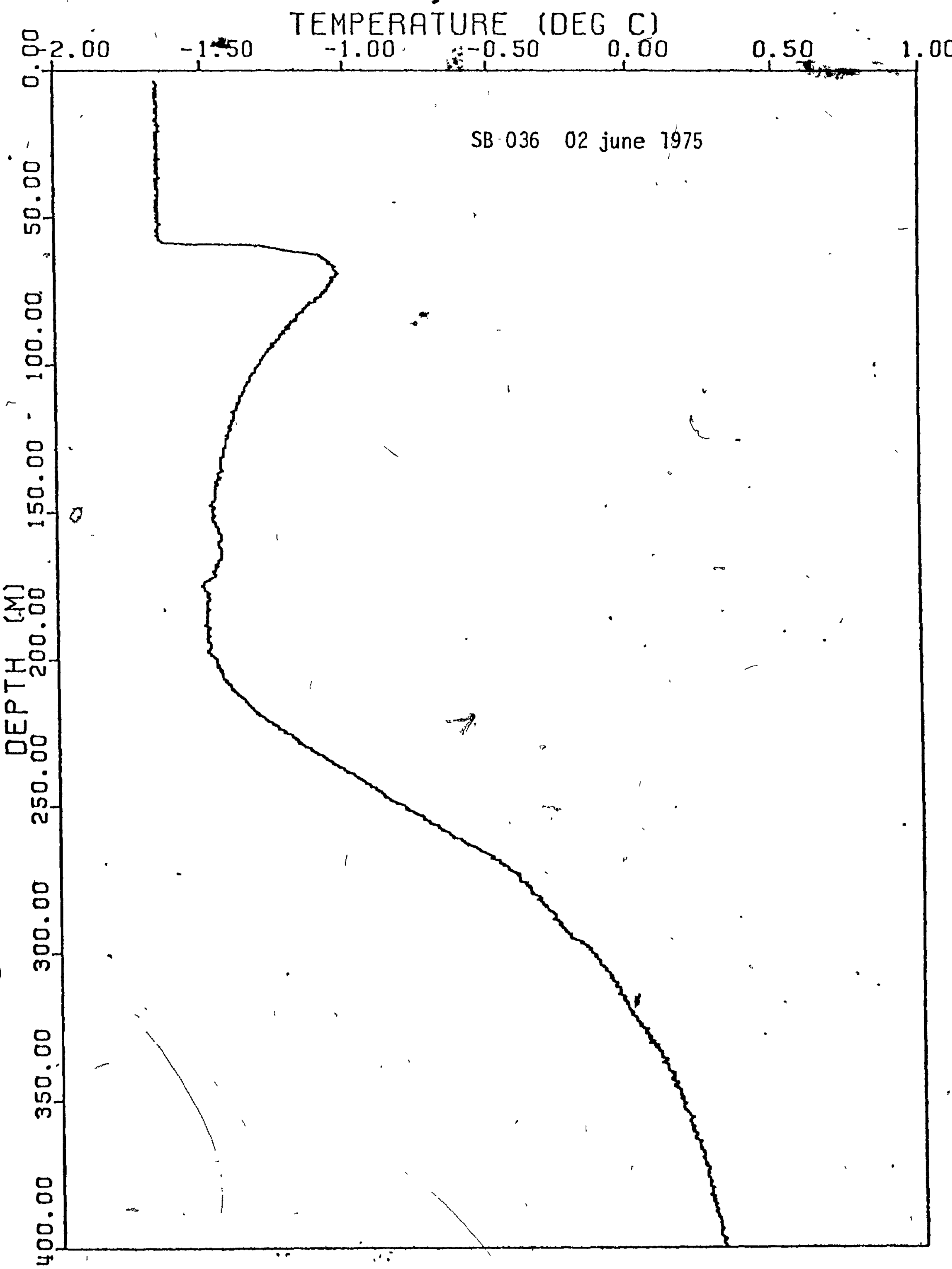
TEMPERATURE (DEG C)
-2.00
-1.50
-1.00
-0.50
0.00
0.50
1.00
SB 036 02 june 1975
DEPTH (M)
0.00
50.00
100.00
150.00
200.00
250.00
300.00
350.00
400.00

Fig 5.5 g

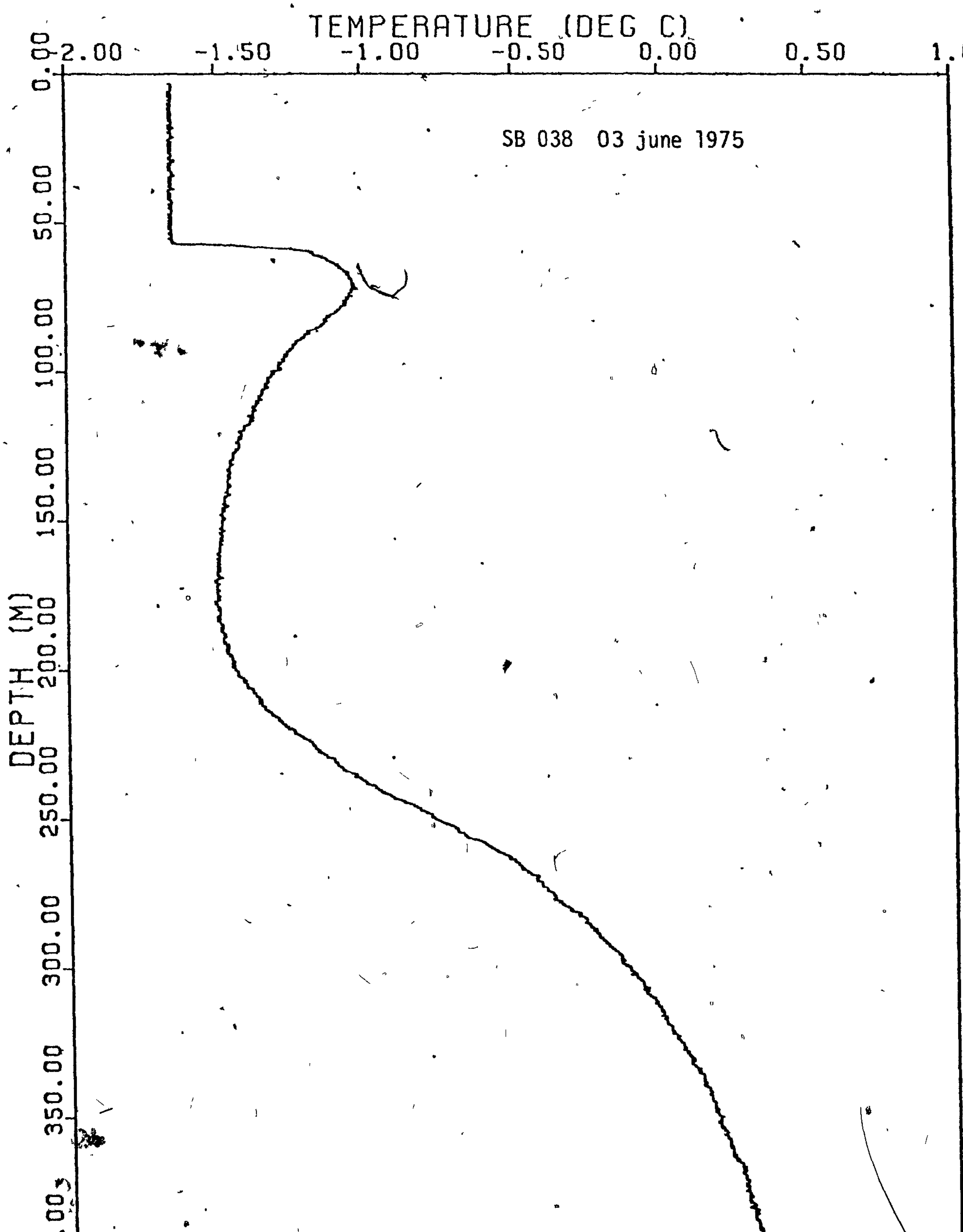
TEMPERATURE (DEG C)
-2.00
-1.50
-1.00
-0.50
0.00
0.50
1.00
SB 038 03 june 1975
DEPTH (M)
0.00
50.00
100.00
150.00
200.00
250.00
300.00
350.00
400.00

Fig 5.5 h

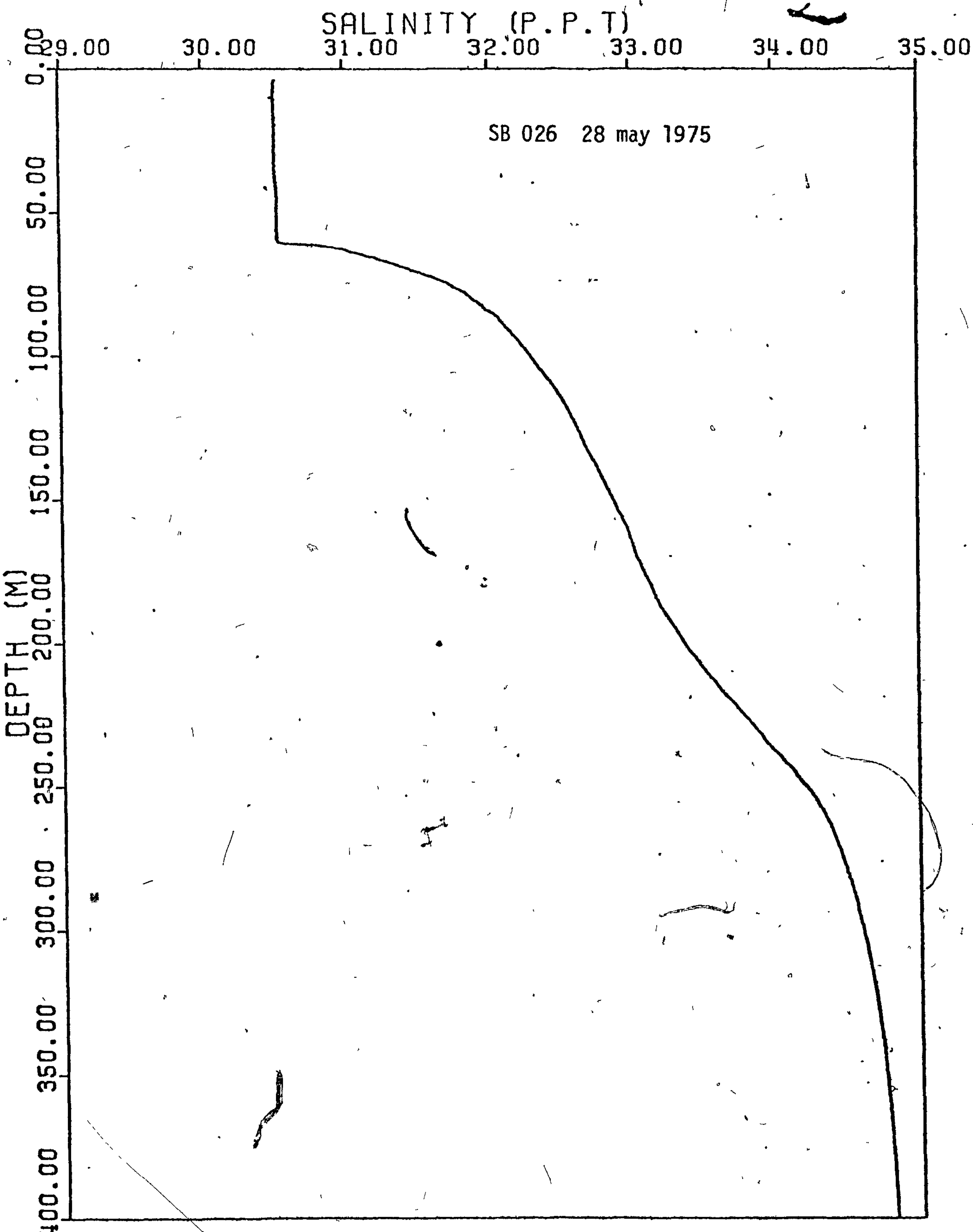
SALINITY (P.P.T)
29.00
30.00
31.00
32.00
33.00
34.00
35.00
SB 026 28 may 1975
DEPTH (M)
0.00
50.00
100.00
150.00
200.00
250.00
300.00
350.00
400.00

Fig 5.5 i

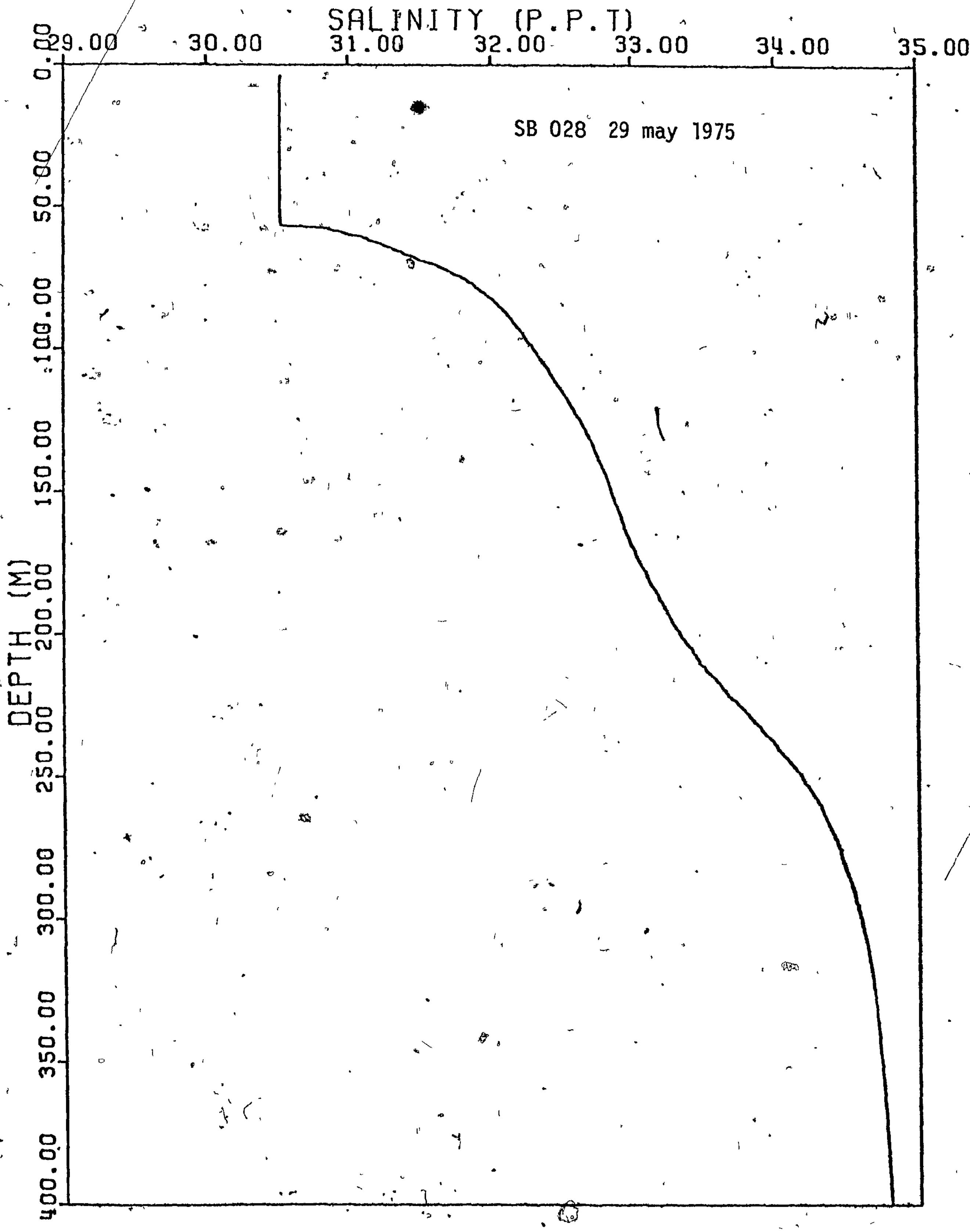
SALINITY (P.P.T)
29.00
30.00
31.00
32.00
33.00
34.00
35.00
DEPTH (M)
0.00
50.00
100.00
150.00
200.00
250.00
300.00
350.00
400.00
SB 028 29 may 1975

Fig 5.5 j

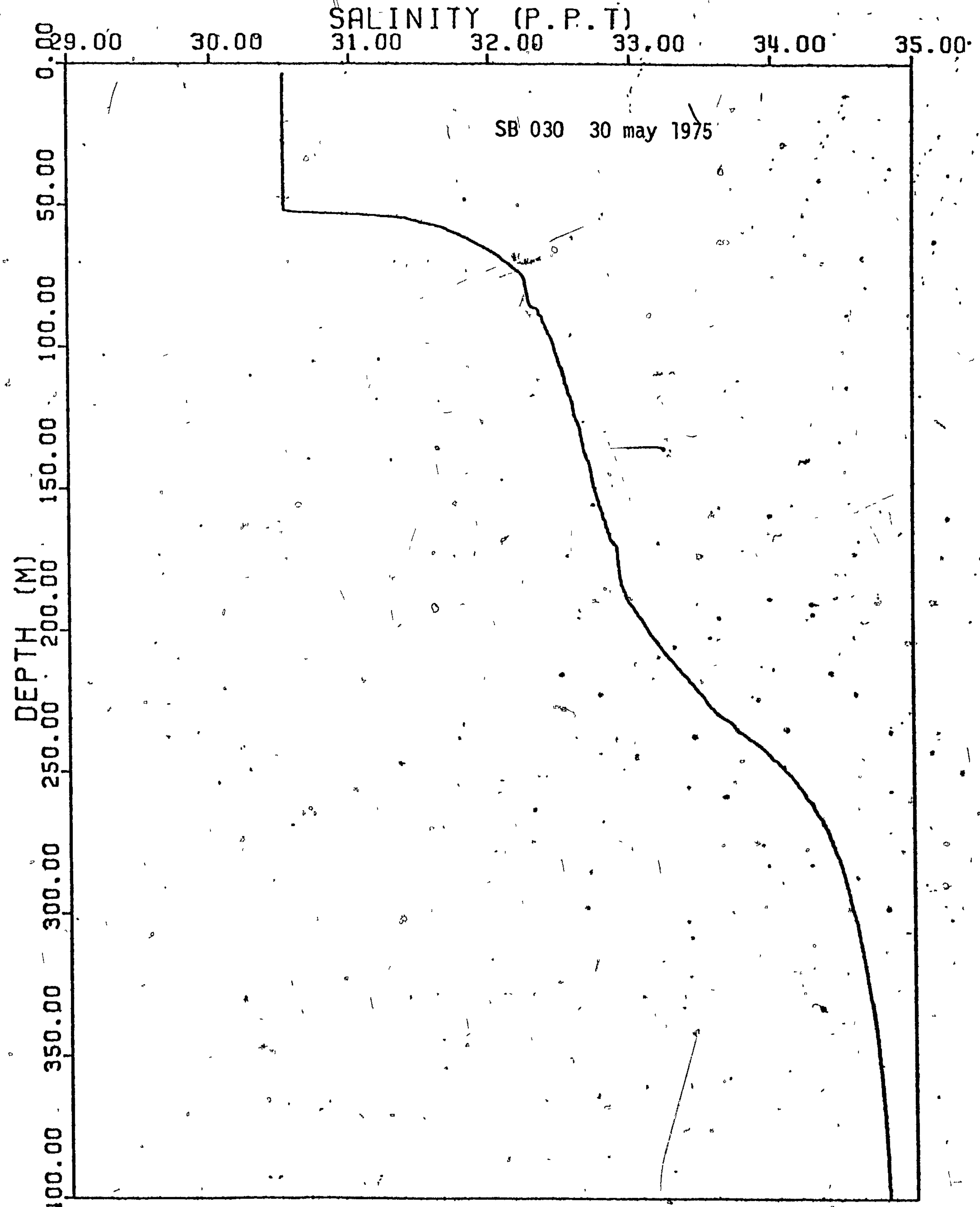
SALINITY (P.P.T)
29.00
30.00
31.00
32.00
33.00
34.00
35.00
SB 030 30 may 1975
DEPTH (M)
0.00
50.00
100.00
150.00
200.00
250.00
300.00
350.00
400.00

Fig 5.5 k

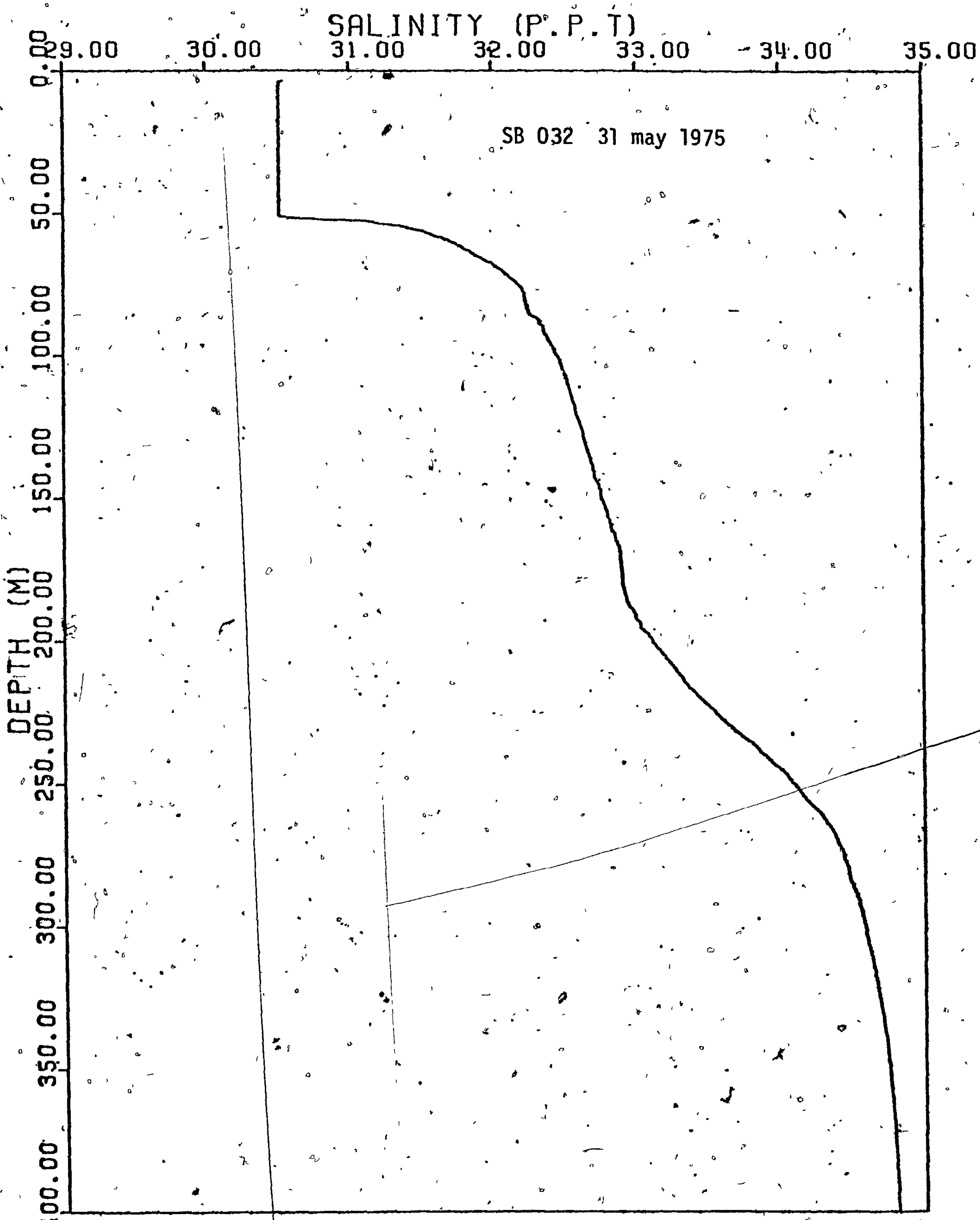
SALINITY (P.P.T)
29.00
30.00
31.00
32.00
33.00
34.00
35.00
SB 032 31 may 1975
DEPTH (M)
0.00
50.00
100.00
150.00
200.00
250.00
300.00
350.00
400.00

Fig 5.5 1

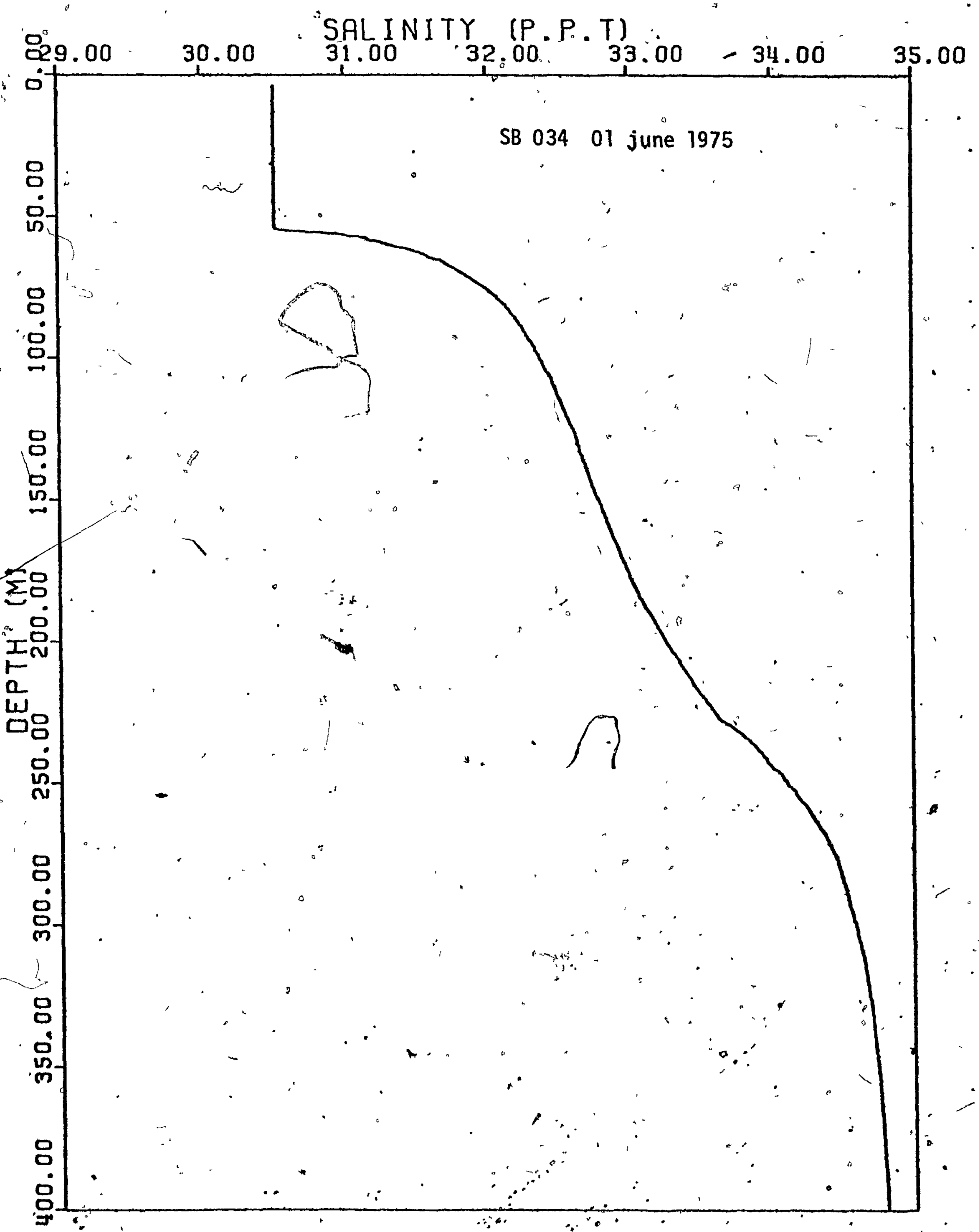
SALINITY (P.P.T)
29.00
30.00
31.00
32.00
33.00
34.00
35.00
SB 034 01 june 1975
DEPTH (M)
0.00
50.00
100.00
150.00
200.00
250.00
300.00
350.00
400.00

Fig 5.5 m

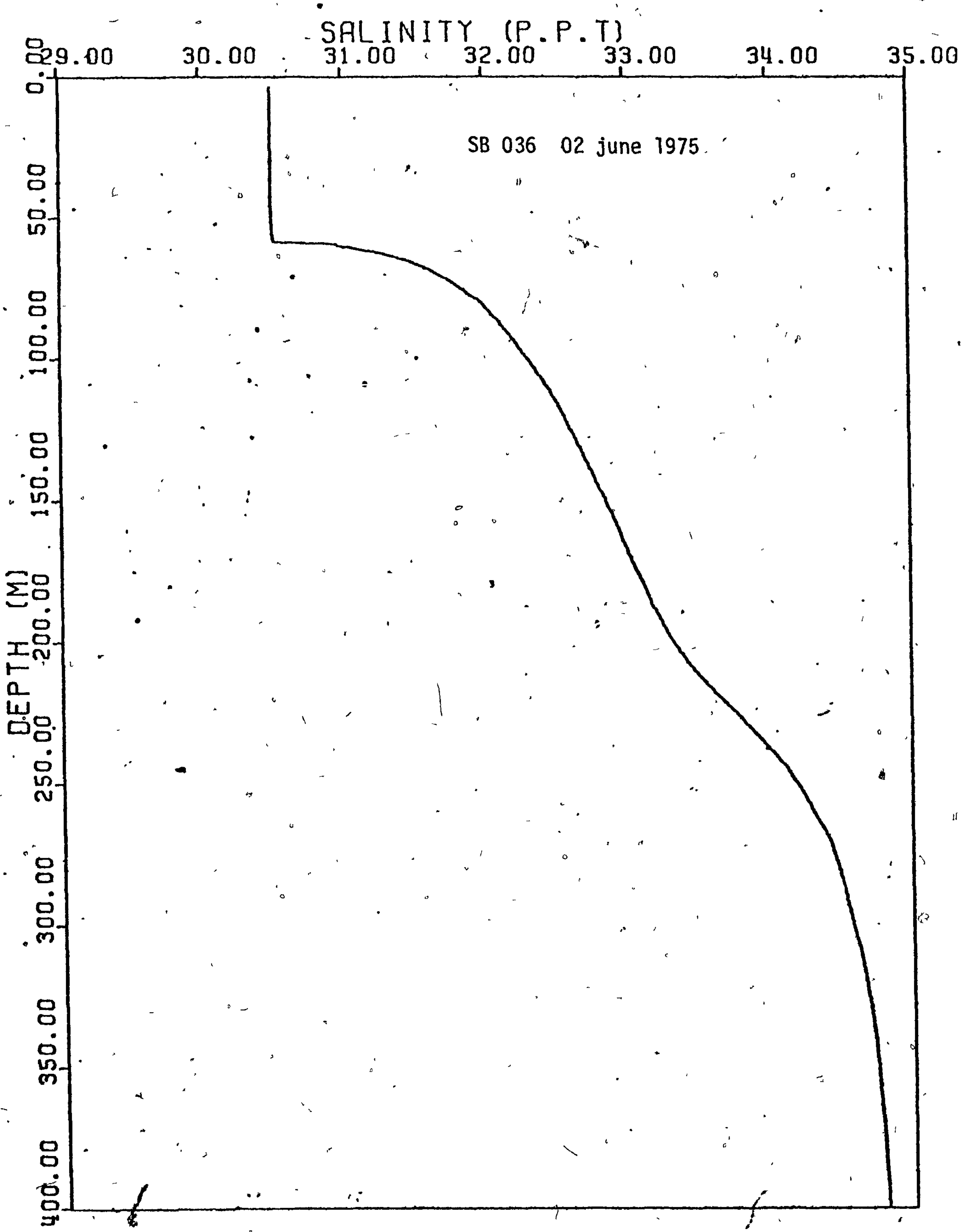

SALINITY (P.P.T)
29.00
30.00
31.00
32.00
33.00
34.00
35.00
0.00
50.00
100.00
150.00
200.00
250.00
300.00
350.00
400.00
DEPTH (M)
SB 036 02 june 1975

Fig 5,5 n

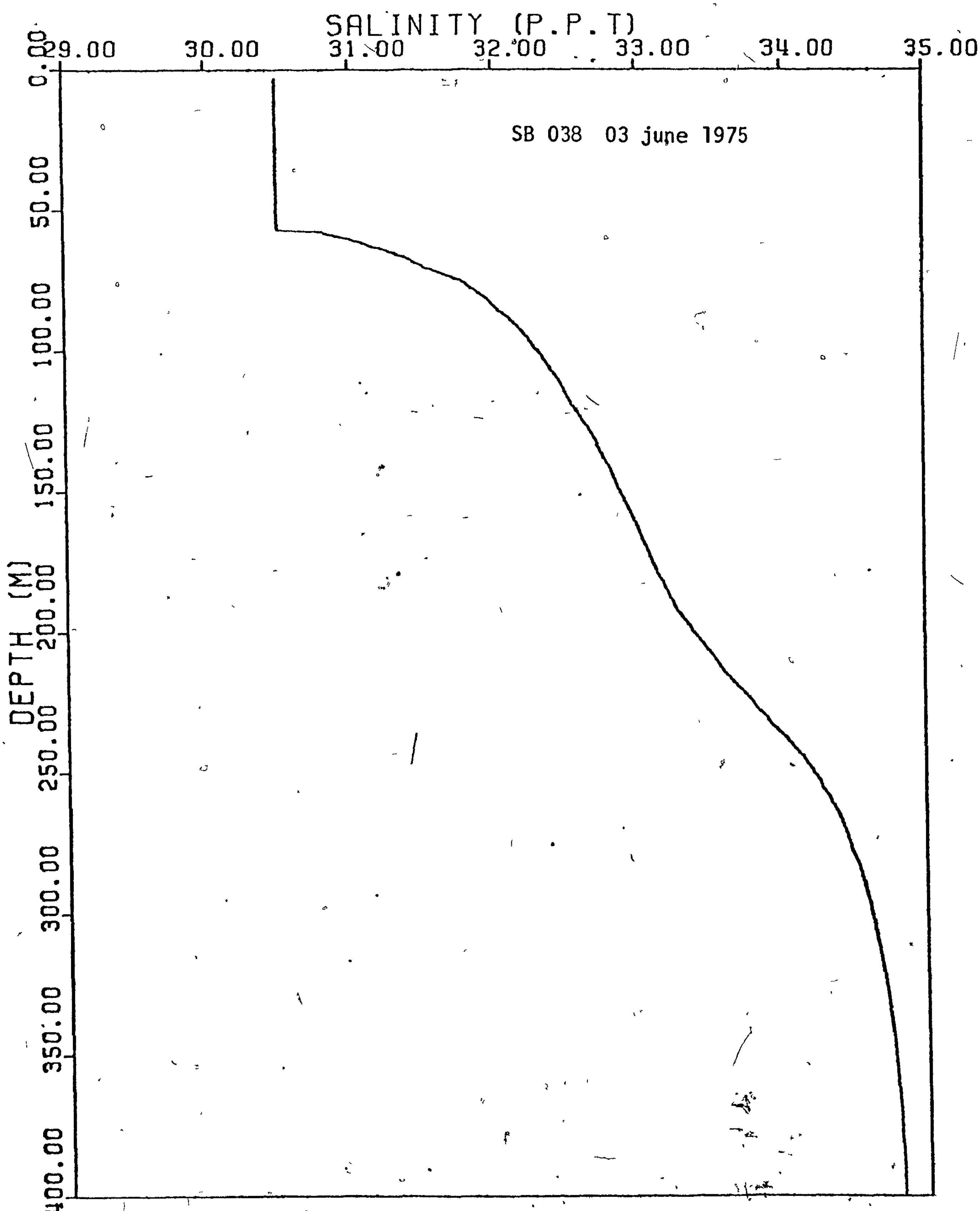
SALINITY (P.P.T)
29.00
30.00
31.00
32.00
33.00
34.00
35.00
SB 038 03 june 1975
DEPTH (M)
0.00
50.00
100.00
150.00
200.00
250.00
300.00
350.00
400.00

Fig 5.6 (a to g) T-S diagrams for an eddy.

Fig 5.6 a

T S DIAGRAM SNOWBIRD

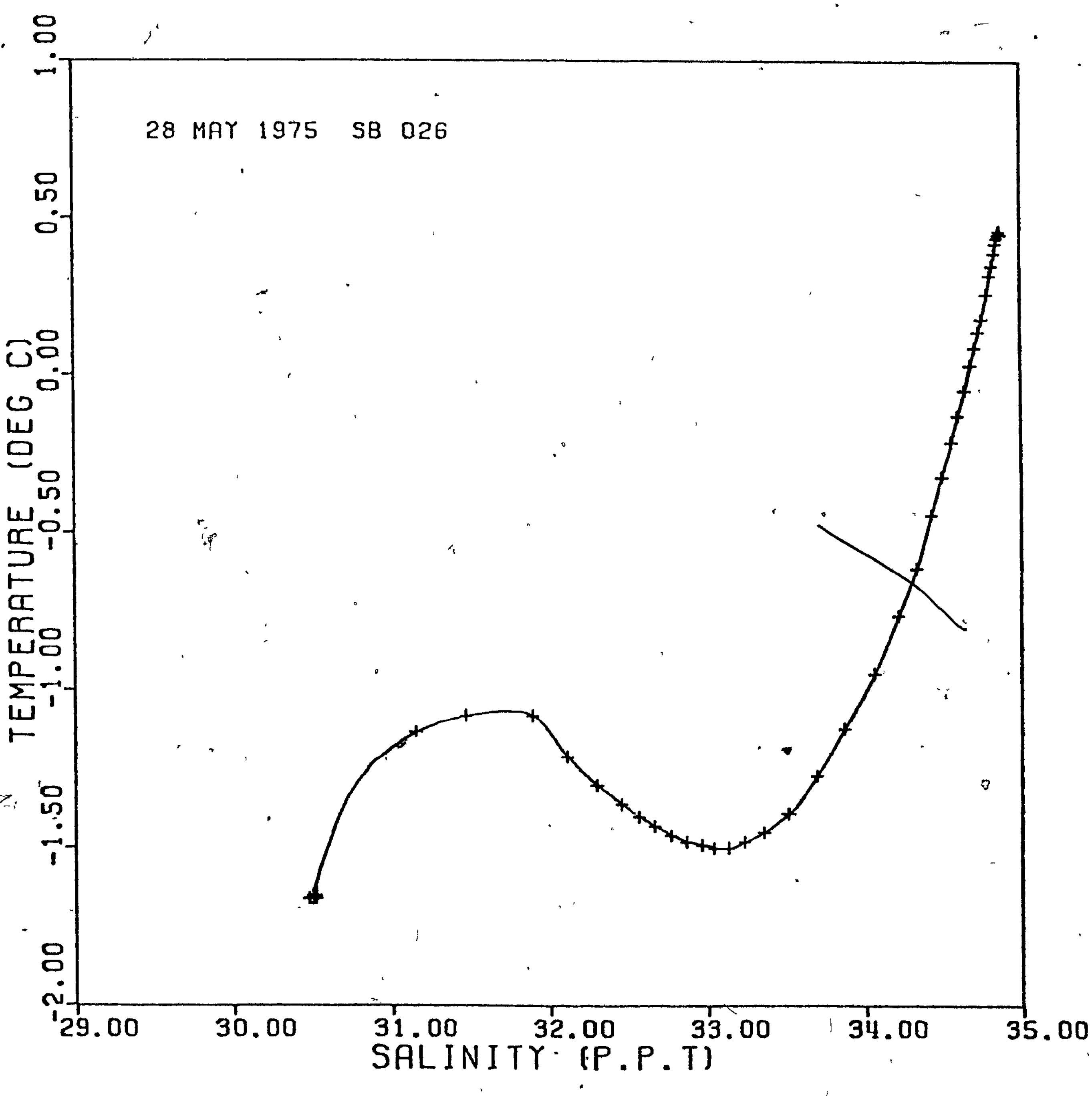

Fig 5.6 b

T S DIAGRAM SNOWBIRD

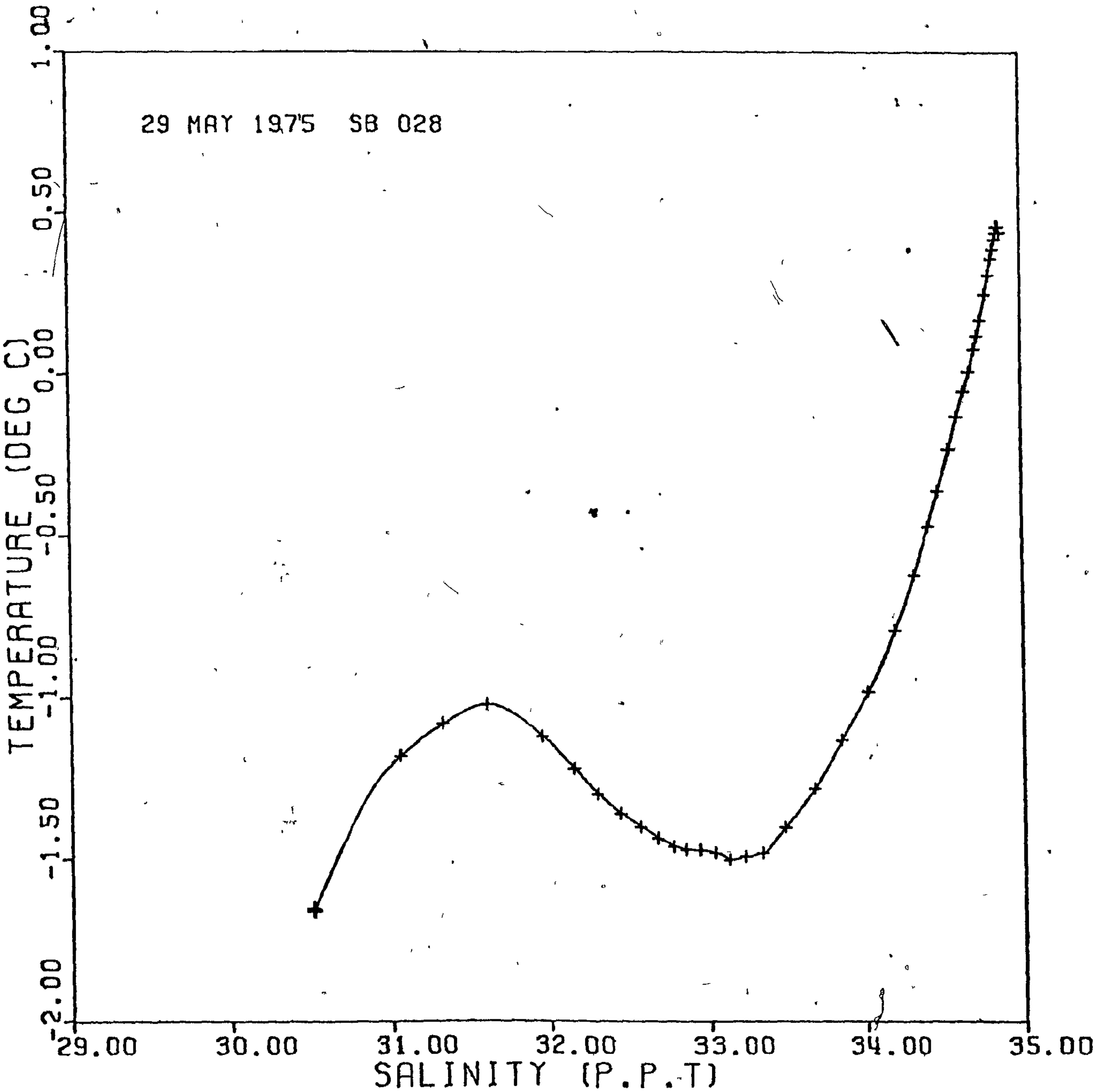

Fig 5.6 c

T S DIAGRAM SNOWBIRD

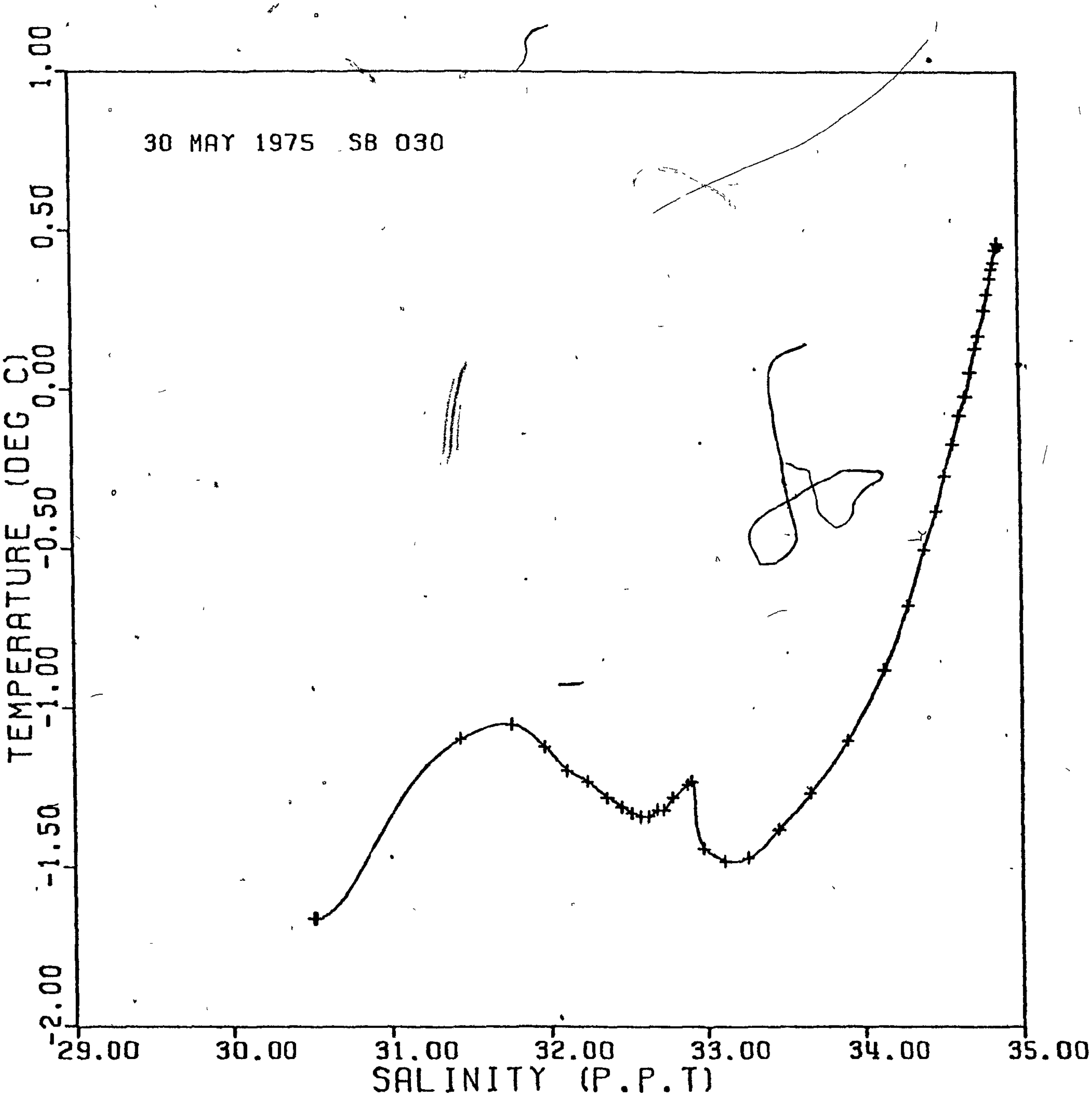

Fig 5.6 d

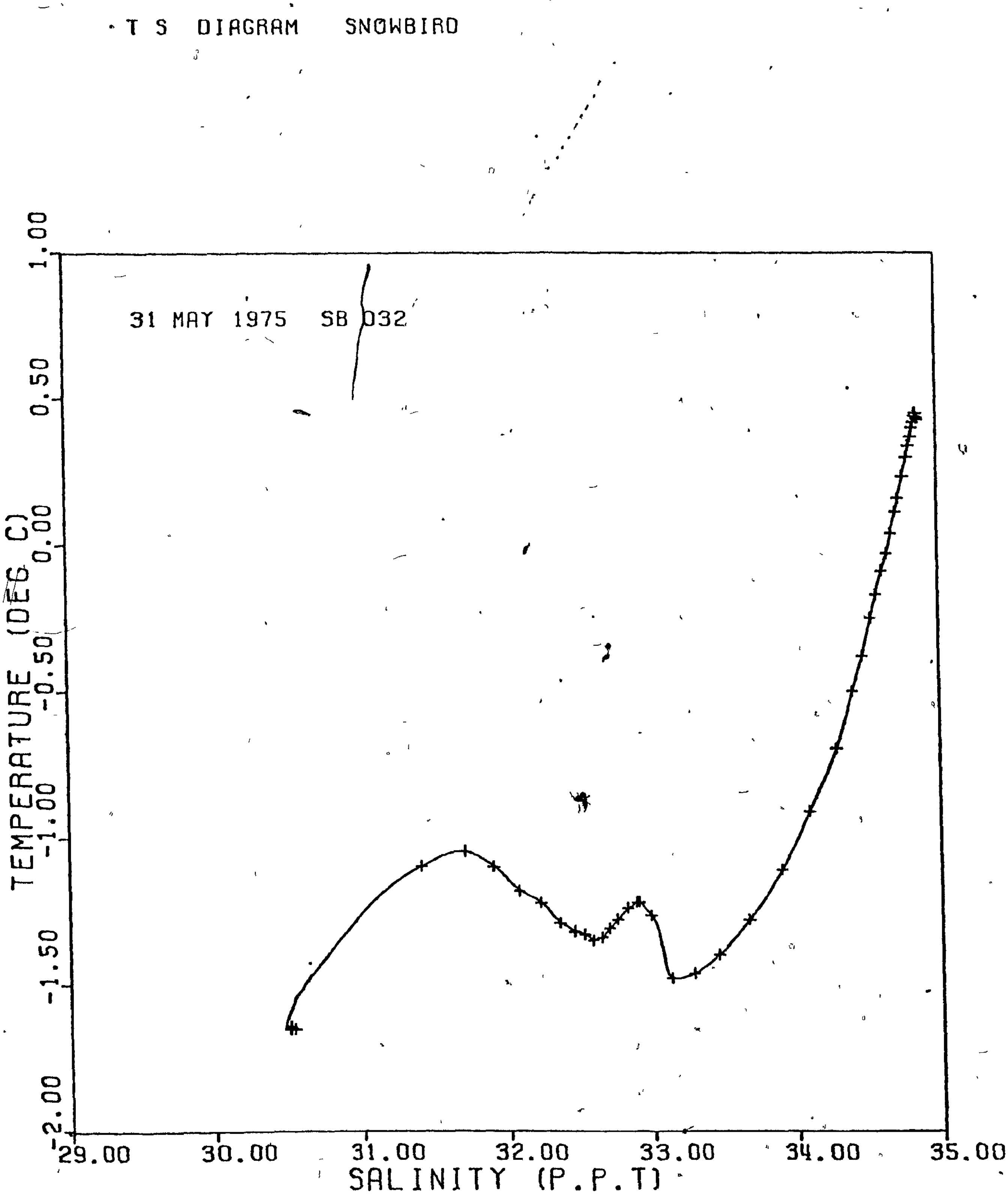
T S DIAGRAM SNOWBIRD
31 MAY 1975 SB 032
TEMPERATURE (DEG C)
1.00
0.50
0.00
-0.50
-1.00
-1.50
-2.00
29.00
30.00
31.00
32.00
33.00
34.00
35.00
SALINITY (P.P.T)

Fig 5.6 e

T S DIAGRAM SNOWBIRD

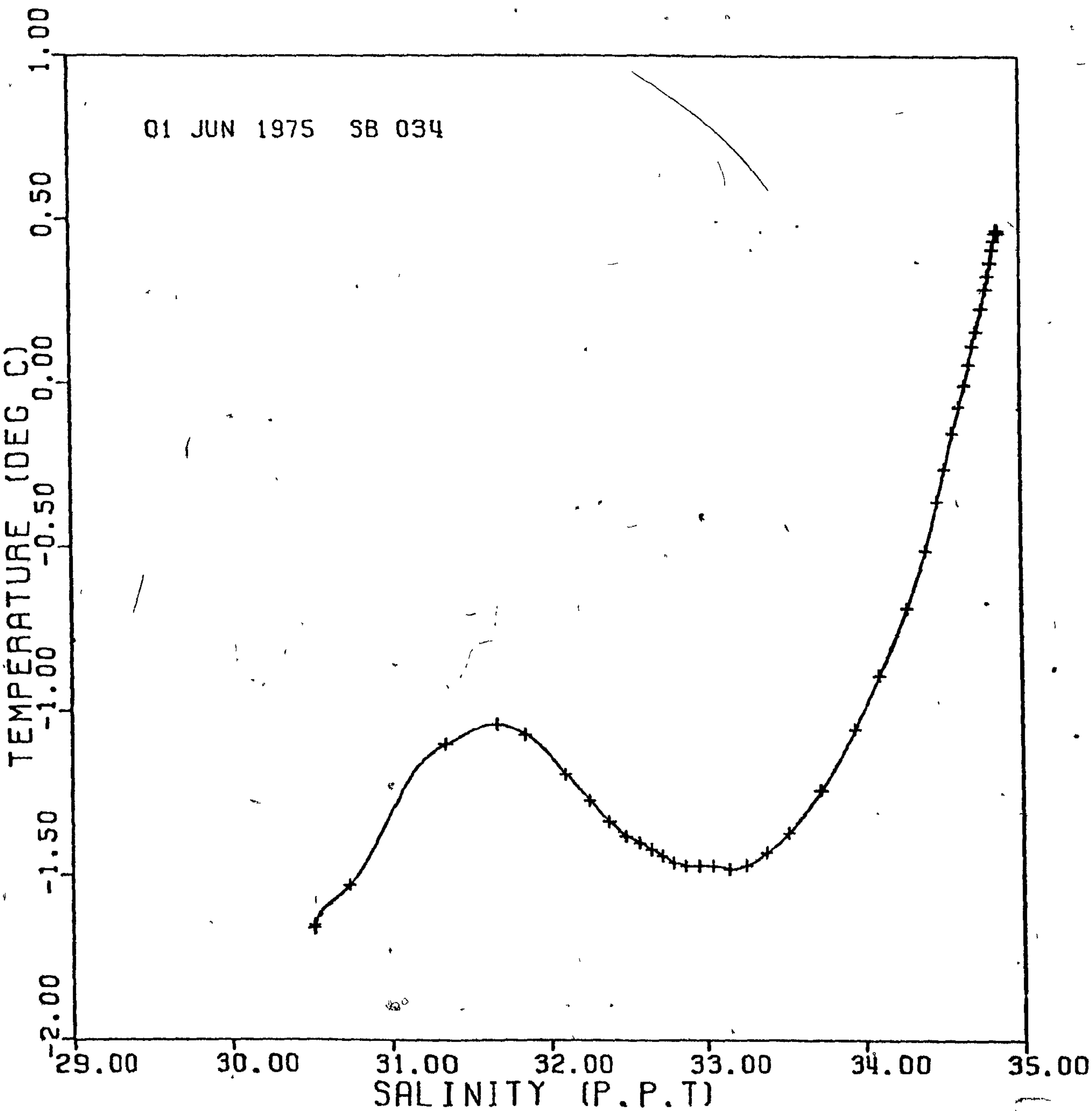

Fig 5.6 f

T S DIAGRAM SNOWBIRD

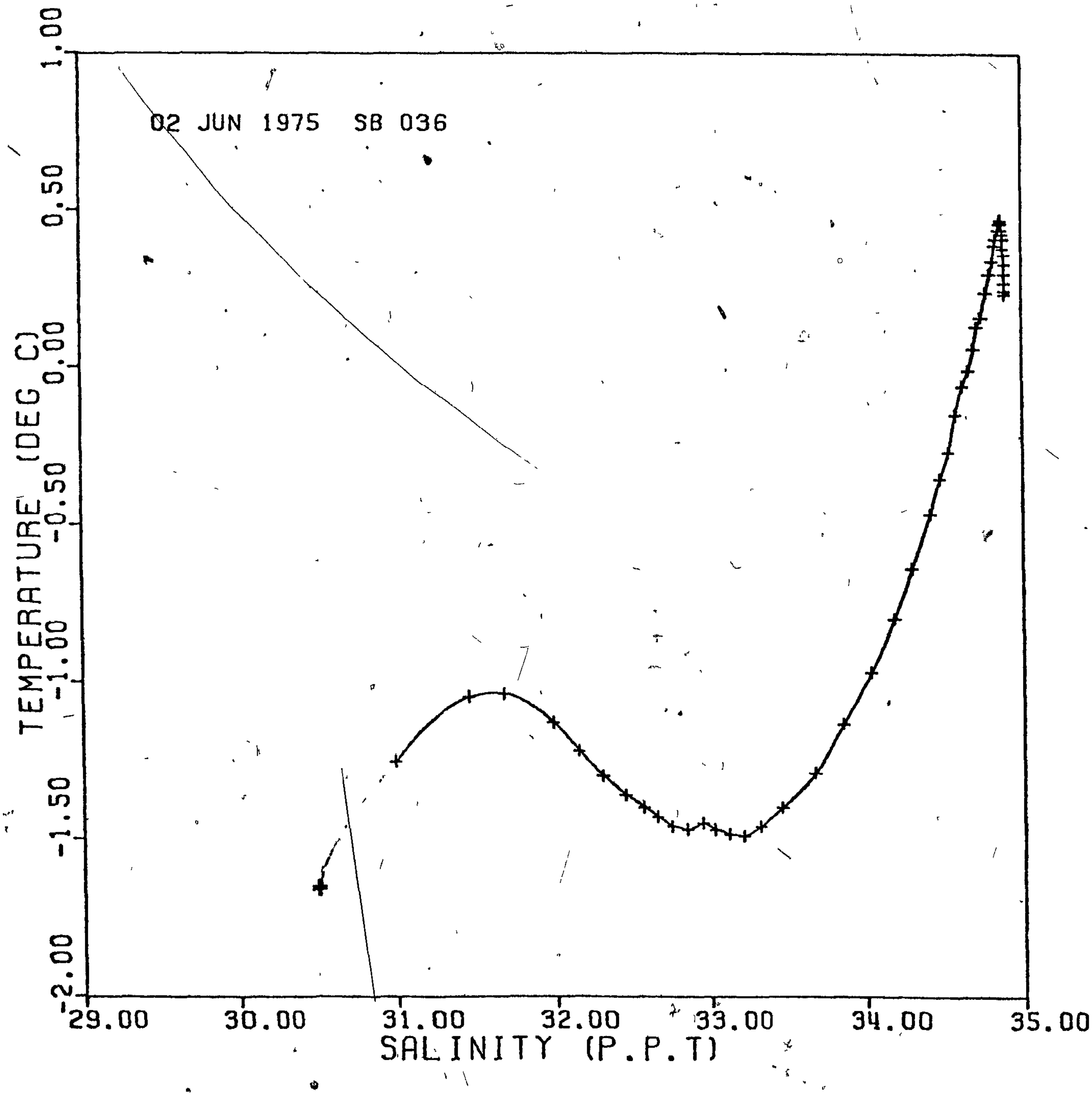

Fig 5.6 g

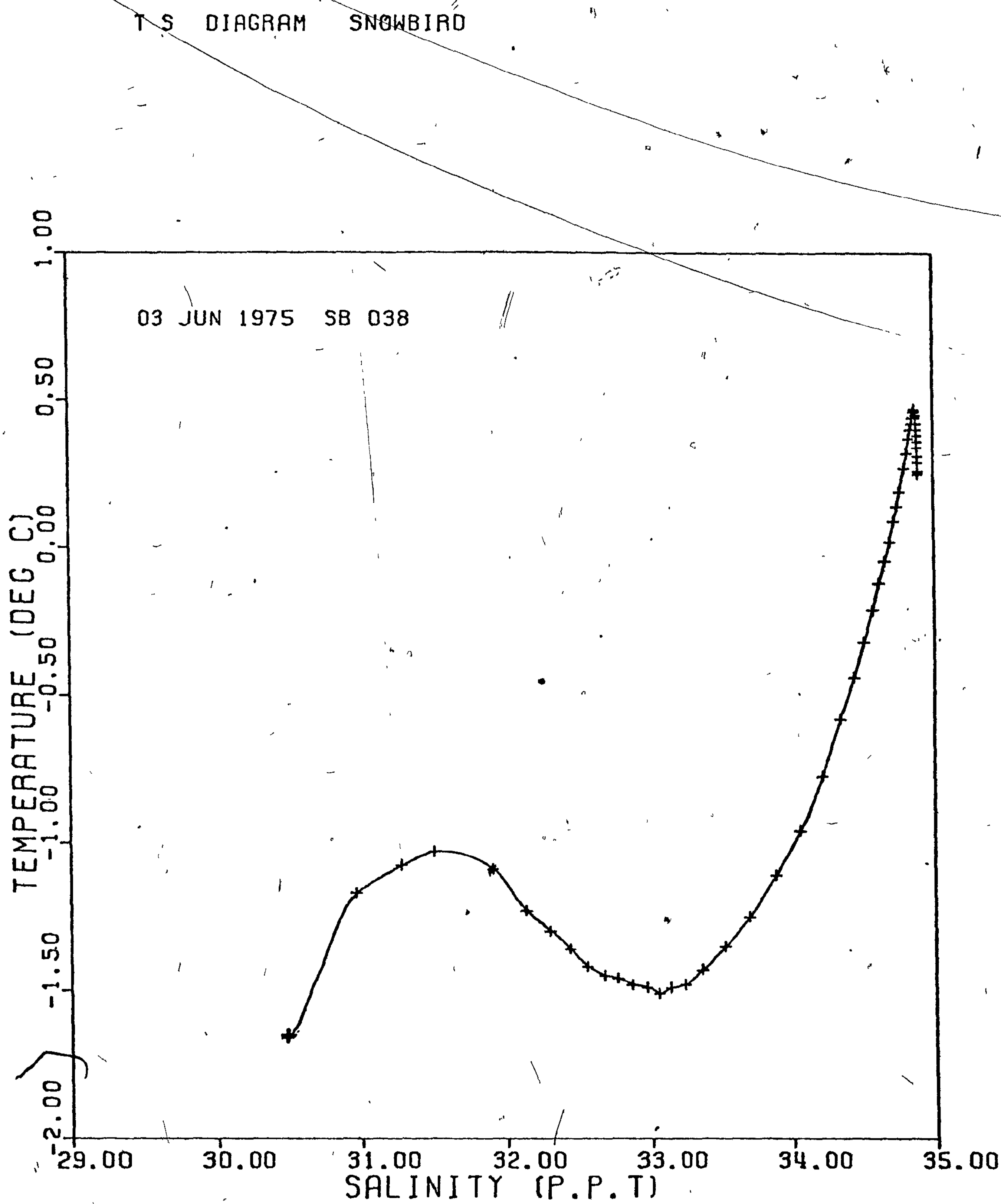
T S DIAGRAM SNOWBIRD
03 JUN 1975 SB 038
TEMPERATURE (DEG C)
1.00
0.50
0.00
-0.50
-1.00
-1.50
-2.00
29.00
30.00
31.00
32.00
33.00
34.00
35.00
SALINITY (P.P.T)

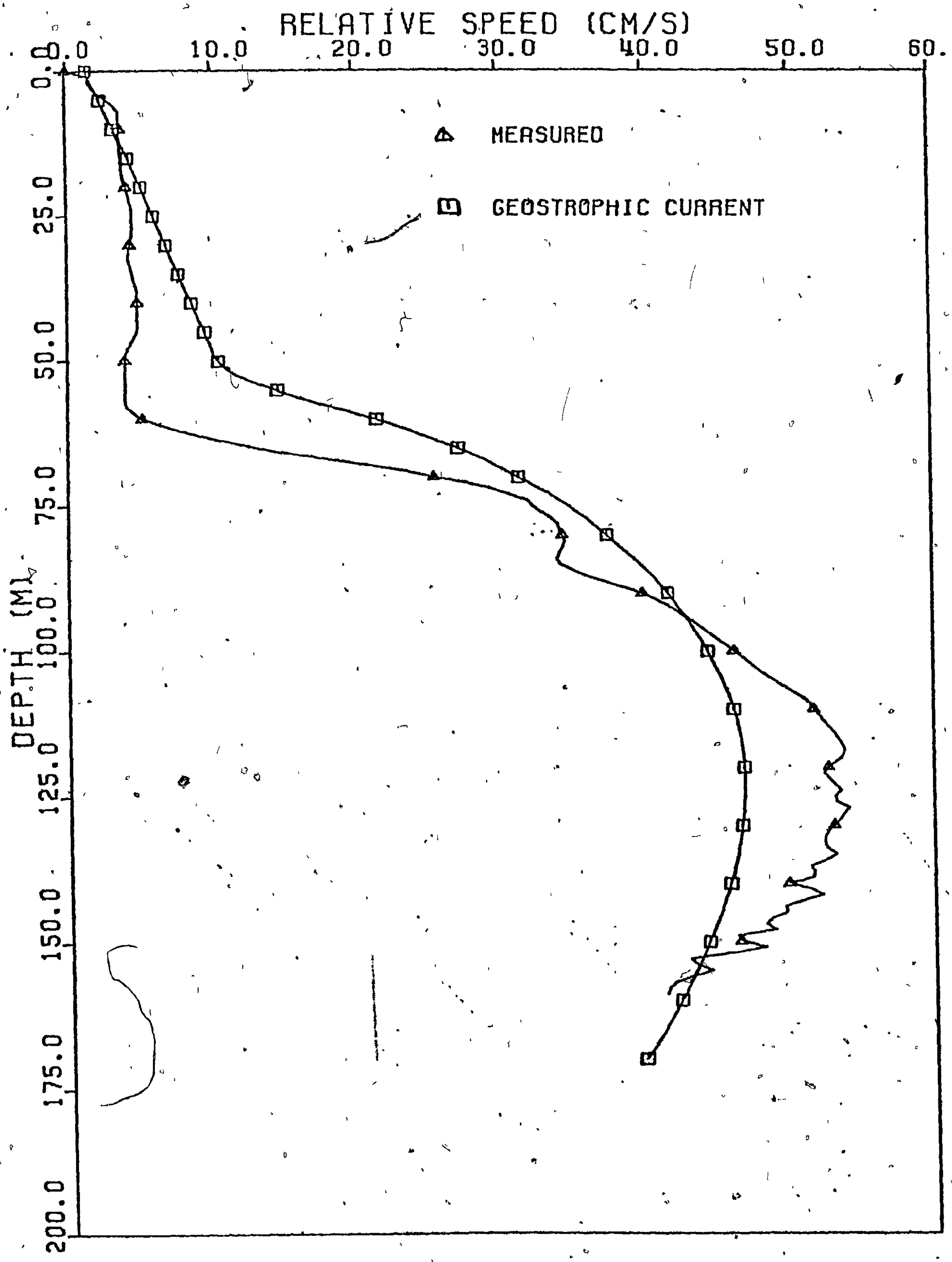

Fig 5.7 Approximate geostrophic balance in an eddy.

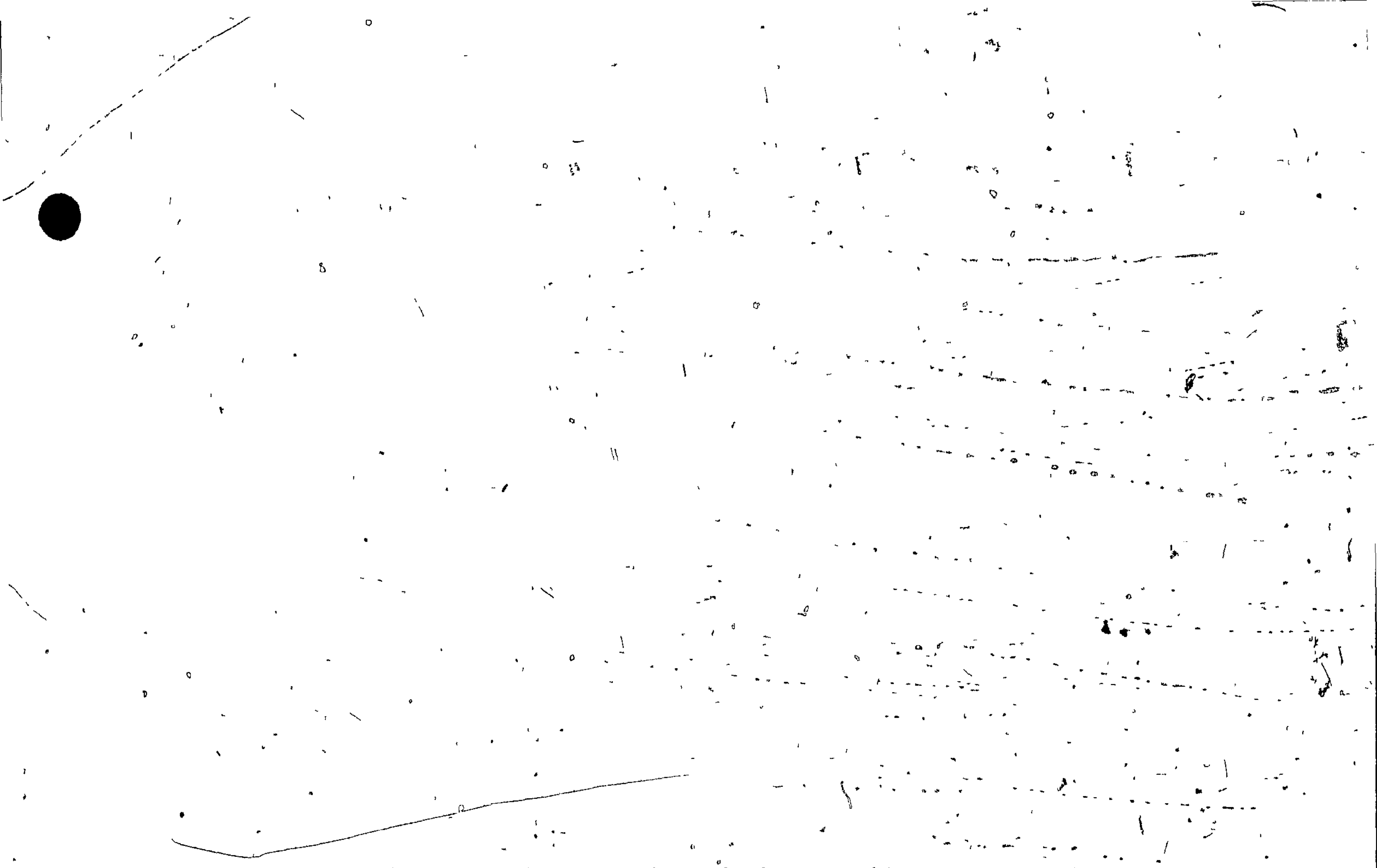

Fig 5.8 Isotemp lines during an eddy.

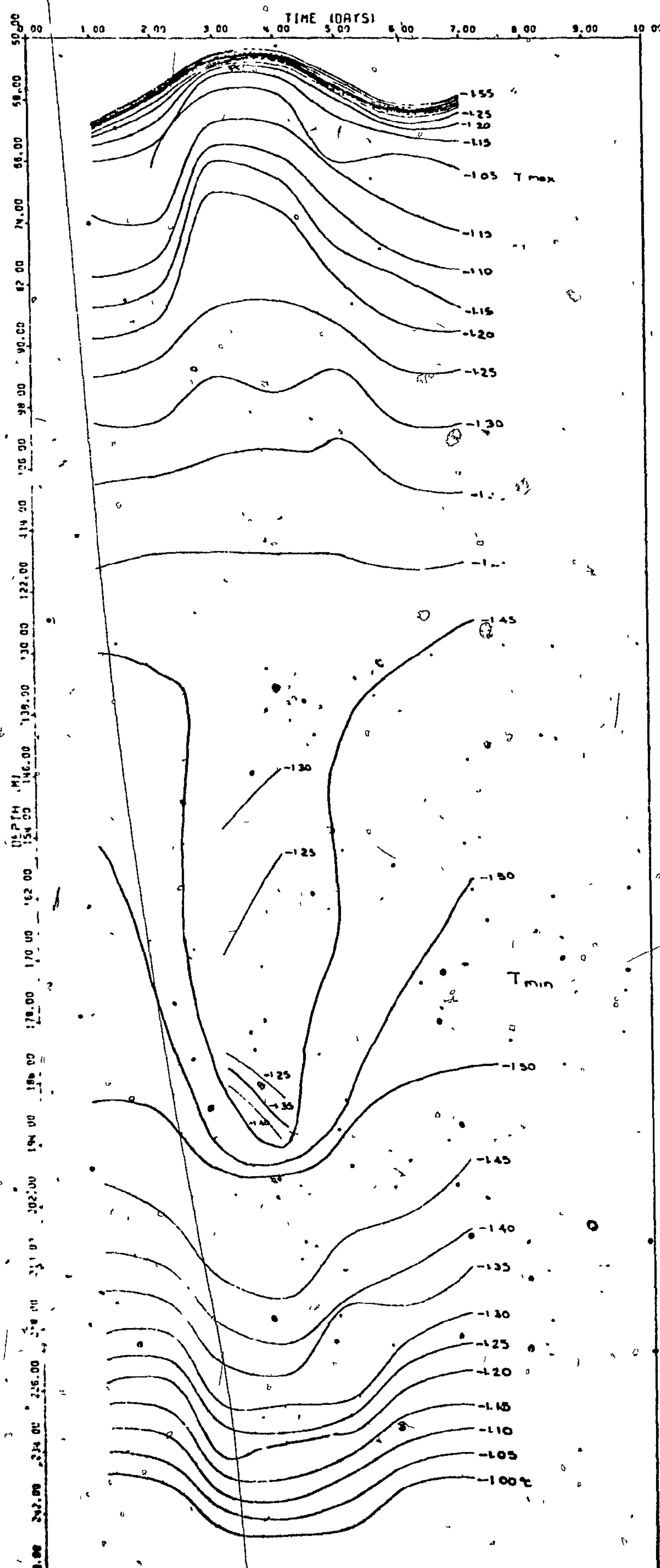
TIME (DAYS)
DEPTH (M)
T max
T min
-1.00°c

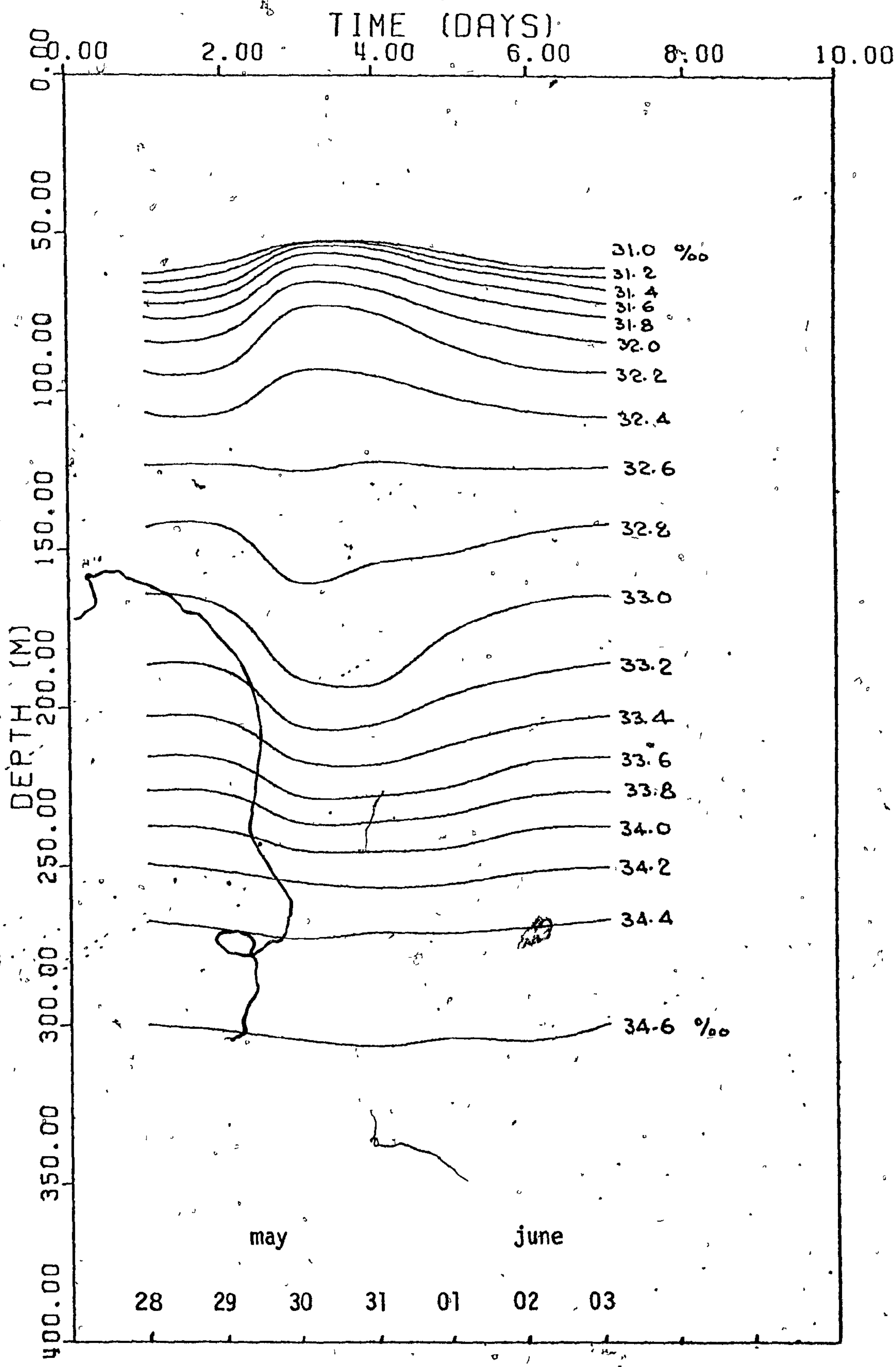

Fig 5.9 Isohaline lines during an eddy.

Hunkins (1974b) has shown, and it is confirmed in this study, that the relationship between the temperature and the current field is nearly geostrophic. The profile shape, level and speed agree fairly well with the geostrophic profile although the observed speeds are slightly higher. For an anticyclonic eddy, as this one, the geostrophically calculated velocity will underestimate the current velocity if centrifugal effects are significant. If a 10 km radius is assumed, a better agreement in speed is achieved. Fig. 5.7 shows the currents in the geostrophic balance for the eddy. The calculated currents seem to be in good agreement with the measured currents at this time. A point to note is that density, the dynamically important parameter, is almost entirely a function of salinity in this ocean. The density increases continuously with depth since the salinity does. The temperature serves as a tracer of the water masses.

The temperature and salinity fields are presented again in Fig. 5.8 and 5.9. The isotemp and isohaline lines are drawn at 0.1°C and 0.2 $^0/oo$ steps. From these figures we see that the density (essentially salinity) variation surfaces are distorted upwards or downwards by as much as 30m. In the salinity surfaces, especially, there is a general movement upwards above the current maximum and downwards below it. This corresponds to a high pressure or anticyclonic (clockwise in northern hemisphere) sub-surface system. This agrees with the eddy track in Fig. 5.4.

5.1.3 Energy balance

The detection of these subsurface eddies provides a new dimension to the energy balance in the Arctic Ocean. Most of the kinetic energy is seen (Fig. 5.10) to be contained in these eddies rather than in the mean current. This is the same conclusion as Hunkins (1974b).

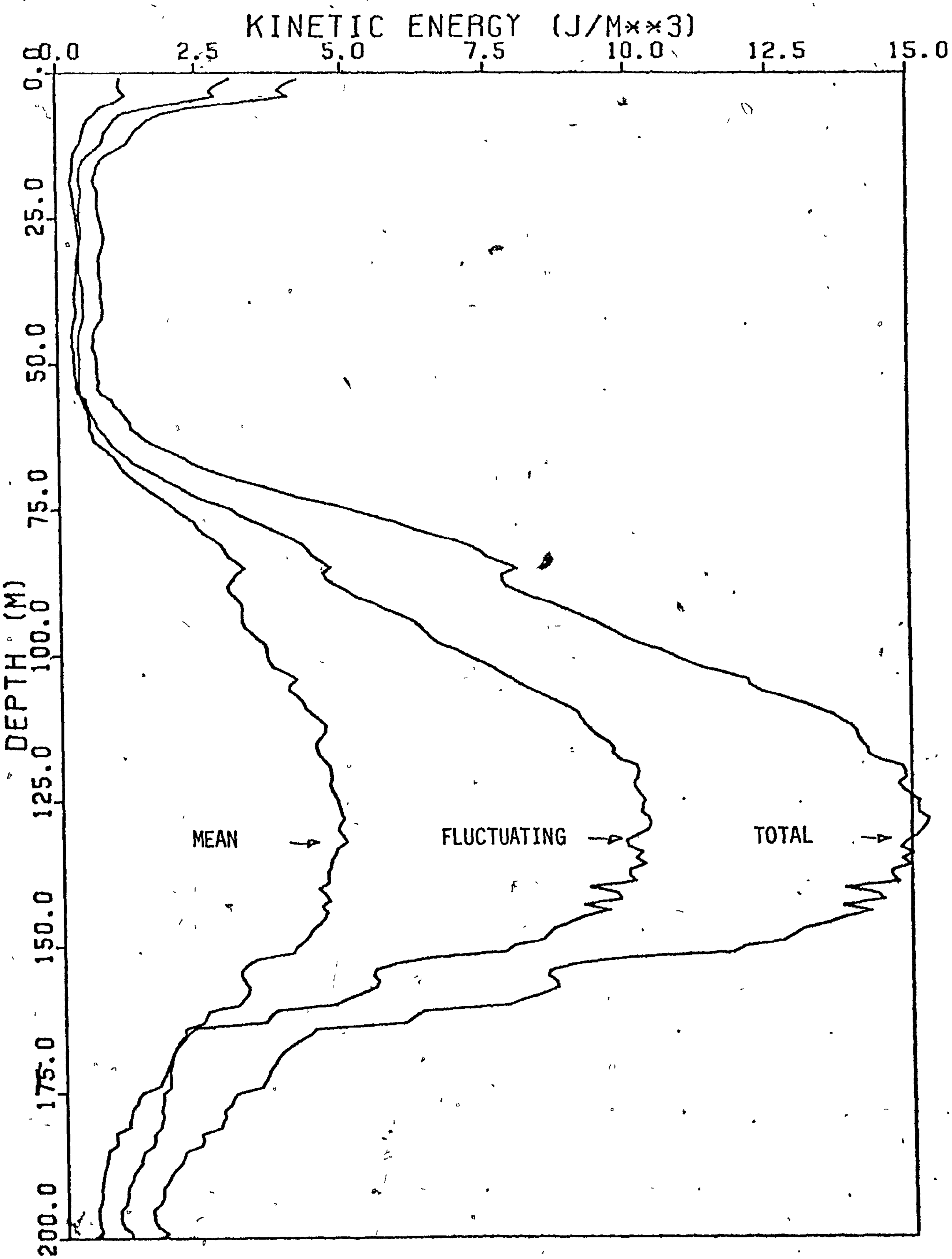

Fig 5.10 Vertical distribution of horizontal kinetic energy.
19 may to 23 june 1975 at Snow Bird

The kinetic energy shown here is for a period of one month around the eddy (i.e. starting from the PCM cast of 19 May to 23 June 1975). The kinetic energy of the mean flow is

$$KE_{mean} = \frac{1}{2}\rho\left\{\bar{u}^2 + \bar{v}^2\right\}$$

whereas the kinetic energy of the time dependent part is

$$KE_{fluctuating} = \frac{1}{2}\rho\left\{\overline{u'}^2 + \overline{v'}^2\right\}$$

with the total kinetic energy being the sum of these two terms.

$$KE_{total} = KE_{mean} + KE_{fluctuating}$$

We get these having divided the flow into the mean and time-dependent parts as

$$u = \bar{u} + u'$$

$$v = \bar{v} + v'$$

The quantity with the bar is the mean value and the primed quantity the departure from the mean.

$$\overline{u'}^2 = \frac{1}{n}\sum_{i=1}^{n} u_i'^2 \qquad \overline{v'}^2 = \frac{1}{n}\sum_{i=1}^{n} v_i'^2$$

n being the number of data points. ρ is taken as 1.024 gm cm^{-3}, the mean density in these calculations. (u and v are the east and north components respectively of the speed).

Fig. 5.10 shows that in the upper layer the total kinetic energy was 0.8 J/m^3 while at 125m, or near the maximum eddy velocity it was 15.1 J/m^3, more than an order of magnitude greater. From Fig. 5.10 and Table 5.2 we also see that the kinetic energy in the Ekman layer

Table 5.2

Vertical distribution of the horizontal kinetic energy.

19 may to 23 june 1975 at Snow Bird.

Depth	Kinetic energy ($J\ m^{-3}$)		
(m)	Mean	Fluctutating	Total
1	3.12	1.15	4.27
10	0.89	0.50	1.39
20	0.46	0.29	0.75
30	0.40	0.41	0.82
40	0.48	0.33	0.81
50	0.40	0.31	0.71
75	2.06	3.07	5.13
100	3.64	7.14	10.78
125	4.83	10.29	15.12
150	4.08	7.93	10.01
175	1.71	1.34	3.04
200	1.14	0.51	1.65

(top 20-30m) is small in comparison with that at 125m. The total kinetic energy, made up of the mean and the fluctuating part, reaches its maximum value as we approach the core of the eddy. The fluctuating flow contains the bulk of the kinetic energy at all levels, ranging from 2 to 5 times that in the steady flow. The kinetic energy is low and relatively constant in the mixed layer between the surface and 50m. Between 50 and 100m the energy generally increases with depth. The overwhelming contribution of the eddies to the energetics of the ocean now requires the reassessment of the role of eddies from being small perturbations in the mean circulation to a more important part.

5.1.4 Mechanism

The detection of these eddies leads to the question of their origin and the possible mechanism of their formation.

The T-S diagrams (Fig. 5.6) show that the water characteristics of the eddied differed considerably and, more significantly, were different from those of the stations before and after the eddy's detection. A local displacement of the σ_t surfaces would not move the T-S points of the eddy water outside the ambient water T-S characteristics; this suggests that the eddies might have had their origins at some other location and subsequently have been advected into the region of observations. The intrusion of the 'warm' water referred to above was noticed only during the eddy sighting. Such relatively warm water is found in the Chukchi Sea area, and the eddy may have formed there. This will be elaborated a little later.

The generation of eddies ~~has~~ been explained by wind-driven means (Browne & Crary (1958); Belyakov (1972)). It is suggested that, just as the generation of surface currents (in the mixed layer) arises from ice driven by winds, the winds also provide energy for deeper currents. Pack ice and wind vorticities might lead to divergences in the mixed layer and hence vertical velocities at its base. The distortion of the σ_t surfaces would then lead to a compensating flow. In AIDJEX 75, however, there was little relation between wind or ice drift and the presence of eddies. They were noted during both calm conditions and strong wind periods. The ice drift follows the winds and has similar synoptic space scales of about 1000 km.

The eddies however are of horizontal space scale of 10 km, two orders of magnitude smaller. This argues against wind as a direct cause.

Freezing is another possible energy source. The cracking of the ice in winter exposes the open water to very low air temperatures. There is quick freezing, releasing salt. As this heavy brine sinks, it disturbs the base of the mixed layer resulting in the distortion of the σ_t surfaces. Again the scales of this phenomenon are wrong because the salt releases occur in open water up to tens of meters. Also we note that this mechanism is valid for winter when freezing occurs but eddies were observed in summer as well as winter.

The Rossby radius of deformation is the ratio of the speed of long gravity waves to the inertial period (frequency). It is written down as

$$R = \left\{ g \frac{\Delta\rho}{\rho} H f^{-2} \right\}^{1/2}$$

Taking typical values for our ocean, $\Delta\rho = 0.004$ gm/cm^3 in the 100m layer H - the depth of the eddy, we get $R \sim 10$ km with f, the Coriolis parameter, equal to 1.4×10^{-3} sec^{-1}. This radius of deformation is roughly the size of the observed eddies. In the case of freezing or wind-induced generation, R will be the lower bound to the size of the phenomena, i.e. the smallest size would be 10 km or so. Above this limit, the eddy size is limited by the dimensions of the source.

Another mechanism is shear instability. For example, near a frontal surface such as the atmospheric polar front or the Gulf Stream, it has generally been found that great shear exists and occasionally vortices break off from the main flow and advect as eddies. For mature systems, at some distance from the shear zone, dissipative forces assert themselves. Thus we can have transformation of energy into small features. This mechanism is similar to that used to explain the break-up of the mean westerly winds in the atmosphere into familiar cyclone or anticyclone.

There is a basic shear of 2-3 cm/s across the pycnocline in this part of the Arctic. Calculations show (Hunkins, 1974b) that this is unstable but has a growth period of many months. The growth period is defined as the time taken for a small-scale disturbance to grow by a factor of e. Growth is a maximum for certain intermediate wavelengths that are of the order of Rossby radius of deformation. With the radius of deformation and eddy size similar in the Arctic, baroclinic instability explanation for the origin of the eddies is reasonable. The slow growth rate in the AIDJEX area and more favourable growth conditions near the Alaskan Continental slope is suggested by Hunkins (1974b) and Hart and Killsworth (1976) as the likely place of generation. The eddies are then advected north to the AIDJEX area. The effect of the bottom slope, enhanced shear and lack of summer ice cover there all favour instability in the Alaskan

Continental slope region. Again we corroborated this by the T-S diagram. As was pointed out then, the warm water of the eddy might have originated here and moved as the eddy traverses the ocean.

The subsurface maximum is one of the unique features of the Arctic eddies which is not found in the open ocean ones. Frictional dissipation against the ice cover is the most likely cause of the decrease in the velocity near the surface. Pounder and LeBlanc (1977) found evidence of this frictional effect in their calculation of the water drag. They observed that the Ekman spiral was modified by these currents and special care had to be taken in the choosing of the geostrophic current.

It is plausible that the eddies are generated in the open water near the Chuckchi Sea - Alaskan Continental slope area in the summer. They are then carried under the ice pack by the mean currents. Once under the ice, the velocity at the surface is slowed by the ice. The Ekman layer, is coincidental with the mixed layer in this part of the Arctic Ocean. The time necessary for these currents to be dissipated by secondary mixing processes is estimated to be in the neighbourhood of 1 day (Hunkins, 1977). The highly stratified layers, below the mixed layer, will lose their momentum much more slowly. If the stratification is strong then no smaller scale mixing might occur and then momentum loss would be by diffusion alone. In this case a simple model may be developed for the eddy behaviour below the mixed layer showing the deepening and decay of the eddy maximum with time. The diffusive response time is of the order $t_d \sim H^2/k$ for eddy diffusion to obtain a depth H. H is the depth below mixed layer for the velocity maximum. The eddy coefficient, k, is an unknown parameter which has ultimately to be determined by observations. There is, however, some information on the size of k from the measurements in the other oceans. It must typically be in the range of 1-10 cm^2/s in a steep pycnocline such as in the Arctic. For k = 1, H = 100m, t_d is 3 years, while for k = 10, t_d is 100 days. Thus the time taken for the eddies to reach their observed form is of the order of months to years according to these ideas. It would be possible to test this if an eddy could be followed for long enough time. But we have to remember that the space scales of the AIDJEX area was not designed for the tracking of these eddies but were rather to look at synoptic meteorological scales.

5.2 Step Structure

Step structure is another kind of oceanographic feature which is detected in the STD profile. Arctic Ocean step-structure has been reported previously by Neshyba et al (1971) with homogeneous layers 3m in thickness between depths of 200m and 500m. The profiles collected in the AIDJEX program show similar features especially in the salinity traces. It is interesting that such small scale features can be detected with the model 9040 STD which was not designed for microprofiling.

Many examples exist of microstructure in the world's oceans (Amos 1973; Johannessen and Lee 1974). Amos (1973) used the same model 9040 STD and has detected microstructure near the bottom of the western North Atlantic basin. The STD model 9040 was used there to show the existence of a 15m layer near the bottom. This proved to be a persistent feature.

Fig. 5.11 shows the STD profile of a Snow Bird station (SB007; 19 May 75). The step structure is visible between depths of 300 to 400m.

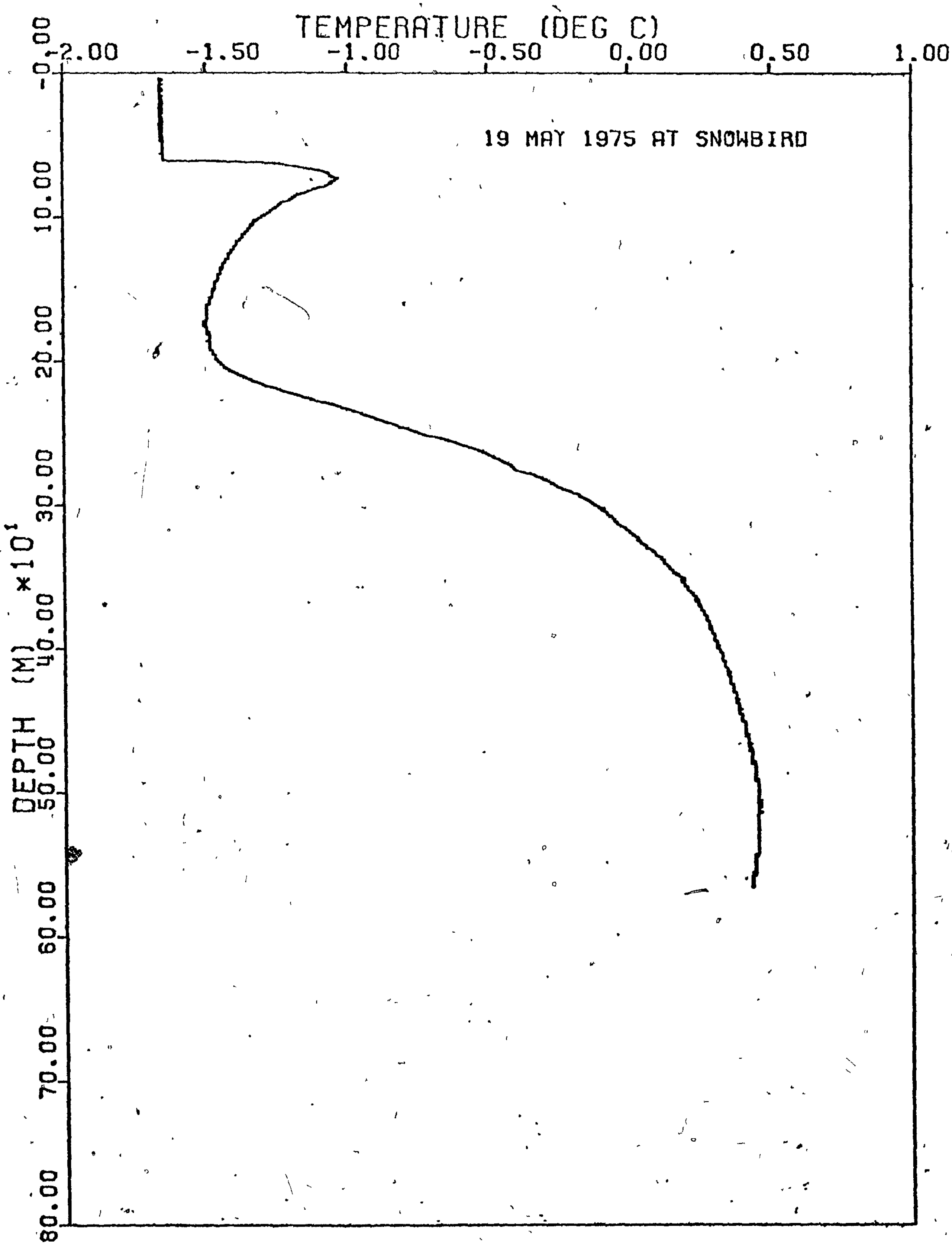

Fig 5.11 a. Temperature profile showing step structure.

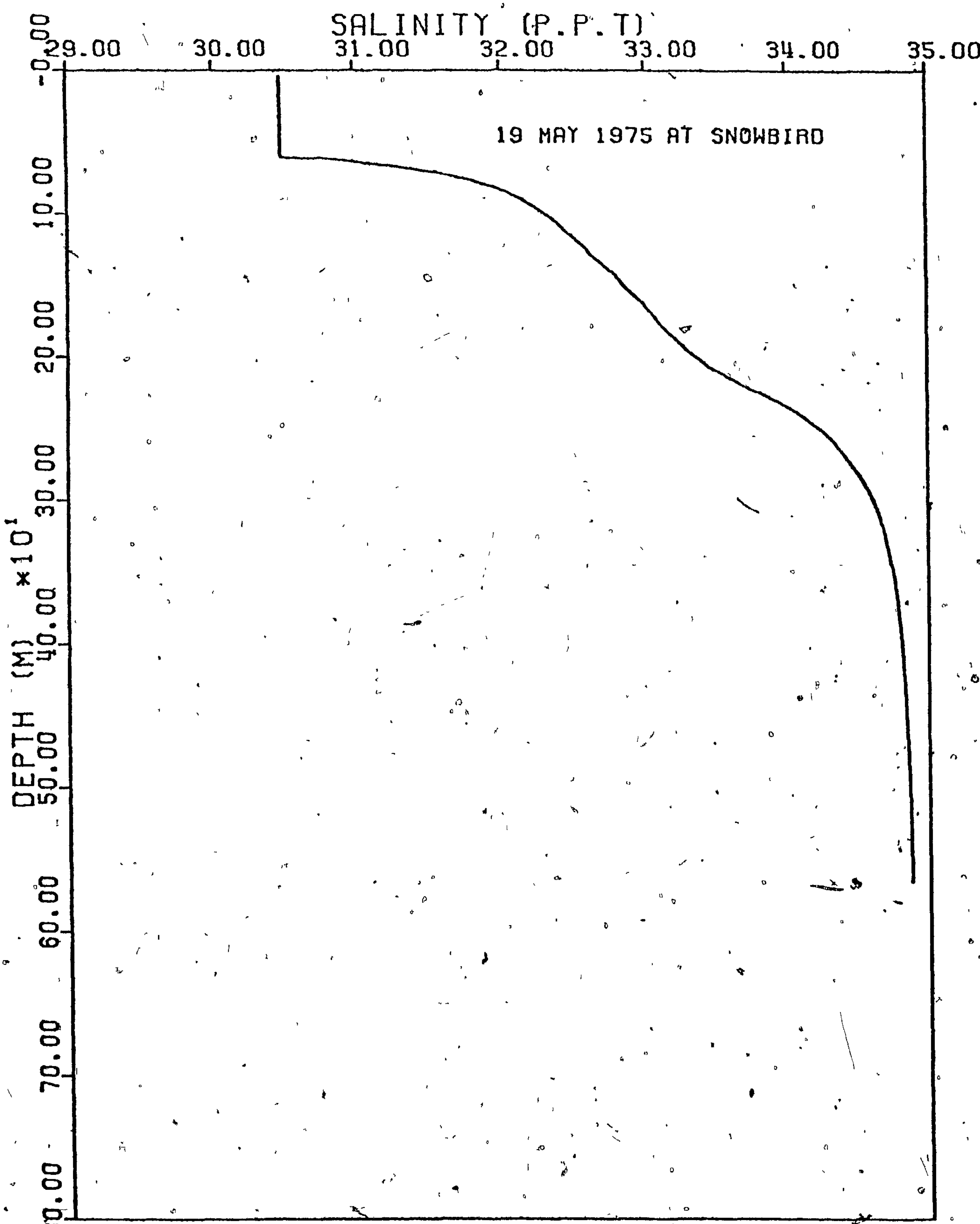

Fig 5,11 b Salinity profile showing step structure.

STEP STRUCTURE SB 007 19 MAY 75

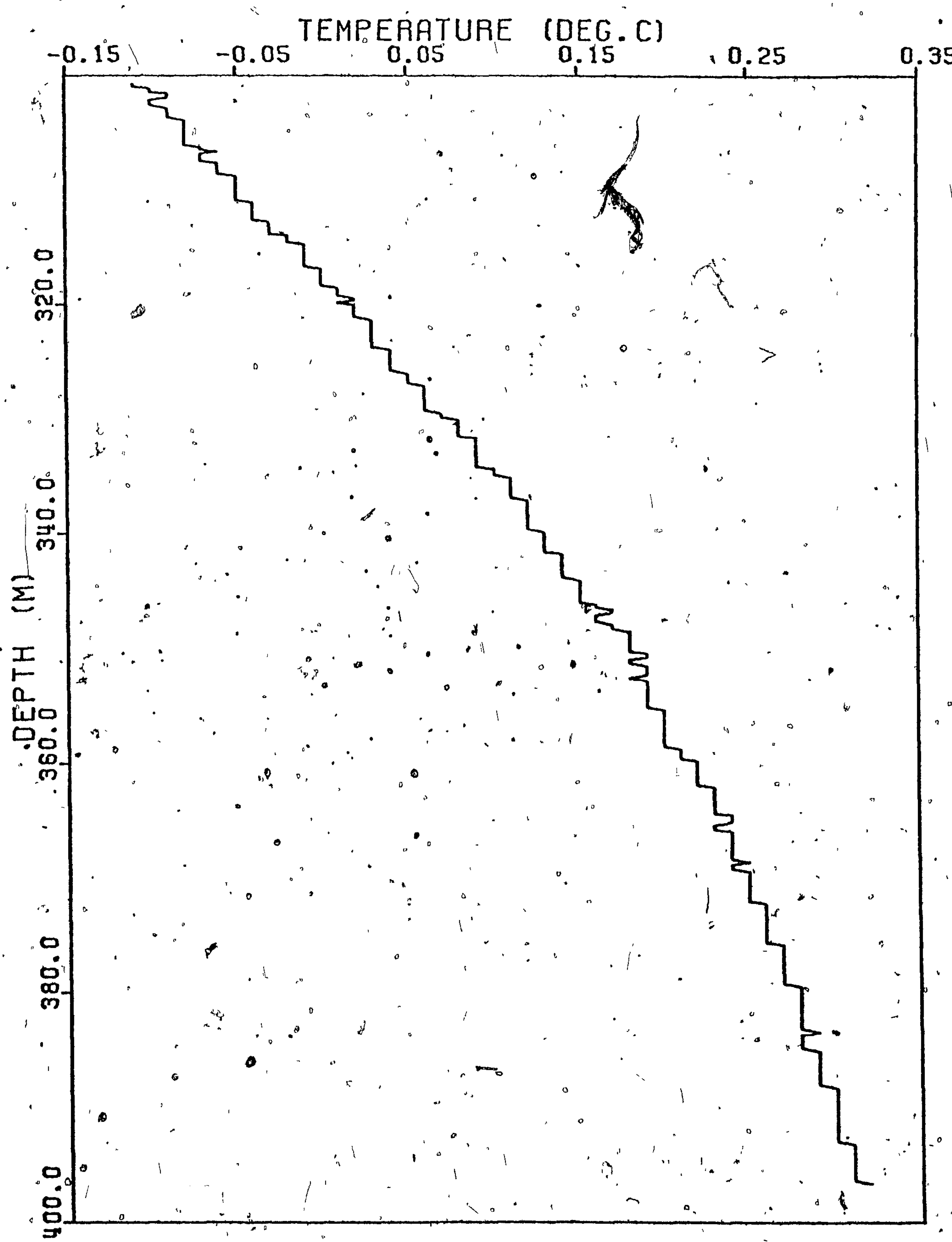

Fig 5.12 a Temperature step structure.

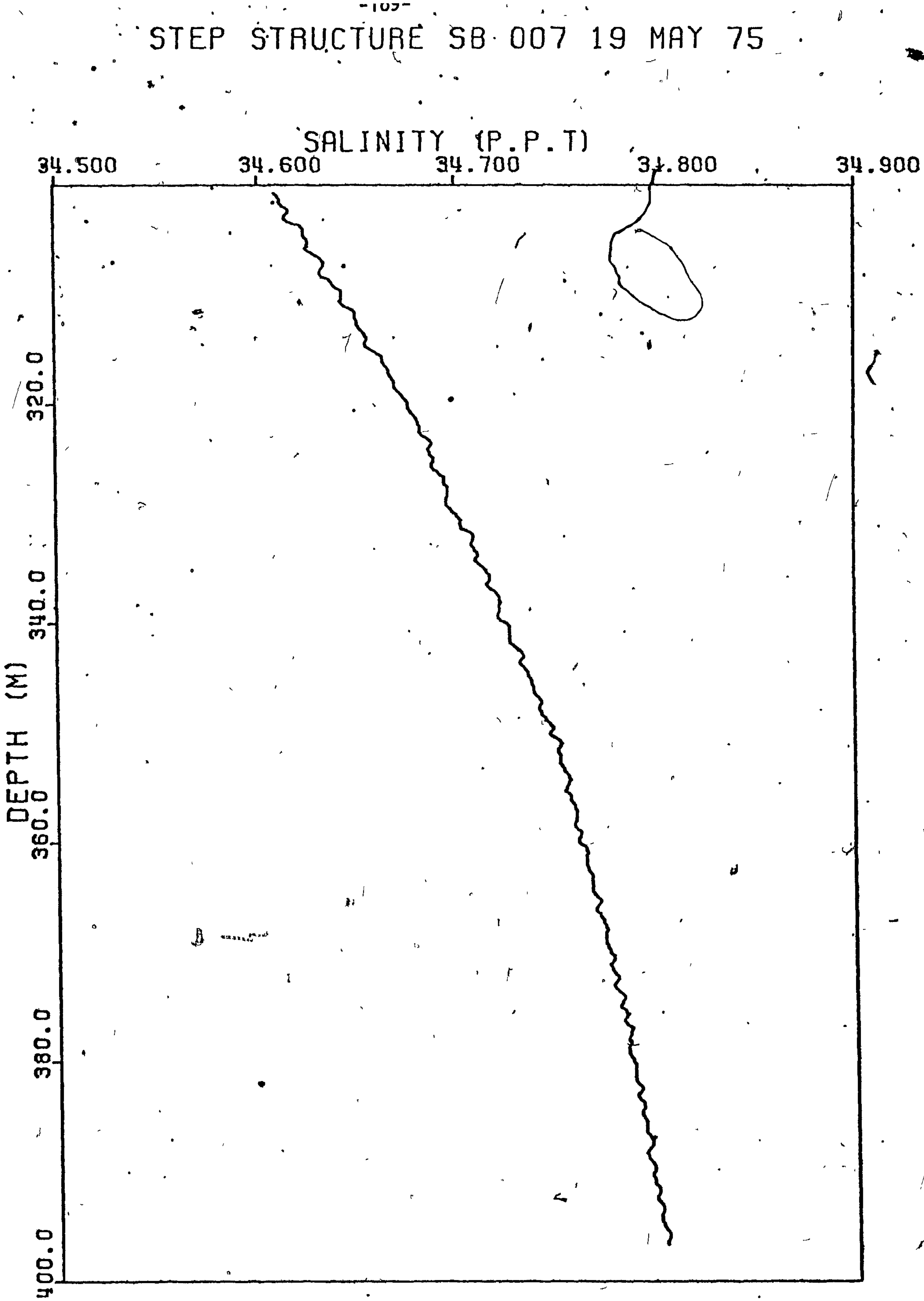

Fig 5.12 b Salinity step structure.

Fig. 5.12 (a,b) show this area expanded. The step-like nature of the salinity profile is clearly delineated in this figure. The temperature profile is less erratic than the salinity because of the resolution of the digitization used in making this plot. There is a great coherency between the temperature and salinity profiles.

As was pointed out earlier, the density of the Arctic waters is largely a function of the salinity with temperature serving as a tracer of different water masses. The density profile thus resembles the salinity trace and has similar steps between the 300 and 400m depth. These steps were observed at Camps Snow Bird and Caribou and at various times of the year. Again for brevity only a representative sample has been shown.

The space scale of the AIDJEX array is important in the discussion of the step structure. Since the AIDJEX scale (100 km) precludes any coherent measurement on the step structure, the discussion is based largely on data at individual camps. The steps were observed, for instance in May 75, at both Snow Bird and Caribou. The camps at this time were about 120 km or so apart, and thus it is difficult to say if these steps have a horizontal scale of the order of 100 km.

From Fig. 5.12 and other similar figures (not presented) we see that the step structure has an approximately vertical step size of 3m (with some small variations but not systematic ones, e.g. increasing with depth). The temperature and salinity steps are 0.02°C and 0.025 $^{0}/oo$ respectively. There are variations in these temperature and salinity steps but generally the figures presented are typical of the step structure. Several steps are observed in the salinity profiles. The steps appear to be uniform in size with depth and persist for long periods of time. No time analysis has been performed yet on these steps to see the seasonal and/or shorter term changes.

The step sizes (for temperature and salinity) are within the resolution and relative accuracy of the model 9040 sensor, as discussed in chapter 3.

There is a striking similarily between the step sizes and depth at stations Caribou and Snow Bird for the same time period. The lack of more data at intermediate points between the two camps (125 km apart) prevents us from making any statement about the horizontal size of these steps. It is conceivable that the steps are only 10-20 km in extent. It is suggested by hydrodynamical studies that these layers are stable and coherent to this extent (Hunkins - symposium talk on the Sea Ice process and model, Seattle 1977). Johannessen and Lee (1974), in their analysis postulate the step extent to about 25 nautical miles (40 km) in the Mediterranean Sea. It is also possible that these steps are coherent throughout the 125 km distance between Snow Bird and Caribou. An analysis of the Blue Fox and Big Bear data for this time period could show if this hypothesis has validity. The lack of this data at the McGill data bank prevents such calculation. Analysis of these data might provide a clue to the horizontal extent of these steps in the Beaufort Sea.

Turner (1967) suggested that layered structures observed west of Gibralter might be caused by salt-fingering, which is a double-diffusive process involving both temperature and salinity. In a water column where density increases with depth but where the contribution to density from salinity (say) decreases with depth, vertical mixing can be generated across the salinity gradients. This type of mixing is called salt-fingering. Salt-fingers are thin columns of brine separated from one another by rising columns of less salty water. This is the type of mixing that might be occurring at depths of 300-400m in the Beaufort Sea.

The circulation in these depths is weak. The weak circulation might be another controlling factor for the layer formation and existence. If the salt fingering is not the process for the formation of these layers, it is possible that the formation of the layers is connected with the slow movement of the Atlantic water over the Arctic bottom water and thus mixing at these depths. Again because of the large space scale of our measurements, we can not say much about the generation, dissipation and regeneration of these layers.

Chapter 6 INTERNAL WAVES AND MIXED LAYER VARIATIONS

6.1 Internal Waves

At the base of the mixed layer there is a sharp gradient in the temperature and salinity fields. The steepness of this slope can be seen in Fig. 1.5, 1.6, 1.7 of Chap. 1, for example. Between the daily deep ocean casts, the STD was moored in this thermo-halocline to observe the presence of internal waves. Because of the density stratification in this upper part of the Arctic Ocean, the movement of pressure ridge keels through the mixed layer can create internal waves in the vicinity of the pycnocline. These waves transport energy away from the keels and thereby generate drag on the ice.

Consider the upper part of the ocean top 75m or so, as a two layer system, the top layer being the mixed layer over the denser water from the Pacific. Looking at the motion of an element of fluid displaced by an amount Z vertically from equilibrium, the equation of motion for this parcel becomes

$$\frac{\partial^2 Z}{\partial t^2} = \left(\frac{g}{\bar{\rho}} \frac{\partial \rho}{\partial z}\right) Z$$

where $\left(\frac{\partial \rho}{\partial z}\right)$ is the density gradient in which the parcel moves with $\bar{\rho}$ the mean density and g the acceleration due to gravity. Z and t are displacement from equilibrium and time respectively. The solution of this equation is the oscillatory motion with a frequency N. This frequency, N, is defined as

$$N^2 = -\frac{g}{\bar{\rho}}\left(\frac{\partial \rho}{\partial z}\right)$$

and is called the Brunt-Väisälä frequency. Thus the parcel of water, if displaced, will oscillate with this period in the absence of other restoring forces, i.e. buoyancy is the only restoring force. This represents the lower limit on the frequency.

Vorticity ($\nabla \times \bar{u}$) is created whenever a non homogeneous fluid is displaced from a stratification in which ∇p and $\nabla \rho$ are parallel. Displacement of density surfaces away from the horizontal will produce vorticity (Fig. 6.1). This will oscillate in magnitude and direction in stable stratification. Internal waves are rotational phenomena.

Richardson number, Ri, is introduced as a measure of the relative sizes of buoyancy and shear forces.

$$Ri = \frac{\text{buoyancy}}{\text{shear}} = \frac{-g/\rho \, \frac{\partial \rho}{\partial z}}{\left(\frac{\partial u}{\partial z}\right)^2} = \frac{N^2}{\left(\frac{\partial u}{\partial z}\right)^2},$$

The size of R_i tells us which force is dominant. Studies (Schlichting, 1968) show that for $Ri > 1/4$ the water column is stable and for $Ri < 0$ unstable, and overturning occurs. Thus we see, depending on the size of Ri, that the internal waves are important mechanisms for mixing of the water at the interface.

Fig. 6.2 shows a representative sample of the temperature, salinity and density (σ_t) variation as a function of time. The STD probe was moored at this time in the steepest part of the pycnocline at a depth of 58m. The section shown in hours 0730 - 0900z and 1215 - 1315z for the 06 July 75 (SB 103). We see a sustained duration of oscillation. The period of these oscillations is determined to be approximately 10 minutes (600 s). The temperature excursions are 0.38°C, for salinity it is 0.55 ^{o}/oo and the corresponding σ_t change is 0.55 σ_t units. The amplitude of the wave is determined to be 6m (Fig. 6.3).

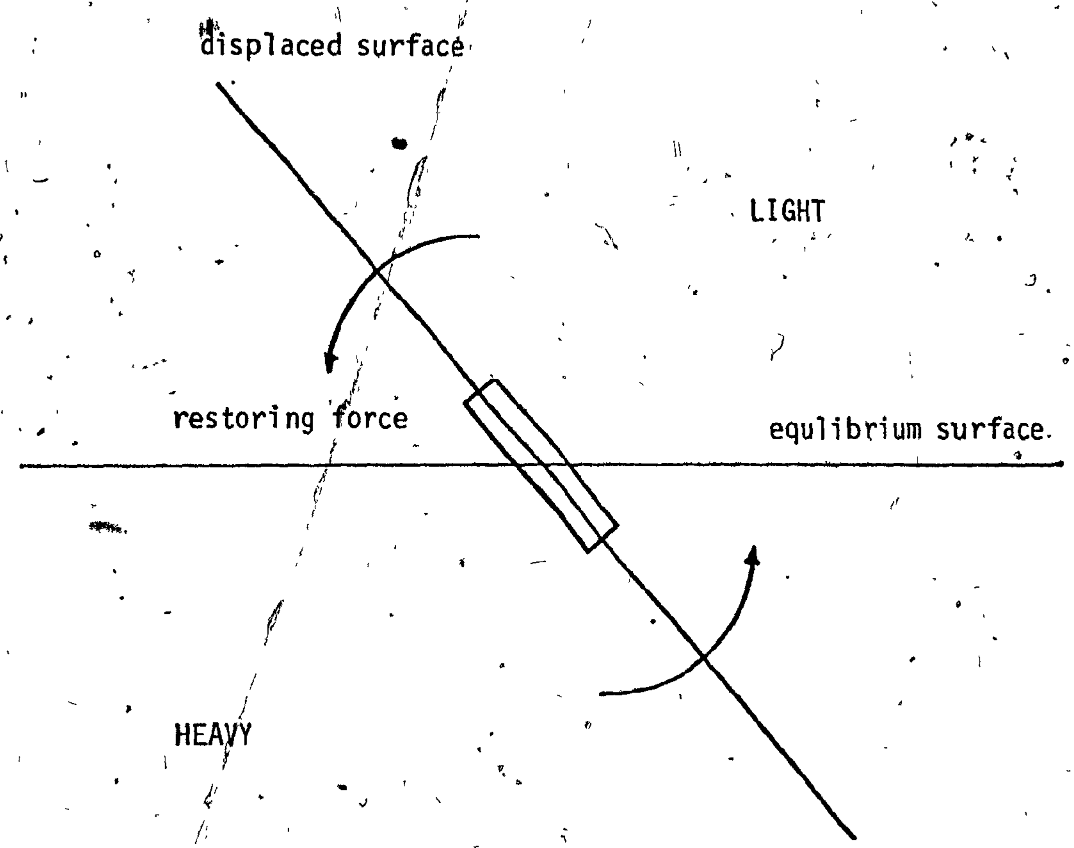

Fig 6.1 Restoring forces for a parcel of displaced water.

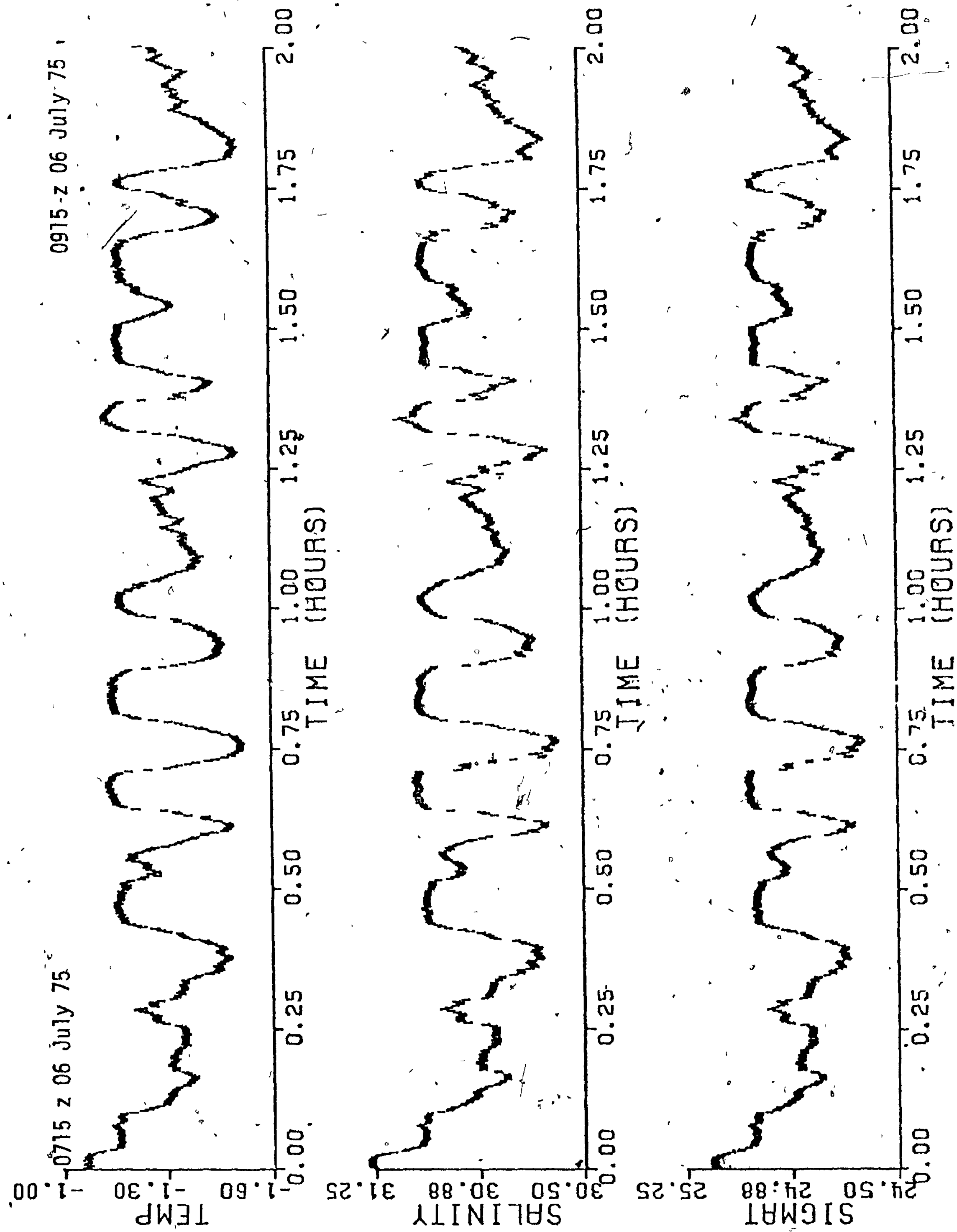

Fig 6.2 a Time series plot of temperature,salinity and sigma-t.
0715 to 0915 z 06 july 1975 at Snow Bird.

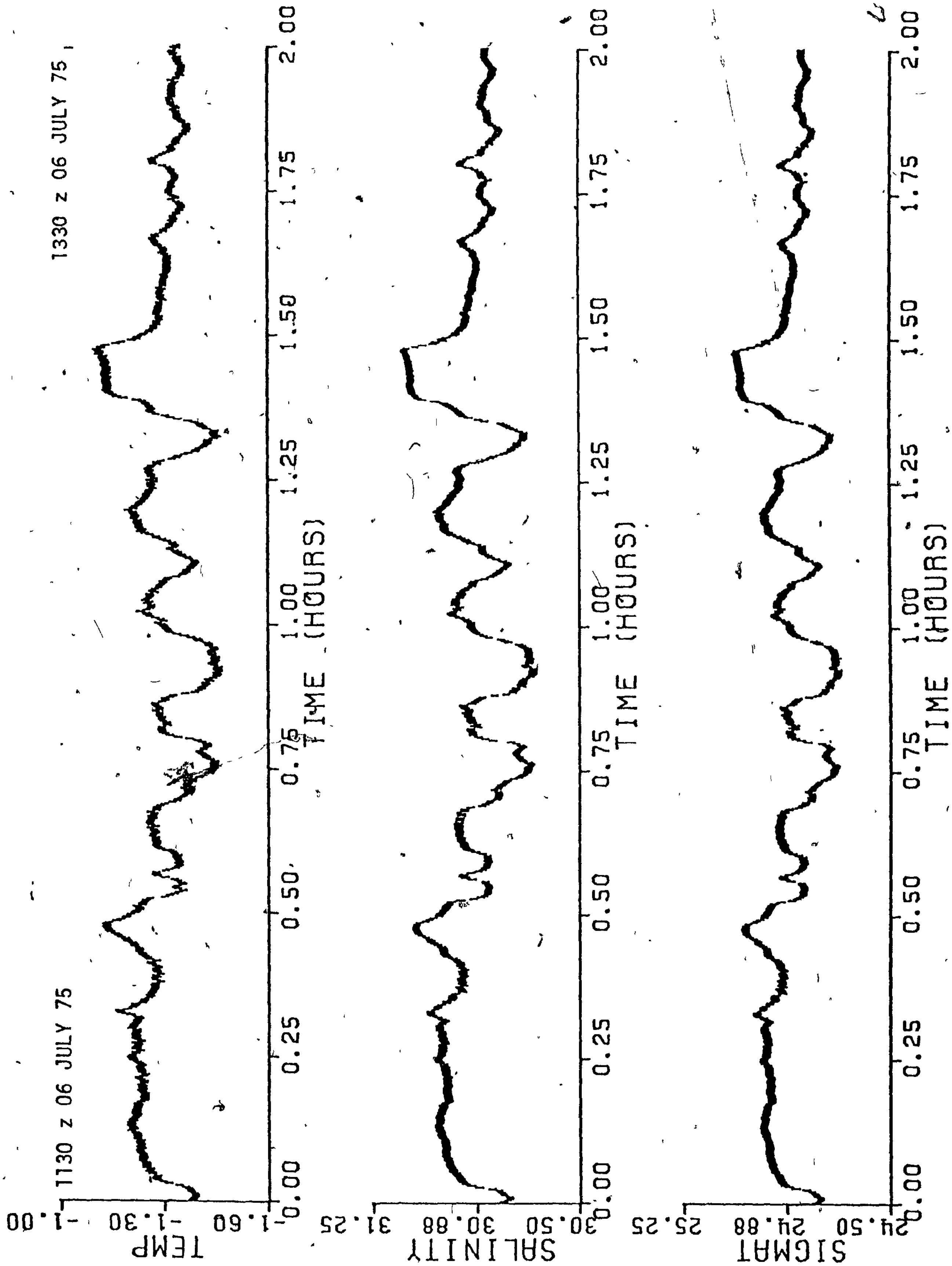

Fig 6.2 b   Time series plot of temperature, salinity and sigma t.
1130 z to 1330 z 06 JULY 75 at Snow Bird

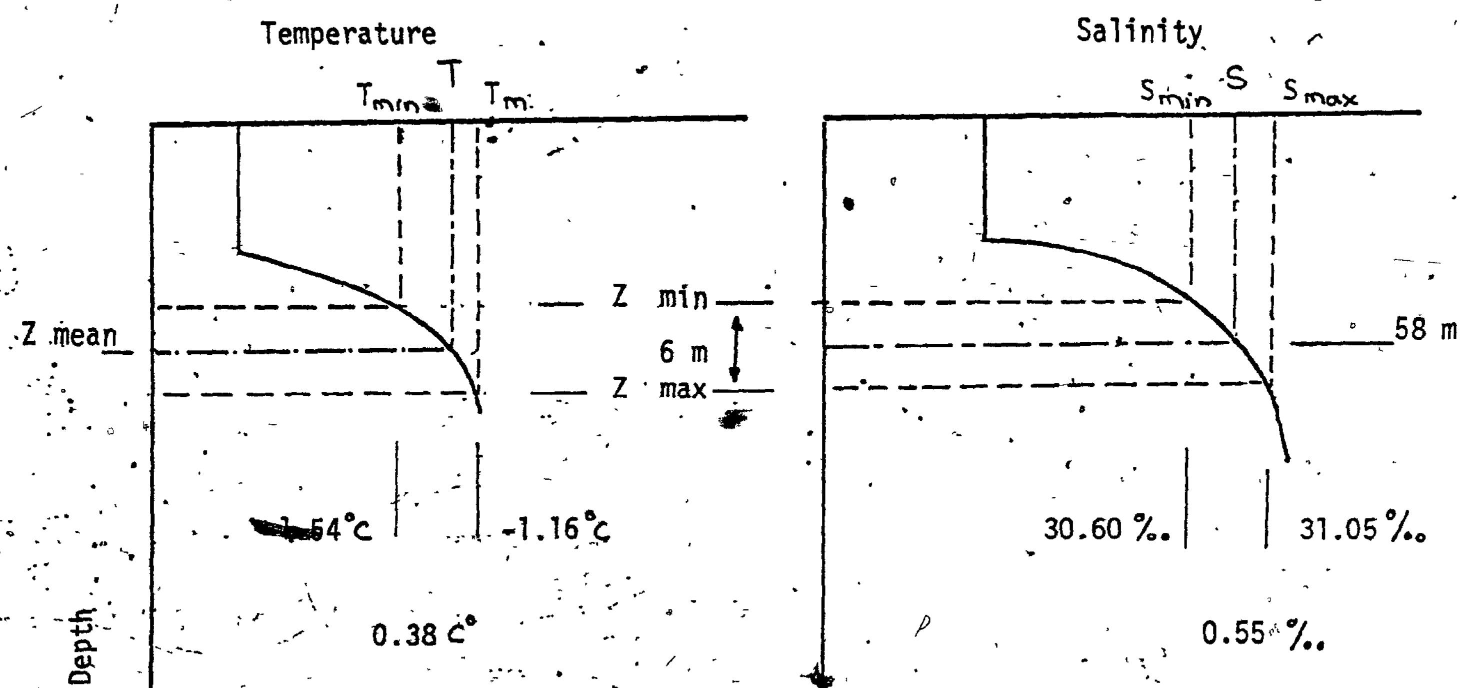

Fig 6.3 Determination of the amplitude of internal wave.

The mean depth is 58m. Yearsley (1966) found waves (internal) with amplitudes as big as 10m at depths of 60m.

With these figures, the Brunt-Vaisaila frequency is calculated to (at 60m) be 9.52×10^{-3} sec^{-1} or a period of 105s. McPhee (1975) calculated (at 60m) this period to be 50 s for the 1972 AIDJEX. An inspection of the PCM profile for approximately this time, shows a velocity shear of about 1.5 cm/s per m at this depth. This yields a Ri = 0.5 (slightly > 1/4) indicating that turbulence induced by shearing might be present.

Very little reduction of the time series data has been performed as the main stress has been to analyse the profiles and claculate geostrophic currents. Of the limited figures available, the internal waves occur at these pycnocline depths and have periods and temperature and salinity extrusions as in the representative sample.

Rigby (1974), with the aid of theoretical model, examines the principal factors that affect the wave drag on an individual keel and attempts to define the condition under which wave drag could be greater than form drag. Hunkins (1974c), on the other hand, uses an experimental approach to estimate wave drag on a particular keel and then applies these results to large scale estimates of the water stress. He concludes that from the conditions that are typical for the Arctic Ocean, internal wave drag is about 10% of the form drag and 20% of the skin friction. Rigby, inferring from Arya's (1973) calculations, states that skin friction is a major part of the water stress. The difference between the local wave drag predictions of Hunkins and Rigby appear to arise primarily from the different assumptions regarding the depth at which internal waves are generated and not from the different approach.

6.2 Mixed Layer Variation

The behaviour of the upper mixed layer was one of the principal objectives of the AIDJEX Oceanographic programme. This layer of nearly homogeneous water extends, during winter, from just below the ice to depths of 23 to 60m. During the summer it disappears as the upper layers become strongly stratified. The aim of the AIDJEX program was to measure as accurately as possible the forces acting on drifting ice including the frictional drag of the ocean. The degree of homogeniety or stratification has an important effect on the water drag. A well mixed upper layer results in more drag than a stratified layer.

The disturbance of this mixed layer by the movement of a keel from the ice cover will produce internal waves (like a boat's keel produces internal waves when it is caught in the "deal water" of the Norwegian fjords). The internal waves can be produced because of this two layered system in the upper ocean.

An example of the throughly mixed layer appearing in water is shown in Figure 6.4. Here temperature and salinity are both uniform, within the resolution of the instrument, from just below the ice to a depth of 61m. The mixing is apparently the result of brine convection. As the ice freezes, heavy brine is released which sinks throughly stirring the upper layer. At times the mixed layer may consist of two or more homogeneous layers. The upper most layer may have been produced by local freezing in a recently open lead. Figure 6.5 shows two layers in the upper mixed layer. Results from the 1975-76 experiment also show that these steps are not coherent over the 100km array of the AIDJEX manned camps. Fluid dynamic arguements suggest that such steps are limited to

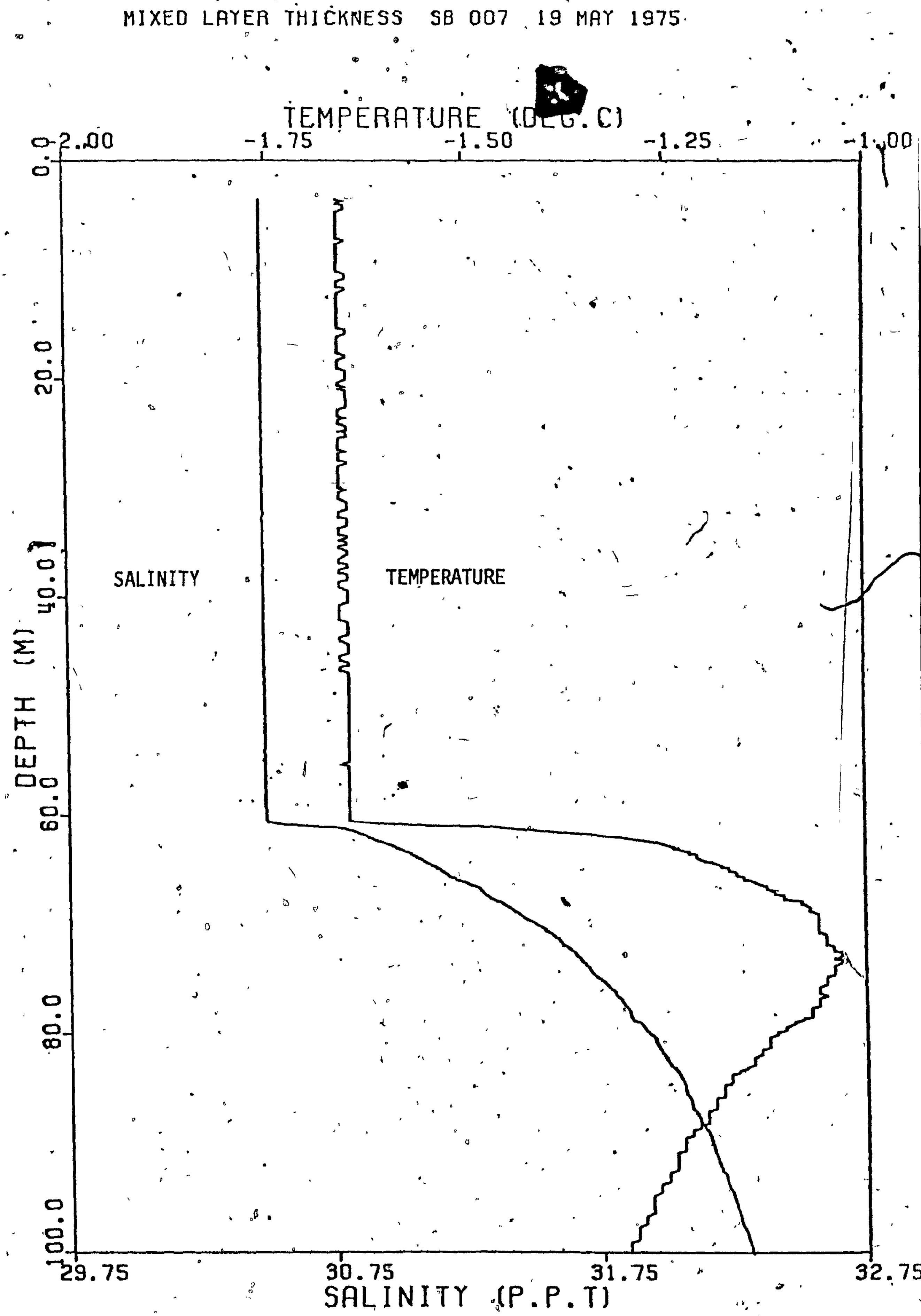

Fig 6.4 Throughly mixed layer , 19 May 75 at Snow Bird.

MIXED LAYER THICKNESS SB 080 24 JUN 1975

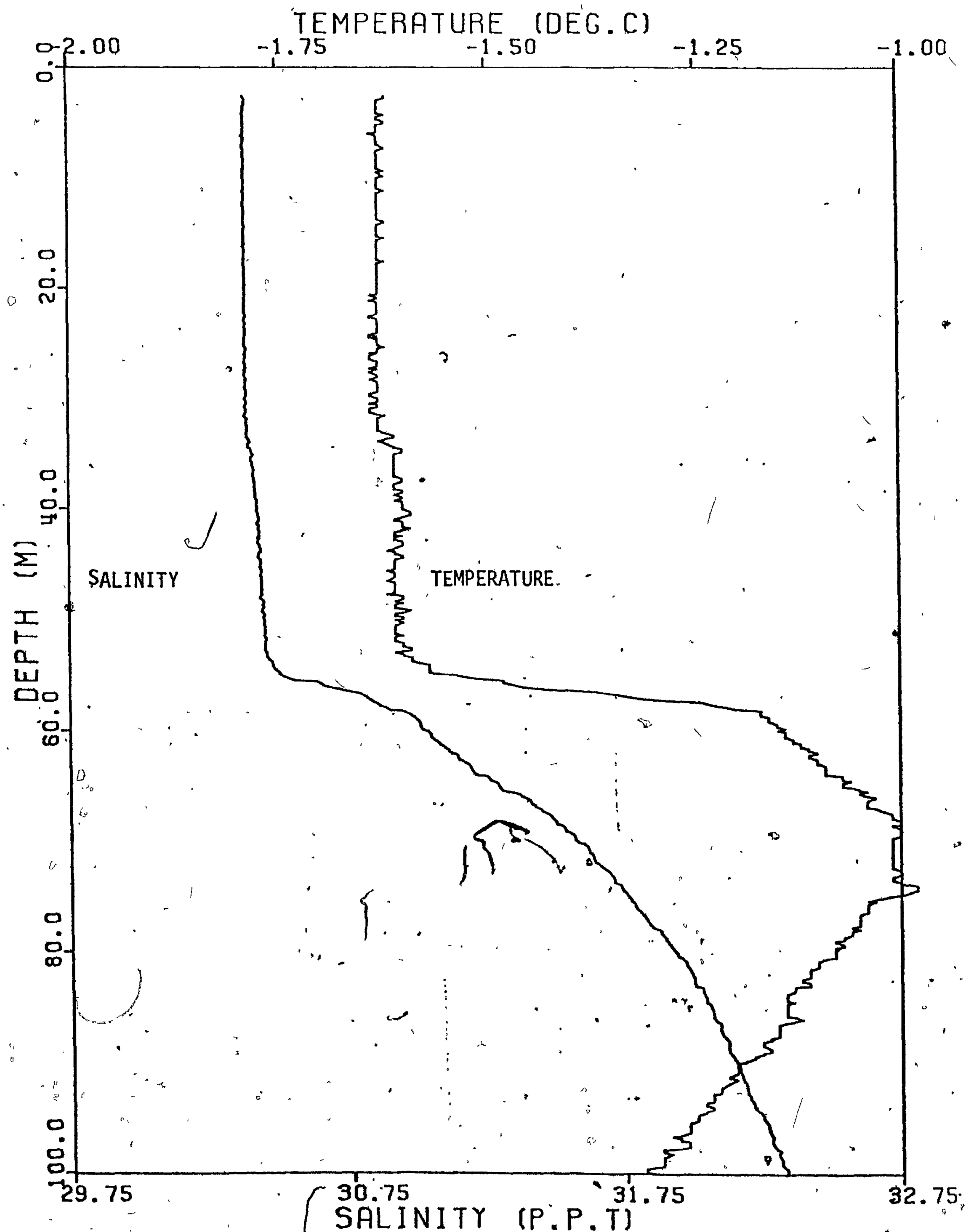

Fig 6.5 Mixed layer showing two layers , 24 Jun 75 at Snow Bird.

a horizontal extent of about 2km. Their horizontal spread is limited to approximately the Rossby radius of deformation, which is small for such small density differences as these steps in the mixed layer (Stommel, 1969).

There are two principle stirring mechanism by which a mixed layer may be formed. Gravitational convection and mechanical stirring. Although the gravitational convection due to brine extrusion during freezing is usually considered most important, mechanical stirring by ice drift must also play some part. Previous studies have not shown the relative importance of the two regimes (Solomon, 1973). The two mechanism should operate on clearly separate horizontal scales with mechanical mixing by ice drift occuring over the 1000km scale of the wind field and brine convection occuring over the 1-10km scale of the open lead. Mechanical stirring is probably dominant during the summer, a period of large ice velocities. Convection plays a significant role during the winter when the open water freezes and produces vast quantities of brine. The presence of internal waves, with its associated vortiticy, could be another essential component in the mixing and deepening of the mixed layer.

On the 20th of April 76, the thickness of the mixed layer increased from 38m to 42m in a time of about 12 hours at SB. It is inconceivable that wind mixing could have caused such a sharp increase in the mixed layer depth in such short a time. Wind mixing also operates on large space scale and it also appears unlikely that this deepening is wide spread. Brine convection is a possible explanation of such a deepening.

Although there is no evidence of a lead opening near Snow Bird at this time, it seems likely that a lead did open and the deepening of the mixed layer is caused by the rapid expulsion of salt as the open water quickly froze. This excess brine caused a local increase in the mixed layer thickness.

During the summer the upper layer has a nearly continuous steep gradient in salinity and temperature beginning at the base of the ice. The disappearance of the mixed layer and the resulting strongly stratified column is shown in Figure 6.6. The stratification is evidently caused by the fresh water from the melting ice and snow which flows down through cracks and holes in the ice. Since the fresh water is lighter than the sea water, it remains on top, stratifying the surface layer. At times the stratification may be less continuous as shown in Figure 6.7. Figures 6.6 and 6.7 are from oceanographic casts taken on the same date but on stations over 100 km apart. The two figures show the extent of horizontal variability that is observed in the Arctic. The amount of snow cover available for run off and the number of cracks available for drainage probably account for this variability.

By the summer's end, a shallow mixed layer, of about 25 m in depth begins to develop again. Figure 6.8 shows the condition by middle September. At this time of the year, areas of open water are beginning to freeze and brine convection commences again. Throughout the winter the mixed layer continues to deepen, reaching a depth of about 35 m by mid-January (Figure 6.9). The process continues as the layer deepens to 40-50 m by April. Then the cycle repeats with the onset of summer (Figure 6.10). Few summertime observations were available on the upper layer

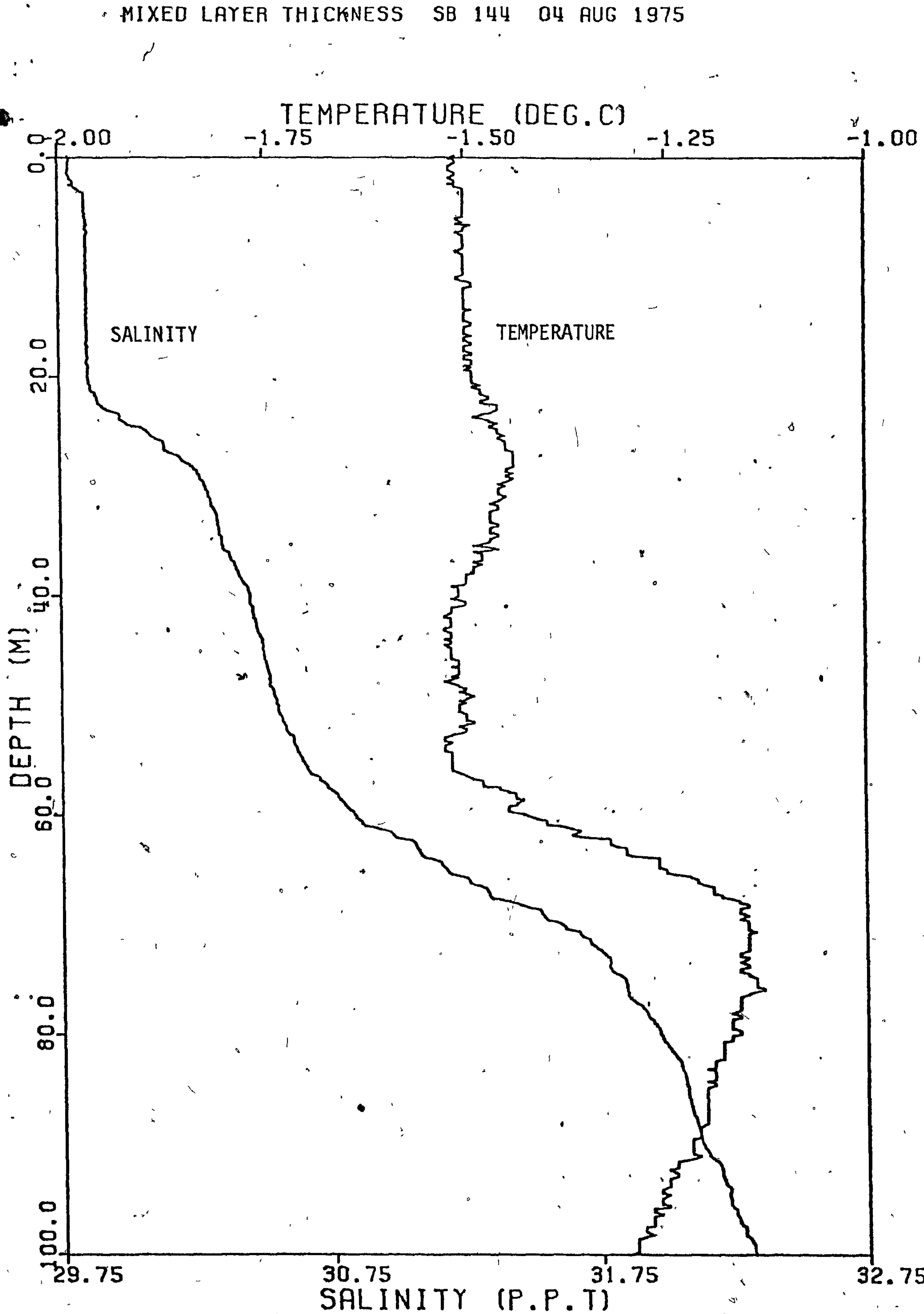

Fig 6.6 Change of mixed layer to stratified column. 04 Aug 75 at Snow Bird.

MIXED LAYER THICKNESS CB 154 04 AUG 1975

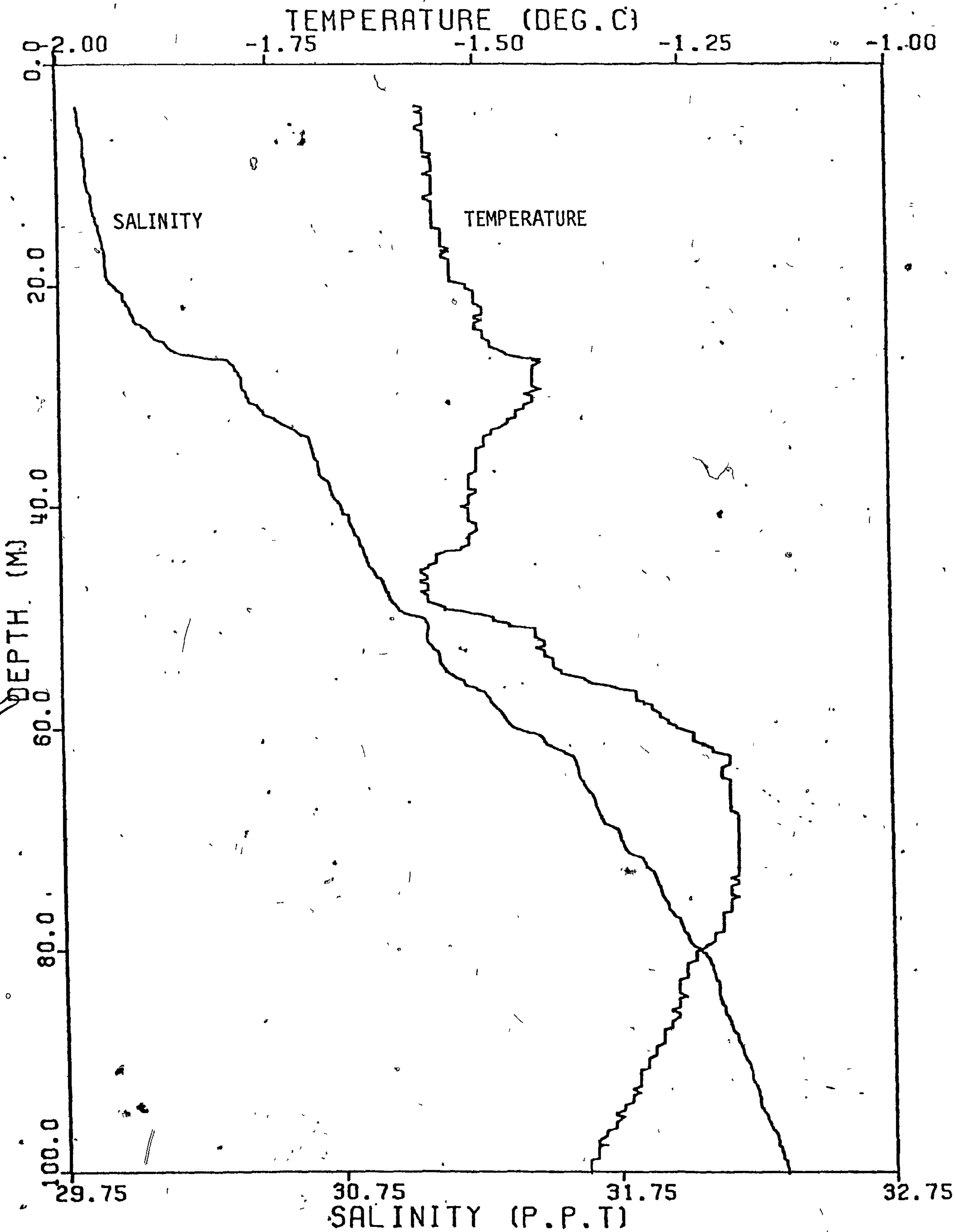

Fig 6.7 Spacial variability in upper layer. 04 Aug 75 at Caribou.

MIXED LAYER THICKNESS SB 224 14 SEP 1975

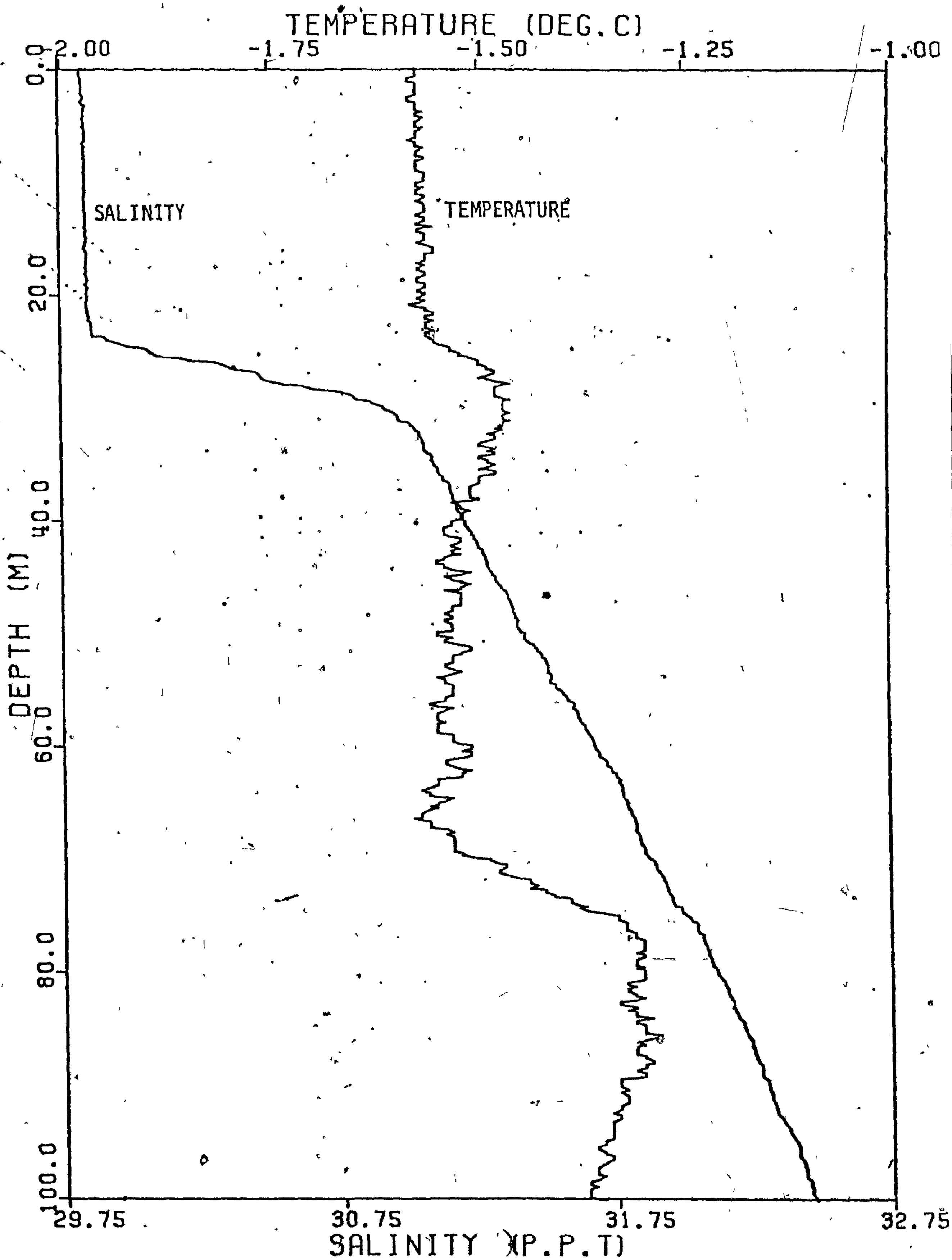

Fig 6.8 Shallow mixed layer in the fall, 14 Sep 75 at Snow Bird.

MIXED LAYER THICKNESS CB 514 14 JAN 1976

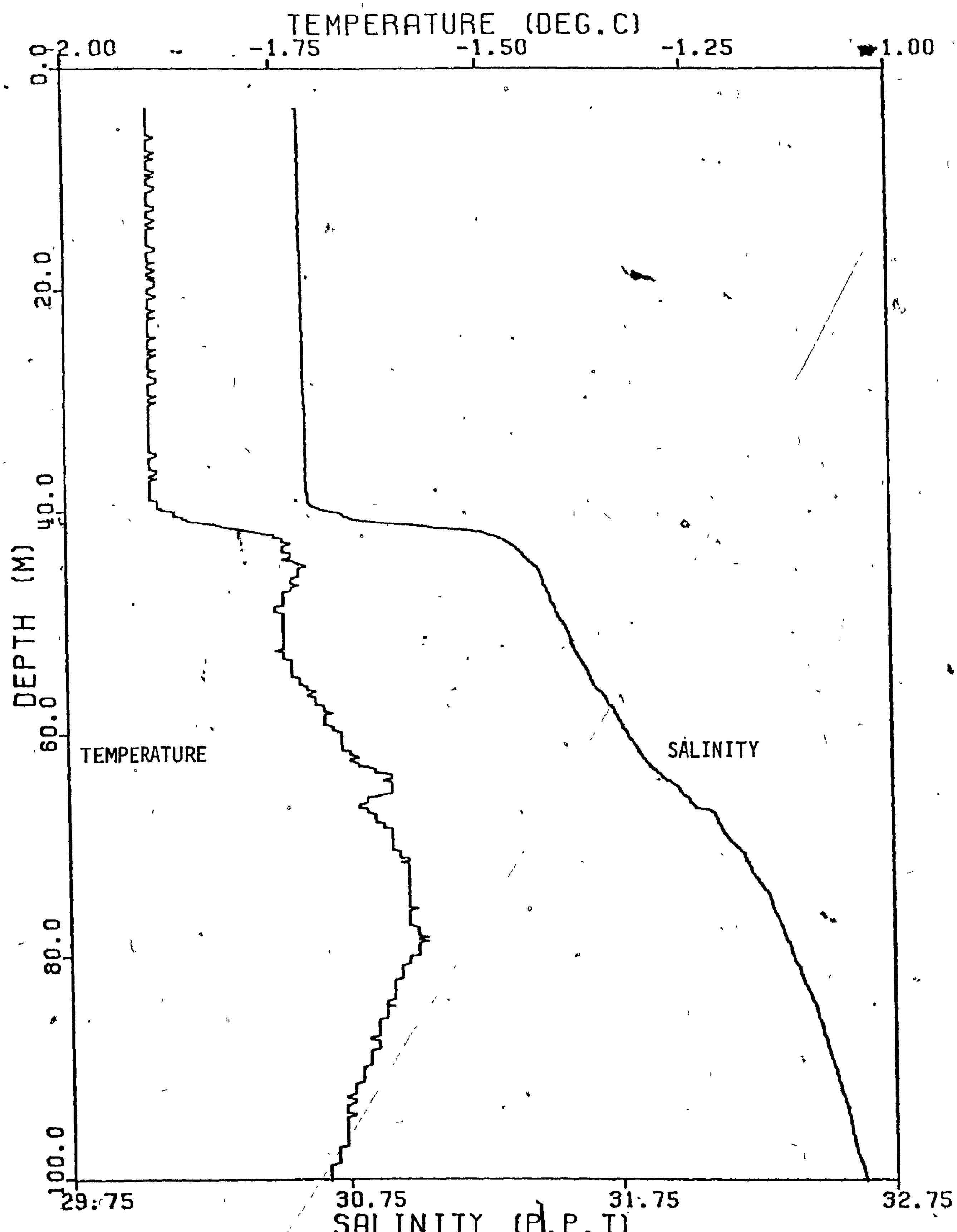

Fig 6.9 Deepening mixed layer by January, 14 Jan 76 at Caribou.

MIXED LAYER THICKNESS SB 604 20 APL 1976

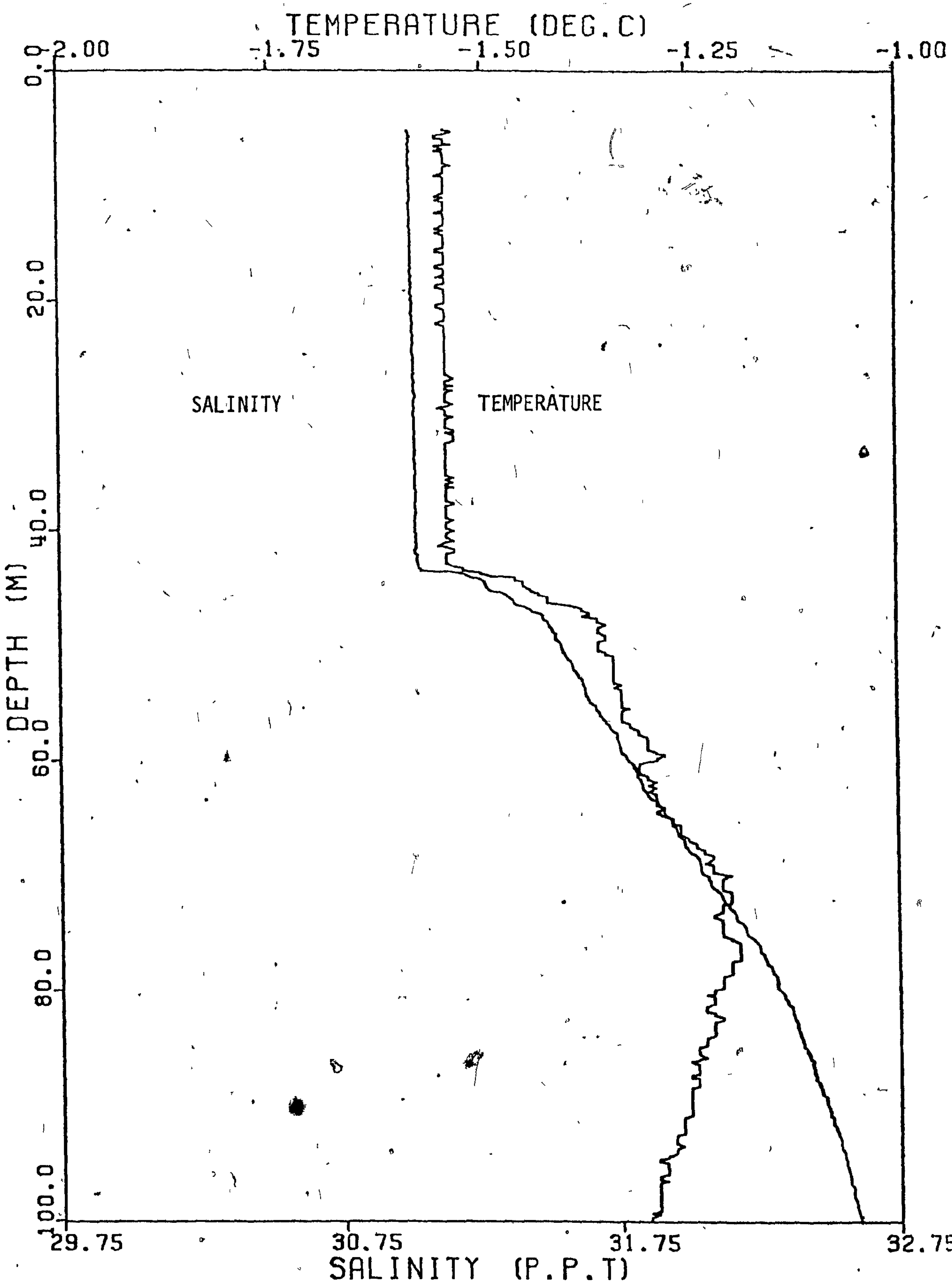

Fig 6.10 Return of the deep mixed layer by spring, 20 Apl 76 at Snow Bird.

prior to the '75 experiment and thus the data should shed some light on the mixing process and the drag values in the summer months.

Figure 6.11 shows the thickness of the mixed layer as a function of time. Again we evoke the idea that the density of the arctic water column is largely a function of salinity. Thus, temperature can increase with increasing density in the pycnocline and serves as a tracer for salinity differences. In the pycnocline it was found that the top of the thermocline is easier to distinguish than the top of the halocline. For this reason, the abrupt change in the temperature is taken as the depth of the mixed layer. From this figure the seasonal changes in the mixed layer thickness is easily seen. The thick winter mixed layer gives way to the strongly stratified water column as the fresh water is input from the melting snow. With the approach of fall and the colder air temperature, the ice freezes and releases brine into the upper layer. By advection and perhaps also by mechanical mixing, the upper mixed layer starts to form and deepen. The deepening continues with internal wave activity perhaps playing a role in the mixing at the bottom of the layer. By mid-winter, the mixed layer reaches an appreciable thickness. At the end of the AIDJEX exploration on the 20 of April, the mixed layer at Snow Bird was 44 m. The process repeats with the summer. The data is from the daily STD casts that were made at the manned camps, Snow Bird and Caribou.

(Analysis of this mixed layer thickness can lead to a statement about the relative importance of the two mixing processes. Also, there are times when the mixed layer shallows and then deepens abruptly. This and the effects of storms on the mixed layer thickness can also be studied by

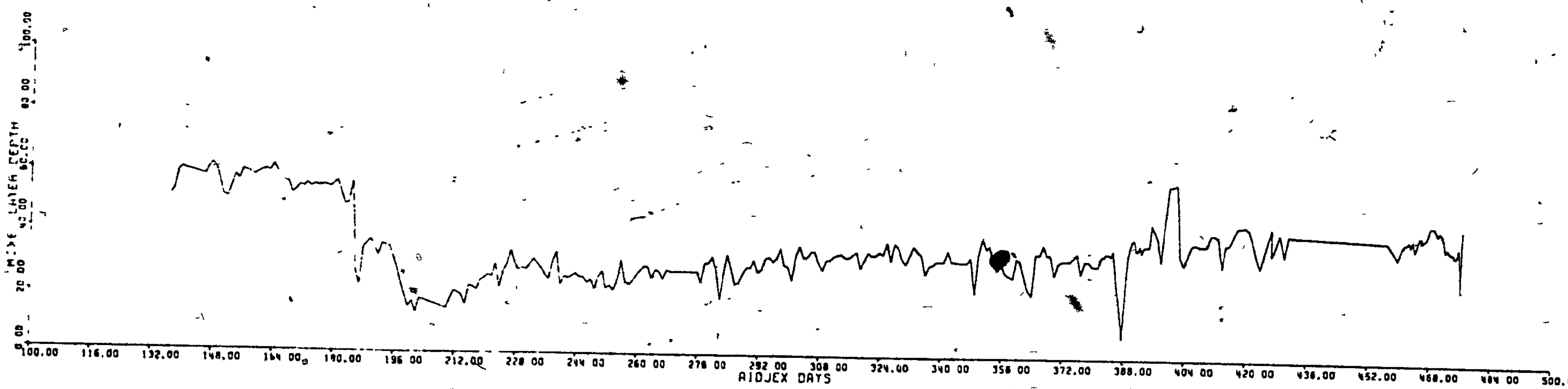

Fig 6.11 Change of the mixed layer thickness at Snow Bird from day 132 to 484.

combining the meterological and oceanographic data. This and other short term fluctuations in the mixed layer thickness remain to be examined. A detailed analysis could lead to insights about the mixing processes and regional effects of storms and eddies.)

Chapter 7 SUMMARY AND CONCLUSION

The data from the AIDJEX main experiment were examined and mesoscale flow features were investigated. The summary of the results and conclusions is given below.

A) Dynamic computations

The geostrophic current was calculated from the measured density fields at two camps in the AIDJEX array. These currents and mass transports from these currents were calculated and compared with the actual measured currents. In comparing the results, only the component of the measured current parallel to the isobaric surfaces is considered. This is done because we have only two camps to calculate the geostrophic currents. In calculating the geostrophic currents (absolute) a layer of no motion at 750 m was assumed. Due to the lack of any other reference level, this was chosen, being the deepest depth of the cast. The mass transport calculated from the geostrophic current are smaller than the mass transport from the actual current meter data. The mass transport in winter (October-November) is much larger than that of summer (June). This conclusion might not be a general trend as the data for deep winter (December 1975-April 1976) has not been investigated. The effect of a strong wind on the mass transport was observed. The mass transport increased with time as the winds continued and lasted for 4 or 5 days after the subsidence of the wind. The trend in the mass transport (from calculated currents) is not as smooth as that from measured currents but, the general pattern is consistent.

The calculations were performed for a large part of the AIDJEX year but only a few of the results are presented as a representative sample.

B) Baroclinic eddies

Several eddies were detected at Snow Bird and the analysis of one of them is presented here. The geostrophic calculations were performed to obtain the eddy currents. The shape, size and depth of the calculated currents is in good agreement with the measured currents. The size of the core is estimated to be about 3-5 km. Energy calculations show that a significant portion of the total kinetic energy is in these eddies. Possible mechanisms of eddy formation are discussed. The eddy presented is anticyclonic and the warping of the isohaline and isotemp surfaces is shown. The possible origin of the eddy water is postulated to be from the Pacific water shear zone near the Chukchi Sea.

C) Step structure

In depths of 300 to 400 m, step like features were observed at the manned camps. The vertical extent of these steps is about 3m and the salinity step is about 0.025%. Analysis to get the horizontal extent and coherency of these features is precluded by the scales (space) of the AIDJEX array.

D) Internal wave

Internal wave activity was investigated in the time series data at the pycnocline. The mean period of 10 minutes was determined for these waves with an amplitude of 6m. These waves last for about 1½ hours at Snow Bird. They are an important mechanism for mixing and deepening the mixed layer.

E) Mixed layer

The depth of the mixed layer changes with time and an analysis is done to show the variation. The smaller time scale changes have not been investigated, in detail, as yet. The long term change is shown. The mixed layer emerges in the fall from the highly stratified summer condition. The layer thickens with the approaching winter reaching its maximum size by spring. With the onset of the summer melt, two or more layers form and we return again to a state of stratification as a result of mixing.

With the data from the other two manned camps we should be able to get the total horizontal current field in the Beaufort Sea gyre. Analysis is continuing on internal waves and on small scale changes to the mixed layer (with reference to storms).

BIBLIOGRAPHY

Amos, A.F. 1973. The deep STD station: Techniques for making surface to bottom STD profiles and some examples of bottom microstructure. Reprint from Proceeding, Second Plessey Environmental System S/T/D Conference and Workshop. Jan. 24-26, 1973, San Diego, California. pp.87-101.

Amos, A.F., A.L. Gordon and E.D. Schneider. 1971. Water masses and Circulation patterns in the region of the Blake-Bahama outer ridge. Deep Sea Research. Vol.18: pp.145-165.

Arya, S.P.S. 1973. Contribution of form drag on pressure ridge to the air stress on the Arctic Ocean. Journal of Geophysical Research. 78: pp.7092-7099.

Badgley, F.I. 1967. Heat budget at the surface of the Arctic Ocean. Contribution No. 121. Department of Atmospheric Sciences. University of Washington, Seattle, Washington.

Belakov, L.N. 1972. Triggering mechanism of deep episodic currents in the Arctic Basin (in Russian). Problemy arctitk i antarkitki. 39: pp.25-32.

Bernstein, R. 1971. Observations of current in the Arctic Ocean. Unpublished doctoral dissertation, Columbia University.

Bjerknes, V. 1900. Das dynamische prinzip der zirkulation bewegung in der Atmosphäre. Meteorol. Z.

__________ and I. Sanchstörm. 1912. Dynamische Meteorologie und Hydrographie. Vol.I.

Bower, D.R. and J.R. Weber. 1978. Estimation of ocean tide from ice surface gravity observations. AIDJEX Bulletin No. 38: pp.151-157.

Brekhovskikh, L.M., K.N. Federov, L.M. Fomin, K.N. Koshlyakov, and A.D. Yampolsky. 1971. Large scale multi-buoy experiment in the tropical Atlantic. Deep Sea Research. Vol. 18: pp.1189-1206.

Brown, R.A. 1975. Planetary boundary layer models and parameters for AIDJEX 1975-76. AIDJEX Bulletin No. 29: pp.113-130.

Campbell, W.T. 1965. Wind driven circulation of ice and water in a polar ocean. Journal of Geophysical Research. Vol. 70, No. 14. pp.3279-3301.

Canadian Hydrographic Service. Chart #897.

Coachman, L.K. 1963. Water masses of the Arctic. In: Proceedings of the Arctic Basin Symposium, October, 1962. Washington, D.C. Arctic Institute of North America. pp. 143-172.

________. 1965. Physical oceanography of the Arctic Ocean. In: Arctic Drifting Stations. Coordinated by J.E. Sater. Proceedings of the Symposium held at Airlie Conference Centre. Warrenton, Va., April, 1966: pp. 255-280.

________ and Aagaard, K. 1974. Physical oceanography of Arctic and sub-Arctic seas. Geology and Oceanography of the Arctic Seas. Chapter 1. Springer, N.Y. pp. 1-72.

________ and Barnes, C.A. 1961. The contribution of the Bering Sea water to the Arctic Ocean. Arctic. No. 14: pp. 146-165.

________ and Barnes, C.A. 1962. Surface water in the Eurasian Basin of the Arctic Ocean. Arctic. No. 15: pp. 251-277.

________ and Barnes, C.A. 1963. The movement of the Atlantic water in the Arctic Basin. Arctic. No. 16: pp. 8-16.

Colony, R. and Pritchard, R.S. 1975. Intergration of elastic-plastic constitutive law. AIDJEX Bulletin No. 30. pp. 55-80.

Coon, M.D. 1977. A review of AIDJEX modeling. Symposium on Sea Ice Processes and Models. September, 1977. Seattle, Wa. pp. 40-55.

____, Maykut, G.A., Pritchard, R.S. and Thorndike, A.S. 1974. Modeling the pack-ice as an elastic-plastic material. AIDJEX Bulletin No. 29. pp. 1-106.

Dantzler, H.L. 1974. Dynamic salinity calibrations of continuous salinity/temperature/depth data. Deep Sea Research. Vol. 21. pp. 675-682.

Defant, A. 1941. Die absolute topographie der physikalischen meeresniveaus und der drukeflächen, sowie die wasserbewegungen in Atlantischen Ozean. "Meteor" werk 6(2). Lief. Berlin.

_____. 1961. Physical oceanography. Vol. 1. Pergamon Press. MacMillan Co.

DeLeeuw, M.M. 1967. New Canadian hydrography chart of the western Arctic Ocean north of 72°. Deep Sea Research. 14 (5). pp. 489-504.

Farmer, H.G. 1970. Long period time dependent motion in the polar ocean. Ph.D. thesis. University of Washington. 145 p.

Felzembaum, A.I. 1958. The theory of the steady drift of ice and the calculation of the long period mean drift in the central part of the Arctic Ocean. Problems of the North.2. pp. 13-44.

Fjeldstad, J.E. 1923. Litt om tidevandet i Nordishavet. Naturen, 47. p. 171.

Fletcher, J.O. 1968. Origin and early utilization of aircraft-supported drifting stations. In Arctic Drifting Stations.

Fomin, L.M. 1964. The dynamic method in oceanography. Elsevier Oceanography Series No. 2. Elsevier Scientific Publishing Co. Amsterdam-London-New York.

Forrester, W.D. 1967. Currents and geostrophic currents in the St. Lawrence estuary. Report B.I.O. 67-5. Bedford Institute of Oceanography. Dartmouth, N.S. Unpublished manuscript.

Galt, J.A. 1967. Current measurements in the Canadian Basin of the Arctic Ocean 1965. Tech. Report #184. University of Washington, Department of Oceanography.

_____. 1973. A numerical investigation of the Arctic Ocean dynamics. Journal of Physical Oceanography. Vol. 3. pp. 379-396.

Gill, A.E., Green, J.S.A. and A.J. Simmons. 1974. Energy partition in the large scale circulation and the production of mid-ocean eddies. Deep Sea Research. Vol. 21. pp. 499-528.

Gordienko, P. 1958. Arctic Ice Drift. Proceedings of the Conference on Arctic Sea Ice. Publ. 598. National Academy of Sciences and National Research Council. Washington, D.C. pp. 210-220.

Gould, W.J., Schmitz, Jr., W.J. and Wunsch, C. 1974. Preliminary field results for the Mid-Ocean Dynamics Experiment (MODE-0). Deep Sea Research. Vol. 21. pp. 911-931.

Goulet, J. and Culverhouse, B. 1972. STD thermometer time constant. Journal of Geophysical Research. Vol. 77. pp. 4588-89.

Gudkovich, Z.M. 1959. Ice drift in the central Arctic Basin. Preprint - Inter. Ocean Congress. American Association for the Advancement of Sciences. pp. 545-547.

Hart, J.E. and Killsworth, P.D. 1976. An open ocean baroclinic instability in the Arctic. Deep Sea Research. Vol. 23. pp. 637-645.

Helland-Hansen, B. 1905. Report on fishery and hydrogr. invest. in the Faroer-Shedland Channel and the northern part of the North Sea in 1902. London.

Hunkins, K.L. 1974a. Ice, Ocean and Atmosphere. Oceanus. Vol. XVII, Spring '74.

_______. 1974b. Subsurface eddies in the Arctic Ocean. Deep Sea Research. Vol. 21. pp. 1017-1033.

_______. 1974c. An estimate of internal wave drag on pack ice. AIDJEX Bulletin No. 26. pp. 141-162.

_______. 1977. Review of the AIDJEX oceanographic program. Symposium on Sea Ice Processes and Models. Seattle, Wa. Vol. 1. pp. 199-211.

_______, Bauer, E. and Amos, A. 1977. Salinity and temperature measurements from the AIDJEX manned array. Symposium on Sea Ice Processes and Models. Seattle, Wa. Vol. 1. pp. 212-222.

_______, and Manley, T. 1977. Ocean current profiles from the AIDJEX manned array. Symposium on Sea Ice Processes and Models. Seattle, Wa. Vol. 1. pp. 223-232.

Johannessen, O.M. and Lee, O.S. 1974. A deep stepped thermo-haline structure in the Mediterranean. Deep Sea Research. Vol. 21. pp. 629-639.

Langleben, M.P. 1977. Water drag coefficient at AIDJEX station Caribou. Symposium on Sea Ice Processes and Models. Seattle, Wa. Vol. 1. pp. 233-239.

LeBlond, D.H. 1964. Planetary waves in a symmetric polar ocean. Tellus. 16(4). pp. 503-512.

McPhee, M.G. 1975. The effect of ice motion on the mixed layer under the Arctic pack ice. AIDJEX Bulletin No. 30. pp. 1-28.

Neshbya, S., Neal, V. and Denner, W. 1971. Temperature and Conductivity measurements under ice island T-3. Journal of Geophysical Research, 76. pp. 8107-8120.

Neuman, G. 1968. Ocean Currents. Elsevier Scientific Publ. Co. Elsevier Oceanography Series #4. Amsterdam-London-New York.

_______ and Pierson, W.J., Jr. 1966. Principles of physical oceanography. Prentice-Hall Inc. Englewood Cliffs, N.J.

Newton, J.L. 1973. The Canada Basin: mean circulation and intermediate scale flow feature. Ph.D. thesis. University of Washington. 158 p.

_______, Aagaard, K. and Coachman, L.K. 1974. Baroclinic eddies in the Arctic Ocean. Deep Sea Research. Vol. 21. pp. 707-719.

Paulson, C.A. and Bell, D.L. 1975. Meteorological observations during the AIDJEX main experiment. AIDJEX Bulletin No. 28. pp. 1-10.

Pharand, D. 1973. The law of the sea of the Arctic, with special reference to Canada. University of Ottawa Press, Ottawa.

Plessey Model 9040. 1969. Instructional manual. Salinity, temperature and depth measuring system. San Diego, California.

Pounder, E.R. 1965. The physics of ice. Pergamon Press. New York and Oxford. 151 p.

_____. and LeBlanc, A. 1977. Ice water stress at station Snowbird, AIDJEX. Symposium on Sea Ice Processes and Models. pp. 251-259.

Pritchard, R.S., Coon, M.D. and McPhee, M.G. 1976. Simulation of sea ice dynamics during AIDJEX. AIDJEX Bulletin No. 34. pp. 73-93.

Rigby, F. 1974. Theoretical calculations of internal wave drag on sea ice. AIDJEX Bulletin No. 26. pp. 129-139.

Sater, J.E. 1969. The Arctic Basin. Arctic Institute of North America.

Scarlet, R. 1975. A data processing method for salinity temperature and depth profile. Deep Sea Research. Vol. 22. pp. 509-515.

Schindler, J.F. 1968. The impact of ice-islands. The story of Arlis II and Fletcher's ice island T-3 since 1962. Arctic Drifting Stations. Coordinated by J.E. Sater. Proceedings of the Symposium held at Airlie Conference Centre. Warrenton, Va., April 1966.

Schlichting, H. 1968. Boundary layer theory. McGraw Hill. 6th Edition.

Smith, J.D. 1971. AIDJEX oceanography investigations. AIDJEX Bulletin No. 4. pp. 1-8.

Solomon, H. 1970. A study of ice dynamics relevant to AIDJEX. AIDJEX Bulletin No. 2. pp. 33-50.

_____., 1973. Winter time surface convection in the Arctic Ocean. Deep Sea Research. Vol. 20. pp. 269-283.

Soule, I.M. 1932. Physical properties of sea water. In Physics of Earth. Vol. 5. Oceanography. N.R.S. Bulletin No. 85.

Stommel, H. 1963. Variety of Oceanographic Experience. Science 139. pp. 572-576.

_____. 1969. Horizontal temperature variation in the mixed layer of the South Pacific Ocean. Oceanology (English translation) 9(1). pp. 76-80.

Thorndike, A.S. and Cheung, J.Y. 1977. AIDJEX measurements of sea ice motion, 11 April 1975 to 14 May 1976. AIDJEX Bulletin No. 35.

Timofeuyev, V.T. 1960. Voidnye massy Artcticheskogo Basseina. Leningrad. Gidromet. Izd-vo. 191 p.

Turner, J.S. 1967. Salt fingers across a density interface. Deep Sea Research. Vol. 14. pp. 599-611.

Untersteiner, N. 1977. AIDJEX review. Symposium on Sea Ice Processes and Models. Seattle, Wa. Vol. 1. pp. 2-9.

U.S. Navy Hydrographic Office. Chart T5, 254-2.

________________. 1958. Oceanographic Atlas of the polar sea. Part IV, Arctic. H.O. Publ. 75. 149 p.

Worthington, L.V. 1953. Oceanographic results of the project SKIJUMP I and SKIJUMP II. Polar Sea. 1951-52. Trans. Am. Geophy. Union 34. pp. 543-51.

______. 1959. Oceanographic observation in scientific studies at Fletcher's ice island T-3 (1952-55). Geophys. Directorate. USAF Comb. Research Centre, Geophys. Research Paper No. 63. Vol. 1. pp. 31-35.

Yearsley, J.R. 1966. Internal waves in the Arctic Ocean. Master's thesis. Mechanical Engineering Department. University of Washington, Seattle, Wa.

APPENDIX 1

Conversion Table from AIDJEX days to Calendar days

A convention of numbering days consecutively, beginning with day 1 = 01 January 1975 and ending with day 500 = 14 May 1976 was adopted for the AIDJEX main experiment. In the following pages the AIDJEX day number, the calendar date and the corresponding day of 1975 or 1976 are presented.

AIDJEX DAY	CALENDAR DATE			DAY #
101	11	APL	75	101
102	12	APL	75	102
103	13	APL	75	103
104	14	APL	75	104
105	15	APL	75	105
106	16	APL	75	106
107	17	APL	75	107
108	18	APL	75	108
109	19	APL	75	109
110	20	APL	75	110
111	21	APL	75	111
112	22	APL	75	112
113	23	APL	75	113
114	24	APL	75	114
115	25	APL	75	115
116	26	APL	75	116
117	27	APL	75	117
118	28	APL	75	118
119	29	APL	75	119
120	30	APL	75	120

AIDJEX DAY	CALENDAR DATE			DAY #
121	1	MAY	75	121
122	2	MAY	75	122
123	3	MAY	75	123
124	4	MAY	75	124
125	5	MAY	75	125
126	6	MAY	75	126
127	7	MAY	75	127
128	8	MAY	75	128
129	9	MAY	75	129
130	10	MAY	75	130
131	11	MAY	75	131
132	12	MAY	75	132
133	13	MAY	75	133
134	14	MAY	75	134
135	15	MAY	75	135
136	16	MAY	75	136
137	17	MAY	75	137
138	18	MAY	75	138
139	19	MAY	75	139
140	20	MAY	75	140
141	21	MAY	75	141
142	22	MAY	75	142
143	23	MAY	75	143
144	24	MAY	75	144
145	25	MAY	75	145
146	26	MAY	75	146
147	27	MAY	75	147
148	28	MAY	75	148
149	29	MAY	75	149
150	30	MAY	75	150
151	31	MAY	75	151

AIDJEX DAY	CALENDAR DATE			DAY #
152	1	JUN	75	152
153	2	JUN	75	153
154	3	JUN	75	154
155	4	JUN	75	155
156	5	JUN	75	156
157	6	JUN	75	157
158	7	JUN	75	158
159	8	JUN	75	159
160	9	JUN	75	160
161	10	JUN	75	161
162	11	JUN	75	162
163	12	JUN	75	163
164	13	JUN	75	164
165	14	JUN	75	165
166	15	JUN	75	166
167	16	JUN	75	167
168	17	JUN	75	168
169	18	JUN	75	169
170	19	JUN	75	170
171	20	JUN	75	171
172	21	JUN	75	172
173	22	JUN	75	173
174	23	JUN	75	174
175	24	JUN	75	175
176	25	JUN	75	176
177	26	JUN	75	177
178	27	JUN	75	178
179	28	JUN	75	179
180	29	JUN	75	180
181	30	JUN	75	181

AIDJEX DAY	CALENDAR DATE			DAY #
182	1	JUL	75	182
183	2	JUL	75	183
184	3	JUL	75	184
185	4	JUL	75	185
186	5	JUL	75	186
187	6	JUL	75	187
188	7	JUL	75	188
189	8	JUL	75	189
190	9	JUL	75	190
191	10	JUL	75	191
192	11	JUL	75	192
193	12	JUL	75	193
194	13	JUL	75	194
195	14	JUL	75	195
196	15	JUL	75	196
197	16	JUL	75	197
198	17	JUL	75	198
199	18	JUL	75	199
200	19	JUL	75	200
201	20	JUL	75	201
202	21	JUL	75	202
203	22	JUL	75	203
204	23	JUL	75	204
205	24	JUL	75	205
206	25	JUL	75	206
207	26	JUL	75	207
208	27	JUL	75	208
209	28	JUL	75	209
210	29	JUL	75	210
211	30	JUL	75	211
212	31	JUL	75	212

AIDJEX DAY	CALENDAR DATE	DAY #
213	1 AUG 75	213
214	2 AUG 75	214
215	3 AUG 75	215
216	4 AUG 75	216
217	5 AUG 75	217
218	6 AUG 75	218
219	7 AUG 75	219
220	8 AUG 75	220
221	9 AUG 75	221
222	10 AUG 75	222
223	11 AUG 75	223
224	12 AUG 75	224
225	13 AUG 75	225
226	14 AUG 75	226
227	15 AUG 75	227
228	16 AUG 75	228
229	17 AUG 75	229
230	18 AUG 75	230
231	19 AUG 75	231
232	20 AUG 75	232
233	21 AUG 75	233
234	22 AUG 75	234
235	23 AUG 75	235
236	24 AUG 75	236
237	25 AUG 75	237
238	26 AUG 75	238
239	27 AUG 75	239
240	28 AUG 75	240
241	29 AUG 75	241
242	30 AUG 75	242
243	31 AUG 75	243

AIDJEX DAY	CALENDAR DATE	DAY #
244	1 SEP 75	244
245	2 SEP 75	245
246	3 SEP 75	246
247	4 SEP 75	247
248	5 SEP 75	248
249	6 SEP 75	249
250	7 SEP 75	250
251	8 SEP 75	251
252	9 SEP 75	252
253	10 SEP 75	253
254	11 SEP 75	254
255	12 SEP 75	255
256	13 SEP 75	256
257	14 SEP 75	257
258	15 SEP 75	258
259	16 SEP 75	259
260	17 SEP 75	260
261	18 SEP 75	261
262	19 SEP 75	262
263	20 SEP 75	263
264	21 SEP 75	264
265	22 SEP 75	265
266	23 SEP 75	266
267	24 SEP 75	267
268	25 SEP 75	268
269	26 SEP 75	269
270	27 SEP 75	270
271	28 SEP 75	271
272	29 SEP 75	272
273	30 SEP 75	273

AIDJEX DAY	CALENDAR DATE	DAY #
274	1 OCT 75	274
275	2 OCT 75	275
276	3 OCT 75	276
277	4 OCT 75	277
278	5 OCT 75	278
279	6 OCT 75	279
280	7 OCT 75	280
281	8 OCT 75	281
282	9 OCT 75	282
283	10 OCT 75	283
284	11 OCT 75	284
285	12 OCT 75	285
286	13 OCT 75	286
287	14 OCT 75	287
288	15 OCT 75	288
289	16 OCT 75	289
290	17 OCT 75	290
291	18 OCT 75	291
292	19 OCT 75	292
293	20 OCT 75	293
294	21 OCT 75	294
295	22 OCT 75	295
296	23 OCT 75	296
297	24 OCT 75	297
298	25 OCT 75	298
299	26 OCT 75	299
300	27 OCT 75	300
301	28 OCT 75	301
302	29 OCT 75	302
303	30 OCT 75	303
304	31 OCT 75	304

AIDJEX DAY	CALENDAR DATE	DAY #
305	1 NOV 75	305
306	2 NOV 75	306
307	3 NOV 75	307
308	4 NOV 75	308
309	5 NOV 75	309
310	6 NOV 75	310
311	7 NOV 75	311
312	8 NOV 75	312
313	9 NOV 75	313
314	10 NOV 75	314
315	11 NOV 75	315
316	12 NOV 75	316
317	13 NOV 75	317
318	14 NOV 75	318
319	15 NOV 75	319
320	16 NOV 75	320
321	17 NOV 75	321
322	18 NOV 75	322
323	19 NOV 75	323
324	20 NOV 75	324
325	21 NOV 75	325
326	22 NOV 75	326
327	23 NOV 75	327
328	24 NOV 75	328
329	25 NOV 75	329
330	26 NOV 75	330
331	27 NOV 75	331
332	28 NOV 75	332
333	29 NOV 75	333
334	30 NOV 75	334

AIDJEX DAY	CALENDAR DATE			DAY #
335	1	DEC	75	335
335	2	DEC	75	335
337	3	DEC	75	337
338	4	DEC	75	338
339	5	DEC	75	339
340	6	DEC	75	340
341	7	DEC	75	341
342	8	DEC	75	342
343	9	DEC	75	343
344	10	DEC	75	344
345	11	DEC	75	345
345	12	DEC	75	345
347	13	DEC	75	347
348	14	DEC	75	348
349	15	DEC	75	349
350	16	DEC	75	350
351	17	DEC	75	351
352	18	DEC	75	352
353	19	DEC	75	353
354	20	DEC	75	354
355	21	DEC	75	355
355	22	DEC	75	355
357	23	DEC	75	357
358	24	DEC	75	358
359	25	DEC	75	359
360	26	DEC	75	360
361	27	DEC	75	361
352	28	DEC	75	362
363	29	DEC	75	363
364	30	DEC	75	364
365	31	DEC	75	365

AIDJEX DAY	CALENDAR DATE			DAY #
366	1	JAN	76	1
367	2	JAN	76	2
368	3	JAN	75	3
369	4	JAN	76	4
370	5	JAN	75	5
371	6	JAN	76	6
372	7	JAN	76	7
373	8	JAN	75	8
374	9	JAN	76	9
375	10	JAN	76	10
376	11	JAN	75	11
377	12	JAN	76	12
378	13	JAN	75	13
379	14	JAN	76	14
380	15	JAN	76	15
381	16	JAN	75	16
382	17	JAN	76	17
383	18	JAN	76	18
384	19	JAN	75	19
385	20	JAN	76	20
385	21	JAN	76	21
387	22	JAN	76	22
388	23	JAN	76	23
389	24	JAN	75	24
390	25	JAN	76	25
391	26	JAN	76	26
392	27	JAN	76	27
393	28	JAN	76	28
394	29	JAN	76	29
395	30	JAN	75	30
396	31	JAN	76	31

AIDJEX DAY	CALENDAR DATE			DAY #
397	1	FEB	75	32
398	2	FEB	76	33
399	3	FEB	76	34
400	4	FEB	76	35
401	5	FEB	75	35
402	6	FEB	76	37
403	7	FEB	76	38
404	8	FEB	75	39
405	9	FEB	76	40
406	10	FEB	76	41
407	11	FEB	75	42
408	12	FEB	76	43
409	13	FEB	76	44
410	14	FEB	76	45
411	15	FEB	75	45
412	16	FEB	76	47
413	17	FEB	76	48
414	18	FEB	75	49
415	19	FEB	76	50
416	20	FEB	76	51
417	21	FEB	75	52
418	22	FEB	76	53
419	23	FEB	76	54
420	24	FEB	76	55
421	25	FEB	75	55
422	26	FEB	76	57
423	27	FEB	76	58
424	28	FEB	75	59
425	29	FEB	76	60

AIDJEX DAY	CALENDAR DATE			DAY #
426	1	MAR	76	61
427	2	MAR	76	62
428	3	MAR	75	53
429	4	MAR	76	64
430	5	MAR	76	65
431	6	MAR	75	55
432	7	MAR	76	67
433	8	MAR	76	68
434	9	MAR	76	69
435	10	MAR	76	70
436	11	MAR	76	71
437	12	MAR	76	72
438	13	MAR	75	73
439	14	MAR	76	74
440	15	MAR	76	75
441	16	MAR	75	75
442	17	MAR	76	77
443	18	MAR	76	78
444	19	MAR	76	79
445	20	MAR	76	80
446	21	MAR	76	81
447	22	MAR	76	82
448	23	MAR	75	83
449	24	MAR	76	84
450	25	MAR	76	85
451	26	MAR	75	85
452	27	MAR	76	87
453	28	MAR	76	88
454	29	MAR	76	89
455	30	MAR	76	90
456	31	MAR	76	91

AIDJEX DAY	CALENDAR DATE			DAY #
457	1	APL	76	92
458	2	APL	76	93
459	3	APL	76	94
460	4	APL	76	95
461	5	APL	76	96
462	6	APL	76	97
463	7	APL	76	98
464	8	APL	76	99
465	9	APL	76	100
466	10	APL	76	101
467	11	APL	76	102
468	12	APL	76	103
469	13	APL	76	104
470	14	APL	76	105
471	15	APL	76	106
472	16	APL	76	107
473	17	APL	76	108
474	18	APL	76	109
475	19	APL	76	110
476	20	APL	76	111
477	21	APL	76	112
478	22	APL	76	113
479	23	APL	76	114
480	24	APL	76	115
481	25	APL	76	116
482	26	APL	76	117
483	27	APL	76	118
484	28	APL	76	119
485	29	APL	76	120
486	30	APL	76	121

AIDJEX DAY	CALENDAR DATE			DAY #
487	1	MAY	76	122
488	2	MAY	76	123
489	3	MAY	76	124
490	4	MAY	76	125
491	5	MAY	76	126
492	6	MAY	76	127
493	7	MAY	76	128
494	8	MAY	76	129
495	9	MAY	76	130
496	10	MAY	76	131
497	11	MAY	76	132
498	12	MAY	76	133
499	13	MAY	76	134
500	14	MAY	76	135

APPENDIX 2

AIDJEX DATA FILES

1. Position of the manned camps and buoys, in latitude and longitude vs time

Approximately 10 positions were calculated each day for each operating station using the Transit navigational satellite or the Nimbus F satellite. Data for the manned camps were taken from 10 April 1975 to 20 April 1976. Data for buoys in the Beaufort Sea were taken from April 1975 up to November 1976. Note that the lifetime of most buoys is about six months. These data characterize the motion of the pack ice in the Beaufort Sea for all seasons of the year.

A new set of 8 buoys were deployed in March 1977. Tracks of these buoys are being added to the available data.

Data are organized in a time series for each station with a separation marker at the end of each 20-day period.

2. Smoothed position, velocity, and acceleration for manned camps and buoys, in cartesian coordinates

Data from file 1 above have been post-processed using a Kalman filter technique. In one form - sorting on time - position, velocity, and acceleration from each operating buoy are arrayed together at three-hour intervals. In another form - sorting on station - position and velocity are given as a time series, separately for each station. A variance measure accompanies each element of data to characerize its error.

3. Source data for Rams Buoys tracked by Nimbus F satellite

Position data acquired from the start of Nimbus F operation in June 1975 have been provided by the NASA Goddard Space Flight Center and, after decoding and editing, have been incorporated into file 1 above. Several land-based rams packages are included in order to determine the temporal and spatial accuracy of the tracking system.

4. Rotation of the manned camp floes

The orientation of the camp floes, to which the navigational satellite positioning system was aligned, was determined together with the camp position. Each camp azimuth, with respect to true North, has been smoothed for the period 10 April 1975 to 22 April 1976. Angular position and rate of rotation for all camps are given at three-hour intervals in a time-sorted data file together with error estimates for each datum.

These data are also available in camp-sorted order, a separate time series for each camp.

5. Ice thickness and snow depth

Periodic measurements were made at various sites near the manned camps. Statistical evaluation of ice and snow conditions were made from frequent measurements around a given site. Data are not continuous. Tabulations of available data for the period 10 April 1975 to 29 June 1975 have been published in AIDJEX Bulletin 32 (June 1976). Data to April 1976 are available in a similar form.

6. Ice surface profile

One profile of the ice surface was taken using a laser altimeter in the NASA 990 as it traveled a 72 km track between two manned camps. A data point is a height above a reference plane every 0.4 m along the track. The measurements were made on 24 April 1975.

7. LANDSAT (ERTS) 1 and 2 images

Satellite photos of the Beaufort Sea region have been obtained from the Eros data Center for qualitative and quantitative analysis. About 1500 photos taken when visibility and cloud cover permitted are on file. Each photo covers a square region 100 miles on the side. Time periods are the spring and fall seasons of 1972, 1973, and 1975.

8. NOAA-4 and NOAA-5 Satellite images

Photos of the Arctic from Greenland to the Bering Straits have been received daily from Ness since 2 January 1975. Two images cover the belt between 70 degrees and 80 degrees N latitude, that is, each photo covers a square area about 600 miles on the side. Only infrared photos are available for the winter (November through January), both IR and visible photos are taken during the rest of the year. These are source data for examining large-scale ice movements in the Arctic as well as large-scale weather patterns.

9. Surface-level air pressure (derived data)

From the combination of national weather service surface pressure maps and pressures measured at scattered points in the Beaufort Sea, two-dimensional pressure contours have been derived for every six-hour interval. These contours are a sixth-order polynomial in X and Y, the grid coordinates overlying the Beaufort Sea region. The grid is rectangular and each element is 75 miles on the side. The coefficients of the polynomial are on the data of this file. They can be used to determine the surface pressure at any point in the area at any six-hour interval by translating latitude and longitude of the point to the grid coordinates and employing the polynomial coefficients for the time desired.

The coefficients have been calculated for the period 11 April 1975 to 20 April 1976.

An alternative surface level air pressure file has been derived from pressure measurements taken at the manned camps and from buoys containing pressure sensors. These data are interpolated at 3 hourly intervals and are combined with the geographic location of the corresponding station. Pressure, position data are given for four manned camps and for up to fourteen buoys at each 3 hour interval for the period April 20 1975 to April 10 1976.

10. Geostrophic surface winds (derived)

From the derived pressure data of file 9 above, geostrophic wind speed and direction have been calculated for specific points at six hour intervals. In the geogrid file these specific points are the grid points of a 16 by 16 overlay of the Beaufort Sea. The geosta file describes the geostrophic winds at the four AIDJEX manned camps and at the nine Navsat buoys.

11. Pressure charts (source data)

Surface and 850 mb pre-sure charts prepared by the National Meteorological Center for the Northern hemisphere have been received for 0000 GMT and 1200 GMT each day since April 1975. Measured pressures at the interior of the Beaufort Sea are combined with these analog data to improve the detailed accuracy of the derived pressures and winds data of files 9 and 10 above.

12. Surface-level meteorological data

Meteorological instruments were in continuous operation at the AIDJEX manned camps from April 1975 through April 1976. Hourly averages of observed wind speed and direction at 10 m and air temperatures at 2 m and 9 m above the surface have been prepared. Time series for each camp are available for the full operating period of the main experiment. There are separation markers between each 20-day interval

13. Atmospheric inversion levels

Inversion heights in the atmosphere were monitored continuously by acoustic radar at the manned camp designated as the main camp. Analog records were digitized at hourly intervals for the periods 13 April - 1 October 1975 and 5 November 1975 - 18 April 1976. As many as seven distinct inversion heights are given when they exist simultaneously.

A second file has been prepared showing the average height of the dominant persistent inversion layer over a 3 hour period for every hour of the experiment.

14. Ocean currents (combined files for manned camps)

The manned camps served as floating platforms from which ocean currents relative to ice motion were measured continuously at depths of 2 m and 30 m. Hourly averages of ocean currents combined with hourly 10 m winds and three-hour smoothed ice velocity (files 10 and 2) from each manned camp for the full operating period of the AIDJEX program are available in a single file. They are sorted by camp by time, with separation markers between 20-day intervals. This file is called W/I/O wind, ice, ocean

15. Ocean currents combined with position measured from Rams buoys

Two Rams spar buoys deployed offshore in the Beaufort Sea in November 1975 contained sensors which measured ocean currents at depths of 2 m and 30 m. A magnetic compass heading for the buoy and internal bearing of the sensors are given with the data at three-hour intervals. These data have been combined with buoy positions to allow for absolute current determination. One buoy operated until 1 October 1976. The other provided meaningful data only until 28 March 1976.

16. Oceanic mixed layer characteristics

The upper ocean mixed layer is defined in depth by the point, or points, at which a rapid change in salinity occurs. This layer was measured for surface temperature, surface salinity, and depth twice daily at each manned camp. All available measurements (one per day) were published in tabular form in AIDJEX Bulletin 32 (June 1976).

17. Ocean depth

The depth of the ocean beneath the path of the main AIDJEX camp was measured during two periods. Acoustic soundings were taken every hour from

25 May to 3 August 1975 and from 18 December 1975 to 25 April 1976. Round-trip time of sound travel is given together with interpreted depth. A file of daily average depth is also available.

18. Surface pressure (validated), offshore Rams buoys.

Four Rams buoys deployed offshore in the Beaufort Sea measured surface pressure. These measurements have been corrected for scale and sensor drift and have been smoothed and interpolated to three-hour readings. Buoys were operational for the following periods, buoy 207, 18 March - 28 August 1976, buoy 1015, 23 March - 30 September 1976, buoy 1245, 4 November 1975 - 1 October 1976, and buoy 1416, 5 November 1975 - 28 March 1976.

The data are sorted by buoy by time, and are merged with buoy position in latitude and longitude.

19. Surface pressure (validated), AIDJEX camps and selected buoys

Navsat systems at the four manned camps and nine navigational satellite buoys had pressure sensors to make detailed measurements not specifically included in the surface pressure charts of file 11 above. After appropriate corrections and calibration, these validated measurements were incorporated into the derivation of area-wide geostrophic winds (file 10). These source date are available with their geographic position at three-hour intervals. Data are sorted by station. The manned camps were operational from April 1975 to April 1976. Some of the buoys (supplemented by nearby Rams buoys) continued to operate as late as 6 December 1976.

These data are also incorporated in the alternative pressure position file noted in data set 9 above.

20. Weather observations, manned camps

Handwritten weather notes logged daily by observers in the manned camps noted wind velocity, surface pressure, temperature, visibility, and weather. They back up the digitized data in the files noted above.

21. Logbook entries, manned camps

Members of the scientific groups recorded informal notes about events, equipment performance, changes or calibration of sensors, etc. Their logbooks back up the data collection procedures followed during the main experiment.

Data being processed but not yet available

The following 3 data sets are in the process of being validated and calibrated. They will be added to the AIDJEX data bank files and made available to the scientific community together with the files noted above.

22. Wind speed and direction measured by pilot balloon

Pibal measurements using two tracking theodolites were made each day at the main camp during the AIDJEX experiment.

The available material is currently being edited (8/3/77)

Two generations of data are being stored in the data bank. Raw data consists of theodolite (angle) measurements taken at uniform intervals of time as the balloon ascended. Drag output (processed profiles) give zonal and meridianal (U,V) wind sp-eds versus altitude.

23. Ocean current profile

Twice a day at each manned camp, a current meter was lowered to a depth of 194 m and raised at a steady rate to determine the stratification of the ocean layers. The analog outputs will be digitized to show time, depth, speed, and direction at uniform depth increments.

24. Salinity and temperature versus depth at manned camps

Standard STD measurements were made twice a day at each manned camp during the main AIDJEX experiment.

One twenty day block for days 181-200 at 3 camps - 57 casts - is available 8/3/77

Available data sets continued

25. Specific Humidity

Hourly averages of vapor pressure, mixing ratio G/G, and specific humidity G/G are derived from measured dew point and atmospheric pressure at the main camps during the entire AIDJEX program.

APPENDIX 3

INSTRUMENTATION

In this appendix we show some of the details about the sensors that were used in the field experiment of AIDJEX. Plate A-1 shows the underwater unit and the terminal deck unit of the Plessey model 9040 S T D system. Fig A-1 depicts the block diagram for the underwater and the terminal deck unit of the model 9040. In plate A-2 the digital data logger used is shown. A sample of the period to oceanographic parameter conversion tables is shown as tables A-1, A-2 and A-3. These tables show the conversion periods for a limited range of salinity, temperature and depth. Fig. A-2 shows the TSK prifiling current meter and plate A-3 shows the underwater unit with it's internal mechanism displayed.

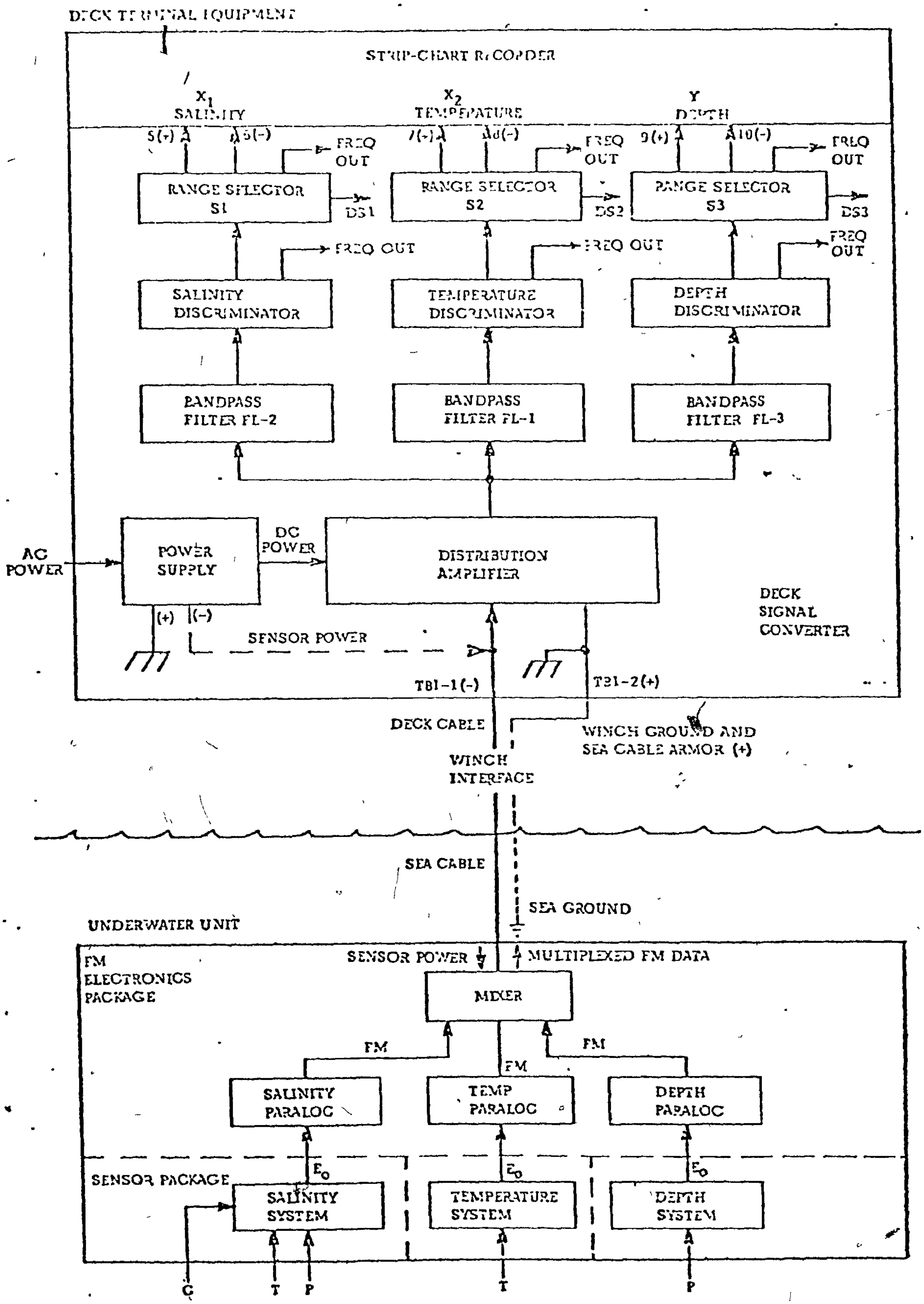

Fig A- 1 Block diagram of the model 9040 Salinity, Temperature and Depth measuring system.

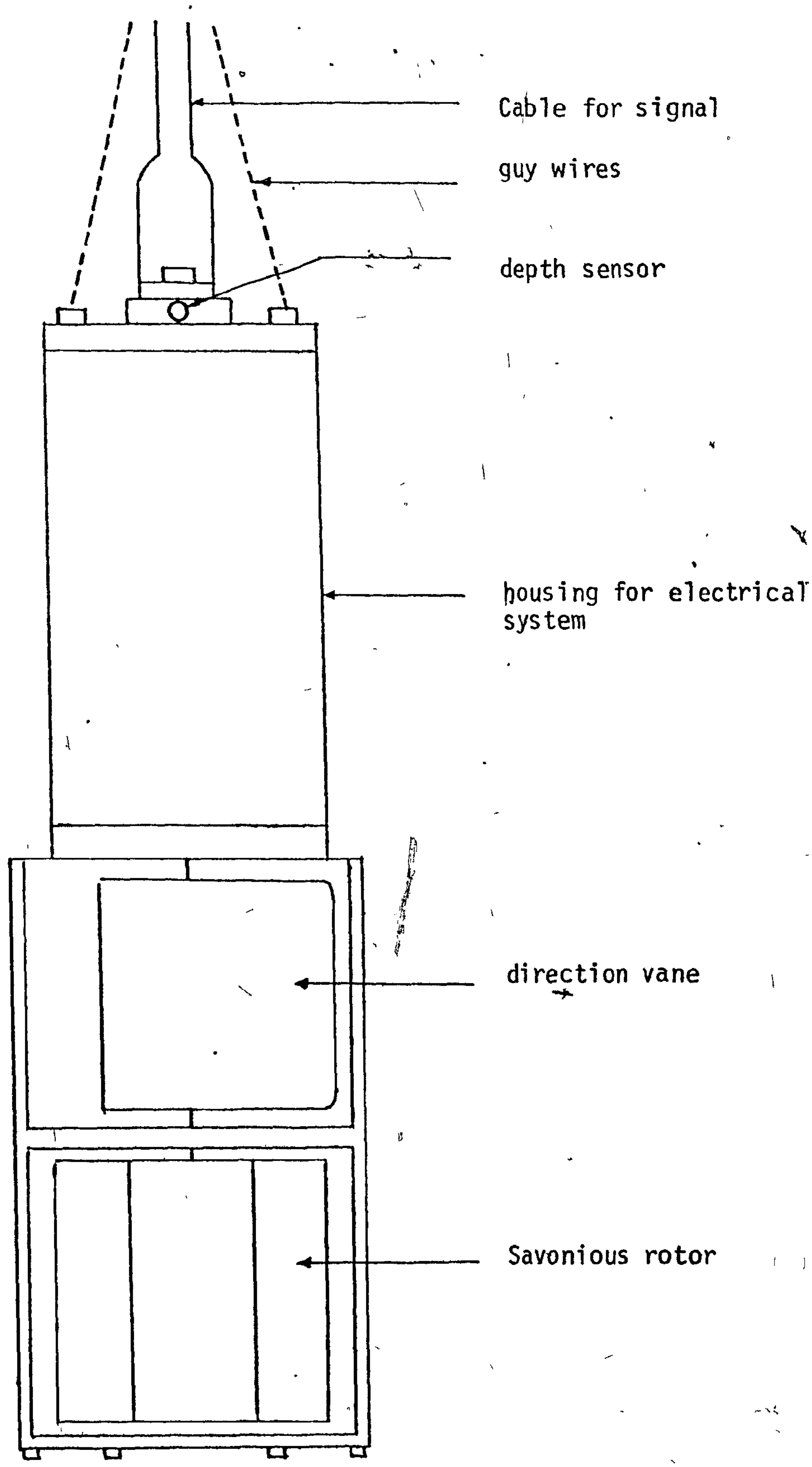

Fig. A-2 Underwater unit of the TSK profiling current meter.

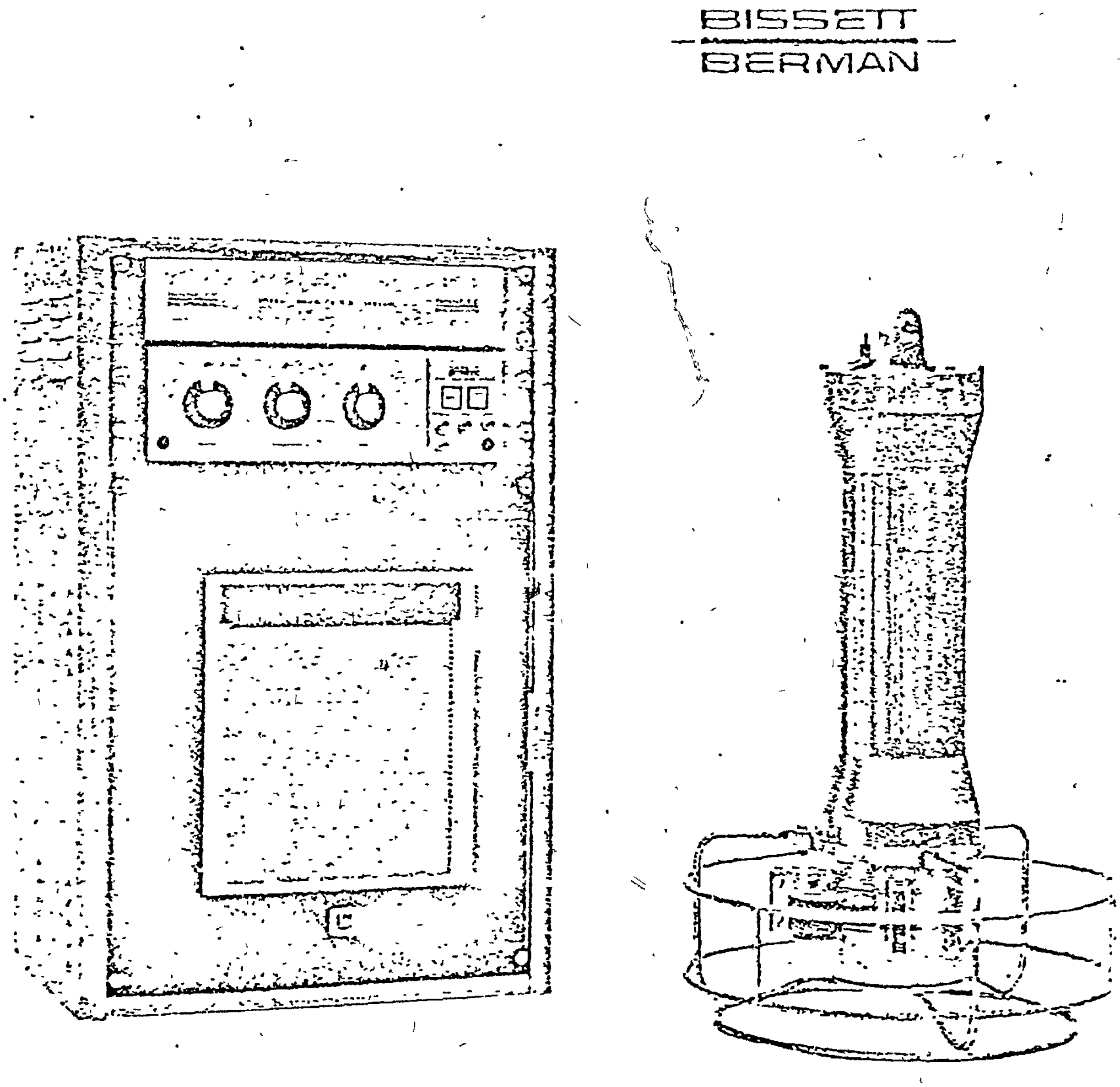

Plate A-1 Plessey model 9040 Salinity, Temperature and Depth measuring system. Deck equipment and underwater unit.

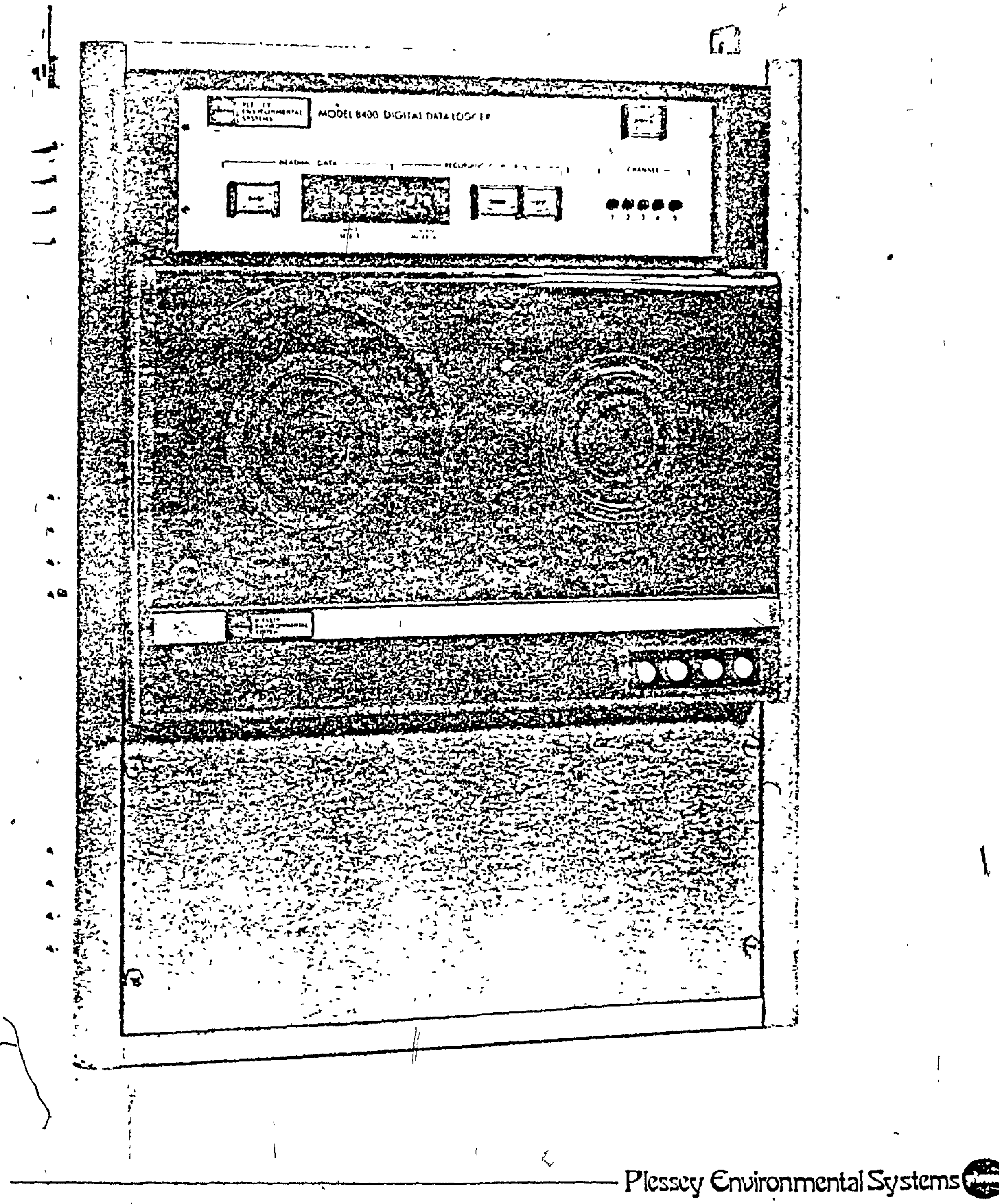

Plate A-2 Plessey model 8400 digital data logger.

Plate A-3 Internal mechanism of the TSK profiling current meter.

Table A-1 Conversion tables for salinity.

SALIN.	PERIOD	SALIN.	PERIOD	SALIN.	PERIOD	SALIN.	PERIOD
29.900	159398	29.950	159 29	30.000	158663	30.050	158298
29.901	159390	29.951	159 22	30.001	158655	30.051	158290
29.902	159383	29.952	159 15	30.002	158648	30.052	158283
29.903	159375	29.953	159 7	30.003	158641	30.053	158276
29.904	159368	29.954	159 0	30.004	158633	30.054	158269
29.905	159361	29.955	158992	30.005	158626	30.055	158261
29.906	159353	29.956	158985	30.006	158619	30.056	158254
29.907	159346	29.957	158978	30.007	158611	30.057	158247
29.908	159338	29.958	158970	30.008	158604	30.058	158239
29.909	159331	29.959	158963	30.009	158597	30.059	158232
29.910	159324	29.960	158956	30.010	158589	30.060	158225
29.911	159316	29.961	158948	30.011	158582	30.061	158218
29.912	159309	29.962	158941	30.012	158575	30.062	158210
29.913	159302	29.963	158934	30.013	158568	30.063	158203
29.914	159294	29.964	158926	30.014	158560	30.064	158196
29.915	159287	29.965	158919	30.015	158553	30.065	158189
29.916	159279	29.966	158912	30.016	158546	30.066	158181
29.917	159272	29.967	158904	30.017	158538	30.067	158174
29.918	159265	29.968	158897	30.018	158531	30.068	158167
29.919	159257	29.969	158890	30.019	158524	30.069	158159
29.920	159250	29.970	158882	30.020	158516	30.070	158152
29.921	159243	29.971	158875	30.021	158509	30.071	158145
29.922	159235	29.972	158868	30.022	158502	30.072	158138
29.923	159228	29.973	158860	30.023	158495	30.073	158130
29.924	159221	29.974	158853	30.024	158487	30.074	158123
29.925	159213	29.975	158846	30.025	158480	30.075	158116
29.926	159206	29.976	158838	30.026	158473	30.076	158109
29.927	159198	29.977	158831	30.027	158465	30.077	158101
29.928	159191	29.978	158824	30.028	158458	30.078	158 94
29.929	159184	29.979	158816	30.029	158451	30.079	158 87
29.930	159176	29.980	158809	30.030	158443	30.080	158 80
29.931	159169	29.981	158802	30.031	158436	30.081	158 72
29.932	159162	29.982	158794	30.032	158429	30.082	158 65
29.933	159154	29.983	158787	30.033	158422	30.083	158 58
29.934	159147	29.984	158780	30.034	158414	30.084	158 50
29.935	159140	29.985	158772	30.035	158407	30.085	158 43
29.936	159132	29.986	158765	30.036	158400	30.086	158 36
29.937	159125	29.987	158758	30.037	158392	30.087	158 29
29.938	159117	29.988	158750	30.038	158385	30.088	158 21
29.939	159110	29.989	158743	30.039	158378	30.089	158 14
29.940	159103	29.990	158736	30.040	158371	30.090	158 7
29.941	159 95	29.991	158728	30.041	158363	30.091	158 0
29.942	159 88	29.992	158721	30.042	158356	30.092	157992
29.943	159 81	29.993	158714	30.043	158349	30.093	157985
29.944	159 73	29.994	158706	30.044	158341	30.094	157978
29.945	159 66	29.995	158699	30.045	158334	30.095	157971
29.946	159 59	29.996	158692	30.046	158327	30.096	157963
29.947	159 51	29.997	158685	30.047	158320	30.097	157956
29.948	159 44	29.998	158677	30.048	158312	30.098	157949
29.949	159 37	29.999	158670	30.049	158305	30.099	157942

Table A-2 Conversion tables for temperature.

TEMPERATURE V/S PERIOD. PAGE 2 -1.99 DEG C TO 0.00 DEG C

TEMP.	PERIOD	TEMP.	PERIOD	TEMP.	PERIOD	TEMP.	PERIOD
-1.99	470 22	-1.49	463934	-0.99	458 2	-0.49	452220
-1.98	469899	-1.48	463814	-0.98	457885	-0.48	452105
-1.97	469776	-1.47	463694	-0.97	457768	-0.47	451991
-1.96	469652	-1.46	463574	-0.96	457651	-0.46	451877
-1.95	469529	-1.45	463454	-0.95	457534	-0.45	451763
-1.94	469406	-1.44	463334	-0.94	457417	-0.44	451649
-1.93	469283	-1.43	463214	-0.93	457300	-0.43	451535
-1.92	469160	-1.42	463 95	-0.92	457184	-0.42	451422
-1.91	469 37	-1.41	462975	-0.91	457 67	-0.41	451308
-1.90	468915	-1.40	462855	-0.90	456950	-0.40	451194
-1.89	468792	-1.39	462736	-0.89	456834	-0.39	451 80
-1.88	468669	-1.38	462616	-0.88	456717	-0.38	450967
-1.87	468547	-1.37	462497	-0.87	456601	-0.37	450853
-1.86	468424	-1.36	462377	-0.86	456484	-0.36	450740
-1.85	468302	-1.35	462258	-0.85	456368	-0.35	450626
-1.84	468179	-1.34	462139	-0.84	456252	-0.34	450513
-1.83	468 57	-1.33	462 19	-0.83	456136	-0.33	450400
-1.82	467935	-1.32	461900	-0.82	456 19	-0.32	450287
-1.81	467812	-1.31	461781	-0.81	455903	-0.31	450173
-1.80	467690	-1.30	461662	-0.80	455787	-0.30	450 60
-1.79	467568	-1.29	461543	-0.79	455671	-0.29	449947
-1.78	467446	-1.28	461424	-0.78	455555	-0.28	449834
-1.77	467324	-1.27	461305	-0.77	455440	-0.27	449721
-1.76	467202	-1.26	461186	-0.76	455324	-0.26	449608
-1.75	467 80	-1.25	461 68	-0.75	455208	-0.25	449495
-1.74	466958	-1.24	460949	-0.74	455 92	-0.24	449383
-1.73	466837	-1.23	460830	-0.73	454977	-0.23	449270
-1.72	466715	-1.22	460712	-0.72	454861	-0.22	449157
-1.71	466593	-1.21	460593	-0.71	454746	-0.21	449 45
-1.70	466472	-1.20	460475	-0.70	454630	-0.20	448932
-1.69	466350	-1.19	460357	-0.69	454515	-0.19	448820
-1.68	466229	-1.18	460238	-0.68	454400	-0.18	448707
-1.67	466108	-1.17	460120	-0.67	454284	-0.17	448595
-1.66	465986	-1.16	460 2	-0.66	454169	-0.16	448482
-1.65	465865	-1.15	459884	-0.65	454 54	-0.15	448370
-1.64	465744	-1.14	459766	-0.64	453939	-0.14	448258
-1.63	465623	-1.13	459648	-0.63	453824	-0.13	448146
-1.62	465502	-1.12	459530	-0.62	453709	-0.12	448 34
-1.61	465381	-1.11	459412	-0.61	453594	-0.11	447922
-1.60	465260	-1.10	459294	-0.60	453479	-0.10	447810
-1.59	465139	-1.09	459176	-0.59	453364	-0.09	447698
-1.58	465 18	-1.08	459 59	-0.58	453250	-0.08	447586
-1.57	464898	-1.07	458941	-0.57	453135	-0.07	447474
-1.56	464777	-1.06	458823	-0.56	453 20	-0.06	447362
-1.55	464657	-1.05	458706	-0.55	452906	-0.05	447250
-1.54	464536	-1.04	458588	-0.54	452791	-0.04	447139
-1.53	464416	-1.03	458471	-0.53	452677	-0.03	447 27
-1.52	464295	-1.02	458354	-0.52	452562	-0.02	446916
-1.51	464175	-1.01	458236	-0.51	452448	-0.01	446804
-1.50	464 55	-1.00	458119	-0.50	452334	-0.00	446693

Table A-3 Conversion tables for depth.

3000M. DEPTH V/S PERIOD. PAGE 1 0M. TO 199M.

DEPTH	PERIOD	DEPTH	PERIOD	DEPTH	PERIOD	DEPTH	PERIOD
0	102965	50	102688	100	102411	150	102137
1	102960	51	102682	101	102406	151	102131
2	102954	52	102677	102	102400	152	102126
3	102949	53	102671	103	102395	153	102120
4	102943	54	102666	104	102389	154	102115
5	102938	55	102660	105	102384	155	102109
6	102932	56	102654	106	102378	156	102104
7	102926	57	102649	107	102373	157	102 98
8	102921	58	102643	108	102367	158	102 93
9	102915	59	102638	109	102362	159	102 87
10	102910	60	102632	110	102356	160	102 82
11	102904	61	102627	111	102351	161	102 76
12	102899	62	102621	112	102345	162	102 71
13	102893	63	102616	113	102340	163	102 66
14	102887	64	102610	114	102334	164	102 60
15	102882	65	102605	115	102329	165	102 55
16	102876	66	102599	116	102323	166	102 49
17	102871	67	102594	117	102318	167	102 44
18	102865	68	102588	118	102312	168	102 38
19	102860	69	102583	119	102307	169	102 33
20	102854	70	102577	120	102301	170	102 27
21	102849	71	102571	121	102296	171	102 22
22	102843	72	102566	122	102290	172	102 16
23	102837	73	102560	123	102285	173	102 11
24	102832	74	102555	124	102279	174	102 5
25	102826	75	102549	125	102274	175	102 0
26	102821	76	102544	126	102268	176	101994
27	102815	77	102538	127	102263	177	101989
28	102810	78	102533	128	102257	178	101983
29	102804	79	102527	129	102252	179	101978
30	102799	80	102522	130	102246	180	101973
31	102793	81	102516	131	102241	181	101967
32	102787	82	102511	132	102235	182	101962
33	102782	83	102505	133	102230	183	101956
34	102776	84	102500	134	102224	184	101951
35	102771	85	102494	135	102219	185	101945
36	102765	86	102489	136	102213	186	101940
37	102760	87	102483	137	102208	187	101934
38	102754	88	102478	138	102203	188	101929
39	102749	89	102472	139	102197	189	101923
40	102743	90	102467	140	102192	190	101918
41	102738	91	102461	141	102186	191	101913
42	102732	92	102456	142	102181	192	101907
43	102726	93	102450	143	102175	193	101902
44	102721	94	102445	144	102170	194	101896
45	102715	95	102439	145	102164	195	101891
46	102710	96	102433	146	102159	196	101885
47	102704	97	102428	147	102153	197	101880
48	102699	98	102422	148	102148	198	101874
49	102693	99	102417	149	102142	199	101869

APPENDIX 4

DYNAMIC CALIBRATION AND SOME COMPUTER PROGRAM BLOCK DIAGRAMS.

The S T D sensors were routinely held at selected depths while samples were taken by Nansen bottles for the purposes of comparison with the sensor output. Although this practice is straight forward, it was observed that abnormal drift occured in the salinity output when the sensor was held motionless in the water. This problem was more pronounced than in shipboard casts. Drifts in the salinity output began the moment the descent was stopped and continued over the time for thermometers to reach equilibrium before tripping the bottles (about five minutes). The values returned to apparent true values when the motion resumed. As stated in the text, periods were recorded immediately upon stopping the winch. As a back-up to this procedure, programming was developed at LDGO, to extract calibration readings from files of reduced data. In this case, the standard depth sensor readings at the time each bottle was tripped are required input. The program searches the station files for residual 'drift spikes' at the indicated depths, interpolates over spikes that are detected and computes an alternative set of calibration readings from these de-spiked files. In the following flow chart (Fig.A-14)the tape handling programs developed at the LDGO are shown.

The dynamic correction applied is further demonstrated by two series of figures. Fig.A-3, A-4 and A-5 show the τ changes in SB 003 again. This time for the full depth of 407 meters. Fig. A-6, A-7, A-8 and A-9 show the analysis for SB 302 , a station at another time. Again τ has the value of 0.7.

The corrections applied from the bottle data are shown in table A-4. A linear, quadratic and cubic corrections were applied to temperature depth and salinity values. The table is for AIDJEX days 181 to 201. This corresponds to 30 June to 20 July 75 period. The mean difference and the standard deviation between bottle data and sensor readings is shown in Fig. A-10 to A-13 and in table A-5. The data analysis is for days 181 to 201 only. Similar analysis is done or is being done for other time periods.

Digitizing of the analog S T D traces had to be done when the digital data logger malfunctioned. The digitizing was performed at the DATAC computer lab. at McGill university. The DATAC uses a VIDAR (IDVM) analog to digital converter to digitize the analog (voltage) signal from the digitizing table. Louis C Vroomen and Dr. Paul Zsombor-Murray assisted in the working of the computer. Fig. A-15 shows the flow of data through the system. The conversion of the 7-track BCD to 9-track EBCDIC was done at I.S.T computing centre in Montreal. Eric Brown was instrumental in the 'translation' of the tapes. Fig. A-16 shows the 'translation' in block form. Rest of the calculation were performed at the McGill University Computing Centre using the IBM 360/ 75 OS system. The programs are too numerous to reproduce here. Calculation of the geostrophic current is shown, however, in block form. (Fig. A-17).

Fig. A-3

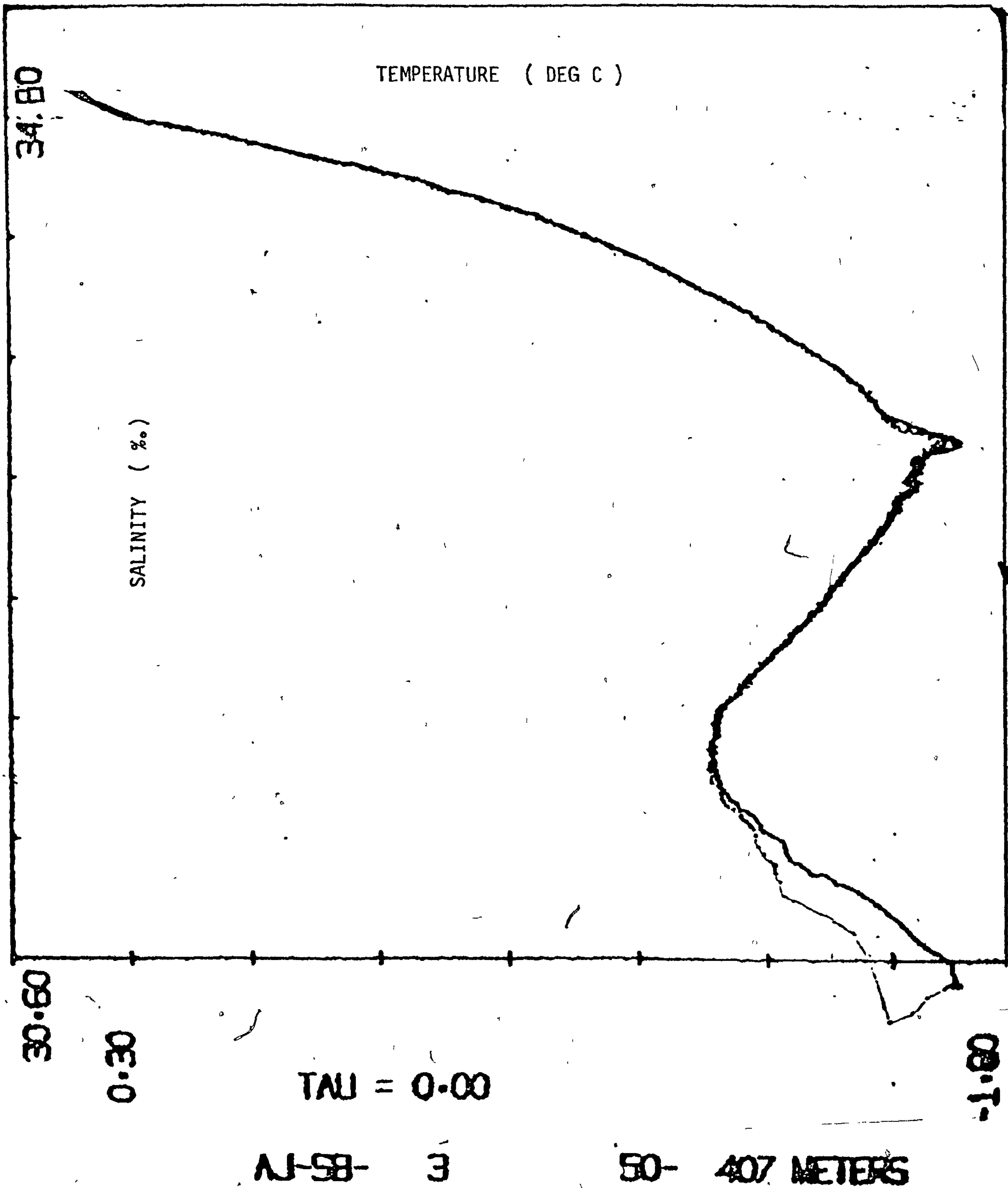
TEMPERATURE (DEG C)
SALINITY (‰)
34.80
30.60
0.30
-1.80
TAU = 0.00
AJ-58- 3
50- 407 METERS

Fig. A-4

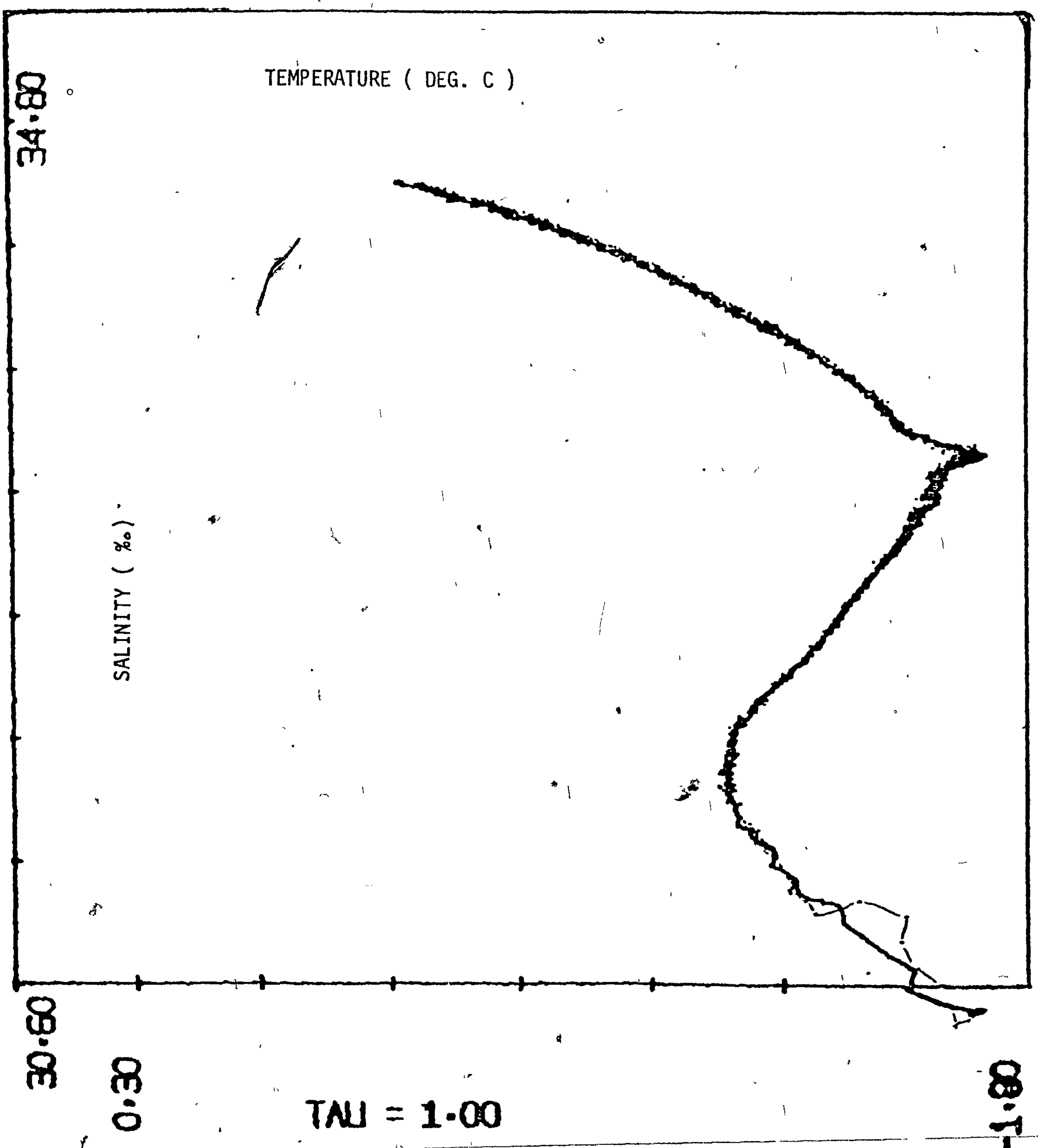

AJ-58- 3 50- 300 METERS

Fig. A-5

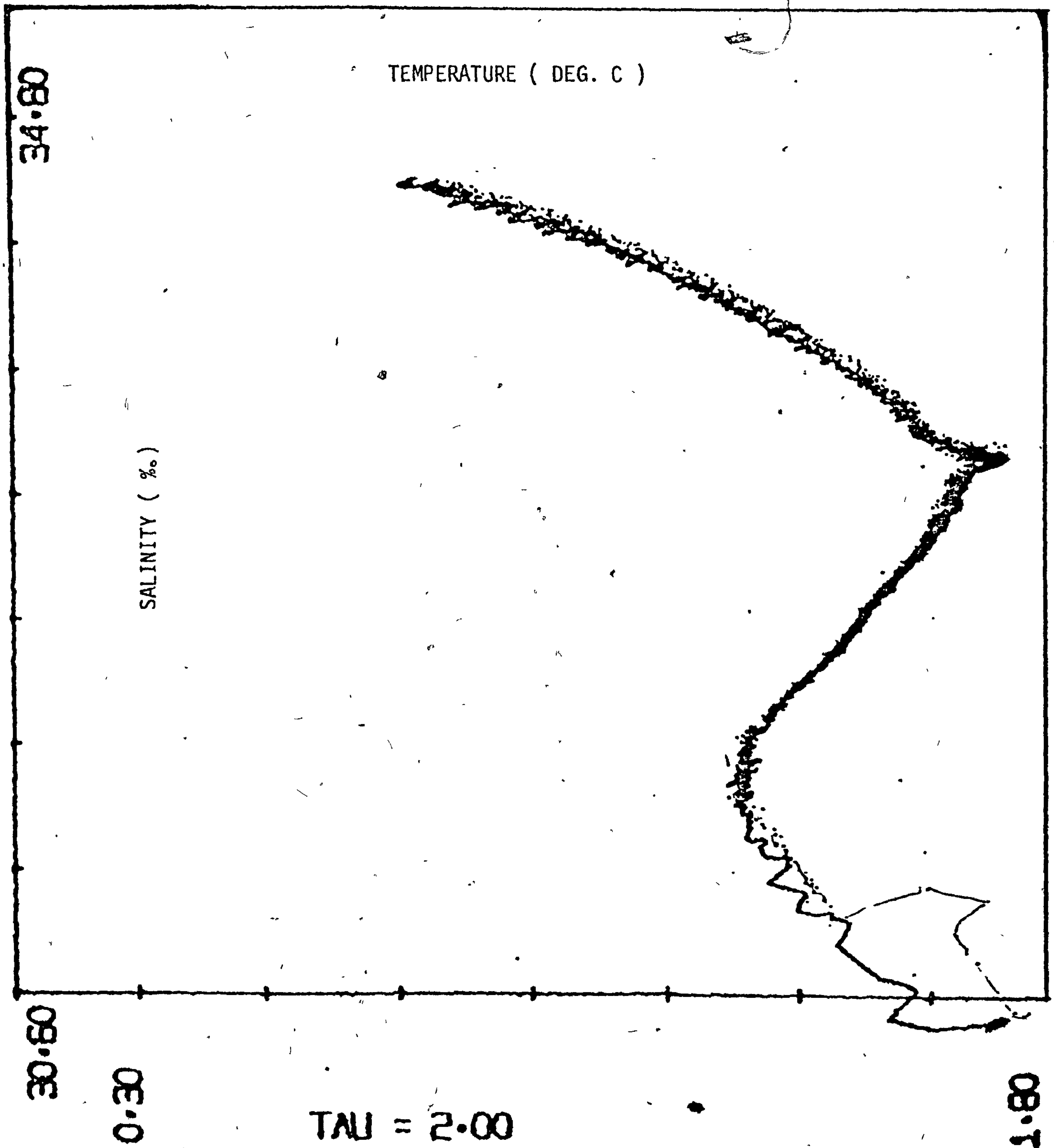

TAU = 2.00

AJ-SB- 3 50- 300 METERS

Fig. A-6

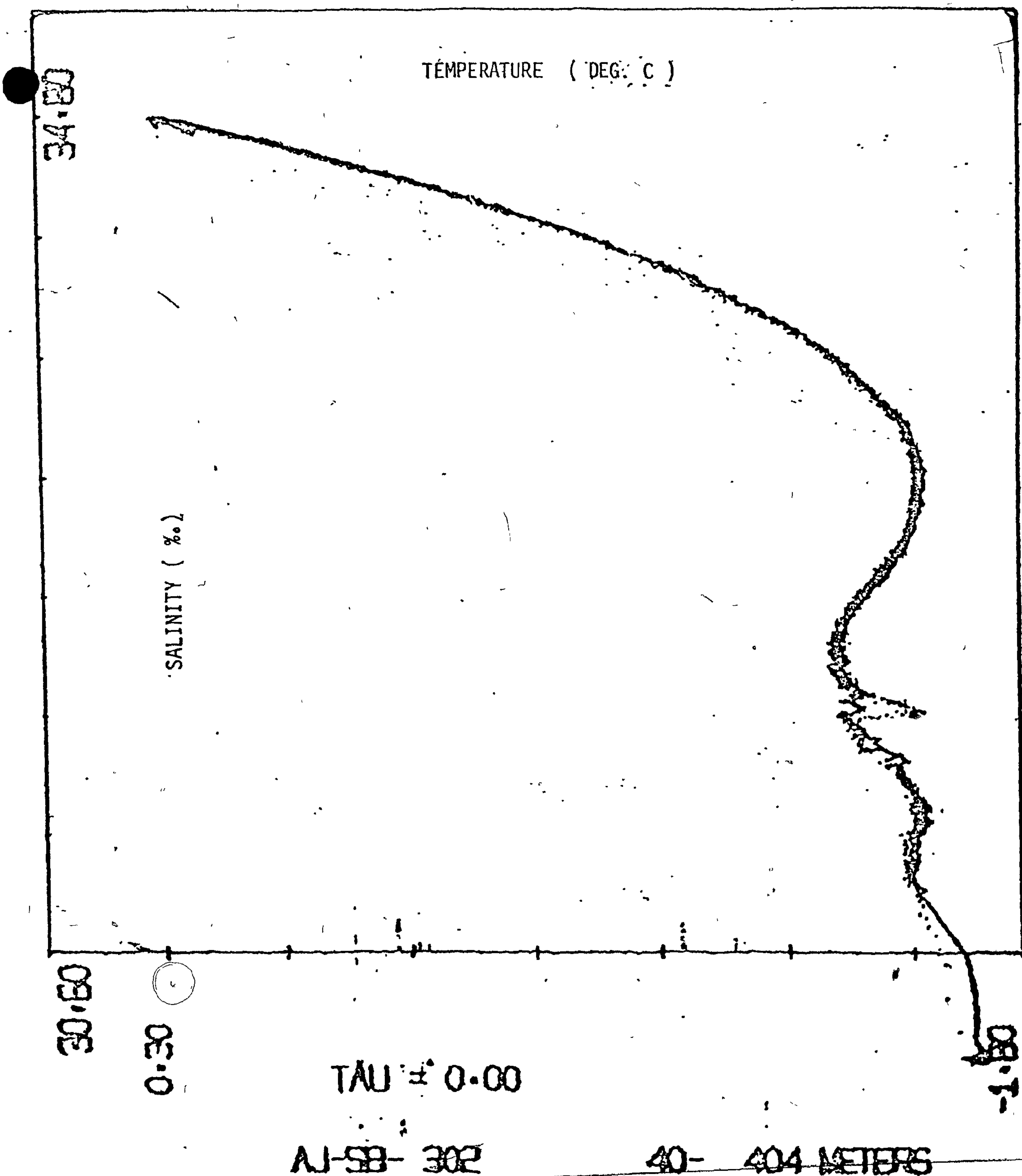
TEMPERATURE (DEG. C)
SALINITY (‰)
34.80
30.80
0.30
-1.80
TAU = 0.00
AJ-SB- 302
40- 404 METERS

Fig. A-7

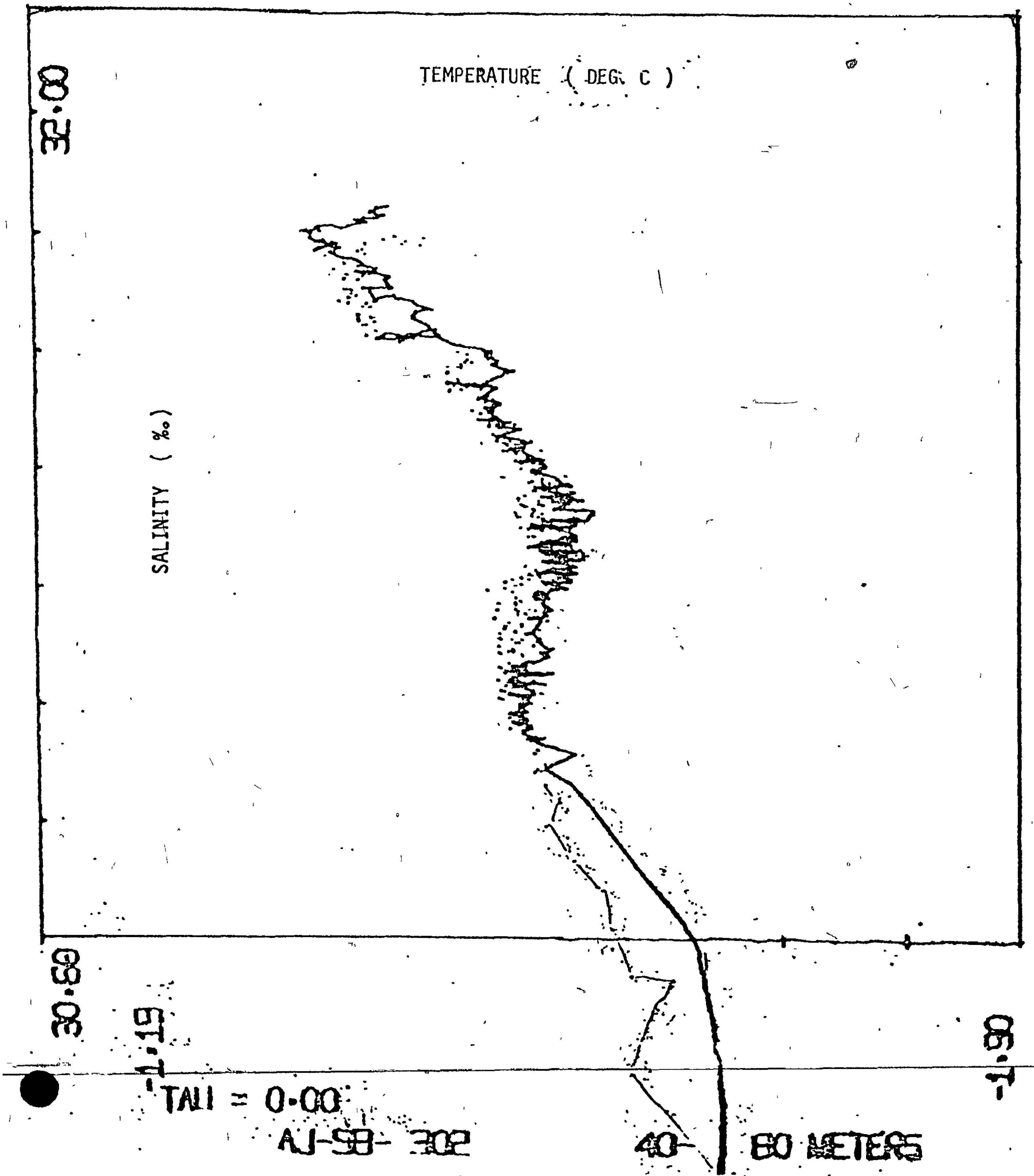
TEMPERATURE (DEG C)
SALINITY (‰)
32.00
30.60
-1.19
-1.90
TAU = 0.00
40
60 METERS

Fig. A-8

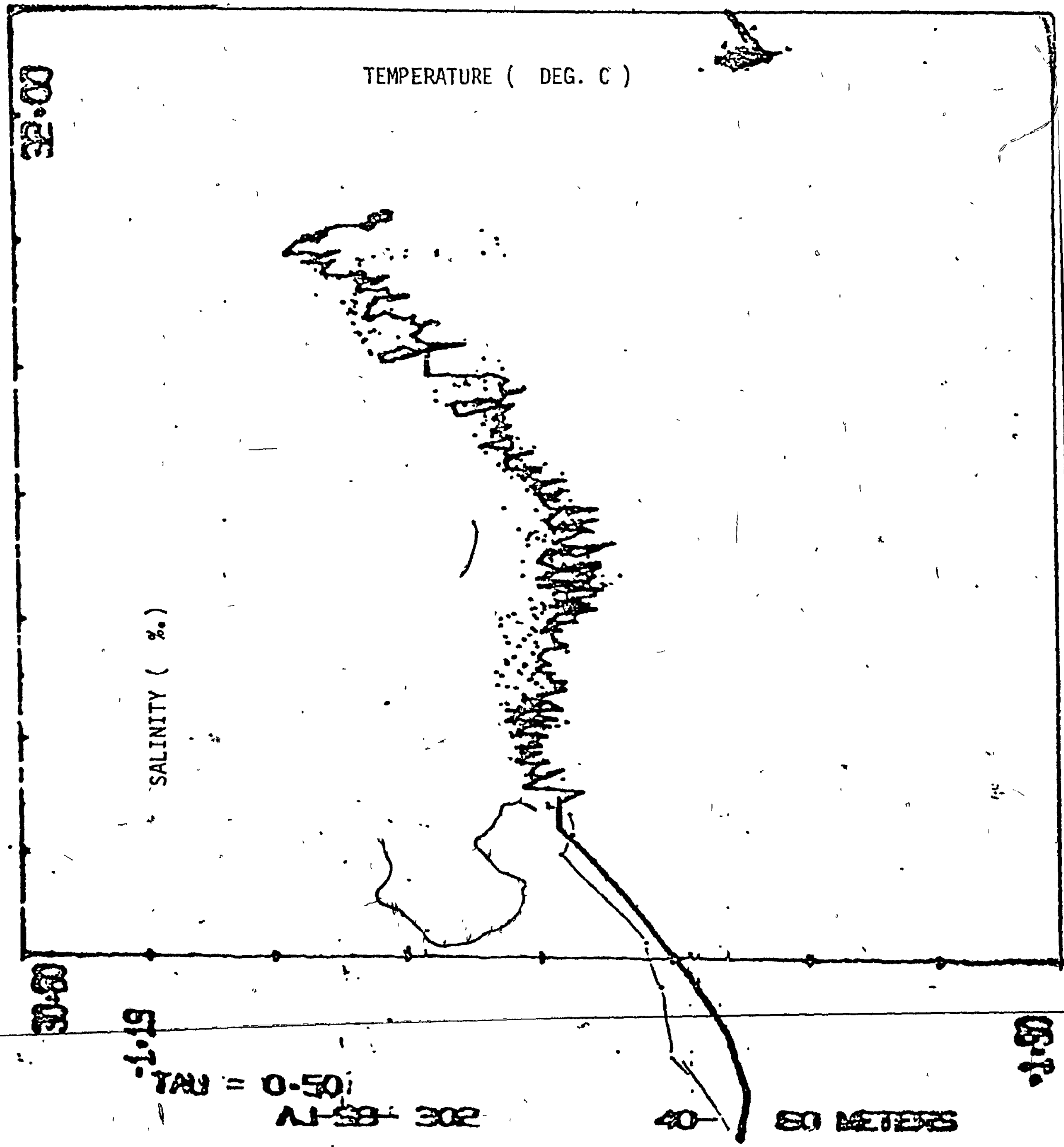
TEMPERATURE (DEG. C)
SALINITY (‰)
32.00
30.80
-1.19
TAU = 0.50
40
80 METERS

Fig. A-9

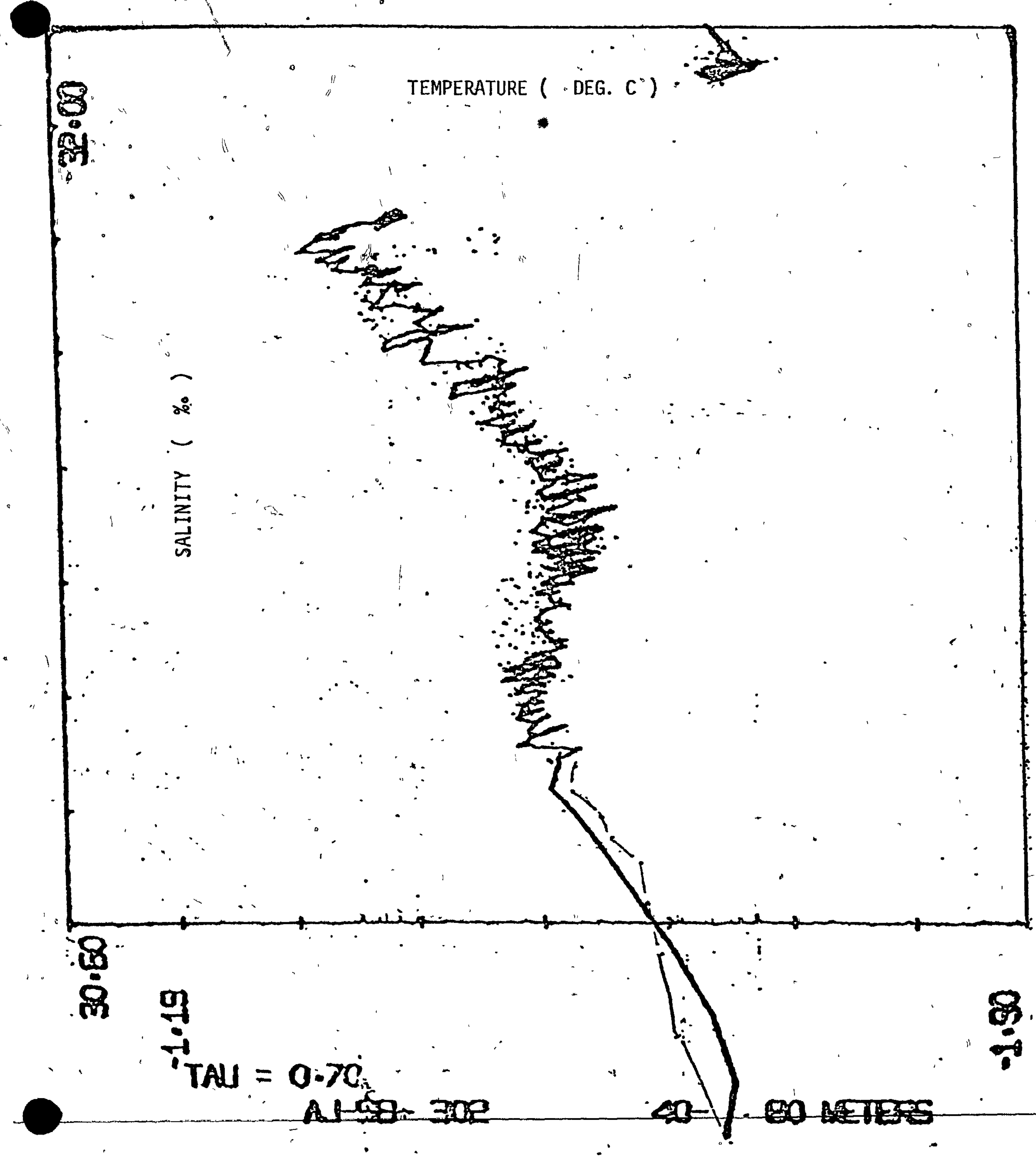
TEMPERATURE (DEG. C)
SALINITY (‰)
32.00
30.60
-1.19
-1.90
TAU = 0.70
40- 60 METERS

TABLE A-4

Correction scheme for bottle data

Following correction scheme was applied to get final data.

CORRT (T)= T + CT

CORRD (D)= D + CD + CD1*D + CD2*D^2

CORRS (S)= S + CS + CS1*D + CS2*D^2 + CS3*D^3

Correction term	Station CB	Station SB
CD	0.109 10^{0}	0.305 10^{0}
CD1	-0.278 10^{-2}	-0.345 10^{-2}
CD2	-0.118 10^{-4}	-0.137 10^{-4}
CT	0.365 10^{-1}	-0.156 10^{-1}
CS	-0.446 10^{-1}	-0.372 10^{-1}
CS1	0.205 10^{-3}	-0.446 10^{-3}
CS2	-0.768 10^{-7}	0.167 10^{-5}
CS3	-0.108 10^{-9}	-0.141 10^{-8}

TABLE A-5

Summary of mean S T D corrections to sensor readings.

	Variable	CARIBOU Δ	SD	SNOW BIRD Δ	SD
SURFACE					
	DEPTH	0.0	0.0	0.0	0.0
	TEMP	0.0365217	0.0104	-0.015614	0.0135
	SAL	-0.0446818	0.0143	-0.037222	0.0061
250 m					
	DEPTH	-1.0	1.9	-0.5	1.6
	TEMP				
	SAL	0.0002	0.0116	-0.0664444	0.0113
500 m					
	DEPTH	-4.58333	1.08	-5.77777	1.9
	TEMP				
	SAL	0.0252727	0.00434	-0.019125	0.0074
750 m					
	DEPTH	-8.55555	2.01	-9.7143	2.8
	TEMP				
	SAL	0.0203333	0.00532	-0.027875	0.0041

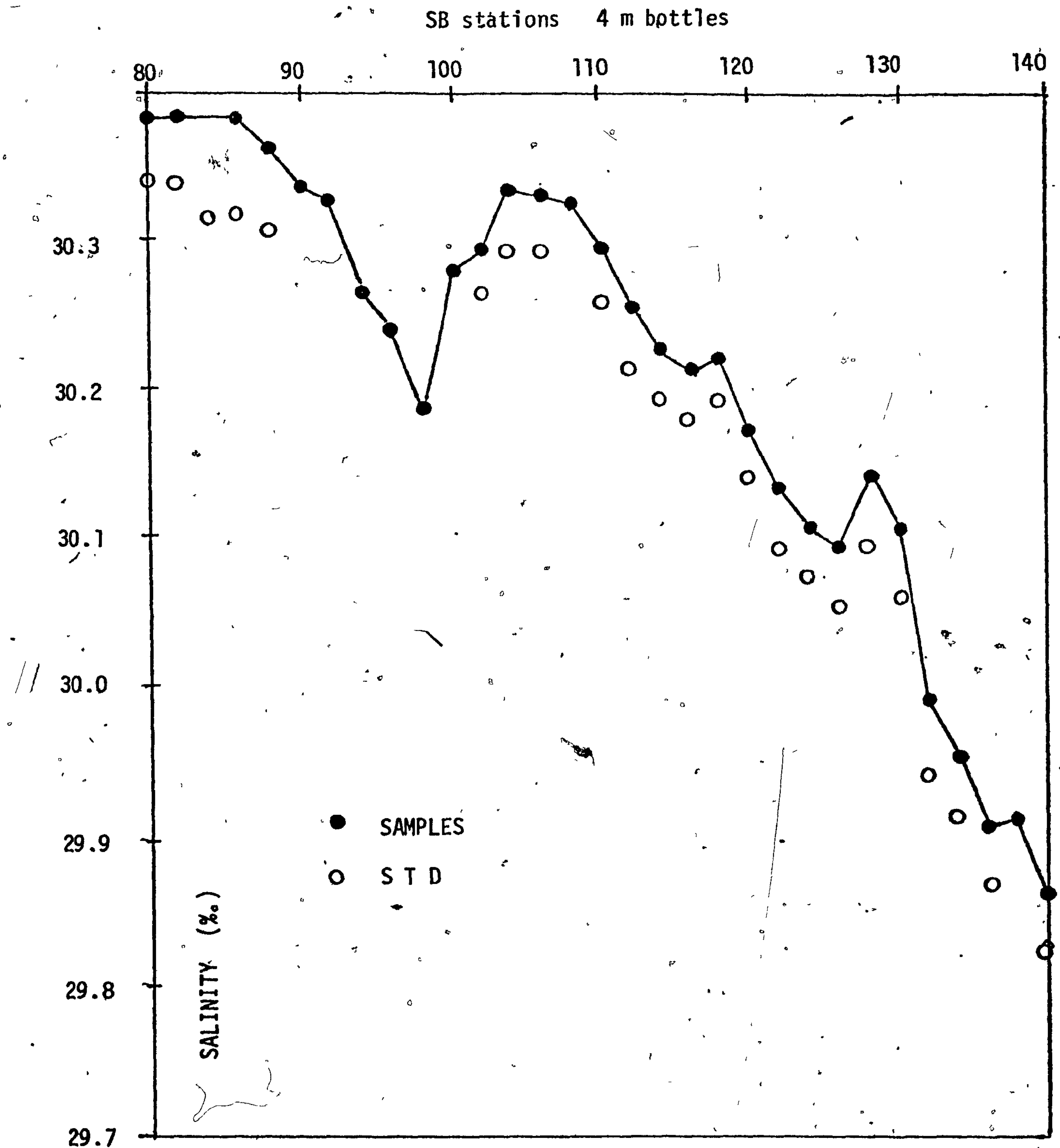

Fig. A-10 Static calibration for SB S T D. 4m bottles

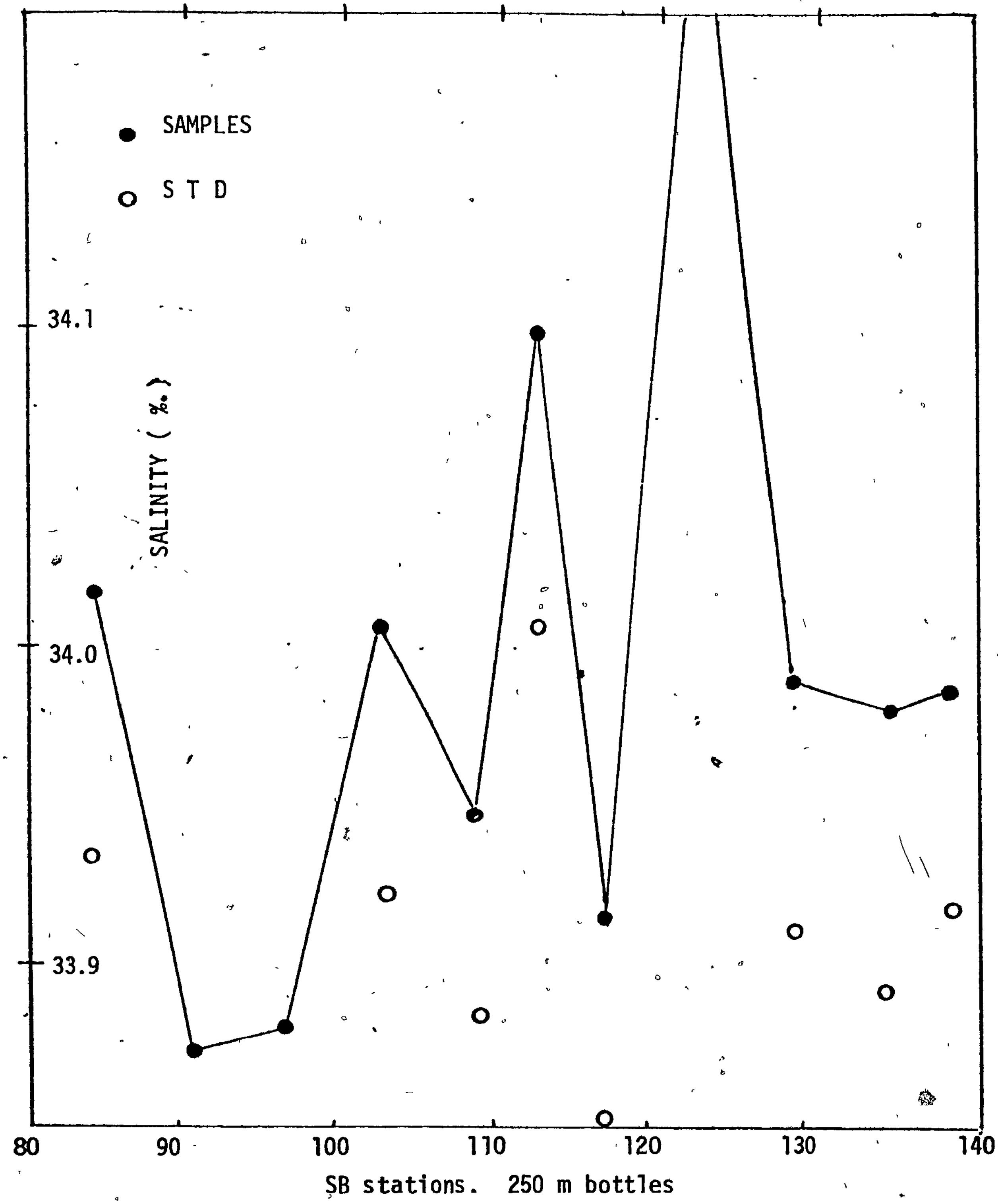

Fig. A-11 Static calibration for SB S T D. 250 m bottles.

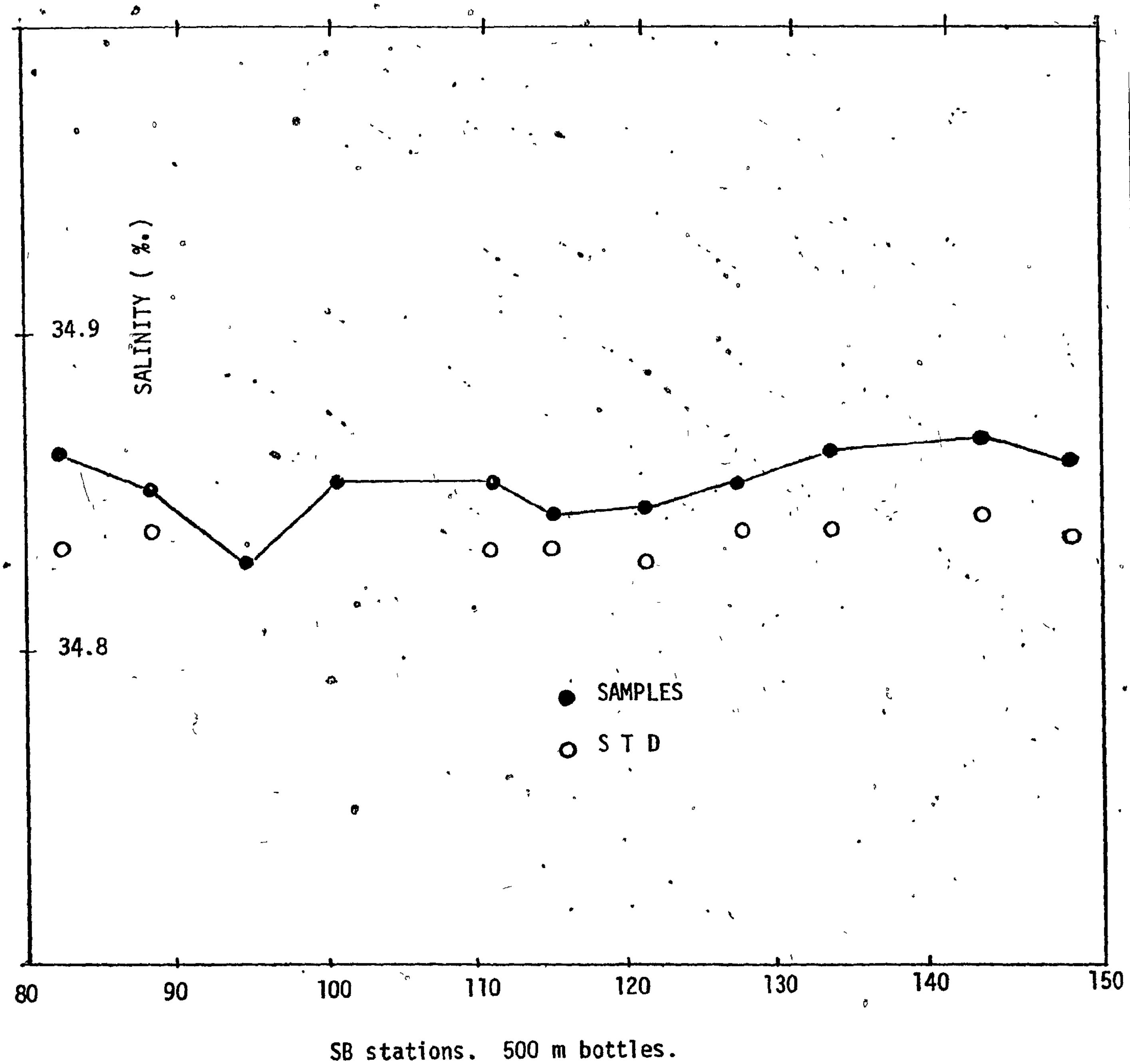

Fig. A-12 Static calibration SB S T D. 500 m bottles.

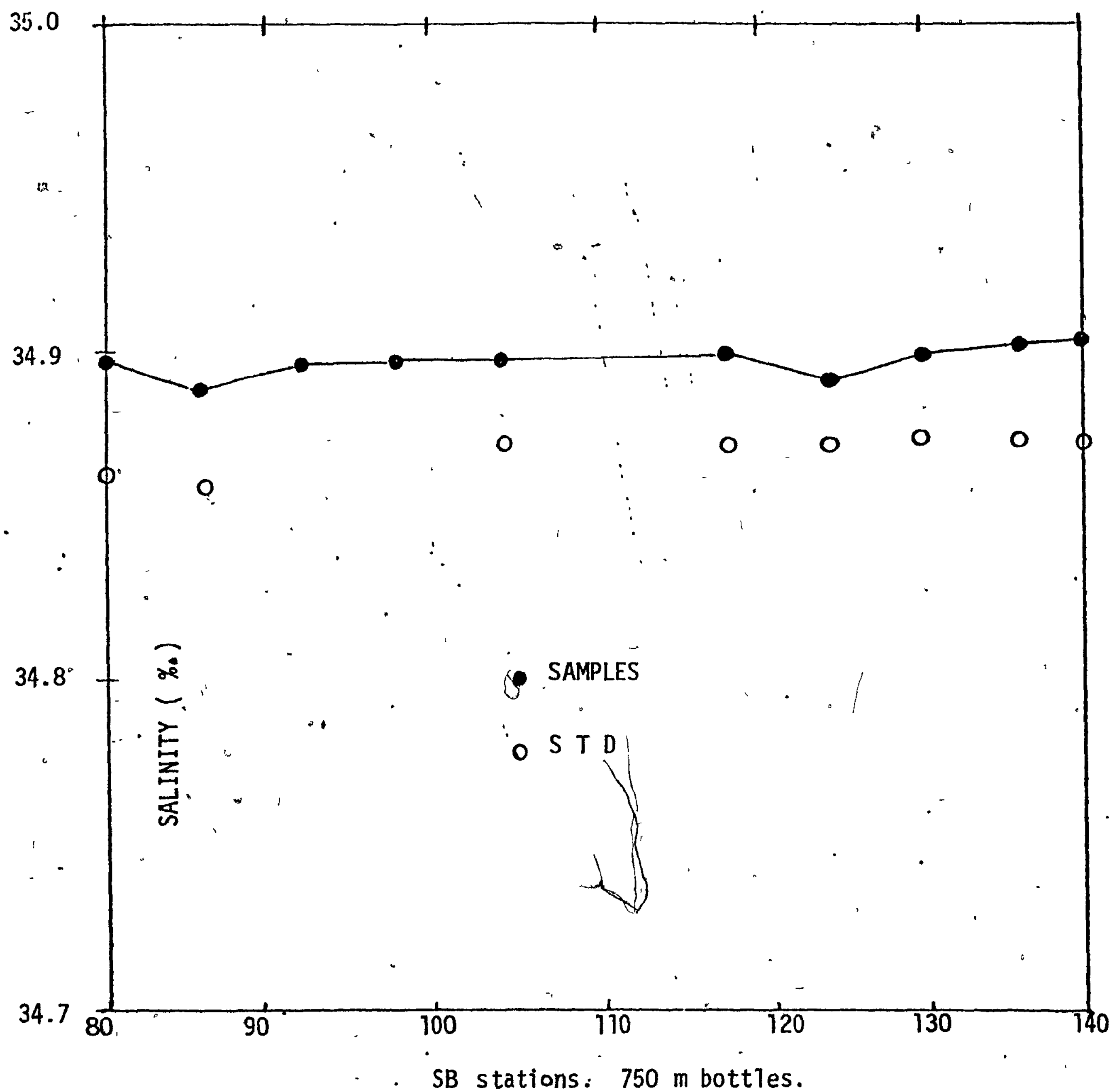

Fig. A-13 Static calibration SB S T D. 750 m bottles.

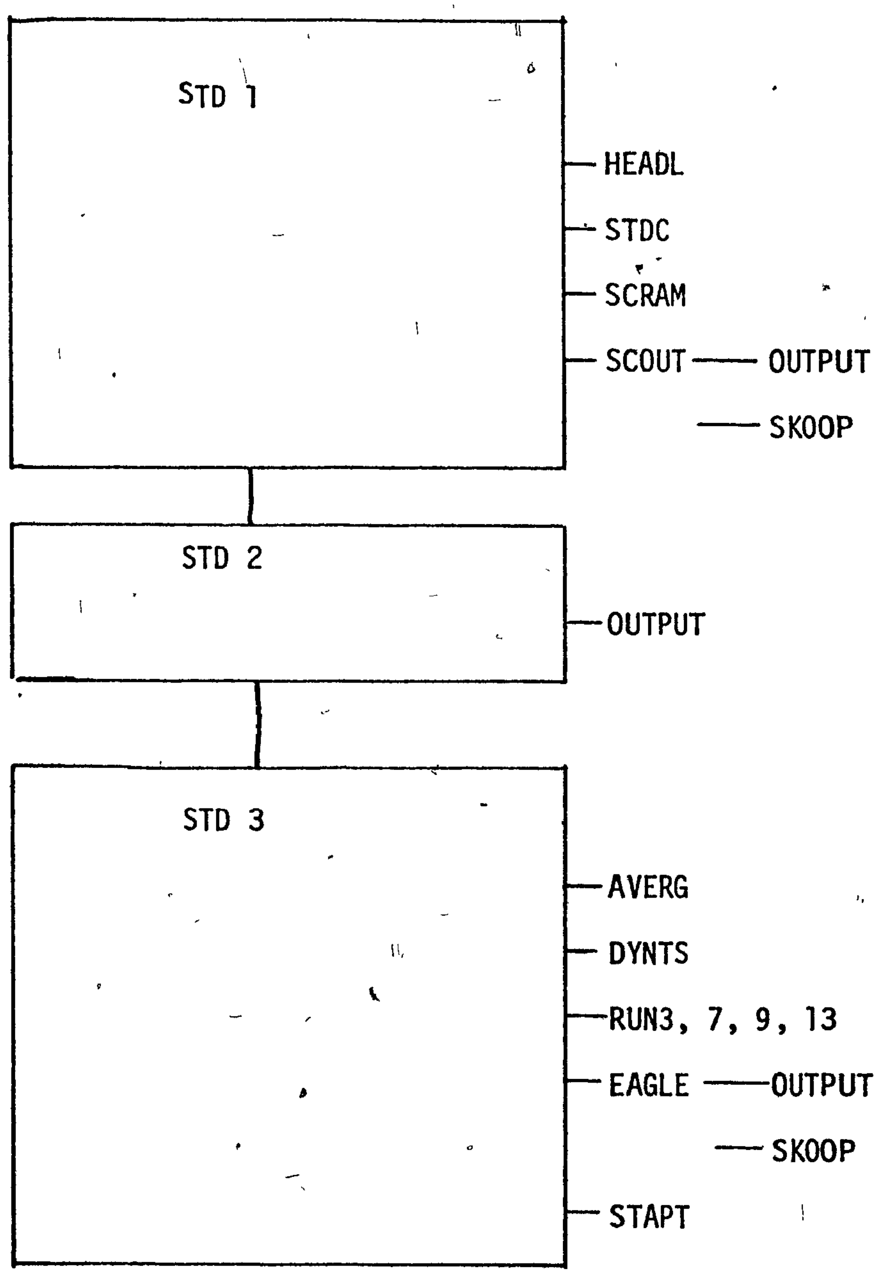

Fig. A-14 Block diagram of the LDGO tape handling programs.

STD 1 -program adapted from GEORGI program for time series reduction of S T D data.

-program reads one station from raw data tapes, provides for card input of header information.

-converts data to S,T,D and scan rate.

-screens data according to set tolerances.

-sets flags to mark segments of acceptable data.

-writes all data on disk file.

-writes tables of flags and headers on another disk file.

STD 2 -plots data screened by STD 1 at approximately 2 second intervals.

-interpolates over segments of bad data of less than one tape record in length.

STD 3 -D, S and T are smoothed with running mean averages to minimize digitizer noise.

-option to correct T and S for time lag in the temperature response. Correction equation based on Scarlet's method using estimated time constant of temperature sensor. Correction applied from surface to specified depth only, downtrace only.

-corrected/smoothed data stored for changing depth and written on magnetic tape for further processing.

AVERG	- does a running mean on the array X
STAPT	- plot data .
SCOUT	- print and/or display data on scope. write 32 scans on disk data file.
STDC	- converts NN scans to oceanographic data -D,S and T. Conversion based on 3 channel format of model 8400 DDL.
SCRAM	- screens data according to set tolerances. Sets flags to mark discontinuities in acceptable data, does interpolation upto 2 points before setting flag.
SKOOP	- display records on scope.
EAGLE	- controls OUTPUT and SKOOP
DYNTS	- processes time series in T and S to account for temperature sensor time lag. (Dynamic Calibration)
HEADL	- checks for and converts header data.
OUTPUT	- prints 32 scan records.
RUN3 RUN7 RUN9 RUN13	- functions for averaging array.

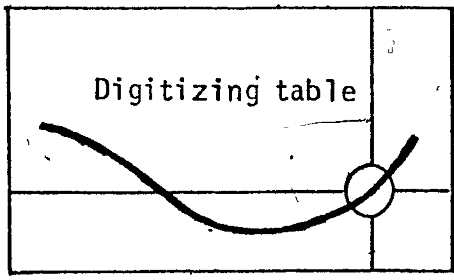

CHTDSK

DATAC digitizing program
using Intergrated Digital Volt Meter

data stored in disk file.

AIDJEX76

checks and makes correction for skewed paper allignment and temperature trace offset.

computes salinity and temperature at 1 m interval after fitting a cubic spline through the digitized points.

print salinity temperature at 1 m depth intervals.

print actual digitized points

store oceanographic parameters on tape.

Fig. A-15 Digitizing program on the DATAC.

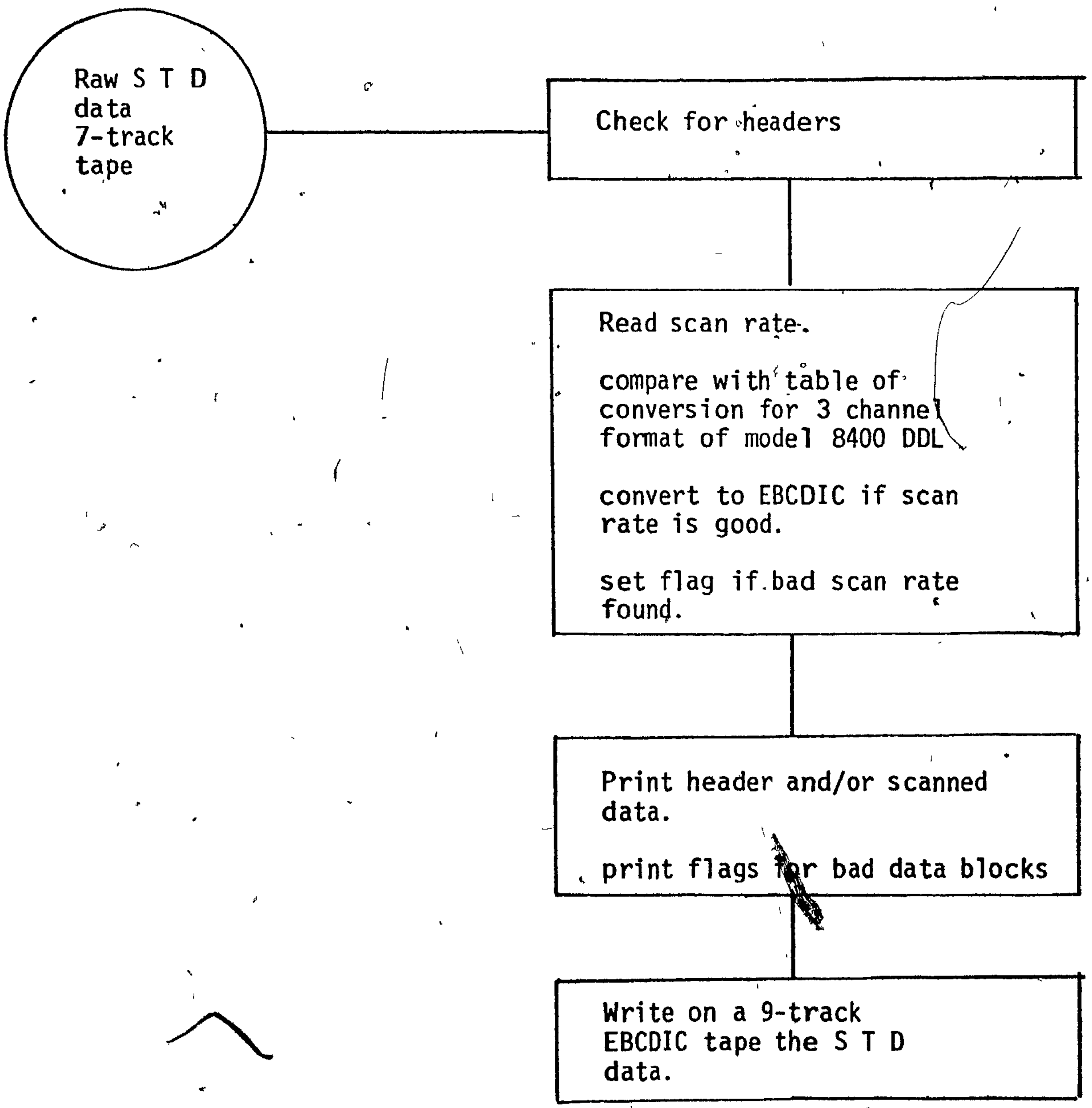

Fig. A-16 I.S.T program for conversion from 7-track BCD to 9-track EBCDIC tape.

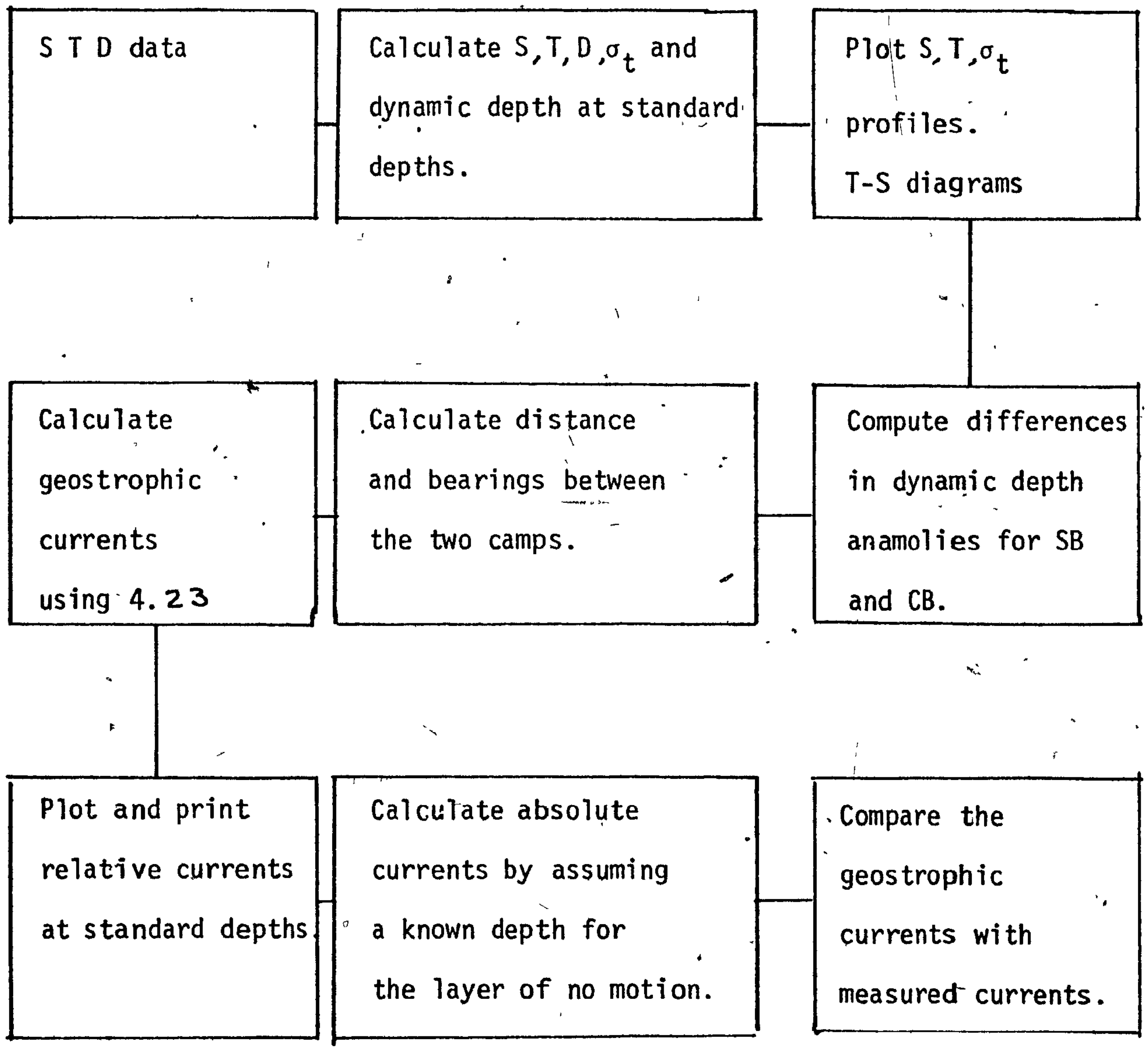

Fig. A-17 Geostrophic current calculations .